Low-Dose 3D Quantitative Vascular X-ray Imaging of the Breast

Pablo Milioni de Carvalho

UNIVERSITE PARIS-SUD

ÉCOLE DOCTORALE
Sciences et Technologie de l'Information, des Télécommunications et des Systèmes
Laboratoire d'*Imagerie par Résonance Magnétique Médicale et Multi-Modalité*

***DISCIPLINE** : PHYSIQUE*

THÈSE DE DOCTORAT

Soutenance le 22/09/2014

par

Pablo MILIONI DE CARVALHO

Low-Dose 3D Quantitative Vascular X-ray Imaging of the Breast

Composition du jury :

Directeur de thèse **:**	Serge MULLER	Directeur de Recherche (GE Healthcare)
Rapporteurs :	Martin YAFFE	Professeur (Faculty of Medicine, Univ. of Toronto)
	Ioannis SECHOPOULOS	Professeur Adjoint (Emory Univ. School of Medicine)
Examinateurs :	Irène BUVAT	Directeur de Recherche (IMNC, Université Paris Sud)
	Alain NOEL	Chercheur (CRAN, Université de Loraine)
	Luc DARRASSE	Directeur de Recherche (IR4M, Université Paris Sud)
	Ann-Katherine CARTON	Chercheur (GE Healthcare)

PhD Dissertation: Final Version
October 21, 2014

Acknowledgements

This PhD thesis research work was funded by GE Healthcare (Buc, France) in collaboration with IR4M laboratory based at the Université Paris Sud (Orsay, France), and with the financial support of the ANRT (Association Nationale de la Recherche Technique) under CIFRE convention n°2010/756.

I am very thankful to everyone who has directly or indirectly helped me in the completion of my thesis. I would like to begin by thanking my thesis advisor, Dr. Serge Muller, as well my academic co-advisor, Dr. Luc Darrasse, for the opportunity of working under their supervision and for welcoming me into their remarkable research groups. Thank you Serge for all the confidence you put in me, from the old days as an intern until my recent official integration in the team. You always inspired me to go further than I thought possible. I wish to convey my deepest gratitude to Dr. Ann-Katherine Carton, who has been my daily scientific advisor, for her continuous encouragement and support, the never-ending scientific discussions as well as the valuable advices and contributions she made to this thesis. I am indebted to her more than she knows.

I would like to thank Dr. Martin Yaffe and Dr. Ioannis Sechopoulos who accepted to review this manuscript. Thank you for the precious time you spent reading this thesis and the valuable comments you provided. I would like to extend my thanks to Dr. Irène Buvat and Dr. Alain Noël for accepting being members of my jury.

I wish to express my gratitude to the other members of the BCARe team. Thanks to Dr. Răzvan Iordache and Dr. Sylvie Saab-Puong, close collaborators who provided important feedback on my research work. Thanks also to Giovanni, Laurence, Nausikaä, Anja and Zhijin for all the good moments we shared during these last years, both inside and outside the office. I would like to extend my gratitude to the many colleagues at Buc. Thanks to Dr. Remy Klauz for the numerous discussions and helpful advices, fruits of a wide experience in X-ray imaging. I would like to express my gratitude to Drs. Cyril Riddell and Vincent Bismuth, who provided me with critical insight on 3D reconstruction and image processing, helping me progress in my investigations. Thanks to Dr. Lilane Ramus, Mathias Cisaruk and Matthieu Guillard, for helping to acquire the data on the interventional guided system. And thanks to Xavier, Matthieu, Yann, Colin, Fred, Richard, Heitor, Laure, Greg, and all others GE colleagues I did not mention. Thank you for your friendship and for making of Buc a wonderful work environment.

I would like to thank the members of IR4M for welcoming me in the lab. Thanks Drs. Xavier Maître and Luc Darrasse for the helpful guidance and feedback during these three years. Thank you Dr. Jean-Christophe Ginefri and Albine Pinseel for the administrative support at the university. Thanks my fellow PhD students at IR4M, in particular Marion and Maya. I owe special thanks to Dr. Clarisse Dromain, for her numerous clinical advices in contrast-enhanced imaging and breast anatomy. I would like to thank Dr. Sandra Canalé and Ariane Dunant, from Gustave Roussy cancer institute, for their cooperation during the reader study.

I would like to express my gratitude to the members of the CatSim collaboration. In particular, I would like to thank Dr. Bruno de Man and Dr. Paul Fitzgerald from GE Global Research Center (GRC), who have maintained the CatSim project alive and cooperated with my work in improving the simulation platform. I would like to thank Dr. Jed Pack for his feedback on simulation aspects,

and Dr. David Langan for sharing precious knowledge on material decomposition. I would also like to thank Dr. Cristina Cozzini and Dr. Dirk Beque for sharing their expertise on Monte Carlo simulation. I extend my gratitude to other GRC colleagues, Scott Zelakiewicz, Eric Tkaczyk, Yannan Jin and many others, for all their advices and feedbacks.

Finally, I owe a deep gratitude to my family, especially my parents and my brother, for their love and support throughout my life, despite always being thousand of kilometers away. And of course, thank you Marion, for being at my side during these last years and for supporting me all the nights, weekends and holidays spent in favor of science.

Summary

Background: Worldwide, breast cancer is the most common cancer and second deadliest cancer in women. Diagnostic imaging techniques are a critical part for screening, diagnosis, tumor staging and cancer therapy of the breast, guiding clinicians towards a more effective treatment planning and resulting in a better health outcome for the patient. Contrast-Enhanced Magnetic Resonance Imaging (CE-MRI) is the current standard imaging technique allowing detection of abnormal vascular development and lesion contrast uptake. CE-MRI is however very costly and not widely available. Moreover, its spatial resolution might not be sufficient to depict certain types of lesions including microcalcifications, whose presence is an important diagnostic indicator. It has been demonstrated that in combination with an iodinated vascular contrast agent, contrast-enhanced X-ray imaging can also give morphological and functional images. The development of Contrast-Enhanced Spectral Mammography (CESM) has made the clinical use of intravenous contrast enhancement with conventional mammography possible. However, CESM is a 2D projection technique and therefore presents limitations to depict the 3D internal structures of lesions and to provide accurate quantitative 3D functional information.

Contrast-Enhanced Digital Breast Tomosynthesis (CE-DBT) and dedicated Contrast-Enhanced Breast CT (CE-bCT) are two breast imaging modalities currently under investigation by academic and industrial research groups. It is however anticipated that the quantitative potential of CE-DBT is limited, due to the inherent low depth-resolution of limited opening angle DBT modality. CE-bCT with quasi-isotropic spatial resolution and voxel signal intensity proportional to the linear attenuation coefficient is believed to offer more accurate quantitative information, though a low-dose operation is still a challenge.

Objectives: The purpose of this thesis has been to study the technical feasibility of CE-bCT and its potential to accurately depict and localize tumors, as well as to provide accurate quantitative morphological and functional imaging information about tumors, at low radiation dose levels. To understand the incremental value of CE-bCT over CE-DBT, the quantitative potential of both technologies have been compared. This investigation has been performed through computer simulations.

Methods: At first, a simulation platform capable of modeling various X-ray breast imaging techniques and providing radiographic images of simple and complex computational phantoms was developed and validated. Secondly, an optimization study of a CE-bCT technique based on a dual-energy approach was performed, aiming to maximize image quality of iodine-enhanced and morphological images. Finally, the quantitative potential of CE-bCT and CE-DBT was compared through the assessment of iodine-enhanced lesion detectability, characterization, localization and 3D extent measurement. In a human observer study, depiction and characterization of iodine-enhanced lesions of different sizes, shapes and iodine uptakes was compared between CE-bCT and CE-DBT using a mesh-based anthropomorphic breast phantom.

Results: Simulation results assuming ideal detectors showed that to obtain optimal iodine detectability in recombined dual-energy images, low energy (LE) and high energy (HE) spectra need to bracket the iodine K-edge and an approximate 50%-50% average glandular dose repartitioning between the LE and HE is required. Comparison between different polychromatic spectral acquisition strategies revealed that iodine K-edge imaging with both energy-discriminating and

non-discriminating detector are feasible. Moreover, under the hypothesis of this study, a careful choice of topologic parameters (*e.g.* pixel and voxels sizes) in combination with noise-attenuating FBP reconstruction kernels and post-processing denoising schemes specific for dual-energy imaging allowed to depict the smallest lesion with minimum iodine concentration expected in clinical practice, at dose levels of 2-view mammography.

With respect to the CE-bCT vs CE-DBT comparison, a quantification study demonstrated that CE-bCT was superior in quantifying iodine concentration, while the artifacts caused by CE-DBT limited depth resolution prevented any precise quantification of iodine uptake (at least not without *a priori* knowledge of the iodine-enhanced lesion dimensions in all axes). In the human observer study, results revealed that sensitivity and specificity in iodine-enhanced lesion detectability and characterization for both geometries are not statistically different, except for lesion margin characterization for which CE-DBT demonstrated superior sensitivity. Results also showed that, for essentially round lesions, CE-DBT is more accurate and more precise in estimating lesion dimensions than CE-bCT, with image noise being the determinant factor in the comparison.

Conclusions: The simulation studies in this PhD thesis suggest that dual-energy iodine-injected CE-bCT could be a feasible technique for breast tumor depiction, localization and characterization, with dose levels comparable to standard mammography. While preliminary comparisons with CE-DBT suggests comparable depiction and characterization performance, the fully 3D information combined with high spatial resolution confirms CE-bCT as an interesting low-dose evolution of CESM toward 3D quantitative assessment of contrast uptakes and potential alternative to CE-MRI for some clinical indications.

Keywords: breast, computed tomography, simulation, dual-energy, spectral optimization, image quality, observer study

Résumé

Contexte : Le cancer du sein est le cancer le plus fréquent et le deuxième cancer le plus mortel chez la femme. Les techniques d'imagerie constituent un élément essentiel pour le dépistage, le diagnostic, la stadification et le traitement du cancer du sein. Elles guident les cliniciens vers une planification du traitement plus efficace, entrainant de meilleurs résultats sur la santé de la patiente. L'imagerie par résonance magnétique avec injection de produit de contraste (CE-MRI) est actuellement la technique d'imagerie standard pour la détection du développement vasculaire anormal et des prises de contraste des lésions mammaires. CE-MRI est cependant très coûteuse et peu disponible. De plus, sa résolution spatiale pourrait être insuffisante pour la détection de certains types de lésions, et ne permet pas d'imager les amas de microcalcifications, dont la présence est un important indicateur diagnostic. Il a été démontré que l'imagerie du sein par rayons X en combinaison avec l'injection d'un produit de contraste peut également fournir des images morphologiques et fonctionnelles. Le développement de l'angiomammographie double-énergie (CESM) a permis l'utilisation des produits de contraste intraveineux en clinique avec des appareils conventionnels de mammographie. Cependant, CESM est une technique de projection 2D et présente, par conséquence, des limites pour décrire la structure 3D interne des lésions et pour fournir une information fonctionnelle 3D précise.

La tomosynthèse numérique du sein avec injection de produit de contraste (CE-DBT) et le scanner dédié du sein avec injection de produit de contraste (CE-bCT) sont deux techniques d'imagerie actuellement en investigation par des groupes de recherche académiques et industriels. Il est cependant anticipé que le potentiel quantitatif de la CE-DBT soit limité, en raison de la faible résolution en profondeur due à l'ouverture angulaire limitée de la DBT. CE-bCT, avec sa résolution spatiale quasi-isotrope et son intensité de signal proportionnelle au coefficient d'atténuation linéaire, est supposée offrir une information quantitative plus précise, bien qu'une utilisation à faible dose de radiation reste toujours un défi.

Objectifs : L'objectif de cette thèse a été d'étudier la faisabilité de la méthode CE-bCT et sa capacité à détecter et localiser des tumeurs vascularisées, ainsi que d'offrir de l'information morphologique et fonctionnelle précise sur les tumeurs. Pour comprendre la valeur ajoutée de la CE-bCT par rapport à CE-DBT, le potentiel quantitatif des deux méthodes a également été comparé. Nos études ont été réalisées grâce à des simulations par ordinateur, validées par des mesures expérimentales.

Méthodes : Dans un premier temps, une plateforme de simulation capable de modéliser différentes techniques d'imagerie du sein par rayons X, et fournissant des images radiographiques de fantômes numériques simples et complexes, a été implémentée et validée. Deuxièmement, une étude d'optimisation pour la technique CE-bCT basée sur une approche double-énergie a été réalisée, dans le but de maximiser la qualité des images équivalentes-iode ainsi que des images morphologiques. Enfin, le potentiel quantitatif des méthodes CE-bCT et CE-DBT a été comparé au travers de l'évaluation de la détectabilité, de la caractérisation, de la localisation et de la mesure de l'étendue 3D des lésions iodées. Dans une étude impliquant des observateurs humains, la détectabilité et la caractérisation des lésions iodées de différentes tailles, formes et concentrations ont été comparées entre CE-bCT et CE-DBT, grâce à l'utilisation d'un fantôme anthropomorphique numérique du sein.

Résultats : Des investigations basées sur des détecteurs idéaux ont démontré que pour obtenir une détectabilité optimale de l'iode dans les images double-énergie recombinées, les spectres basse-énergie et haute-énergie doivent être placés autour de la discontinuité K de l'iode, avec une répartition de la dose glandulaire entre les acquisitions basse et haute énergies d'environ 50%-50%. La comparaison entre différentes stratégies d'acquisition spectrales polychromatiques a révélé que l'imagerie de la discontinuité K de l'iode est réalisable avec des détecteurs tant discriminants que non-discriminants en énergie. En outre, il a été démontré avec les hypothèses de cette étude qu'un choix judicieux des paramètres topologiques (p.ex. la taille des pixels et voxels) en combinaison avec des noyaux de reconstruction FBP et des méthodes de débruitage en post-traitement spécifiques à l'imagerie double-énergie, permettent de détecter la lésion de plus petite dimension et de plus faible concentration d'iode que l'on peut espérer rencontrer en clinique, avec une dose de radiation comparable à la mammographie conventionnelle.

En ce qui concerne la comparaison entre les méthodes CE-bCT et CE-DBT, une étude de quantification a démontré que la CE-bCT est supérieure pour la quantification de la concentration de l'iode, tandis qu'en CE-DBT les artefacts causés par la résolution limitée en profondeur empêchent toute quantification précise de la prise de contraste (au moins, sans avoir une connaissance a priori des dimensions des lésions selon les trois axes). Dans une étude avec des observateurs humains, les résultats ont révélé que la sensibilité et la spécificité de détectabilité et de caractérisation des lésions prenant le contraste n'ont pas été statistiquement différentes entre les deux méthodes, à l'exception de la caractérisation du contour des lésions pour laquelle CE-DBT a démontré une sensibilité supérieure. Dans la même étude, les résultats ont également montré que pour les lésions essentiellement rondes, CE-DBT est plus précise dans l'estimation des dimensions des prises de contraste, le bruit étant le facteur déterminant dans la comparaison.

Conclusions : Les études de simulation menées pendant cette thèse suggèrent que le scanner dédié du sein avec injection de produit de contraste iodé pourrait être une technique réalisable pour la détection, localisation et caractérisation des tumeurs du sein, pour un niveau de dose comparable à une mammographie standard. Bien que les comparaisons préliminaires avec CE-DBT suggèrent une performance comparable sur la détection et caractérisation, l'information 3D complète combinée avec une haute résolution spatiale font de CE-bCT une évolution intéressante de CESM vers une évaluation quantitative 3D des prises de contraste, et une alternative potentielle à CE-MRI pour certaines indications cliniques.

Mots-clés : sein, tomodensitométrie, simulation, double-énergie, optimisation spectrale, qualité image, étude d'observateur

Contents

List of Figures

List of Tables

List of Acronyms

ACNR	Anti-Correlated Noise Reduction
ACR	American College of Radiology
AGD	Average Glandular Dose
bCT	breast CT
BI-RADS	Breast Imaging-Reporting and Data System
CE-bCT	Contrast-Enhanced breast CT
CE-DBT	Contrast-Enhanced Digital Breast Tomosynthesis
CE-DM	Contrast-Enhanced Digital Mammography
CE-MRI	Contrast-Enhanced Magnetic Resonance Imaging
CESM	Contrast-Enhanced Spectral Mammography
CE-US	Contrast-Enhanced Ultrasound
CNR	Contrast-to-Noise Ratio
CNR$_{eff}$	effective Contrast-to-Noise Ratio
CNRD	Contrast-to-Noise Ratio normalized by Dose
CsI	Cesium Iodide
CT	Computed Tomography
DBT	Digital Breast Tomosynthesis
DE	Dual-Energy
DgN	Normalized Glandular Dose Coefficient
DQE	Detective Quantum Efficiency (MTF^2/NPS)
DS-DF	Dual-Source with Dual Filtration
EI	Energy-Integrating
FBP	Filtered BackProjection
FOM	Figure-of-Merit
FOV	Field-of-View
FPD	Flat Panel Detector
HE	High-Energy
HVL	Half Value Layer
IGS	Image Guided System
KERMA	Kinetic Energy Released per unit Mass
LE	Low-Energy
MC	Monte Carlo
MRI	Magnetic Resonance Imaging
MTF	Modulation Transfer Function
MX	Mammography
NNPS	Normalized Noise Power Spectrum
NPS	Noise Power Spectrum
PC	Photon-Counting
PDF	Probability Density Function
PMMA	Poly Methyl MethAcrylate
PSF	Point Spread Function
QDE	Quantum Detection Efficiency ($\eta(E)$)

ROI	Region-of-Interest
SDD	Source-to-Detector Distance
SI	Signal Intensity
SID	Source-to-Isocenter Distance
SNR	Signal-to-Noise Ratio
SPR	Scatter-to-Primary Ratio
SS-DF	Single-Source with Dual Filtration
SS-FkV	Single-Source with Fast kV Switching
SS-PC	Single-Source with Energy-Resolved Photon-Counting
TV	Total Variation
U/S	Ultrasound
VBD	Volume Breast Density
VL	Value Layer
VOI	Volume-of-Interest

Introduction

Worldwide, breast cancer is the most common non-skin cancer and second deadliest cancer in women, with nearly 1.7 million new cases diagnosed in 2012 [1]. In the United States, 12.3% percent of women will be diagnosed with breast cancer at some point during their lifetime. For 2013, approximately 232 000 new cases and 39 000 deaths are estimated[1]. In France, approximately one woman in ten will develop a breast cancer during her lifetime. With 53 000 new cases and almost 11 500 deaths estimated in 2011 [2], breast cancer is the most common cancer among women in France and is the leading cause of cancer death.

In the light of these statistics, breast cancer is a major problem for global public health. In response, the government of various countries worldwide have adopted organized breast *screening examination* programs for an asymptomatic population satisfying certain eligibility criteria, *e.g.* age group, breast density, family history etc. Mammography is the only technique which has shown to reduce the mortality from breast cancer in a cost-effective way [3], and is today the standard technique for population-based screening. Ultrasound (U/S) and Magnetic Resonance Imaging (MRI) are complementary imaging techniques used mostly for dense breasts and high-risk women [4, 5].

During breast cancer development, the formation of new pathological blood vessels through angiogenic process provides irrigation for tumors beyond 1-2 mm and thus fuel their growth [6]. The new vascular network replenishes the tumors with nutrients, oxygen and enables them to eliminate metabolic wastes. In a breast cancer diagnosis, staging and therapy follow-up setting, imaging techniques combined with intravenous contrast agents have been developed to visualize breast tumor angiogenesis. When injected in the body, the contrast media enhances the visibility of abnormal vascular development and cancerous lesions, which could ultimately improve cancerous lesion detection, characterization and localization. Contrast-Enhanced Magnetic Resonance Imaging (CE-MRI) is the current standard imaging technique allowing detection of abnormal vascular development and lesion contrast uptake [7]. CE-MRI is however very costly and not widely available. Moreover, its spatial resolution might not be sufficient for certain types of lesions and does not allow microcalcifications depiction, whose presence is an important diagnostic indicator. Other techniques such as contrast-enhanced full-body Computed Tomography (CT) [8], Positron Emission Tomography (PET) combined with full body CT [9] and contrast-enhanced Doppler U/S (CE-US) [10] have also shown positive results in emphasizing breast tumor angiogenesis. However, these techniques each have their own limitations with respect to each technical aspects including spatial resolution, radiation dose, cost, operator dependent outcome and economical aspects including availability.

Contrast-enhanced X-ray imaging of the breast, as a potential less costly alternative, is currently under investigation. With an iodinated vascular contrast agent, contrast-enhanced X-ray imaging can also provide morphological and functional images. Two imaging techniques have been proposed: temporal and dual-energy recombination. In the temporal technique, radiographic images of the breast are acquired before and after intravenous administration of an iodinated contrast agent, using X-ray spectrum containing energies predominantly above the K-edge of iodine [11, 12].

[1] National Cancer Institute, `http://seer.cancer.gov/statfacts/html/breast.html` (Accessed on April 4th, 2014)

Although clinical studies revealed some potential of the temporal approach in highlighting tumor angiogenesis uptake and contrast-agent kinetics [13–15], this technique has not been implemented in clinical practice. The main reason is that the temporal approach required two injections of iodine to image two breasts, entailing in longer examinations and increased iodine toxicity exposition. Additionally, Diekmann *et al.* [15] evidenced in a multicenter clinical study that the most important diagnostic information comes from the morphological analysis of the contrast enhancement and its intensity, rather than the contrast-agent kinetic information. Substantial patient motion artifacts due to the extended time between pre- and post-contrast acquisitions and consequent loss of lesion morphologic detail were also observed. Alternatively, 2D Contrast-Enhanced Spectral Mammography (CESM) technique was proposed to overcome the limitation of the temporal approach. In CESM, a dual-energy recombination approach is used, leveraging the iodine K-edge absorption discontinuity for contrast enhancement while minimizing patient motion artifacts with rapid successions of low-energy (LE) and high-energy (HE) acquisitions. The feasibility of this technique was shown in 2003 [16] and became clinically available in 2010 with the introduction of SenoBright™ application (GE Healthcare; Chalfont St Giles, UK). CESM is however a 2D projection technique of a 3D object, therefore limiting morphologic characterization of contrast uptakes when compared to 3D techniques. An alternative 3D X-ray imaging technique, with wide availability, low-cost, specifically designed for breast imaging and providing accurate quantitative position, morphologic and functional lesion information would be therefore a natural evolution of contrast-enhanced X-ray imaging.

Contrast-Enhanced Digital Breast Tomosynthesis (CE-DBT) and Contrast-Enhanced dedicated breast CT (CE-bCT) are two potential 3D evolutions of CESM and currently under investigation by academic and industrial research groups. It is however anticipated that the quantitative potential of CE-DBT is limited, due to the inherent low depth-resolution of limited opening angle DBT modality. CE-bCT with quasi-isotropic spatial resolution and voxel signal intensity proportional to linear attenuation coefficients is believed to offer more accurate quantitative information, though a low-dose operation could still be a challenge. Today, the incremental value of CE-bCT over CE-DBT in their ability to provide quantitative information at low radiation dose levels is still unknown. A complete evaluation on the quantitative performance of both technologies would be beneficial.

For the same reasons as CESM, both CE-DBT and CE-bCT techniques would benefit from iodine K-edge imaging techniques using dual-energy acquisitions. While some research effort has been oriented towards the assessment and optimization of dual-energy CE-DBT geometry, acquisition parameters and protocols [17–26], little investigation on dual-energy recombination techniques for iodinated contrast-agent and tumor angiogenesis enhancement in a dedicated breast CT setup was performed. As a consequence, before any comparison with CE-DBT, an optimization study aiming to reveal the dual-energy acquisition strategy and acquisition parameters maximizing the performance of CE-bCT in depicting contrast-agent uptake is imperative.

This PhD thesis research has been focused on two topics: 1) the optimization and assessment of an iodine-enhanced dual-energy breast CT technique and 2) its comparison with CE-DBT in their potential to accurately depict and localize tumors, as well as to provide accurate quantitative information on contrast uptake morphology and concentration, at radiation dose levels comparable to a two-view mammogram. A cone-beam geometry was considered both for CE-bCT and CE-DBT, since there is an interest in investigating techniques based on typical mammography geometries. This choice would allow for instance to provide different exams with the same equipment, reducing cost and improving accessibility. All investigations have been performed through realistic computer simulations. This theoretical approach allows quantifying the effect of each individual parameter in a complex imaging chain on image quality.

In Chapter 1, a short description on the breast anatomy, the development of cancerous tumors and its association to pathological angiogenesis is provided. An overview on established clinical vascular imaging techniques for breast cancer treatment is presented. Recently developed and commercially available techniques with increasing acceptance and usage are also discussed. Finally, CE-DBT and CE-bCT techniques are presented as two new potential candidates for vascular

contrast-agent imaging. Details on technological aspects, and their individual advantages and limitations are provided.

In Chapter 2, a detailed description of the simulation platform software developed for our research is provided. This platform is based on CatSim, a computer software initially conceived at GE Global Research Center (*CT and X-ray Laboratories*, Niskayuna, NY, USA) to simulate 3rd generation CT projection images using analytical test objects [27]. As part of this PhD thesis research, modules for CatSim simulation chain have been developed to model X-ray projections of breast phantoms at a typical energy range used in breast imaging. The design of digital breast phantoms aiming to emulate the compressed and uncompressed breast anatomy is presented. Both simple phantoms, combining simplistic geometric shapes and complex mesh-based anthropomorphic phantoms, providing more realistic allure of the breast anatomy, are considered.

In Chapter 3, in order to make sure that the implemented simulation chain is capable of emulating realistic physical phenomena underlying an X-ray breast imaging system, an extensive validation of the developed models with regard to previously published and experimentally obtained data is provided. The accuracies of X-ray spectrum modeling, Monte Carlo simulation of photon interactions with matter as well as signal and noise propagation in digital detectors are qualitatively and quantitatively evaluated.

In Chapter 4, the main existing spectral imaging acquisition techniques and the algorithms used to combine spectral images into exploitable functional information are discussed. A brief overview on the different methods allowing to obtain dual-energy data is also provided. A formulation of the dual-energy three-material decomposition allowing for iodine K-edge imaging in digital breast tomosynthesis and dedicated breast CT setups are discussed.

In Chapter 5, the optimization of dual-energy spectra and acquisition strategies for CE-bCT is performed, leveraging the implemented simulation platform and the dual-energy recombination framework described in Chapters 2 and 4, respectively. The critical factors and optimization criteria are defined, and the spectral optimization is performed using monochromatic hypothesis. Then, a new spectral optimization is performed for different polychromatic dual-energy acquisition strategies (dual-source, fast kVp switching, energy-discriminating detector). The performance of the different dual-energy acquisition strategies is subsequently compared. Finally, since columnar structured Cesium Iodide (CsI) scintillators have been widely used for digital breast X-ray imaging, a spectral optimization study considering different CsI layer thicknesses is performed.

In Chapter 6, using previously optimized dual-energy acquisition parameters for CE-bCT and CE-DBT, their quantitative potential is evaluated and compared through a series of experiments. Two preliminary studies evaluate the effect of CE-bCT and CE-DBT system topologies on lesion 3D extent estimation precision and iodine uptake quantification accuracy. For a more complete evaluation, a human observer study comparing iodine-enhanced lesion depiction and characterization in simulated CE-DBT and CE-bCT iodine-equivalent images is presented.

In Chapter 7, the optimized CE-bCT acquisition is discussed with particular focus on radiation dose requirements to depict iodine-enhanced lesions with minimal size and minimal uptake expected in clinical practice, while dose levels are compared to those expected for CE-DBT and current two-view standard mammography. Different post-processing denoising strategies are evaluated to improve iodine-enhanced lesion detectability in recombined CE-bCT images and potentially reduce the associated radiation dose.

Finally, we conclude on the main results and contributions of this PhD thesis research, and put forward research development perspectives for CE-bCT and CE-DBT applications.

Chapter 1

Clinical Context

1.1 Breast Anatomy and Cancer Development

Anatomy of the Healthy Breast
The human breast is mainly composed of fibroglandular and adipose tissues. The mammary gland is enveloped by a thin layer of connective and adipose tissues called Cooper's ligaments. It provides a connection between the pectoral muscle and its deep surface, as well as between the skin and the superficial surface. The internal structure of the mammary gland is composed by a tree-like structure of lactiferous ducts, which originate at the nipple through lactiferous sinuses, and grow towards the pectoralis muscle. At the terminal part of the lactiferous ducts we encounter lobules regrouping milk-secreting glands, *i.e.* the alveoli or acinii. The glandular tissue refers to the aggregation of terminal ductal lobular units (0.5 to 2 mm diameter), each containing between ten and hundred alveoli (approximately 0.12 mm diameter). The latter are surrounded by dense fibrous connective tissues with adipose cavities [28–30], as well as epithelial cells which are responsible for milk production during the lactation period. The glandular and connective tissues together are known as *Fibroglandular tissue*. Beside the intraglandular adipose tissue, adipose tissue is further divided in two types based on their anatomical location: subcutaneous adipose compartments are positioned under the skin and retromammary adipose tissue is found near the chest wall. The proportion of adipose and fibroglandular tissue varies among individuals. After the menopause, the proportion of glandular tissues tends to decrease, being replaced by adipose tissue. Figure 1-1a illustrates a sagittal cross-section of the breast anatomy.

A dense vascular network carries nutrients and oxygen inside the breast. Arteries carry oxygenated blood from the heart to the chest and the breasts, while the veins bring the deoxygenated blood to the heart. The axillary artery extends from the armpit and drains the outer half of the breast. The internal mammary artery leaves the neck down to the breast, draining its inner part. A lymphatic network is concentrated in the armpit area. Axillary lymphs located near the armpit drain 97% of lymphatic fluid in the breast. Another lymph chain extends along the median axis of the thorax (internal mammary chain) and drains the remaining 3% of lymphatic fluid. Figure 1-1b illustrates the lymphatic system network in the breast and adjacent regions.

Breast Cancer Development
Breast cancer is most commonly linked to cancerous development in the lactiferous ducts or the glandular lobules. There are many types of associated diseases, resulting in lesions most often classified into *benign* or *malignant lesions*. Benign lesions do not endanger the life of the patient while malignant lesions have the potential to lead to her death.

Among benign lesions we distinguish mainly the *cysts, fibroadenomas, papillomas, abscess, hematoma, inflammation, radial sclerosis, ductal ectasia, lipomas* and *cytosteatonecrosis*. Although

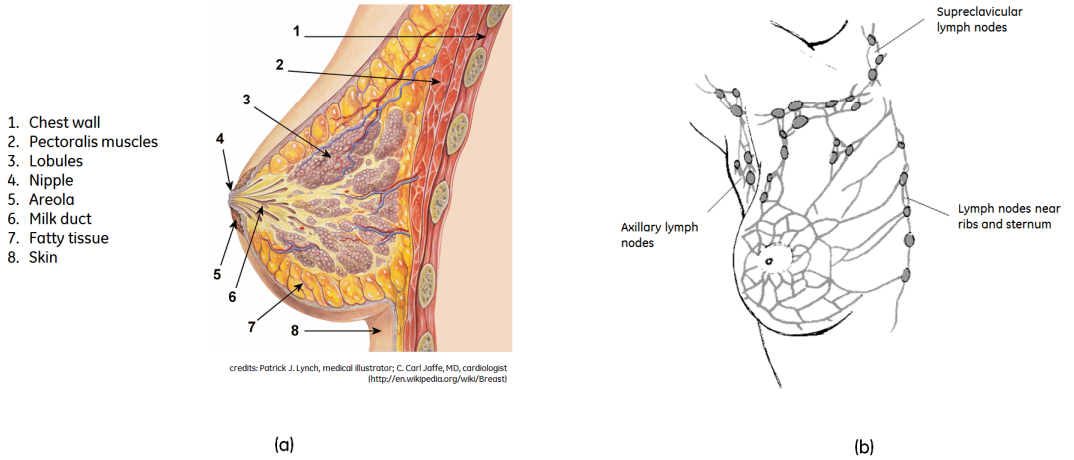

Figure 1-1: (a) Sagittal cross-section illustration of the breast anatomy and (b) lymphatic system network illustration

benign lesions are not life-threatening, they can cause symptoms and sometimes be linked with a higher risk of developing breast cancer in the future. Benign lesion are usually classified into 3 general groups of lesion, based on the cells growth (proliferative) and abnormality (atypia): *non-proliferative lesions* do not seem to affect cancer risk, *proliferative lesions without atypia* slightly increase cancer risk and *proliferative lesions with atypia* raise the risk of cancer.

Malignant lesions are primarily classified by their histological appearance (*in situ* or *invasive*) and their tissular origin (ducts or lobules). Carcinoma *in situ* is a form of pre-invasive cancer, characterized by a proliferation of cancerous cells within a particular tissue compartment without invading the surrounding tissue. *Ductal Carcinoma In Situ*, or DCIS, is associated to cancerous development within the mammary ducts, while *Lobular Carcinoma In Situ*, or LCIS, is associated with cancerous development in the lobules. On the other hand, *invasive* carcinoma does not confine itself to the initial tissue compartment. Three-quarters of invasive carcinomas are *Invasive Ductal Carcinoma* (IDC), in which tumor cells progress not only inside the ducts but also around them. The IDCs are often lobulated masses containing spicules radiating from their center. Around 10 to 15% [31] of invasive carcinomas are *Invasive Lobular Carcinoma* (ILC), in which tumor cells infiltrate the tissue filaments running along the ducts and vessels, thus preserving the original architecture of the breast. Due to the small creation of new connective tissue, it is hard to distinguish an ILC from the normal parenchyma.

The presence and proximity of lymph nodes are important factors influencing breast cancer spreading and the appearance of metastasis. Cancerous cells from the breast can infiltrate the lymph nodes and be transported to other areas of the body through the lymphatic system. Treatment and survival is often determined by whether or not breast cancer remains localized or spreads to other locations in the body. The latter case is usually associated with a dramatically decreases in a patient's likelihood of survival.

There are several known physiological factors that can be associated with the risk of developing a breast cancer. Firstly, the gender, age and reproductive or hormonal factors such as early first period, late first pregnancy, late parity, low number of live-born children, oral contraceptive and hormone replacement therapy (HRT). Other factors to be considered are: radiotherapy through the chest wall during childhood, close family history of breast or ovarian cancers constituting a genetic predisposition to the development of breast cancer, the BRCA1 and BRCA2 gene mutations, the presence of diseases diagnosed as benign which can evolve to a cancer, smoking, obesity, increased alcohol consumption, etc.

For a more detailed description on breast cancer development and the associated benign and

malign lesions, we refer the reader to the work of A. Cooper [32].

Tumor Angiogenesis

Almost all tissues growing larger than a few millimeters in size develop a vascular network through a process known as *angiogenesis*. Once formed, the vascular network is a stable system that regenerates slowly. The normal regulation of angiogenesis is governed by a fine balance between factors that induce the formation of blood vessels and those that halt or inhibit the process. When this balance is destroyed, it usually results in pathological angiogenesis which causes increased blood-vessel formation in diseases which depend on the angiogenesis to grow. Pathological angiogenesis, or the abnormal rapid proliferation of blood vessels, is implicated in over 20 diseases, including cancer.

During breast cancer development, formation of new pathological blood vessels will provide irrigation for tumors beyond 1–2 mm and thus fuel to their growth [6], replenishing them with nutrients, oxygen and enabling them to eliminate metabolic wastes. Angiogenesis and tumor growth is then accompanied by the disruption of the basement membrane and the cancer, until now *in situ*, becomes invasive.

Imaging techniques combined with intravenous contrast agents have been developed to highlight breast tumor angiogenesis. When injected in the body, the contrast media enhances the visibility of abnormal vascular development and cancerous lesions, which could ultimately improve lesion detection, characterization, localization and vascularization quantification. A brief description on the most widely used imaging techniques highlighting breast tumor angiogenesis is provided in Section 1.2.

For breast imaging, clinical studies have hypothesized that tumor angiogenesis could be associated with the diagnostic outcome of breast cancer [33]. The calculation of the Microvessel Density (MVD), which consists in counting microvessels stained by immunohistochemistry and observed by optical microscopy, is commonly used to quantify angiogenesis associated with breast cancer. It could be an effective prognostic factor for invasive breast cancer [34–36]. Additionally, several studies have shown that vascular density is also associated with a more aggressive disease in patients with no lymph node invasion and in those with *in situ* [37–39] breast cancer.

Epidemiology

Worldwide, breast cancer is the most common non-skin cancer and second deadliest cancer in women than any other cancer, with nearly 1.7 million new cases diagnosed worldwide in 2012. This represents about 12% of all new cancer cases and 25% of all cancers in women [1]. In the United States, 12.3% percent of women will be diagnosed with breast cancer at some point during their lifetime. For 2013, approximately 232 000 new cases are estimated, representing 14.1% of all new cancer cases in the U.S., and 39 000 deaths [1].

In France, approximately one woman in ten will develop breast cancer in her life. With 53 000 new cases estimated in 2011 [2], breast cancer is the most common cancer among women, representing 33% of all new cancer cases in women. Breast cancer is also the leading cause of cancer death in France, with almost 11 500 deaths estimated in 2011, accounting for 18.3% of female cancer deaths.

Figure 1-2 shows the cancer incidence and mortality rates in France, per cancer type, as disclosed by the Institute for Public Health Surveillance (Institut de Veille Sanitaire - InVS) and the National Cancer Institute (Institut Nationale du Cancer - INCa), in 2011 [2]. We can see that breast cancer leads both incidence and mortality rates, followed by colon rectum and lung cancers.

Figure 1-3 illustrates the evolution of breast cancer incidence and mortality in France from 1980 to 2005, as disclosed by the InVS [41]. The incidence of breast cancer in France has increased

[1] National Cancer Institute, `http://seer.cancer.gov/statfacts/html/breast.html` (Accessed on April 4th, 2014)

Figure 1-2: Incidence and mortality rates in France per cancer type (standardized to the world population), in 2011. Data source: *Projection de l'incidence et de la mortalité par cancer en France en 2011.* Rapport technique. Saint-Maurice: Institut de veille sanitaire; 2011, 78 p – Ref. [2]

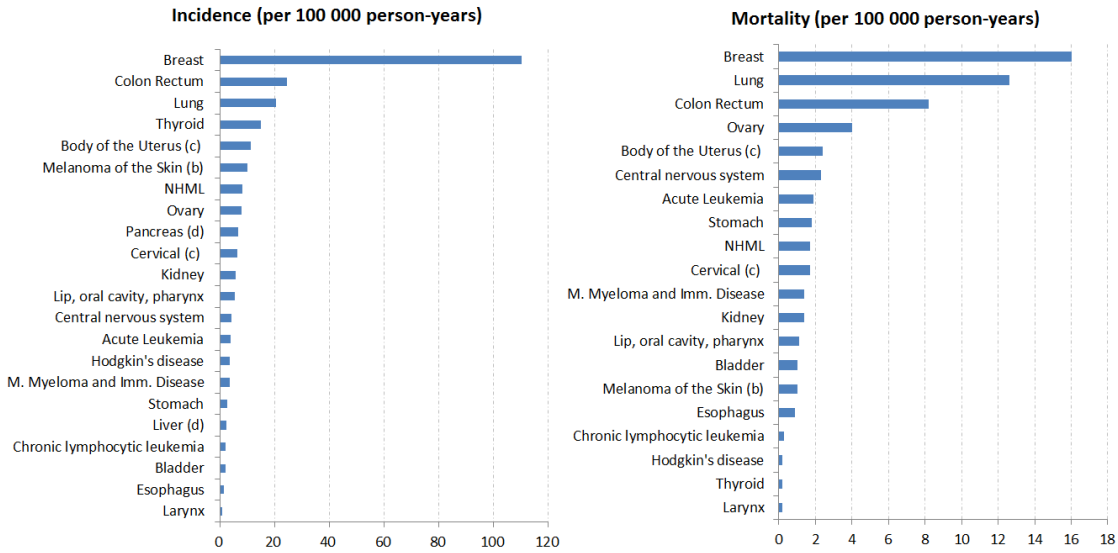

(a) Hematological tumors are excluded from solid tumors

(b) The skin cancers other than melanoma, are excluded.

(c) The shares of deaths from cervical cancer of the uterus and uterine cancer were estimated by a specific method [40]

(d) Mortality estimates are not presented due to the uncertain quality of the data.

significantly and steadily between 1980 and 2005 with an incidence rate (standardized to the world population), which has almost doubled from 56.8 to 101.5 cases per 100 000 women. The mortality rate (standardized to the world population) decreased from 19.8 to 17.7 cases per 100 000 women from 1995 to 2005, thanks to screening and early detection, as well as to progress in treatment. Accordingly, and along with the substantial mortality rates described above, we may conclude that breast cancer remains today a major problem for global public health.

Early Breast Cancer Detection

Knowing that the probability of a tumor producing metastasis increases with its size, it has been shown that its early detection reduces mortality [42]. In response, the government of various countries worldwide have adopted organized breast *screening examination* programs for an asymptomatic population satisfying certain eligibility criteria, *e.g.* age group, breast density, family history etc. These criteria vary from one country to another, depending on public health policies and local statistics. In France, for example, since January 1st 2004, the female population between 50 and 74 years-old is invited every 2 years to participate in a free screening examination [43].

Mammography is the current standard for population-based screening. When applied in a screening setting, mammography is the only technique which has shown to reduce the rate of death from breast cancer in a cost-effective way [3], especially among women aged over 50 years [44]. Mammography is a low radiation x-ray projection technique providing morphological images of breast tissue. Clinical studies have shown a 25% to 30% reduction of the mortality associated with this disease in women aged 50 to 69 years and a reduction of approximately 16% for those aged between 40 and 49 years [45]. Ultrasound (U/S) and Magnetic Resonance Imaging (MRI) are complementary imaging techniques used mostly for dense breasts and high-risk women [4, 5].

In France, mortality which had remained stable since 1980, began to decrease, as illustrated in Figure 1-3. This increased survival, concurring with the results described in most Western

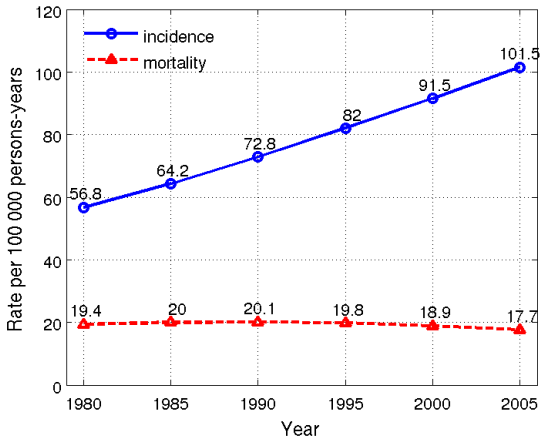

Figure 1-3: Evolution of breast cancer incidence and mortality rates in France (standardized to the world population), from 1980 to 2005. Data source: Belot *et al.*, 2008 – Ref. [41], `www.invs.sante.fr/surveillance/cancers/estimations_cancers/default.htm` (Accessed 06 Dec 2013)

countries [1], can be explained in part by increasing the proportion cancers detected at an early stage in connection with the development of screening practices and secondly the major therapeutic progress in the early 2000's [46].

1.2 Standard Vascular Imaging Techniques for Breast Cancer Treatment

This section provides a brief overview on established vascular imaging techniques, widely accepted in clinical practice for breast cancer management, as well as additional descriptions on recently developed and commercially available techniques with increasing acceptance and usage. For more in-depth description on the different breast imaging techniques and their individual technological aspects, we refer the reader to the work of D.B. Kopans [47].

For an illustrative guidance, in Figure 1-4 we summarize the clinical workflow of breast cancer screening, diagnostics, staging and therapy monitoring, and the corresponding imaging techniques for which vascular imaging is clinically available or under development. Figure 1-4 also summarizes the main benefits and limitations of each imaging technique, as discussed below.

1.2.1 Contrast-Enhanced Magnetic Resonance Imaging

In certain situations, such as when a woman has a very high risk of breast cancer and high breast density, Contrast-Enhanced MRI (CE-MRI) in combination with mammography is recommended as a screening tool [4, 5, 7, 48–51]. CE-MRI has the advantage that it does not involve exposure to ionizing radiation, for which high-risk women may exhibit an increased sensitivity [52–55]. It has been shown that CE-MRI can increase detection of breast cancer for certain groups of women [56,57]. Using gadolinium chelates as a vascular contrast agent, CE-MRI does not only provide 3D images of breast morphology, but also functional images allowing detection of abnormal vascular development and lesion contrast uptake. The signal intensity of gadolinium-enhanced lesions in CE-MRI was shown to be correlated with the Microvessel Density (MVD) [58,59]. Another important information in CE-MRI, complementary to the contrast-enhanced lesion morphology, is the kinetics of the contrast agent. Early studies have shown that malignant lesions tended to take an earlier and more pronounced contrast than the benign lesions [60, 61]. Hence, the shape of the curve of contrast enhancement can be used as an indication of the benign or malignant nature of the lesion.

In a tumor staging and treatment setting, CE-MRI is currently the most recommended technique by the European Society of Breast Imaging (EUSOBI) [7], the European Society of Breast Cancer Specialists (EUSOMA) [51] and the American College of Radiology (ACR) [7]. CE-MRI results have shown to strongly correlate with the extent of disease [62–64], which forms the basis for treatment decisions. CE-MRI is also recommended for monitoring early cancer response to chemotherapy so as to avoid unnecessary toxicity and cost without potential benefit from treatment and to decide whether or not to continue or change the therapy plan [65]. After neo-adjuvant chemotherapy, assessment of residual tumor [66] before surgery allows the surgical approach to be optimized to ensure negative margins and maximize breast conservation surgery.

Despite its great success, CE-MRI presents some important limitations. From a technical standpoint, the first limitation is the inability to rapidly image the whole breast volume while preserving a good spatial resolution. The speed of the MRI acquisition comes at the expense of its spatial resolution, which may negatively affect the morphological analysis of the contrast uptake. Another important limitation is the appearance of non-pathological contrast uptakes linked to hormonal fluctuations [67], surgery and radiotherapy [68]. In addition, some benign fibroadenomas may behave identically to malignant tumors. From a socio-economic standpoint, two big disadvantages of CE-MRI are its high cost and limited availability [69, 70]. In France, a CE-MRI costs about five times a bilateral mammography exam (293€ for a CE-MRI exam, 66€ for a bilateral mammography exam [71]) and only 20% of prescribed CE-MRI exams are performed due to limited availability. In addition, as discussed above, CE-MRI has a high rate of false-positives [72], which may result in more unnecessary biopsies and other additional examinations. Other practical disadvantages that should be highlighted are the discomfort encountered by claustrophobic patients and the safety issues for patients who posses metal implants and non-MRI-compatible foreign bodies.

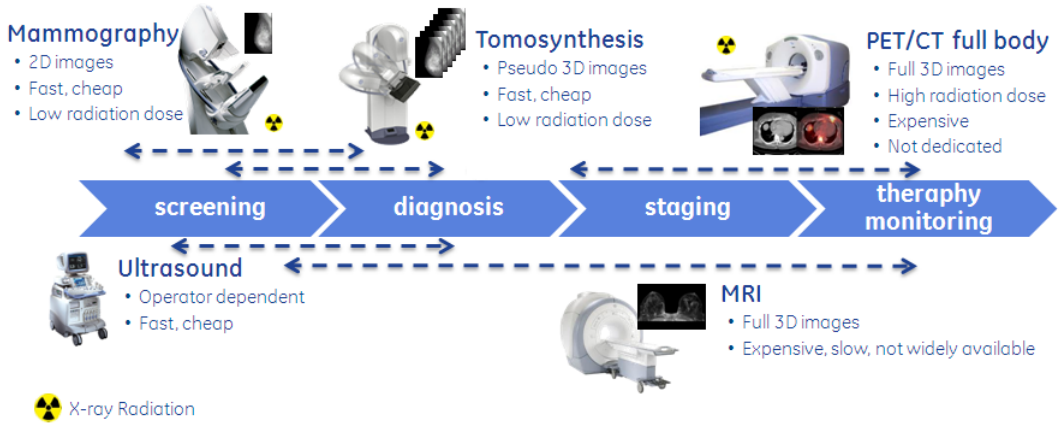

Figure 1-4: Clinical workflow for breast cancer management and the corresponding main imaging techniques associated to each step. The main limitations of each technique are summarized

1.2.2 Contrast-Enhanced Digital Mammography

The advent of digital mammography and the ability to develop post-processing techniques have stimulated interest in Contrast-Enhanced Digital Mammography (CE-DM). Two imaging techniques have been developed: temporal and spectral recombination. Both techniques take advantage of the sudden increase in iodine attenuation coefficient (*absorption edge*) as a function of X-ray photon energy; just above its K-shell binding energy (33.2 keV), iodine attenuation is 5.5 time higher than just below its K-edge (cf. Annex A for more details in x-ray photon interaction with matter).

CE-DM using a temporal subtraction technique was pioneered in 2002 [11,12]. In this approach, radiographic images of the breast are acquired before and after intravenous administration of an iodinated contrast agent using a high-energy (HE) X-ray spectrum containing energies predominantly above the K-edge of iodine. Logarithmic subtraction of the pre- and post-contrast images are used to obtain functional iodine enhancement images in which signal intensities are proportional to the quantity of iodine crossed by the X-ray beam. This technique feasibility was demonstrated in two clinical pilot studies [13, 73]. Later clinical studies have shown some potential of the temporal approach in highlighting tumor angiogenesis uptake and contrast-agent kinetics, ultimately improving the final diagnosis when it complements a standard mammography examination [13–15]. Although these clinical studies revealed the prognostic potential of the temporal approach, this technique has not been implemented in clinical practice. The main reason is that the temporal approach required two injections of iodine to image two breasts, entailing in longer examinations and increased iodine toxicity exposition. Additionally, Diekmann *et al.* [15] evidenced in a multicenter clinical study that the most important diagnostic information comes from the morphological analysis of the contrast enhancement and its intensity, rather than the contrast-agent kinetic information. Moreover, substantial patient motion artifacts due to the extended time between pre- and post-contrast acquisitions was observed and entailed in the loss of lesion morphologic detail.

To overcome the limitation of the temporal approach, dual-energy (DE) contrast-enhanced digital mammography, also named contrast-enhanced spectral mammography (CESM) has been proposed as an alternative solution [16]. In CESM, after iodinated contrast-agent injection, low-energy (LE) and high-energy (HE) image pairs are acquired at energies that closely bracket the iodine K-edge, simultaneously or in rapid successions. Iodine-enhanced images are then obtained by recombining the two images. GE Healthcare is currently the only company with a commercial CESM application as extension of the existing indications for diagnostic mammography with the GE Senographe® Essential or Senographe® DS systems (GE Healthcare; Chalfont St Giles, UK).

This imaging technique can be used as an adjunct following mammography and ultrasound exams to help localize a known or suspected lesion. A clinical study, with 26 patients, demonstrated the feasibility and potential of dual-energy technique for mammography [16].

CE-DM techniques have simpler implementations and faster acquisitions when compared to CE-MRI and CE-US, and much with higher spatial resolution. However, CE-DM images are still acquired from 2D projection of a 3D object, limiting morphologic characterization and localization of iodine-enhanced lesions.

1.2.3 Other Vascular Imaging Techniques Used in Clinical Practice

Contrast-Enhanced Full-Body CT
The feasibility of tomographic breast imaging using a standard whole body scanner was assessed in early 80's by Muller *et al.* [74]. The authors concluded that although the system being technically capable of providing good images and the ability to detect distant metastases through incidental findings, the trade-off between the new diagnostic information and the high amount of radiation dose delivered to the breast and neighboring body tissues in the thorax was insufficient when compared to standard mammography. Moreover, the contemporaneous dedicated breast computed tomography (CT) scanners produced better results.

Later on, the development of multidetector CT (MDCT) scanners with faster acquisitions and improved resolution encouraged further research on breast imaging. Many clinical studies were conducted to evaluate MDCT when associated with the administration of iodinated contrast-agents as a tool for breast lesion diagnosis, cancer extent and conservation surgery planning [8,75–79]. For these applications, contrast-enhanced MDCT imaging of the breast has shown to provide excellent sensitivity (especially for patients with dense breast) but limited specificity [80]. Moreover, Inoue *et al.* [77] also noted that that contrast-enhanced MDCT could be used for dynamic CT and distinguish carcinoma from benign lesions. However, in all these studies radiation dose to the patient was still substantially higher than standard mammography levels [78]. More recently contrast-enhanced CT has been combined with Positron Emission Tomography (PET) imaging systems [81,82] in order to produce in order to generate additional functional information. However, a practical limitation is that nuclear imaging techniques have a relatively long implementation time and are very expensive [9].

Contrast-Enhanced Ultrasound
Breast Ultrasound (U/S) can be used to solve equivocal radiological signs detected on a single incidence of mammography, particularly in the differentiation of cystic lesions from solid masses. It also allows for a better appreciation of the lesion composition. Breast US imaging has however some limitations. Rather unusually, adipose tissues in the breast are hypoechoic when compared to the parenchyma. The majority of masses and breast cancers are also hypoechoic. As a consequence, a substantial number of cancers are difficult or impossible to depict, since they have the same echogenicity as the surrounding tissue. Normal breast structures may be confused with cancer, generating a high rate of false-positives.

Contrast-Enhanced Ultrasound (CE-US), combining the use of Doppler with gas-filled microbubbles contrast agents (1 to 10 microns in diameter), have shown to improve the detection of blood vessels and down to diameters of the order of 40 microns [10]. As in CE-MRI, the assessment of contrast uptake kinetics, in particular the derived outputs such as the peak of uptake intensity, the mean transit time, the slope of the wash-in curve, the washout time and the area under the curve of contrast, can be important parameters to distinguish benign and malignant lesions [83,84]. In CE-US however, microbubbles contrast agents are rather unstable, due to their size, and consequently their lifetime inside the body is short (between 2 and 5 minutes). Hence, this time constraint might jeopardize the contrast uptake curve assessment and prevent the examination to cover the whole breast volume. From a more practical standpoint, another limitation of breast

US is that the examination quality depends on the operator, and is therefore poorly reproducible. Moreover, the manipulation is highly difficult due the lack of anatomical landmarks to guide the review. Thus, it may still remain unclear whether the entire breast was imaged or not.

In summary, today the standard imaging techniques used for breast cancer diagnosis, staging and therapy follow-up is CE-MRI; it provides morphologic, topological and functional information of the tumor. CE-MRI is however very costly and is not widely available. Contrast-Enhanced full body CT is characterized with limited spatial resolution and a substantial radiation dose to the patient. Techniques based on U/S such as Doppler and contrast-enhanced Doppler have also shown positive results in emphasizing breast tumor angiogenesis. However, the examination quality is highly dependent on the operator. More recently, CE-DM has shown promising results, though its benefits compared to CE-MRI and CE-US are still to be demonstrated. CE-DM 2D projection nature may however limit the characterization of cancerous lesions when compared to 3D techniques.

In order to improve the accuracy of tumor diagnostics, staging and cancer therapy monitoring, with wider accessibility and better dose-cost effectiveness, an alternative technique specifically designed for breast imaging, providing accurate 3D quantitative position, morphologic and functional lesion information is definitely welcome. In the next section Contrast-Enhanced Digital Breast Tomosynthesis (CE-DBT) and Contrast-Enhanced Dedicated Breast CT (CE-bCT) are presented as two potential candidates.

1.3 Novel X-Ray Techniques for Vascular Imaging of the Breast

1.3.1 Contrast-Enhanced Digital Breast Tomosynthesis

Digital Breast Tomosynthesis (DBT) is a low-dose x-ray tomographic technique recently introduced in clinical practice. In DBT, pseudo-tomographic images of the breast are reconstructed from a limited number of projection images acquired over a limited angular range, partially overcoming the loss of three-dimensional (3D) information in standard mammography [85]. Because of data incompleteness, an analytical solution for data reconstruction is not unique. The pseudo-3D reconstructed volume is characterized by a very high spatial resolution in the planes parallel to the detector, but limited depth resolution. This is translated by the generation of focal planes where in-plane structures are sharp, while out-of-plane structures are blurred [86]. Meanwhile, the focal planes can be affected by several artifacts originated from high contrast signals present outside the in-focus plane, such as microcalcifications [87,88]. Despite that, DBT partly removes the confusion of superimposed tissue encountered in standard mammography, resulting in better lesion depiction and decreasing rate of false positives [89, 90]. The interpretation of DBT images is very similar to standard mammography images, with clinical protocol and equipment cost also comparable.

As discussed in the previous sections, although the clinical results with CE-DM are promising, CE-DM provides 2D projection images that do not depict 3D morphology nor 3D location of contrast-enhanced lesions. To overcome these limitations, 3D Contrast-Enhanced Digital Breast Tomosynthesis (CE-DBT), *i.e.* the combination of DBT and iodine-injected CE-DM, has been proposed. For CE-DBT, temporal [91–95] and DE subtraction [17–20, 22] techniques are currently under investigation by academic and industrial research groups. Preliminary clinical studies have shown that CE-DBT iodine enhancement images can demonstrate vascular characteristics of breast lesions that are consistent with the vascular information provided by CE-MRI [91,96,97]. However, in the temporal subtraction case, the presence of artifacts due to patient movement between acquisitions of pre- and post-contrast projections is even more important than in temporal CE-DM, because of the multi-view acquisition and consequent extended time interval between pre-contrast and post-contrast image sets. Dual-energy techniques have the potential to minimize patient motion artifacts when each pair of spatially correlated LE and HE images is acquired within a short period of time [22, 96]. Different image recombination methods, either on projection [20] or volume [23] domains, as well as the use of energy-discriminating photon counting detectors [25] have been investigated to minimize motion artifacts and ameliorate residual texture cancellation.

On the other hand, following the same reasoning as for morphological DBT images, the limited depth resolution caused by the limited angular range and its consequent imaging artifacts may still be a limitation for CE-DBT when compared to other fully 3D techniques such as CE-MRI and contrast-enhanced full-body CT. Nonetheless, when compared to these techniques, the CE-DBT prototypes under evaluation present a much higher spatial resolution in the focal planes, with lower predicted cost, higher accessibility and radiation dose levels comparable to current standard mammography and morphological DBT acquisitions. When compared to CESM, with the attainment of pseudo-3D images, it is also expected that CE-DBT could provide potential improvement in specificity, as it was for DBT when compared to standard mammography. Improved lesion localization and improved characterization of the contrast-agent uptake morphology is likewise expected.

1.3.2 Contrast-Enhanced Dedicated Breast CT

The concept of performing dedicated breast CT (bCT) scans as alternative for breast cancer screening was first introduced in the late 70's [98–102], but was rapidly dismissed due to the amount of radiation dose, as well low spatial resolution and cost-effectiveness. With the advent of digital detectors with sufficient spatial resolution in the early 2000's, dedicated CT scanners for the breast were proposed by different academic research groups [103–106]. Various bCT system

designs have been investigated [107]. Main differences between the various designs are the detector technology and system geometry. Photon-counting and energy-integrating detectors dedicated for breast imaging have been proposed. Helical [108, 109], cone-beam [103–106] and inverse-geometry [110] geometries have been studied. In all three geometries, the x-ray tube and an opposite detector are rotated about the pendant breast, with the woman lying prone on a tabletop. In helical bCT, the x-ray tube and a narrow detector ring perform also a continuous translation along the pendant breast. In cone-beam CT, the x-ray tube emits a half-cone beam towards a large area flat panel detector. Inverse-geometry bCT consists of a large-area scanned source opposite a detector array that is smaller than the source in the transverse direction. For all three geometries, the projection images are subsequently reconstructed to tomographic images with quasi-isotropic spatial resolution. For these system designs, much research efforts have been oriented toward technology development addressing radiation dose [103, 111, 112], x-ray scatter [113, 114], incident x-ray spectrum [115–117], acquisition orbit [118], system topology and spatial resolution [119–123], anatomical noise [124, 125], and image artifacts management [126].

The first clinical trial with the "new-generation" of dedicated breast CT scanners was carried by Boone *et al.* at the University of California, Davis Medical Center (UC Davis), published in 2008 [127], with the objective to prospectively compare bCT with screen film mammography on ten healthy women and 69 women with suspicious abnormality (BI-RADS[2] 4) and highly suggestive of malignancy (BI-RADS 5). In this study, the cone-beam bCT prototype presented similar performance for lesion visualization, significantly better for masses but worse performance in depicting microcalcifications smaller than 300 μm. In a more recent clinical study with 23 patients, O'Connell *et al.* [128] concluded that most calcifications and all masses detected with mammography were also detected with their clinical cone-beam breast CT prototype. The authors also reported a better coverage of the inferior, posterior, medial, and lateral portions of the breast when compared to conventional mammography, an equivalent coverage in the superior portion of the breast but limited coverage in the axilla on the basis of visualizing lymph nodes. In addition to the clinical findings, both studies included subjective questionnaires to the patient, who reported that breast CT exams were significantly more comfortable. Several aspects of bCT technique still need to be improved in order to provide more reliable morphological images, in particular axillary tail coverage and microcalcification depiction. With recent advances in high-resolution low-noise detector technology such as photon-counting detectors [129–131] or electron-multiplying CCD [132] as well as novel iterative reconstruction algorithms [133, 134], it has been shown by simulation [108] and by experimentation [123, 135] the possibility of visualizing microcalcification clusters of about 100-150 μm. New table designs and complex gantry trajectories for better axillary coverage and patient comfort are also under study [136, 137].

Similarly as for DBT, bCT combined with a vascular contrast agent, or Contrast-Enhanced Breast CT (CE-bCT), can provide morphologic and functional information of breast lesions in synergy [138]. The relationship between contrast concentration and CT enhancement is straightforward as there is a direct linear relationship between enhancement change and iodine concentration. Moreover, assuming the same geometry as for morphologic dedicated breast CT prototypes described above, compared CE-MRI and contrast-enhanced full-body CT, CE-bCT could provide higher spatial resolution and consequently better characterization of enhanced lesion morphology. Early clinical trials using a dedicated bCT system [139] and with a conventional CT scanner [75] suggested that the analysis of contrast medium enhancement in post-contrast bCT images, *i.e.* without temporal or dual-energy recombination, could differentiate malignant from benign lesions. This was confirmed in a more recent study by Prionas *et al.* [138] where iodine enhancement was quantified in post-contrast CE-bCT images, and their conspicuity compared with that at un-

[2]The American College of Radiology (ACR) has developed a standard way of describing mammogram findings and included in BI-RADS (Breast Imaging-Reporting and Data System) categories numbered 0 through 6. BI-RADS 0 indicates that an additional imaging evaluation and/or comparison to prior mammograms is needed. BI-RADS 1 indicates that no significant abnormality to be reported. BI-RADS 2 and 3 indicate a benign finding and a probably benign finding (follow-up with repeat imaging suggested), respectively. BI-RADS 4 indicates a suspicious abnormality that should be biopsied, while BI-RADS 5 suggests an abnormality with high malignancy. Finally, BI-RADS 6 indicates a biopsy-confirmed malignancy.

enhanced bCT and conventional mammography. Forty-six patients with 54 lesions classified as BI-RADS 4 or 5 were invited for examination. Results suggested that conspicuity of malignant breast lesions, including ductal carcinoma *in situ*, is significantly improved at CE-bCT.

Since unenhanced breast tissue can still be depicted in post-contrast images, we expect that background texture cancellation and enhanced iodine uptake obtained from temporal or dual-energy recombination techniques would further benefit CE-bCT, entailing in better cancerous lesion detection, localization and characterization. In the particular case of bCT geometry with the patient in prone position and the breast under none or minimal compression, temporal subtraction CE-bCT technique is likely to suffer from patient motion artifacts between pre- and post-contrast acquisitions, perhaps even more than temporal subtracted CE-DM and CE-DBT. A dual-energy recombination technique for CE-bCT is in this case preferable.

As far as we know, at the beginning of this PhD thesis research, little investigation on dual-energy recombination techniques for contrast-agent and tumor angiogenesis enhancement in a dedicated breast CT setup was performed. The main contributions were from Shikhaliev *at al.*, who proposed dual-energy recombination for multi-material enhancement using a scanning multi slit multi slice (MSMS) x-ray system prototype equipped with a Cadmium Zinc Telluride (CdZnTe) energy-resolved photon-counting detector [129, 130, 140, 141]. In their technical feasibility studies, the combination of high spatial resolution, the low noise properties of the CZT detector and the intrinsic scatter rejection geometry, resulted in enhanced material detectability when compared to bCT with a conventional energy-integrating detector. However, in these studies, the main adopted contrast agent was based on Gadolinium (Gd); the minimum photon energy sensitive to the CZT detector (26 keV), prevented from exploring the iodine K-edge (33.2 keV), due to low x-ray quanta detected in the small energy bin ($25 - 33.2\ keV$). It must be emphasized that although Gd-based contrast media available in clinical practice are less nephrotoxic than iodine-based contrast media [142, 143], to obtain comparable X-ray image quality, a higher toxic load is expected with Gd-based contrast medium than with iodinated contrast medium[3]. This is due to the substantially higher X-ray attenuation of iodine when compared to Gd. Further studies assessing dual-energy applications for iodinated contrast-agent enhancement as well as other dual-energy recombination strategies for CE-bCT are therefore required.

In summary, CE-DBT and CE-bCT are two potential candidate techniques for contrast-enhanced vascular imaging of the breast. Probably the most significant advantage of CE-DBT is that it can be performed on existing digital mammography systems with relatively minor modifications. In spite of that, we can expect that the potential of CE-DBT in quantifying contrast medium uptake is limited, due to the incomplete tomographic reconstruction and subsequent artifacts inherited from the low depth-resolution of limited opening angle DBT acquisition. CE-bCT with quasi-isotropic spatial resolution and voxel signal intensity proportional to the linear attenuation coefficient is believed to offer more accurate quantitative information, though a low-dose operation could still be a challenge. Today, the incremental value of CE-bCT over CE-DBT in their ability to provide quantitative information is still unknown and a complete evaluation on the quantitative performance of both technologies would be beneficial.

In order to achieve dose levels comparable to two-view mammography, both CE-DBT and CE-bCT techniques would benefit from iodine K-edge imaging techniques using dual-energy acquisitions. While dual-energy iodine-enhanced CE-DBT geometry, acquisition parameters and protocols have been previously assessed and optimized [17–26], little investigation on dual-energy recombination techniques for iodinated contrast-agent and tumor angiogenesis enhancement in a dedicated breast CT setup was performed. As a consequence, before any comparison with CE-DBT,

[3]The guidelines for contrast medium from the European Society of urogenital radiology does not approve Gd-based contrast medium for X-ray imaging due to nephrotoxicity at higher than approved doses and low X-ray IQ at approved doses

a preliminary optimization of the dual-energy acquisition parameters maximizing the performance of CE-bCT in depicting contrast-agent uptakes is imperative.

In the next chapter, we provide a detailed description of the simulation platform software developed for our research and providing the means for optimizing CE-bCT acquisition parameters and comparing its quantitative performance with CE-DBT. An extensive validation is presented in the subsequent chapter.

Chapter 2

3D Breast X-ray Imaging Simulation: evolution of CatSim

General Presentation of CatSim

CatSim, "**C**omputer **A**ssisted **T**omography **SIM**ulator", is an X-ray imaging simulation platform software. It was initially conceived in the late 2000's by Samit Basu, Bruno De Man and Jed Pack at GE Global Research Center (*CT and X-ray Laboratories*, Niskayuna, NY, USA). CatSim was originally developed to simulate 3rd generation computed tomography projection images using "simple" analytical test objects [27].

Today, thanks to the contributions of an increasing number of researchers and developers throughout GE Global Research Center, GE Healthcare and external academic partners[1], CatSim allows not only to simulate simple imaging system topologies, but also very advanced X-ray imaging chains, including X-ray spectrum polychromaticity, realistic quantum and electronic noise models, finite focal spot emission, detector cross-talk, detector lag or afterglow, bowtie filtration, detector efficiency, non-linear partial volume, X-ray photon scatter (Monte Carlo) and absorbed dose estimation. It supports complex analytic objects, such as the Forbild Phantoms[2], complex polygonal meshed surfaces, dynamic NURBS[3] objects such as the XCAT/NCAT phantoms [144], as well as voxelized phantoms which can, in principle, be made from reconstructed scans of actual subjects or from voxelized versions of analytic and polygonal phantoms.

CatSim is structured in a set of modular functions, each one describing a particular physical phenomenon or an architectural component underlying an X-ray imaging system. The modular functions are written in Matlab (The MathWorks Inc.; Natick, MA, USA). They allows for simple, flexible and customizable implementation, enabling to modify a single component (*f.e.* the detector type) without affecting the rest of the acquisition chain. In order to increase efficiency, some modules call for external functions written in C++. This allows building optimized and parallelized implementation for heavier calculations, such as object projection and backprojection, as well as the Monte Carlo engine.

CatSim includes material files and energy-dependent Photoelectric, Compton and Rayleigh interaction database developed by members of the Geant4 Collaboration[4].

[1] Stanford (Dr. Pelc), U Michigan (Dr. Fessler), Virginia Tech (Dr. GE Wang), Technische Universitat Munchen (TUM), Duke U (Dr. Segars, Jim Colsher, Dr. Samei), U Washington (Dr. Kinahan) and RPI (Dr. Yazici)

[2] Forbild Phantoms – `http://www.imp.uni-erlangen.de/phantoms/index.htm`

[3] Non-Uniform Rational Basis Spline (NURBS)

[4] `http://cern.ch/geant4`

Contributions of This PhD Thesis Research to CatSim Development

As part of this PhD thesis research, various modules for the CatSim simulation chain have been developed and validated allowing to design, optimize and compare digital mammography (MX), digital breast tomosynthesis (DBT) and dedicated breast computed tomography (bCT) systems while considering realistic cone-beam geometries and X-ray spectra typically used for breast X-ray imaging. More specifically, among other contributions, we highlight:

- The integration of X-ray spectrum models for Molybdenum, Rhodium and Tungsten anodes, for the X-ray energy range considered in breast imaging
- The integration of a recently developed meshed-based digital breast phantom with existing X-ray image projection routines
- The development of average glandular dose calculation routines in the context of a Monte Carlo engine designed to track X-ray photon trajectory inside voxelized objects
- The development of an indirect X-ray detection cascade model based on a columnar structured Cesium Iodide (CsI) scintillator coupled to amorphous Silicon (a-Si) Thin-Film Transistors (TFT)
- The development of a flat panel detector model for primary photons simulation
- The development of a flat panel detector model for scattered photons simulation
- The extension of an existing Filtered Backprojection (FBP) reconstruction algorithm, from a fan-beam to a cone-beam acquisition geometry

The next sections give a description on the design and development of these modules. They provide detailed information on the CatSim acquisition chain, from X-ray beam generation to image formation, including the calculations involved at each step. In Section 2.1, the geometry framework used for our simulations is defined. In Section 2.2, the X-ray spectrum generation models for anode materials and energy ranges used throughout this thesis are introduced. Flat and bowtie filtration are also described. In Section 2.3, analytical and mesh-based test objects emulating respectively geometrical and more complex anthropomorphic breast phantoms are illustrated. The projection algorithms for both analytic and meshed phantoms are briefly discussed in Section 2.4. In Section 2.5 and 2.6, Monte Carlo simulations of X-ray scattering and absorbed radiation dose occurring in breast phantoms at typical breast X-ray imaging energies are described. In Section 2.7, the developed cone-beam detector model is presented. Signal and noise propagation are defined for a noise-free blur-free detector, which was the main model used throughout this thesis. For experimental validation purposes, signal and noise propagation inside a realistic indirect conversion scintillator-based detector are also detailed.

Since X-ray photon production, interaction with matter and detection by digital converters are well known processes, their physical aspects are not discussed in this chapter. For further details, we refer the reader to a short overview on the physics of medical imaging and imaging science presented in Annex A.

Results from an extensive validation of the developed models with regard to previously published and experimentally obtained data are provided further on, in Chapter 3.

2.1 Coordinate System and Acquisition Geometry Definition

In this PhD thesis research, a cone-beam geometry was assumed for the simulation of DBT and bCT projection images. These topologies can be generalized into the diagram illustrated in Figure 2-1, alongside with the adopted coordinate systems.

With the gantry in its initial centered position, the detector plane was defined such as to be parallel to the x-z plane. The axis perpendicular to the x-z plane, passing through the intersection of the x axis and z axis was defined as the y axis, with positive values towards the X-ray source. The Center-of-Rotation (COR), or *isocenter*, is defined as the intersection between the gantry's rotation axis and any plane perpendicular to the detector plane and containing the X-ray source. The isocenter was chosen to be the origin of the Cartesian coordinate system (x,y,z), with rotation axis defined as the z axis. The distance between the source and the isocenter was defined as the *source-to-isocenter distance* (SID).

At the detector plane, two more axes u and v were defined, for detector pixel columns and rows, respectively. The origin $(u, v) = (0, 0)$, or (u_0, v_0), represents the intersection of the line passing through the X-ray source, the isocenter and perpendicularly incident over the detector plane. The angles between this line and a given point coordinate in the u and v axes are the *fan angle* α and *cone angle* γ, respectively. The distance between the source and the point (u_0, v_0) was defined as the *source-to-detector distance* (SDD).

The gantry rotation angle, or acquisition angle β, was defined as the angle between the line through a new source position and the isocenter, and the same line when the gantry is in its initial centered state (*i.e.*, $\beta = 0$). For dedicated breast CT, the source and the detector were assumed be fixed with respect to each other, while the gantry rotates the detector-source around an axis located at the center of the longitudinal section of the uncompressed breast, thus performing a full 360˚ orbit around the breast. For DBT, we assume a static flat detector and a gantry allowing the source to rotate around the COR, usually located inside the compressed breast.

Table 2.1 summarizes the variables describing the dedicated breast CT and DBT cone-beam geometries, as well as the other main variables defined further in this chapter.

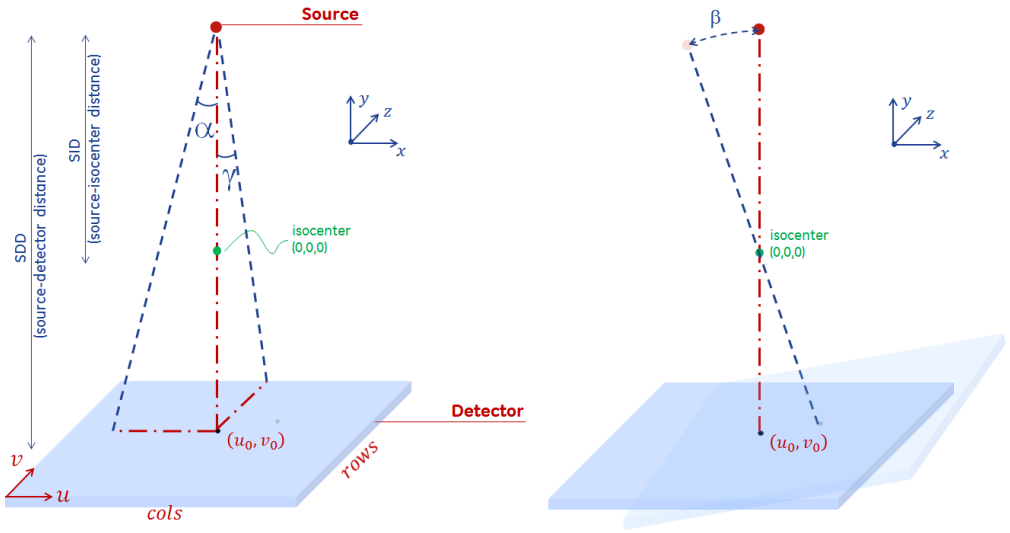

Figure 2-1: Illustration of a cone-beam X-ray system geometry

Table 2.1: Definition and units of the main variables used along Chapter 2

Variable	Definition	Units
Cone-Beam Geometry		
(x, y, z) coordinates	global coordinates system	mm
(u, v) coordinates	detector coordinate system	mm
f_u, f_v	detector coordinates in frequency domain	mm^{-1}
SID	source-to-isocenter distance	mm
SDD	source-to-detector distance	mm
α	fan angle	$rad\,(radian)$
γ	cone angle	$rad\,(radian)$
β	gantry (or acquisition) angle	$rad\,(radian)$
X-ray Source		
s	point source	-
E	X-ray photon energy	keV
S	X-ray photon fluence	mm^{-2}
mAs	product of tube current and exposure time	$mA \cdot s$
$S_{raw}(E)$	normalized anode X-ray fluence spectrum	$mm^{-2}\,mA^{-1}\,s^{-1}$
$\mu_m(E)$	linear attenuation coeff. of filter material m	mm^{-1}
$t_m(\alpha, \gamma)$	thickness of filter material m	mm
$S_{net}(E, \alpha, \gamma)$, $S_{net}(E, i)$	filtered X-ray fluence spectrum	mm^{-2}
Object		
$\mathbf{r}$	object position in (x,y,z) coordinates	mm
$\mu_o(\mathbf{r}, E)$	linear attenuation coeff. of object o	mm^{-1}
t_{iso}	thickness of object o in the $\mathbf{i} - \mathbf{s}$ ray path	mm
Monte Carlo		
N	number of shot X-ray photons	-
j	interaction event index	-
$\mathbf{p}_j$	interaction location in (x,y,z) coordinates	mm
$\vec{d}_j$	photon traveling direction before interaction	mm
E_j	photon energy before interaction	keV
τ_j	interaction type	-
Σ_j	collection of information on interaction j	-
$\vec{\beta}_{i,j}$	vector linking interaction site j to *del* i	mm
$d\Omega_j(i)$	*del* solid angle as seen by the site j	sr
$\Psi(E, i)$	scatter probability field	-
$D(\mathbf{r})$	absorbed radiation dose	$mrad, mGy$
X-ray Detector		
i	detector element, *del*	-
$S_{scatter}(E, i)$	incident scattered X-ray fluence spectrum	mm^{-2}
$S_{inc}(E, i)$	incident primary X-ray fluence spectrum	mm^{-2}
A_i	detection element surface	mm^2
$\vec{w}_i$	unit vector normal to active surface	-
$\vec{L}_{i,s}$	vector linking the source s to *del* i	mm
$d\Omega_s(i)$	*del* solid angle as seen by the source s	sr
$I_{inc}(E, i)$	incident X-ray intensity spectrum	-
$\eta(E)$	quantum detection efficiency, QDE	-
$H(f_u, f_v)$	optical spread transfer function	mm^{-1}
$\Pi(f_u, f_v)$	photodiode aperture transfer function	mm^{-1}
$\xi(E)$	conversion function (E for EI, 1 for PC)	-
k, G	product of efficiencies and scaling factors	$d.u.$, $d.u./keV$
$SI(i)$	projection image signal intensity	*digital units* ($d.u.$)

2.2 X-ray Source Modeling and Emitting Fluence Spectra

To generate an energy-dependent and direction-dependent X-ray photon beam, the simulated X-ray source was defined by three components: a finite-sized focal spot, an X-ray photon fluence energy spectrum generated by the anode and a filtration step.

2.2.1 X-ray Source Modeling

Focal Spot
X-rays are generated when electrons are accelerated and collide with the target anode, in a region called *thermal focal spot*. In a real X-ray tube, the focal spot may emit X-rays from each point of its surface. Different emission patterns have been observed depending on the X-ray tube design [145–148]. The focal spot size and emitting pattern may degrade the X-ray system spatial resolution, known as *focal spot blurring* [149]. Another source of degradation is linked to the continuous X-ray tube movement during the sinogram acquisition, *i.e.* a *tube motion blurring* [120, 150, 151].

Although CatSim allows to simulate both blurring effects, for the investigations carried during this PhD thesis research, the impact of focal spot and tube motion blur on the system's spatial resolution was disregarded. A single point source emitting isotropically at every direction was considered for all simulations. Moreover, projections were assumed to be acquired in a "step-and-shoot" mode with instantaneous displacement (infinite speed) between two consecutive view angles (*i.e.* without tube motion blur). The time interval for one view integration and during which the X-ray source emits photons continuously, is used for exposure calculation (*i.e.*, mAs values).

Anode-Emitting X-ray Spectra Models
The second component required to build the X-ray source model concerns the definition of an energy-dependent X-ray fluence emitted by the anode. In practice, the anode X-ray fluence energy spectrum can be either predicted according to known analytic models of atomic interaction in the anode or measured directly from the X-ray tube window using appropriate energy-sensitive tools [152–154]. In this research work, two spectrum models were adopted according to the imaging technique and its specific energy range: SpeXim and TASMIP. Table 2.2 summarizes the information on both models.

Table 2.2: Spectrum models used in this study

Name	Reference	Anode Material	En. Range	Validation
SpeXim	Birch and Marshal, 1979[a] Cranley *et al.*, 1997[b]	Mo,Rh	$0 - 49$ kV	Section 3.1
TASMIP	Boone *et al.*, 1997[c]	W	$30 - 140$ kV	Ref. [155]

[a] Ref. [154]
[b] Ref. [156]
[c] Ref. [155]

SpeXim is a short for "Spectrum Simulator" and is a software package previously developed at GE Healthcare. The *SpeXim* model provides low-energy spectra for Molybdenum (Mo) and Rhodium (Rh) anodes, typically used in single and dual-energy mammography, as well as single and dual-energy breast tomosynthesis. The model is based on the Bremsstrahlung spectrum model developed by Birch and Marshall [154], with characteristic rays added from tabulated data [156]. Validation of SpeXim model beam quality with regard to experimentally obtained data is provided in Chapter 3.

TASMIP stands from "Tungsten Anode Spectral Model using Interpolating Polynomials", and was developed and published by Boone *et al.* [155]. The model relies on interpolating polynomials through measured constant potential Tungsten (W) anodes X-ray spectra, published by Fewell

et al. [157, 158]. Additional modifications from Fewell's measurements were introduced in the TASMIP model (numerical hardening) in order to better fit the given modern X-ray tubes and generators. The TASMIP model generates high-energy spectra for W anodes typically used in CT systems and has been widely adopted for breast CT system prototypes with W-based X-ray tubes [113, 117, 120]. Validation of TASMIP model beam quality can be found in Ref. [155].

Both spectrum models were implemented such as to provide X-ray fluence spectra for Mo, Rh and W anodes, in units of *photons* per mm^2 per energy bin, at $1\,m$ from the source and normalized by the X-ray tube current and the exposure time (mAs product). Figure 2-2a illustrates the normalized raw anode X-ray fluence spectra, $S_{raw}(E)$, generated using SpeXim model for Mo and Rh anode materials (considering only the intrinsic filtration of the tilted anode and the beryllium window). Characteristic rays for Mo anodes are located at 17.9 keV (K-alpha) and 19.5 keV (K-beta), while for Rh anodes characteristic rays are located at 20 keV and 22.5 keV (cf. Annex A.1 for detailed description X-ray production and characteristic X-rays). Figure 2-2a also illustrates the normalized raw W anode X-ray fluence spectra, generated using the TASMIP model.

Energy and Direction-Dependent X-ray Fluence Filtration
Additional filtration was used to further shape the energy-dependence and direction-dependent X-ray fluence generated by the anode. This can be performed using both flat (mainly energy shaping) and bowtie filters (mainly direction shaping).

Flat filters are typically flat sheets of a metallic alloy of high atomic number, high purity and homogeneous thickness. Through mainly photoelectric interactions, the lower energy photons are absorbed, shifting the spectra to higher energies (hardening). Filter materials containing absorption discontinuities in the energy range of X-ray imaging can be used to attenuate photons with energy higher than its electronic shells binding energies, due to the jump in attenuation. They are usually called *K-edge filters*.

Bowtie filters can be used to shape a X-ray beam fluence depending on the beam's take-off angle. Typically they are built to provide higher photon fluence for beam paths with higher object thickness to be crossed. Direct results of bowtie filtration are (but not exclusively): reduction of cupping artifacts due to scattered radiation and beam hardening [114], average decrease and better distribution of radiation dose inside a cylinder volume to be imaged [141] as well as better homogeneity of X-ray fluence across the whole detector surface, entailing in improved contrast-no-noise ratio and noise uniformity over the image [141].

2.2.2 Pre-patient X-ray Fluence Spectrum Calculation

Pre-patient X-ray fluence spectrum calculation was based on the definition of energy-dependent and direction-dependent transmission factors of a set of filter materials. According to the Beer-Lambert Law (cf. Annex A.2), the filtered net X-ray fluence spectra transmitted of the tube housing, S_{net} (in *photons per* mm^2 at $1\,m$ from the source), can be expressed as:

$$S_{net}(E,\alpha,\gamma) = mAs \cdot S_{raw}(E) \cdot \exp\left(-\sum_m \mu_m(E) \cdot t_m(\alpha,\gamma)\right) \tag{2.1}$$

where mAs is the product of tube current and exposure time, $S_{raw}(E)$ is the raw X-ray fluence spectra (output of SpeXim and TASMIP models) emitted isotropically by a point source s over the anode, α and γ are the fan and cone angles, respectively, and μ_m and t_m are respectively the energy-dependent linear attenuation coefficient and the thickness of every material m crossed by a X-ray beam with direction (α,γ).

As an example, Figure 2-2b shows the linear attenuation coefficient of two filter materials, Tin (Sn) and Copper (Cu), as a function of the X-ray photon energy. Figure 2-2c illustrates the W anode X-ray fluence spectrum of Figure 2-2a after being filtrated by 0.3 mm of Sn and 0.3 mm

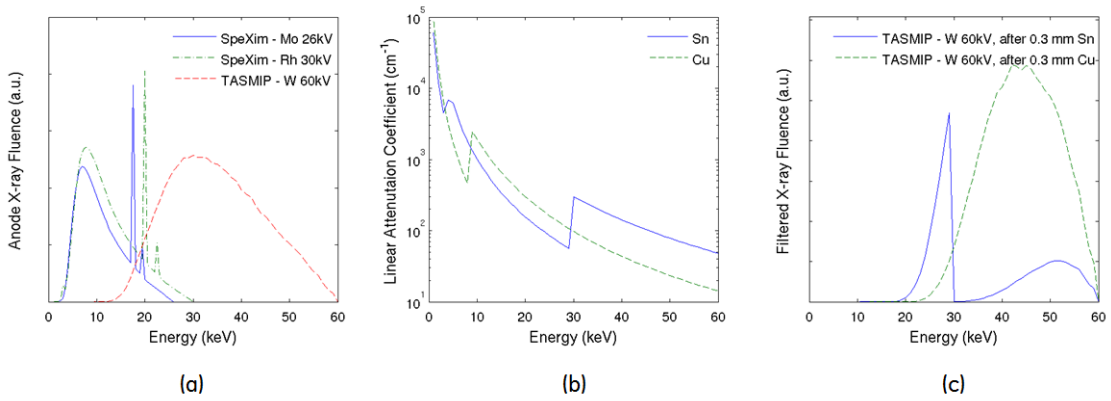

Figure 2-2: (a) X-ray fluence energy spectra, normalized by the tube current and exposure time, generated by SpeXim and TASMIP models for: Mo anode and 26 kV tube voltage, Rh anode and 30 kV tube voltage, and W anode and 60 kV tube voltage (considering only the intrinsic filtration of the tilted anode and the beryllium window); (b) Energy-dependent linear attenuation coefficients of Tin (Sn) and Copper (Cu); (c) W anode and 60 kV spectrum filtered with 0.3 mm of Sn and 0.3 mm Cu

of Cu. Notice that since Sn possesses a K-shell absorption discontinuity at 29.2 keV, a Sn-based filtration induces a discontinuity in the output spectra.

Figure 2-3 illustrates an example of bowtie filtration combining three materials: Aluminum (Al), graphite and Copper (Cu). Figure 2-3b shows an example of the thickness profile of each material as function of the fan angle α of the bowtie filter illustrated in Figure 2-3a. The resulting transmission factor S_{net}/S_{raw} per mAs, for a given fixed energy, is illustrated in 2-3c. This filter shapes the X-ray fluence from a isotropic distribution to a fluence concentrated around the zero degree fan angle. This particular example would be, for instance, well suited for cylindrical objects, were the thickness to be crossed by the X-ray beam is highest at zero degree fan angle and decreases for more peripheral angles.

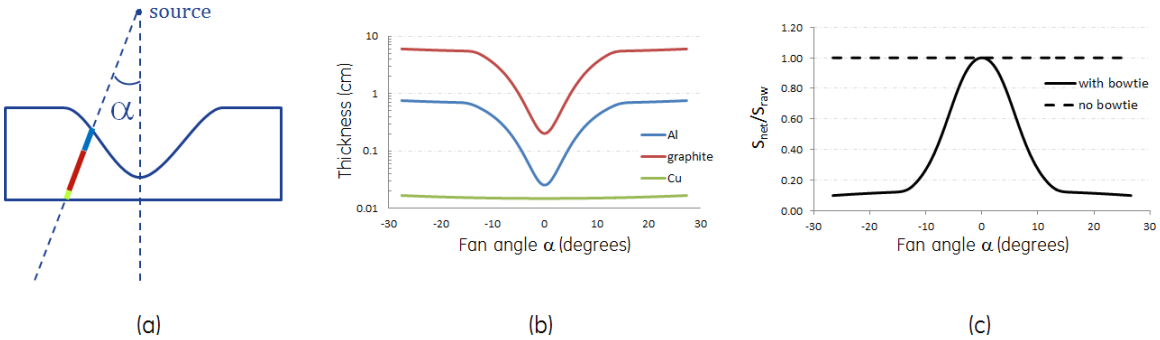

Figure 2-3: (a) Bowtie filter illustration combining three materials (aluminum, graphite and copper); (b) a given thickness profile for the three materials as function of the fan angle α, as well as the (c) resulting transmission factor for a given beam energy

Definition 2.1. *For the remainder of this thesis manuscript, we define the net X-ray fluence spectrum S_{net} with respect to a detection element i. In other words, for each X-ray beam with take-off direction (α, γ), we associate S_{net} to a detector element i such as:*

$$\begin{cases} x_i = SDD \cdot \tan(\alpha) \\ z_i = SDD \cdot \tan(\gamma) \end{cases} \quad \textit{and} \quad S_{net}(E, \alpha, \gamma) \xrightarrow{(\alpha,\gamma)\to i} S_{net}(E, i)$$

where x_i and z_i are the coordinates of the detector pixel reached per X-ray photon emitted by the source under (α, γ) angles (cf. Figure 2-1), SDD is the source-to-detector distance and E is the X-ray photon energy.

2.3 Computational Human Breast Phantoms

Three types of breast tissue equivalent phantoms, representing the compressed and uncompressed breast were considered for our investigations: 1) analytic models, representing the breast through geometric primitives. They allow for very fast projection calculation and are well suited to assess the spatial and noise properties of a given imaging setup; 2) polygonal meshed models, with increased flexibility to define complex surfaces with high anatomical fidelity. They are preferable for simulations involving detectability and characterization tasks in the presence of anatomical background; 3) voxelized models of the previous analytic and meshed phantoms, necessary in our investigations for Monte Carlo calculations of X-ray photon scattering and absorbed radiation dose.

In all breast phantom models, independently of their internal structure, the breast was assumed to be composed of fibroglandular and adipose tissues, or a homogeneous mixture of both tissues (found either through mass or volume conservation hypothesis). Depending on the simulation objectives, a skin layer was also added. The chemical composition of fibroglandular tissue, adipose tissue and the skin was based on the work of Hammerstein *et al.* [159]. Chemical composition of microcalcifications was modeled as Calcium Hydroxyapatite (CaHa).

As follows we provide a more detailed description on all three types of simulated breast phantoms.

2.3.1 Analytic Models

Throughout this PhD thesis research, analytical models of the compressed and uncompressed breast were implemented to assess physical image quality, through measurements of image contrast, noise and spatial resolution (Chapters 3, 5 and 6)

Using CatSim, analytic breast phantoms were built based on known geometric equations defining three-dimensional surfaces (*e.g.* cylinder, spheres, boxes, hyperboloids, cones, tori, ...) and additional clipping planes. Generically, each surface can be fully described by defining four parameters: i) its geometric center position, ii) its 3D extent depending on the geometrical primitive (*e.g.* semi-axes for ellipsoids, face lengths for cubes, radius and height for cylinders, ...), iii) a rotation/scaling matrix and iv) the material filling its convex hull. More complex analytical breast phantoms, comprising the skin and eventual embedded lesions, were therefore created by defining a ordinated set of analytic objects. Their specific order determine their projection priorities, *i.e.* the volume of a newly define object replaces the same volume of a previously defined object wherever they overlap.

For DBT, a half-cylinder or a half-ellipsoid shape cropped by two parallel clipping planes (Figure 2-4a) were used as approximations of the compressed breast shape in a cranial-caudal (CC) view [160]. The height of the half-cylinder or half-ellipsoid, representing the compressed breast thickness, was varied from 2 to 8 cm. The half-axis of both cylindrical and ellipsoidal shapes, representing the breast surface area, was varied from 8.5 to 11.5 cm. Both height and half-axis values are in agreement with realistic conditions [161].

For the breast CT geometry studied in this thesis research, cylindrical [112, 162–164] or half-ellipsoid [104,165–168] approximations for the uncompressed breast shape with the patient in prone position were assumed (Figure 2-4b). The diameter of the cylinder or half-ellipsoid (measure close to the chest wall) varied from 10 to 18 cm. Their length (or height) was assumed to have 1.5 times its measured radius. Both diameters and length values are in agreement with realistic conditions, as evidenced by Boone *et al.* [111]. Moreover, the same research group verified in a clinical study conducted with over 200 patients that an uncompressed breast with 14 cm diameter corresponds to a 5 cm thick breast under typical mammography compression [162].

We refer the reader to the work of Huang *et al.* for a complete analysis of breast anatomical metrics [169].

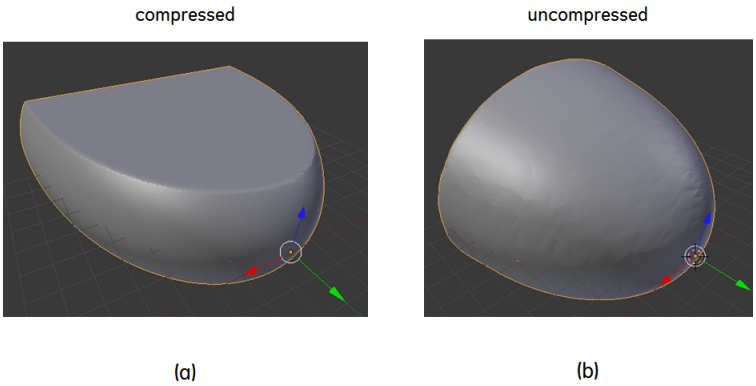

Figure 2-4: Analytic phantom models for (a) compressed and (b) uncompressed breasts

2.3.2 Meshed Models

Other evaluation and optimization procedures in breast imaging research could benefit from test objects modeling the complex anatomical structure of the breast with greater realism and known ground truth. In this PhD thesis research, more realistic anthropomorphic representations of the compressed and uncompressed breasts were used specifically to compare lesion detectability and characterization with CE-bCT and CE-DBT (cf. Section 6.3) and to quantitatively assess image quality in CE-bCT (cf. Section 7).

Anthropomorphic Human Breast Phantom and Lesion Models
The computational breast model exploited in this investigation was developed by colleagues at GE Healthcare [170]. The work associated to this PhD thesis consisted in ensuring to have an image acquisition chain for the breast phantom.

The full anthropomorphic breast model is able to simulate the skin with subcutaneous adipose columns, the Coopers ligaments, adipose tissue compartments, the ductal network, fibroglandular tissue, blood vessels, a chest wall with ribs and the pectoralis muscle. In this investigation however, blood vessels, chest wall and pectoralis muscle were not considered in the model.

The shape, size and distribution of the internal breast structures are based on a review of published breast anatomy research through anatomical dissections [32], ultrasound [171, 172] and computed tomography technology [169,173,174] and histological sections [175]. Model of the internal structures has been conducted to make simulated mammography, digital breast tomosynthesis (DBT), contrast-enhanced spectral mammography (CESM) and dedicated breast computed tomography (bCT) images visually and statistically similar to real patient images acquired with these imaging modalities.

In practice, the computational breast model is defined by triangular surface meshes. Internal structures were modeled by a variety of geometric mesh primitives, 3D Bézier curves and voronoi cells. Computerized operations, such as surface subdivision and decimate mesh modifiers, were used for geometry deformation, curve to mesh conversion and simplification of the meshes. The internal structures are constructed with Blender (Blender Foundation, `www.blender.org`, v2.63), a free and open source computer graphics software product developed for creation of 3D animation, Python (v2.6.5) as internal scripting language, and Voro++, a free software library for carrying out three-dimensional computations of the Voronoi tessellation. A main C++ code envelopes the several modules both to ensure the communication between them and control input/output functions. The main C++ code provides in the end the spatial coordinates of the various internal structures, writing the vertex and face coordinates of meshed objects into a format compatible

with CatSim polygonal projector.

Two breast outline configurations were modeled: i) an outline representing a compressed breast in cranio-caudal (CC) view during a mammography exam and ii) an outline representing an uncompressed breast of a woman in prone position, as in MRI or dedicated bCT exams. Lesions with different sizes and shapes defined by triangular surfaced meshes were simulated in a similar way.

Figure 2-5 illustrates the meshed breast phantom creation process, as described in Ref. [170]. Examples of low-energy morphologic breast X-ray images simulated using mammography, DBT and bCT geometries are shown in Figure 2-6.

Aside from the breast phantom convex hull (phantom border and skin layer), the many submodules linked to the phantom construction contained as many random processes as possible: the location of adipose columns, Copper's ligament, the growth direction of the ducts and the fibroglandular tissue, etc. In other words, a given set of parameters would define the overall disposition of fibroglandular tissue in the volume and its overall texture allure, however different "runs" of the algorithm would never provide the same phantom.

It must also stay explicit that the phantom generator algorithm as it is today does not provide a compressed and uncompressed breast phantoms that have perfect anatomic correlation, but rather two independent phantoms obtained from separate "runs" of the algorithm. Nevertheless, since the algorithm is based on the breast anatomy development, if the same input parameters are used, both phantoms provide comparable anatomical properties. Examples and evidences of this statement can be found in Ref. [170].

2.3.3 Voxelization of Analytic and Meshed-Based Models

Exclusively during Monte Carlo simulation for scattered radiation (Section 2.5) and absorbed radiation dose (Section 2.6), a voxelization algorithm based on parallel beam projections was used to produce a voxelized version of the analytic and meshed breast phantoms described above.

The voxelization algorithm available in CatSim produces 3D volumes for each material in the phantom, representing the volume fraction of that material within each voxel. Each 3D volume is formed by computing the object intersection points along a series of parallel rays through the phantom. For voxels that are intersected by analytic or meshed shapes, their contents for a given volume represent the average material content inside the voxel. To account for partial volume effect, the precision with which partial voxels are calculated is determined by a projection oversampling factor, *i.e.* the number of parallel ray crossing a single voxel. The higher this factor, the better the estimate of the content in each voxel, though longer calculation times are required.

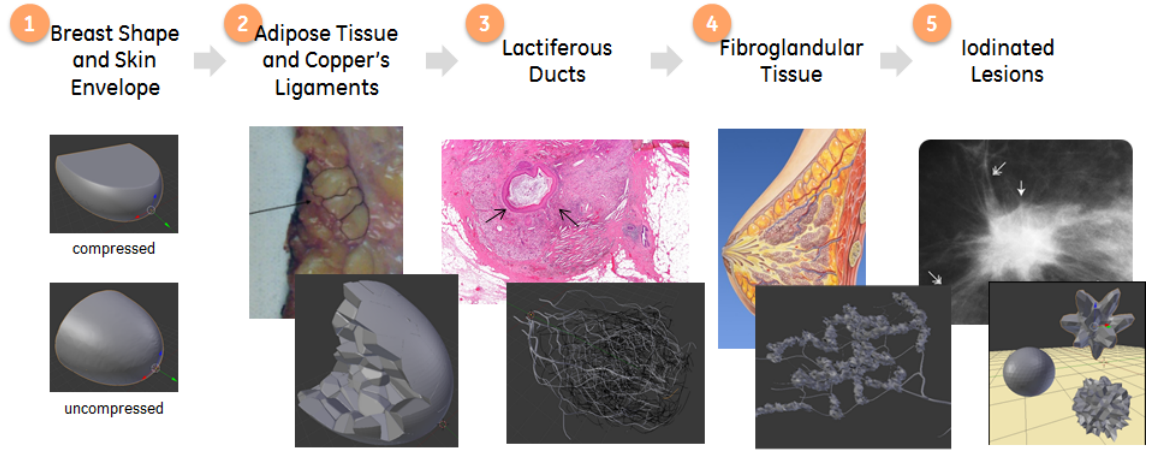

Figure 2-5: Meshed-based anthropomorphic breast model used in this study; it emulates the skin with subcutaneous adipose columns, Cooper's ligaments, adipose tissue compartments, the ductal network, fibroglandular tissue and embedded lesion

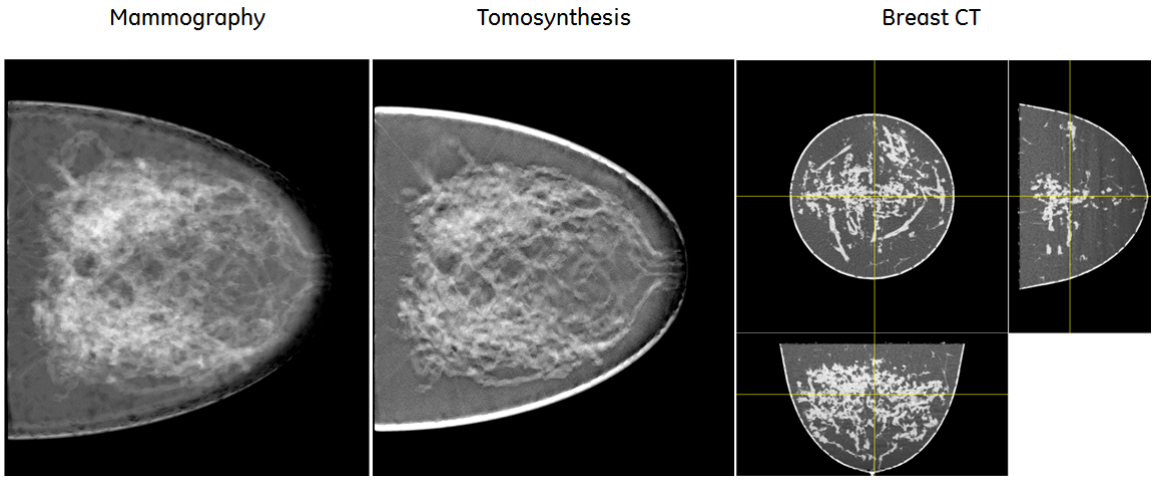

Figure 2-6: Example of simulated mammography, tomosynthesis and breast CT morphological images using the breast phantom model. Images were simulated with a low-energy monochromatic beam and without photon scattering

2.4 X-ray Projection

X-ray projection images of primary X-ray photons transmitted through the breast models described in Section 2.3 were generated using the Beer-Lambert law (cf. Annex A.2). The imaged object energy-dependent transmission factor $I(E)/I_0(E)$ for an X-ray beam travelling from the point source s to a detector element i is given by:

$$\frac{I(E)}{I_0(E)} = exp\left(\sum_{o \in \mathcal{O}} -\mu_o(E) t_{iso}\right) \tag{2.2}$$

where $I_0(E)$ and $I(E)$ are respectively the incident and transmitted X-ray photon intensities, $\mathcal{O}$ is the ordered set of structures o composing the imaged object, t_{iso} is the thickness of each structure o in the X-ray beam path $\mathbf{i} - \mathbf{s}$ and $\mu_o(E)$ is the linear attenuation coefficient of the primitive structure o at energy E.

In the case of multiple structures inside a simulated object (cardinality of $\mathcal{O}$ greater than 2), there exists an order of priority among the element of $\mathcal{O}$ which dictates their volume occupation in 3D space.

Definition 2.2. *(Ordered set $\mathcal{O}$) A simulated test object is defined as N structures o ordered in a set $\mathcal{O} = \{o_1, o_2, \cdots, o_N\}$. The order among the elements of $\mathcal{O}$ dictates their volume occupation in 3D space with respect to one another, such as:*

$$\begin{cases} o_n = o_n^* - \bigcup_{k=n+1}^{N} o_k^* & n = 1, 2, \cdots, N-1 \\ o_n = o_n^* & n = N \end{cases} \tag{2.3}$$

*where the structure o_n^* denotes the individual primitive shapes of structure o_n (*e.g. *any meshed-surface or analytically defined sphere, ellipsoid, cylinder,...).*

Equation 2.3 defines that a given structure replaces the volume of all structures with lower order wherever their volumes intersect. Figure 2-7 illustrates the case where an object $\mathcal{O}$ is composed of three structures, $\mathcal{O} = \{o_1, o_2, o_3\}$. In this example, o_2 replaces de volume of o_1 where they intersect; similarly, o_3 replaces de volume of o_2 and o_1 where they intersect. Their respective thickness t_{iso_1}, t_{iso_2} and t_{iso_3} in the X-ray beam path $\mathbf{i} - \mathbf{s}$ are calculated considering the priorities in ordered set $\mathcal{O}$. The same reasoning can be generalized for any number of structures in $\mathcal{O}$.

Ray-Tracing

The problem about object projection is summarized in knowing t_{iso}, for each structure $o \in \mathcal{O}$. For both analytic and polygonal meshed phantoms, the calculation of piece-wise thicknesses t_{iso} was performed by using a ray-tracing algorithm. The latter calculates all intersections points between an X-ray beam and the different primitive structures o^* composing the imaged object. Once all intersections points are known, the sum of the distances between the consecutive points defining straight lines within the primitive structure convex surface represents the total crossed thickness (cf. intersection points in Figure 2-8). The actual thickness t_{iso} is then calculated by accounting for the order of priority in $\mathcal{O}$, as described by Equation 2.3 and illustrated in Figure 2-7.

For analytical test objects, ray-tracing was performed by calculating the intersection between a parametrized line equation for the $\mathbf{i} - \mathbf{s}$ ray path and the mathematical equation describing each primitive structure surface defining the imaged object. Figure 2-8 illustrates two examples of projections, one with a sphere and another with a torus. In the case of a sphere, the set of points

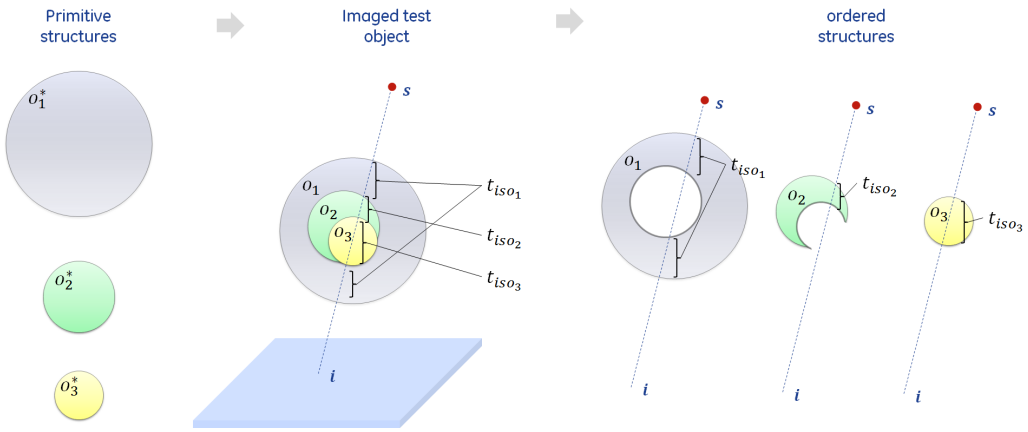

Figure 2-7: Illustration of primitive structure priorities in a multi-structure phantom and its consequence in total object thickness calculation. An object $\mathcal{O}$ is composed of three structures $\mathcal{O} = \{o_1, o_2, o_3\}$. Their respective thickness t_{iso_1}, t_{iso_2} and t_{iso_3} in the X-ray beam path $\mathbf{i} - \mathbf{s}$ are calculated considering the priorities in ordered set $\mathcal{O}$

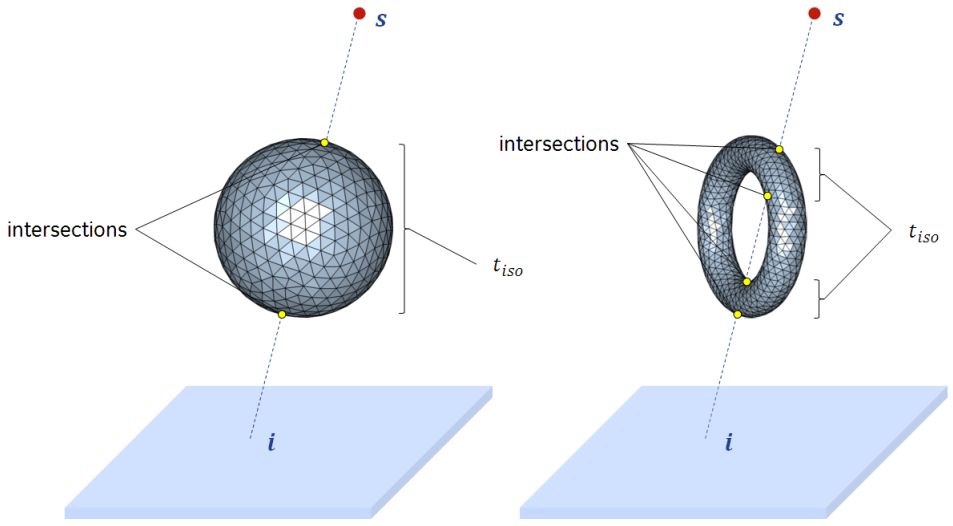

Figure 2-8: Illustration of ray-tracing projection on two meshed objects: a sphere (at left) and a torus (at right). The X-ray path from the source s to the detector element i intersects with the surface of the sphere and torus in respectively two and four triangular surface planes. Using an analytical method, the points of intersection with these planes are computed

$\mathbf{p}$ where the intersections occur is found by solving the following system:

$$\begin{cases} \mathbf{p} = \mathbf{s} + q(\mathbf{s} - \mathbf{i}) & 0 \leq q \leq 1 \\ (\mathbf{p} - \mathbf{p}_0)^T \mathbf{R}^T \mathbf{S} \mathbf{R} (\mathbf{p} - \mathbf{p}_0) = r \end{cases} \tag{2.4}$$

where the first equation refers to the $\mathbf{i} - \mathbf{s}$ ray path, parametrized by q, and the second equation is the an algebraic representation of the sphere surface, with $\mathbf{p}_0$ being the center of the sphere, $\mathbf{R}$ and $\mathbf{S}$ the rotation and scaling matrices respectively, and r the sphere radius. In the case of a torus object, the second equation is written as a 4th order algebraic equation. The idea can be extended to any other object type, as long as their surfaces can be expressed as an algebraic equation. Finally, the system of equations represented in Equation 2.4 can be resolved either by using a root-finding algorithm such as the Newton-Raphson method, or by analytical calculation using, for example, general Ferrari's method or Lagrange resolvent for generic quartic polynomials.

In CatSim, for polygonal (mesh-based) test objects, ray-tracing was performed by identifying the faces intersecting the $\mathbf{i} - \mathbf{s}$ ray path, and subsequently calculating the intersection points with the triangular surface plane equation by using a system of equations similar to Equation 2.4. Compared to analytical solutions, the main disadvantage of ray-tracing on polygonal objects relies on the amount of calculations necessary to discover the faces indexes. This is particularly true for complex structures with very short-range spatial variations, where hundreds of thousands of faces are defined. Nevertheless, polygonal meshed objects allow for much higher flexibility when defining a phantom, therefore allowing to provide a higher level of realism when compared to analytical objects.

2.5 Monte Carlo Simulation of X-ray Photon Scattering

The ray-tracing projection methods described in Section 2.4 combined with the Beer-Lambert law provide the X-ray photon spectra after primary interaction with the imaged breast phantom. However, changes in the X-ray photon trajectory due to Compton and Rayleigh scattering allow for multiple interactions, at different sites in the breast.

Monte Carlo (MC) approaches [176–179] are commonly used to individually track the transport of large numbers of photons through the object being imaged, therefore allowing to estimate the scattered X-ray photon fluence. They are based on the cross sections of the various physical processes. Scatter probabilities are computed for each photon interaction in the object, down to the detector surface, accounting this way for high-order interactions. For high statistical confidence in the final result, an increasing number of photons are simulated until the scatter signal achieves a given confidence level. Conventional MC simulation techniques are however computationally very inefficient. Commonly a very small fraction of the simulated photons are actually intercepted by the active area of the detector, particularly if they suffered high-order scattering. Moreover, a sizable number of photons are absorbed by the phantom itself, particularly when imaging large phantoms. Therefore, conventional MC techniques usually require high computation time to achieve low noise and exploitable results.

Numerous methods concerning hardware-accelerated [180] and *variance reduction* scatter estimators have been developed to overcome the disadvantages of conventional MC technique. Variance reduction methods [181, 182] used in scatter simulation generally include spatial smoothing techniques, in which the low-frequency nature of the scatter signal is exploited. Another approach for variance reduction lies on *forced detection* methods [183]. In these methods the random selection process for the photons is modified so that the photons are more likely to be detected. For instance, instead of allowing photons to terminate their trajectory in a photoelectric event, the probability of the photon interaction is modified allowing the photon to continue to propagate. Variance reduction techniques can significantly accelerate MC simulations, but do not provide enough acceleration to make MC simulation practical use such as in real data scatter estimation and correction.

An alternate approach to simulate scattered radiation is based on analytic techniques. Analytic scatter estimation methods describe the X-ray photon fluence at each point in space as a *scatter field* [184, 185]. The integral equations describing photon absorption and scattering are calculated to model how the X-ray photon fluence evolves given the flux at all other points in the object. An iterative process drives the fields to equilibrium. In these techniques however, the scatter field accuracy is directly linked to how the object and the field is sampled, as a function of photon direction and energy. Hence, for an accurate solution, the computational time required is still high.

In CatSim, a combination of Monte Carlo simulation and analytic calculations to calculate the scatter field has been implemented. The hybrid approach consists in using conventional MC engine for photon transportation inside the object and an analytic calculation of scatter probability to build up an approximation of the photon's scattering behavior inside the object and a smooth scatter field. The approximation to the field improves with the increasing number of shot photons. In the limit, the computed scatter field converges to the true field, which translated a scattered photon probability map over the detector surface. The result is exceptionally fast, allowing for the calculation of a scatter field in practical time frames.

For the investigation conducted during this PhD thesis, the hybrid analytic-MC model was used. Modifications were introduced in the original MC code allowing to simulate cone-beam geometries. Accordingly, an extensive validation of scatter intensity estimation for MX/DBT and bCT cone-beam geometries was performed and the results are presented in Chapter 3.

As follows we present a brief description on how conventional Monte Carlo photon transport engine is instrumented as well as the main principles behind the hybrid method.

2.5.1 Overview on the Hybrid Analytic-MC Method

Initialization Using a Conventional MC engine
The hybrid approach is initialized by using a conventional MC engine to track X-ray photon transport in the imaged object. Departing from the X-ray source, each photon is shot with random energy and direction sampled from a probability density function (PDF) described by the energy- and direction-dependent filtered X-ray fluence spectrum, $S_{net}(E, i)$. For every voxel in the photon's path, the probability of the photon being transmitted (*i.e.* passing to the next voxel) or undergoing an atomic interaction is calculated, based on known cross sections values for Compton, Rayleigh and Photoelectric events (cf. Annex A.2 for more details on X-ray interactions with matter). Depending on the interaction type, the effects on the photon's energy and travelling direction are the following:

- **Compton**: change in direction and energy
- **Rayleigh**: change in direction, conservation of energy
- **Photoelectric**: photon is entirely absorbed

For every photon, the MC engine keeps track of the following information during the photon "lifetime":

- The location $\mathbf{p}_j$ of the interaction event
- The direction unit vector $\vec{d_j}$ in which the photon was traveling before the interaction event
- Energy E_j of the photon before the interaction event
- The type τ_j of interaction event (Compton, Rayleigh or Photoelectric)

where j is the event index (or its order).

The conventional MC engine described above is used to track and register each event until the photon escapes from the voxelized phantom volume or until it is completely absorbed by the object [5]. Differently from conventional MC scatter simulation, for the hybrid method the photon's final destination after escaping from the voxelized volume has no importance, since we are only interested in the information at each interaction site. We denote by Σ_j the collection of information about every interaction j the photons underwent during its lifetime:

$$\Sigma_j = \left\{\mathbf{p}_j, d_j, E_j, \tau_j\right\} \tag{2.5}$$

Because the Monte Carlo simulation of photon transport is a well-known process, we do not describe it in any detail. Several widely available packages are available to perform Monte Carlo photon transport (Geant4 [186], MCNP [187], ESG4 [188], ...) and they can all be instrumented to provide Σ_j.

Analytical Approach for Energy-Dependent Scatter Field Estimation
The next step in the hybrid method is the analytic calculation of the energy-dependent *scatter field* by leveraging the collection of information Σ_j previously obtained. For all multiple tracked scatter events j, the scatter probability spectrum $\Psi(E'_j, i)$ that the photon would scatter with an energy E'_j and be completely transmitted in its way to the sensitive surface of a detector cell i, can be expressed as:

$$\Psi(E'_j, i) = P\left(\text{scatter from } \vec{d_j} \text{ to } \vec{\beta}_{i,j} \mid \Sigma_j\right) \times P\left(\text{transmission from } \mathbf{p}_j \text{ to } i \mid \Sigma_j\right) \tag{2.6}$$

[5] Notice that in order to take into account photon scattering in the imaging systems components such as the compression paddle, bucky, X-ray tube housing etc, they simply need to be considered as being part of the voxelized object

where $\vec{\beta}_{i,j}$ is the vector from the interaction site j to the detector element i (cf. Figure 2-9). The first term of Equation 2.6 is the scattering probability function, which can be generalized as:

$$P\left(\text{scatter from } \vec{d}_j \text{ to } \vec{\beta}_{i,j} \mid \Sigma_j\right) = \sum_Z f(\Sigma_j, \vec{\beta}_{i,j}, Z) d\Omega_j(i) \tag{2.7}$$

where $f(\Sigma_j, \vec{\beta}_{i,j}, Z)$ is an analytic function specific for Compton or Rayleigh interactions, Z denotes every atom inside the voxel at event position $\mathbf{p}_j$ and $d\Omega_j(i)$ is the solid angle under which the detector element i is seen from $\mathbf{p}_j$.

The function $f(\Sigma_j, \vec{\beta}_{i,j}, Z)$ takes into account the density of every atom Z inside the voxel and their respective differential cross sections based on the event characteristics $\{\Sigma_j, \vec{\beta}_{i,j}\}$. These cross sections are described by Klein-Nishina (for Compton interactions) and Lorenz-Mie equations (for Rayleigh interactions). In the case of Compton interactions, the detected photon energy E'_j is a fraction of E_j, and is analytically computed as function of the scattering angle [146].

The solid angle $d\Omega_j(i)$ ensures the transformation into a PDF and is calculated as:

$$d\Omega_j(i) = \frac{A_i \cdot |\langle \vec{\beta}_{i,j}, \vec{w}_i \rangle|}{\|\vec{\beta}_{i,j}\|^3} \tag{2.8}$$

where A_i is the sensitive area of the detector element i, $\vec{w}_i$ is the unit vector normal to the detector element surface and $\langle \cdot, \cdot \rangle$ denotes the scalar product operator.

The second term in Equation 2.6 is easier to calculate, relying solely on the Beer-Lambert law for primary X-rays transmission (Equation 2.2):

$$P\left(\text{transmission from } \mathbf{p}_j \text{ to } i \mid \Sigma_j\right) = exp\left(-\int_0^1 \mu(\mathbf{p}_j + q\vec{\beta}_{i,j}, E'_j) dq\right) \tag{2.9}$$

where $\mu(\cdot, E'_j)$ is the linear attenuation coefficient at energy E'_j of the individual material composing each voxel in the $\vec{\beta}_{i,j}$ chord length, parametrized by q. Figure 2-9 summarizes the steps of the scatter probability field estimation process for an individual photon.

Event Iteration and Scatter Field Convergence

The scatter field calculated with Equation 2.7 can be seen as a probability density function (PDF), evaluated for a photon with given initial energy and traveling direction. This PDF is evaluated for every detector element, at every tracked interaction site during an individual photon lifetime, therefore accounting for high-order interactions. The contribution of the multiple events in the photon lifetime is accumulated to a total energy-dependent scatter probability field for Compton and Rayleigh interactions, while being rebinned to the closest energy bin E defined by the pre-patient fluence spectra $S_{net}(E, i)$. The process is repeated iteratively with the increasing number of shot photons and normalized by the total number of photons:

$$\frac{1}{N} \sum_{n=1}^{N} \sum_{j \in \Sigma_j^n} \left[\Psi_C(E'_j, i) + \Psi_R(E'_j, i)\right] \xrightarrow[E'_j \to E]{rebinning} \Psi(E, i) \tag{2.10}$$

where indexes C and R refers to Compton and Rayleigh interactions, respectively, $n = 1, \ldots, N$ is the index of each shot photons and Σ_j^n is the collection of information of every interactions j underwent by the photon n.

For a sufficient number of shot photons, the energy-dependent scatter field $\Psi(E, i)$ will converge to the true probability distribution that a photon with initial energy and direction picked randomly from $S_{net}(E, i)$, will fall with final energy E over a detector element i after being scattered in the imaged object.

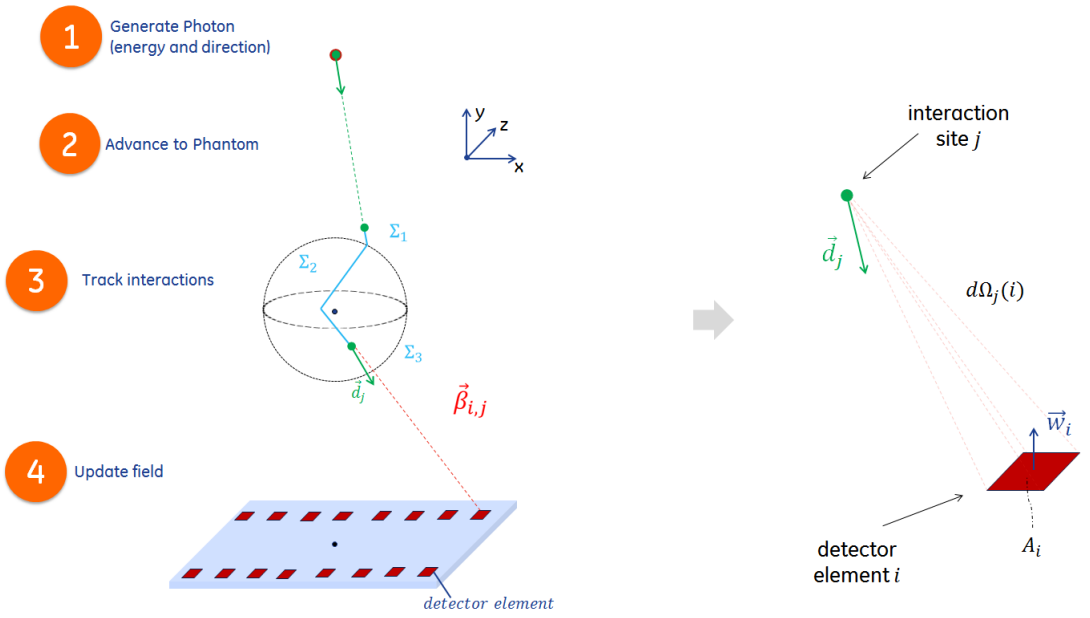

Figure 2-9: Overview of hybrid MC-analytic scatter simulation

2.5.2 Detector Incident Scattered Photon Fluence Calculation

From Equation 2.10, the X-ray photon intensity spectrum, $I_{scatter}(E,i)$, incident on the detector and contributed from scattered photons only, can be calculated as:

$$I_{scatter}(E,i) = \Psi(E,i) \cdot \sum_{i \in \mathcal{I}} \sum_{E^* \in \mathcal{E}} S_{net}(E^*,i) d\Omega_s(i) \tag{2.11}$$

where $\mathcal{I}$ is the set of elements i forming the flat detector, $\mathcal{E}$ is the set of energy bins considered in the filtered X-ray fluence spectra $S_{net}(E^*,i)$, and

$$d\Omega_s(i) = \frac{A_i \cdot |\langle \vec{L}_{i,s}, \vec{w}_i \rangle|}{\|\vec{L}_{i,s}\|^3} \tag{2.12}$$

is solid angle of detector element i as seen from the source s and $\vec{L}_{i,s}$ is the vector from the source s to the detector element i. The second term of Equation 2.11 scales the normalized probability field to a scatter intensity spectrum generated by the total number of photon in $S_{net}(E,i)d\Omega_s(i)$.

For simplicity, and to be consistent with the variables defined in this chapter, the scatter intensity spectrum of Equation 2.11 can be transformed into a scattered X-ray photon fluence spectrum, defined at $1m$ from the source, using the following relation:

$$S_{scatter}(E,i) = \frac{I_{scatter}(E,i)}{d\Omega_s(i)} \tag{2.13}$$

Notice that since photon scattering is a low-frequency phenomenon, it is not necessary to calculate the scattered X-ray fluence for every detector element. For large detectors with small detector element areas, the required calculation time to achieve convergence can increase rapidly. In this case, it is sufficient to decimate the total number of detector elements in which the scatter fluence is estimated (as illustrated in Figure 2-9), and then perform an up-sampling interpolation. In CatSim, this interpolation is performed using B-splines.

2.6 Monte Carlo Simulation of Absorbed Radiation Dose

Besides scattered radiation estimation, the Monte Carlo engine described in Section 2.5 was also used to estimate the absorbed radiation dose deposited in breast phantoms during X-ray projection simulations. The delivered radiation dose was calculated in terms of average glandular dose (AGD), *i.e.* the total dose delivered to fibroglandular tissues only.

Similarly to the photon tracking procedure previously described, individual photons are shot from the X-ray source with random energy and direction sampled from a probability density function (PDF) described by the energy- and direction-dependent filtered X-ray fluence spectrum, $S_{net}(E,i)$. The MC engine tracks the X-ray photon transport inside the voxelized object, with changes in energy and direction of movement foreseen by Photoelectric, Compton and Rayleigh interaction models. During the photon's lifetime, whenever Photoelectric or Compton interactions occur, the energy (in keV) absorbed by the voxelized object is accumulated.

The spatial distribution of the deposited energy, $E_{dep}(\mathbf{r})$, at a position $\mathbf{r}$ in space, accumulated after N photons, can be transformed into glandular dose (in units of mGy) using the following relation:

$$D(\mathbf{r}) = \frac{\overbrace{E_{dep}(\mathbf{r}) \cdot G_f(\mathbf{r})}^{\text{per interaction}} \cdot 1.6021 \times 10^{-10}}{mass(\mathbf{r})} \cdot \frac{1}{N} \sum_{i \in \mathcal{I}} \sum_{E^* \in \mathcal{E}} S_{net}(E^*, i) d\Omega_s(i) \tag{2.14}$$

where $G_f(\mathbf{r})$ is a correction factor to account for the fibroglandular part of the breast only [189], 1.6021×10^{-10} is a conversion factor with units of $mGy \cdot keV^{-1} \cdot g^{-1}$, N is the total number of photons shot during MC simulation, $mass(\mathbf{r})$ is mass associated to the fibroglandular tissue inside the voxel at position $\mathbf{r}$, $\mathcal{I}$ is the set of elements i forming the flat detector, $\mathcal{E}$ is the set of energy bins considered in the filtered X-ray fluence spectra $S_{net}(E,i)$ and $d\Omega_s(i)$ is solid angle of detector element i as seen from the source s. As in scattered X-ray photon fluence simulation, the second term in Equation 2.14 scales the average radiation dose per event to the total number of photons in $S_{net}(E,i)d\Omega_s(i)$.

The correction factor G_f can be seen as a weighting factor accounting for eventual partial volume effects between the fibroglandular tissue and the surrounding breast tissue. It can also be used to estimate AGD in test objects composed of homogeneous mixtures of fibroglandular tissue and other materials, usually adipose tissue. As suggested by Wilkinson and Heggie [190], the correction factor G_f needs to be applied at each photon interaction by weighting any eventual energy deposition with the scaling factor G_f. Assuming the fibroglandular tissue to be surrounded by adipose tissue only, G_f can be calculated as [189]:

$$G_f(\mathbf{r}) = \frac{\nu_g(\mathbf{r})(\frac{\mu_{en}}{\rho})_g}{\nu_g(\mathbf{r})(\frac{\mu_{en}}{\rho})_g + (1 - \nu_g(\mathbf{r}))(\frac{\mu_{en}}{\rho})_a} \tag{2.15}$$

where $\nu_g(\mathbf{r})$ is the weight fraction of glandular tissue in the voxel at position $\mathbf{r}$ (*e.g.* $\nu_g = 0.5$, for 50% fibroglandular equivalent material), and $(\mu_{en}/\rho)_a$ and $(\mu_{en}/\rho)_g$ are the mass attenuation coefficients of adipose and fibroglandular tissues, respectively. Accordingly, the mass associated to the fibroglandular tissue can be calculated as:

$$mass(\mathbf{r}) = \nu_g(\mathbf{r}) \times vol_{voxel} \times \rho(\mathbf{r}) \tag{2.16}$$

where vol_{voxel} is the voxel volume and $\rho(\mathbf{r})$ is the density of the mixture inside the voxel.

The transformation into AGD is found by tallying the radiation dose deposited in the subset

$\mathcal{G}$ of voxels which contain fibroglandular tissue:

$$AGD = \sum_{\mathbf{r} \in \mathcal{G}} D(\mathbf{r}) \tag{2.17}$$

Normalized Glandular Dose Coefficients
For investigations where a fixed breast phantom was considered for different input spectra, AGD was expressed in terms of Normalized Glandular Dose coefficients (DgN) [160, 191] resulting from monochromatic input beams.

From Equation 2.14, DgN values for a monochromatic beam with energy E, expressed in radiation per exposure units, $mGy \cdot R^{-1}$, at a reference point $\mathbf{p}$ in space, are obtained as:

$$DgN(E) = \sum_{\mathbf{r} \in \mathcal{G}} \frac{\overbrace{E_{dep}(\mathbf{r}) \cdot G_f(\mathbf{r})}^{\text{per interaction}} \cdot 1.6021 \times 10^{-10} \cdot \lambda^{-1}(E)}{mass(\mathbf{r}) \cdot S_{\mathbf{p}}(E)} \tag{2.18}$$

where $\lambda(E)$ is an energy-dependent factor converting photon fluence to Air Kerma (radiation units per number of photons crossing a unit of area, $R \cdot mm^2$) and $S_{\mathbf{p}}(E)$ is the incident monochromatic beam fluence calculated from the N photons shot with energy E during MC simulation, at a reference point $\mathbf{p}$ in space.

As defined by Boone *et al.* [160], a polychromatic normalized glandular dose (DgN_{poly}) can be calculated as the weighted sum of monochromatic DgN coefficients:

$$DgN_{poly} = \sum_{E \in \mathcal{E}} \frac{S_{\mathbf{p}}(E)\lambda^{-1}(E)DgN(E)}{\sum_{E \in \mathcal{E}} S_{\mathbf{p}}(E)\lambda^{-1}(E)} \tag{2.19}$$

where $S_{\mathbf{p}}(E)$ is the incident X-ray fluence calculated from $S_{net}(E, i)$ at a reference point $\mathbf{p}$ in space and $\mathcal{E}$ is the set of energy bins considered in $S_{net}(E, i)$.

For the remainder of this PhD thesis manuscript, we express DgN values in units of mGy/mGy. The conversion[6] from mGy/R to mGy/mGy units is provided by multiplying DgN values obtained with Equations 2.18 and 2.19 with a factor 0.1145.

[6]**Radiation units:** 1 gray (Gy) = 100 rad; 1 gray (Gy) = 114.5 Rontgen (R)

2.7 X-ray Detection Modeling

For the cone-beam geometry considered during this PhD thesis research, a Flat Panel Detector (FPD) model was developed and integrated in CatSim simulation chain. The implemented modules allowed to define energy-integrating (EI) detectors, with simplified modeling of the scintillator's collection efficiency, as well as photon-counting (PC) detectors with simplified modeling of photon pile-up. They also allowed to define multiple sample points for a detection element, incorporating this way spatial sampling process. Moreover, simplified models of X-ray crosstalk, optical crosstalk, lag, and other phenomena deteriorating image quality in X-ray projections are also present in CatSim, but were not used nor discussed in this this PhD thesis research.

In this section, signal and noise propagation for a hypothetical noise-free blur-free detector, which was the main detector model we used in our research, are described. For experimental validation purposes, signal and noise propagation inside a realistic indirect conversion scintillator-based detector are also described.

Flat Panel Detector Definition
In our simulator, Flat Panel Detectors were defined as the concatenation of detector cells (or detection elements, *del*), distributed uniformly along a flat surface and forming this way the detector pixel matrix (with rows and columns). Each cell has an active surface, *i.e.* sensitive to X-rays, defined by a *fill fraction* factor. The detector fill fraction models the fact that it could exist a dead zone between cells (due to electronic components for example), which is not sensitive to the incoming quanta. A fill fraction of 1 means that the detector has no dead space. A fill fraction of 0 means that the detector is completely inactive. A detector cell oversampling factor can be defined, associating multiple sample points over each cell's sensitive surface. Detector fill fraction and detector cell oversampling are essential to emulate a continuous sampling window, *i.e.* the *detector aperture*, which is discussed in details below.

Figure 2-10a illustrates an example of FPD construction. In the zoomed detector cell, an example of 3×3 detector cell oversampling is illustrated, with sample points distributed uniformly inside the cell's sensitive surface.

Incident Photon Intensity Calculation
Assuming an X-ray point source s, the X-ray fluence spectrum incident on the detector element i, $S_{inc}(E,i)$, considering both primary (cf. Equation 2.2) and scattered radiation (cf. Equation 2.13) is given by:

$$S_{inc}(E,i) = S_{scatter}(E,i) + S_{net}(E,i)\frac{1}{n_i}\sum_{i'=1}^{n_i} exp\left(\sum_{o \in \mathcal{O}} -\mu_o(E)t_{i'so}\right) \tag{2.20}$$

where $S_{scatter}(E,i)$ is the incident X-ray photon fluence contributed from scattered photons only, $S_{net}(E,i)$ is the pre-patient X-ray fluence, $i' = 1,\ldots,n_i$ are the indexes of the n_i sample points inside the detector element i, $\mu_o(E)$ is the linear attenuation coefficient of each primitive structures o in the imaged object $\mathcal{O}$ the at energy E and $t_{i'so}$ is the thickness of every structure o in the X-ray beam path $\mathbf{i' - s}$.

Equation 2.20 assumes that the net X-ray fluence spectrum $S_{net}(E,i')$ transmitted by the tube housing is the same for all detector sample points $i' \in i$. Finally, the X-ray fluence spectrum $S_{inc}(E,i)$ incident on the detector can be transformed into an intensity spectrum $I_{inc}(E,i)$ (in number of photons per energy bin) over each detector element i:

$$I_{inc}(E,i) = S_{inc}(E,i)d\Omega_s(i) \tag{2.21}$$

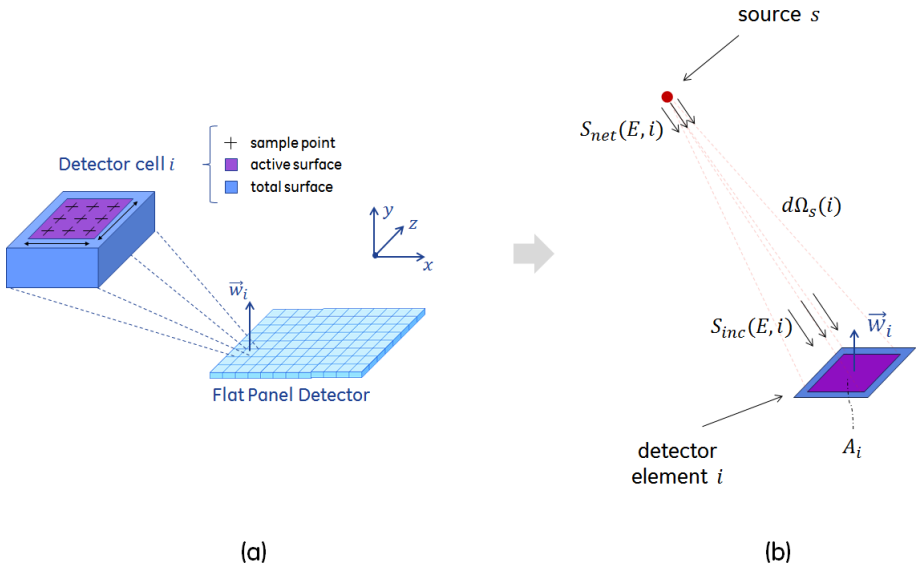

Figure 2-10: A scheme of the Flat Panel Detector (FPD) model. The detector is defined as a concatenation of detection cells. Each cell is defined by its total surface area, an active (or sensitive) area and a finite number of uniformly distributed sampling points

where $d\Omega_s(i)$ is solid angle of detector element i as seen from the source s (Equation 2.12 and Figure 2-10b).

2.7.1 Signal and Noise Propagation in Noise-Free Blur-Free Detectors

The signal intensity (SI) in a hypothetical noise-free blur-free detector, *i.e.*, that does not generate any kind of noise or blurring and for which quantum noise (modeled as a Poisson distribution) is the only random component, can be approximated as:

$$SI(i) = \kappa \cdot \sum_{E \in \mathcal{E}} \xi(E) \mathcal{P}\left\{\eta(E) \cdot I_{inc}(E,i)\right\} \tag{2.22}$$

where κ is a scaling factor for digital units, $\mathcal{E}$ is the set of energy bins considered in $I_{inc}(E,i)$, $\xi(E)$ is the detector conversion response, $\mathcal{P}\{\cdot\}$ denotes the Poisson distribution, $\eta(E)$ is a function translating an eventual energy-dependent efficiency in detecting photons, $I_{inc}(E,i)$ is the X-ray intensity spectrum incident over the detector element i.

For ideal energy-integrating and counting detectors $\xi(E) = E$ and $\xi(E) = 1$, respectively, which translates the integration or counting processes. The function $\eta(E)$ can be an extremely complex function accounting for different energy-dependent inefficiencies during the detection process, such as the absorption of X-ray photons within the scintillators or the spectral response of energy-discriminating photon-counting detectors during energy threshold.

2.7.2 Signal and Noise Propagation in Indirect-Detection Detectors

Signal and Noise propagation inside indirect-detection X-ray detectors can be modeled as a cascade model with 7 stages, as suggested by Siewerdsen *et al.* [192]. These stages comprise 1) the X-ray interaction with the scintillator, 2) generation of light photons, 3) spreading and 4) coupling of

optical quanta inside the detector, 5) the collection (aperture) and integration of light photons by the photodiode, and finally 6) sampling and 7) additive electronic noise during readout.

This process assumes linearity, shift invariance, and stationarity of first- and second-order statistics. Under these assumptions, it has been shown that the mathematical framework developed to model each stage allows for commutative operations [147], *e.g.*, binomial collection and spreading, spreading and integration. It also allows the combination of multiplicative factors such as optical gain, optical collection efficiency, coupling, and other scaling factors. Therefore, disregarding other nonlinearities (*e.g.* lag, crosstalk,...), for the investigations carried in this work, signal and noise propagation was expressed in 4 major steps, plus an additional Analogic/Digital conversion step, as illustrated in Figure 2-11. The 5-steps are summarized as:

1. **X-ray Interaction:** the energy-dependent Quantum Detection Efficiency (QDE) and X-ray quantum noise modeled as a Poisson distribution $\mathcal{P}\{\cdot\}$
2. **Optical Gain:** the merging of various multiplication factors such as scintillation gain, light reflection, optical collection efficiency, photodiode efficiency, etc. It can be seen as the detector's total optical efficiency, and is generally expressed in *light photons per keV*.
3. **Optical Spreading:** stochastic spreading of the optical quanta inside the converter. In the frequency domain, it can be approximated as Lorentzian decay[7] functions $H(f_u, f_v)$ [192–194].
4. **Integration and Sampling:** the integration of quanta by the photodiode over its sensitive surface (photodiode aperture transfer function, $\Pi(f_u, f_v)$, expressed in the frequency domain) and assignment of signal content to each detector element (detector sampling grid). Optical spreading and photodiode aperture form the detector pre-sampling MTF, and depending on its frequency content, signal sampling may cause aliasing artifacts.
5. **Data Acquisition System:** the charge readout by the Data Acquisition System (DAS), adding electronic noise, and A/D conversion from *electrons* to digital units (*d.u.*, *gray levels*, or *counts*), forming the output image.

The 5 steps framework described above allows to summarize the signal intensity (SI) associated to a given detector element i in a single mathematical expression. For a simple case where optical

[7] A generic representation of the Lorentzian function can be written as

$$L(f) = \frac{1}{\pi} \frac{(\frac{1}{2} \cdot \Gamma)}{(f - f_0)^2 + (\frac{1}{2} \cdot \Gamma)^2}$$

where f_0 is the central frequency and Γ is a parameter specifying the full width at half maximum. The Lorentzian function is normalized so that $\int_{-\infty}^{\infty} L(f) = 1$ and has a maximum at $f = f_0$, with $L(f_0) = \frac{2}{\pi\Gamma}$

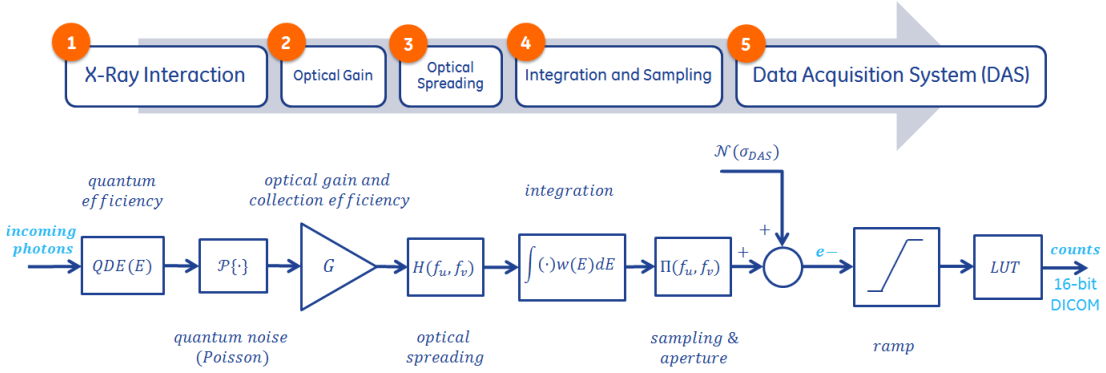

Figure 2-11: Simplified 5-steps cascade model for indirect-detection

spreading, photodiode aperture and any other spatial variation are not considered, the SI before A/D conversion (in number of electrons) can be written as:

$$SI(i) = \mathcal{N}(0, \sigma_{DAS}) + G \sum_{E \in \mathcal{E}} E \cdot \mathcal{P}\Big(\eta(E,i) \cdot I_{inc}(E,i)\Big) \tag{2.23}$$

where $\mathcal{N}(0, \sigma_{DAS})$ corresponds to the additive electronic noise modeled as a Gaussian distribution $\mathcal{N}\cdot$ with null average ($\mu = 0$) and standard deviation σ_{DAS}, G is the total detector gain (combining optical and electronic gains), $\mathcal{E}$ is the set of energy bins considered in $I_{inc}(E,i)$, $\mathcal{P}\{\cdot\}$ denotes the Poisson distribution, $\eta(E)$ is a function translating the energy-dependent QDE and $I_{inc}(E,i)$ is the X-ray intensity spectrum incident over the detector element i.

For the energy-integrating scintillator-based detectors used in this PhD research, the function $\eta(E)$ was approximated as:

$$\eta(E,i) = 1 - e^{\mu_{scint}(E) t_{scint}(i)} \tag{2.24}$$

where $\mu_{scint}(E)$ is the linear attenuation coefficient at energy E of a continuous and homogenous scintillator material and $t_{scint}(i)$ is the oblique thickness of the scintillator at detector element i.

Different studies have demonstrated that it exists a large variation in optical photon spreading and spatial resolution across the detector surface due to incident X-ray beam obliquity over the scintillator [194, 195]. More precisely, the response to an infinitely thin X-ray pencil beam, or Point Spread Function (PSF), becomes asymmetric as the incidence angles increases. In this case, indirect-detection becomes a nonstationary process. This is particularly true in the case of a breast tomosynthesis geometry in which the detector remains static. The incidence angle can exceed 30° and blurring due to oblique X-ray incidence can have a strong impact in resolution. For instance, Mainprize *et al.* [195] have reported that at an incidence angle of 40°, the MTF of a bench-top tomosynthesis system leveraging a GE Senographe® 2000D detector (GE Healthcare; Chalfont St Giles, UK) falls by 35% at 5 cycles/mm and 65% at 8 cycles/mm, for a typical low-energy mammography spectrum (Mo/Mo 26kV). Other than resolution degradation, beam obliquity result in different absorption efficiencies across the detector surface, which may impact signal and noise transfer to reconstructed breast tomosynthesis images. In our validation studies, only small incident angles were considered. Hence, for simplicity, X-ray beam obliquity was disregarded in $\eta(E,i)$ calculation and optical spreading modeling, since it would entail only for small differences in signal intensities [195, 196].

Equation 2.23 only takes into account the detector sampling process. In order to fully simulate the spatial resolution of a given detector, the optical spread $H(f_u, f_v)$ and the photodiode aperture $\Pi(f_u, f_v)$ must be included. These two aspects can be implemented on the frequency domain, while using multiple uniformly distributed samples over the detector cell to avoid aliasing artifacts. The degree of oversampling will depend on the frequency contents of $H(f_u, f_v)$ and $\Pi(f_u, f_v)$. If the hypothesis of linearity, shift invariance, and stationarity are held, then the SI for a detector element i can be written as:

$$SI(i) = \mathcal{N}(0, \sigma_{DAS}) + G \cdot \mathcal{F}^{-1}\left\{\mathcal{F}\left\{\sum_{E \in \mathcal{E}} E \cdot \mathcal{P}\Big(\eta(E) \cdot I_{inc}(E,i)\Big)\right\} H(f_u, f_v)\Pi(f_u, f_v)\right\} \tag{2.25}$$

where $\mathcal{F}\{\cdot\}$ and $\mathcal{F}^{-1}\{\cdot\}$ denotes respectively direct and inverse Fourier transform operators in the detector u-v space.

2.8 Discussion

In this chapter, we provided a detailed description of the main components of the simulation platform developed specifically for this PhD thesis research work. X-ray point source models, emitting low and high-energy fluence spectra, were introduced. Computational breast phantoms based on analytical and meshed-based structures, as well as the equations modeling the primary X-ray photons projections were described. X-ray scattering and absorbed radiation dose estimation using a Monte Carlo engine was detailed. Finally, the detection of transmitted X-ray photons in digital converters was described for a noise-free blur-free detector and a realistic indirect-conversion detector. The developed acquisition chain provides the basic tools necessary to achieve the main objectives of this PhD thesis research and to be discussed in later chapters.

In the light of the Figures-of-Merit exploited in this PhD thesis, a series of assumption and simplifications were made to the simulation chain in order to keep simulation time manageable and with no significant impact on the metrics under evaluation.

Previously developed analytical models for low-energy spectra typically used in mammography (Mo and Rh anodes) and high-energy spectra typically used in current breast CT prototypes (W anodes) were implemented. A point source emitting X-ray isotropically in every direction was assumed. This hypothesis is justified for the assessment of low-frequency variations of signal intensity (*e.g.* metrics based on average signal, contrast and noise, measured in large regions-of-interest) but becomes unrealistic for high-frequency variations (especially close to the system resolution) due to focal spot blurring. For a more realistic source model, one could define multiple point sources, uniformly distributed over a finite thermal focal spot area. Moreover, a relative weight representing the local intensity of emitted X-rays could also be associated to each of the point sources. Focal spot oversampling and point source weighting would allow to emulate a given X-ray tube emission pattern (uniform, Gaussian, trapezoidal,...) and include the Heel effect.

In the presented model, the acquisitions were assumed to be performed in an ideal "step-and-shoot" mode, with no blur introduced from tube motion. Step-and-shoot acquisition was the main model used in this PhD thesis. However, many DBT and bCT systems today are equipped with continuous X-ray acquisitions, entailing in decreased total acquisition time and reduced patient motion artifacts. In order to simulate tube motion and its consequent spatial resolution degradation in projected images, one could define an angular oversampling factor and approximate continuous motion as the integration of stepwise sub-view projection data into one final projection view. The result would be a blurring effect due to spatial uncorrelation between sub-views. Combination of source, detector and angular oversampling are imperative to emulate more realistic spatial properties of an X-ray acquisition system.

With respect to the indirect-detection X-ray detector model, X-ray beam obliquity was disregarded in the scintillator's energy-dependent absorption efficiency $\eta(E)$ calculation. As demonstrated by Hajdok and Cunningham [196], oblique X-rays incident over a scintillator-based detector has no effect on the NPS, but may reduce the MTF, and as consequence, the Detective Quantum Efficiency[8] (DQE). However, the authors in Ref. [196] showed that these effects are negligible at low spatial-frequencies (below 5 cycles/mm), but become more pronounced above this threshold, to finally decrease at higher frequencies. Despite results in Ref. [196] being demonstrated for a direct-conversion a-Se detector model, similar trends were observed later by Mainprize *et al.* [195] using a CsI-based detector model. Nonetheless, as discussed further on in Chapter 5, this effect is negligible in the light of the Figures-of-Merit and cone-beam geometries under evaluation in this PhD thesis investigations.

Another notable simplification in the indirect-detection X-ray detector model is that generation and re-absorption K-fluorescence photons in the scintillator were not fully implemented. Re-absorption of K fluorescence affects the detected signal intensity due re-absorption of light photons, the noise associated with the X-ray to light conversion process (energy-dependency of

[8] $DQE(f) = MTF^2(f)/NNPS(f)$

the Swank factor) and the detector spatial resolution due to spreading of the additional quanta inside the scintillator [197]. However, for the experimental validation purposes discussed in the Chapter 5, the inclusion of a dedicated model for K-fluorescence was not necessary. As it will be demonstrated, spatial resolution and local variations of signal intensities were well approximated through calibration of the total detector gain G and the optical spreading transfer function $H(f_u, f_v)$ (Equation 2.25). For the other investigations carried in this PhD thesis (Chapters 5, 6 and 7), no assumption was made on the detector technology and a hypothetical noise-free blur-free detector was considered.

Finally, before exploiting the developed simulation platform, we wanted to make sure that it describes with sufficient realism the behavior of actual breast X-ray imaging systems for which we have access to real data. For this purpose, a complete validation of the different CatSim modules for X-ray energy ranges and breast thickness and compositions expected in clinical practice are provided in the next chapter.

Chapter 3

Validation of CatSim for Breast X-ray Imaging

As described in Chapter 2, new modules for CatSim simulation chain have been developed to model realistic 2D/3D breast X-ray imaging systems. To make sure that the implemented simulation chain is in agreement with realistic physical phenomena underlying an X-ray breast imaging system, an extensive validation of the developed models with regard to previously published and experimentally obtained data is provided in this chapter.

The validation was conducted in a modular way, *i.e.* isolating as best as possible each component of the acquisition chain and performing individual evaluation on their performance compared to expected values. In Section 3.1, the X-ray spectrum models exploited for CE-DBT were compared to GE Senographe® DS prototype based Molybdenum and Rhodium anodes. In Section 3.2, the results of X-ray photon scattering simulation validation are reported. Since we only explored scattered radiation in a breast CT geometry, simulation results are presented for typical cone-beam geometry, energy range and phantom sizes expected for CE-bCT. Results were compared to previously published results. In Section 3.3, Monte Carlo based estimation of average glandular dose absorbed by the computational breast phantoms was validated. Both typical mammography and breast CT geometries were considered. Simulation results were compared to previously published results based on well-known Monte Carlo packages (*e.g.* Geant4). In Section 3.4, X-ray detector model was validated while considering the simplified cascade model for scintillator-based indirect conversion detectors. A series of experiments on three different X-ray systems, using both low-energy and high-energy spectra, was performed to assess variations in the detected signal intensities.

3.1 Spectrum Model Validation

In this section we focus on assessing the beam quality of the SpeXim spectrum model with respect to experimental data acquired from a mammography system. Conversely, an extensive validation data on the TASMIP model can be found in Ref. [155] and will no further be discussed.

The term "beam quality" generally refers to the beam's penetrating ability. The N-th Value Layer (VL) is a typical metric to describe the penetrating ability of a spectrum. The N-th VL is defined as the thickness of a material at which the transmitted radiation fluence is reduced by a factor N. Beam quality is typically assessed through Half Value Layer (HLV) measurements, *i.e.*, $N = 2$. Measurements of higher order N-th VL (*e.g.* $1/4th$, $1/8th$,...) allow for more accurate evaluation of the beam quality. In this study, N-th VL values were obtained through Air Kerma measurements using Aluminum as attenuating material.

The procedure relied on measuring the exposure, at a fixed distance from the source, for different thicknesses of Aluminum. In this setup, disregarding the X-ray beam attenuation in air, the Air Kerma K transmitted by a thickness t_{Al} of Aluminum at a distance r from the source, can be written as:

$$K(t) = \frac{1}{r^2} \int_0^\infty \lambda^{-1}(E) S_{net}(E) e^{-\mu_{Al}(E) \cdot t_{Al}} dE \tag{3.1}$$

where $S_{net}(E)$ is the filtered X-ray fluence spectrum at 1 m from the source, $\lambda^{-1}(E)$ is the exposure per fluence conversion factor (radiation units per number of photons crossing a unit of area, $R{\cdot}mm^2$) and $\mu_{Al}(E)$ is the linear attenuation coefficient of Aluminum. From Equation 3.1 we may assume that the relationship between the measured Air Kerma K and the increasing aluminum thickness can be described as a nearly exponential relationship. This is because beam hardening inside the aluminum sheets decreases X-ray fluence beyond the exponential decay foreseen by the Beer-Lambert law (cf. Annex A.2 for further details on X-ray interaction with matter), particularly for high thickness values. Equation 3.1 can, in this case, be approximated as

$$K(t) = K_0 \cdot \exp\left(-cte \cdot t_{Al}\right) \tag{3.2}$$

where K_0 is the reference exposure measurement obtained without aluminum, and cte is a proportionality constant.

Finally, in order to invert Equation 3.2, a log-interpolation was performed to calculate the aluminum thickness that reduces the reference exposure K_0 by a factor N.

3.1.1 Nth Value Layer Assessment for Mo and Rh anodes

To validate the SpeXim model, N-th VL values ($N = 2, 4, 8, 10$) of simulated spectra were compared to N-th VL measured on a GE Senographe® DS system (GE Healthcare; Chalfont St Giles, UK). Four sets of acquisition parameters were considered, covering the pairs of anode and filter available on a GE Senographe DS system, including one high-energy spectrum typically used for contrast-enhanced mammography [198]. Table 3.1 summarizes the spectra configuration as well as the expected HVL and Tube Yield values range, according to GE Senographe DS's *"Mammograph Quality Test Control Manual"*.

Table 3.1: X-ray spectra used in the SpeXim validation experiments and the expected HVL and Tube Yield values, as required by GE Senographe DS Quality Control (QC) manual

Spectrum	**HVL (mm)**	**Yield (mGy/mAs)**
Mo/Mo 26 kV	0.29 – 0.38	35 – 130
Mo/Rh 28 kV	0.31 – 0.47	35 – 130
Rh/Rh 30 kV	0.33 – 0.5	35 – 130
Mo/Cu 49 kV	∼3.3	N/A

Simulation Setup
For the simulation part, $K(t)$ was analytically calculated as function of the Aluminum thicknesses using Equation 3.1, at 10 μm step, using analytic test objects. The net fluence spectra $S_{net}(E)$ were calculated using raw anode fluence spectra $S_{raw}(E)$ provided by the SpeXim model with added flat filtration as foreseen by Equation 2.1. A log-interpolation was performed to inverse Equation 3.2 and calculate individual 1/2, 1/4, 1/8 and 1/10 VLs.

Experimental Setup
For the experimental part, Air Kerma was measured according to the experimental setup illustrated

in Figure 3-1 and for increasing Aluminum thickness. Aluminum sheets of various thicknesses were piled up on top of the compression paddle, which was turned upside down and positioned as close as possible to the X-ray source. This setup greatly reduces scattered X-rays influence on the dose measurements. A metallic support was placed on the detector surface to hold a 6 cm^3 ionization chamber (RadCal® 10X6, RadCal Corporation; Monrovia, CA, USA) at 592 mm from the X-ray source. This support also protects the detector from high exposure levels. The X-ray beam was collimated to 9×9 cm^2 Field-of-View (FOV) and the ionization chamber was positioned to be aligned with the beam's path.

The reference Air Kerma K_0 was measured with no aluminum filtration in the radiation field of view. The following Air Kerma measurements $K(t)$ were repeated while combining Aluminum sheets of 100, 200 or 300 μm thicknesses, progressively increasing the total Aluminum thickness t_{Al}. Finally, in same manner as for the simulation part, by exploring the log-interpolation of Equation 3.2 we calculate the 1/2, 1/4, 1/8 and 1/10 VLs.

Results

Figures 3-2a and 3-2b illustrates measured (markers) and simulated (solid lines) relative Air Kerma values $K(t)/K_0$ as function of aluminum thickness, for all four considered spectra. Air Kerma measurements were repeated 6 times and showed on average ~ 0.01 mGy standard deviation. This resulted in a maximum 2% error in measured $K(t)/K_0$ values and error bars for Figures 3-2a and 3-2b that were too small to be displayed. From visual inspection, we note the very good qualitative agreement between measured and simulated curves values.

The bottom row in Figures 3-2a and 3-2b shows the absolute error in $K(t)/K_0$ between simulated and measured data. Absolute errors in $K(t)/K_0$ ratio were below 2%. The correlations in error curves seen in Figure 3-2a might be explained by the possible deviation in Aluminum sheets thickness with respect to their nominal values.

Table 3.2 compares measured and simulated 1/2, 1/4, 1/8 and 1/10 Value Layers. The last column displays the SpeXim model error relative to the measured values. The last three rows provide 1st and 2nd order statistics on the relative error. Average error was 1.04%, with one standard deviation of 1.43%. Median of error values was 0.64%. The highest error (3.65%), found for Mo/Mo 26 kV spectrum. Notice that, for the high-energy spectra, 1/8 and 1/10 VLs were not calculated. This is because any further increase in aluminum thickness would decrease X-ray beam fluence to the ionization chamber's lower limit of sensitivity, therefore being unable to provide an accurate Air Kerma measurement.

Discussion

Typical beam quality assessment in X-ray imaging system is limited to the evaluation of HVL (N=2). In our study, in order to have greater credibility in the implemented model, we evaluated the agreement between simulated and real X-ray beam penetration ability up to 1/10 Value Layers.

For SpeXim model validation, we presented qualitative (shape of the curves of relative Air Kerma as function of the Aluminum thickness in Figures 3-2a and 3-2b) and quantitative (errors in relative Air Kerma and N-th value layer measurements) that the beam penetrating ability reflects well the behavior of a typical mammography X-ray tube for both LE and HE spectra, with approximately 1% error on average.

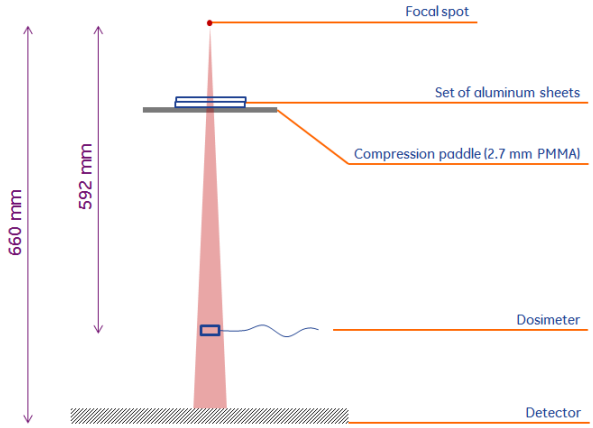

Figure 3-1: Experimental set-up for beam quality validation between SpeXim model and a real mammography system

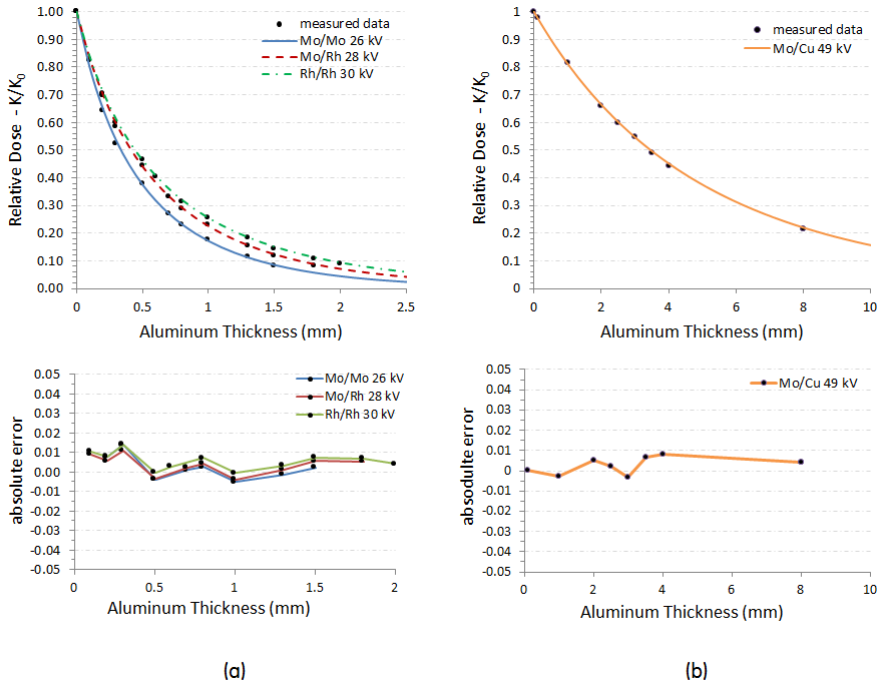

Figure 3-2: The top row shows relative dose values $K(t)/K_0$ as function of the aluminum thickness, calculated using experimental (markers) and simulated (solid lines) data for (a) low-energy and (b) high energy spectra. The bottom row shows absolute error of $K(t)/K_0$ between simulated and measured data

Table 3.2: Experimentally assessed and simulated N-th value layers. Simulations were performed with CatSim using the SpeXim spectrum model

Spectrum	**FOM**	**CatSim**	**Measurement**	**error (%)**
Mo/Mo 26 kV	HVL (mm)	0.339	0.327	3.65
	1/4 VL (mm)	0.752	0.748	0.57
	1/8 VL (mm)	1.225	1.235	-0.86
	1/10 VL (mm)	1.385	1.382	0.24
Mo/Rh 28 kV	HVL (mm)	0.417	0.415	0.53
	1/4 VL (mm)	0.921	0.925	-0.44
	1/8 VL (mm)	1.493	1.499	-0.46
	1/10 VL (mm)	1.691	1.679	0.72
Rh/Rh 30 kV	HVL (mm)	0.446	0.441	1.05
	1/4 VL (mm)	1.019	1.020	-0.12
	1/8 VL (mm)	1.700	1.642	3.53
	1/10 VL (mm)	1.935	1.875	3.19
Mo/Cu 49 kV	HVL (mm)	3.469	3.415	1.59
	1/4 VL (mm)	7.288	7.193	1.31
	1/8 VL (mm)	-	-	-
	1/10 VL (mm)	-	-	-
			MEAN	1.04
			STD DEV	1.43
			MEDIAN	0.64

3.2 X-ray Scatter Simulation Validation

The goal of this section is to validate the performance of CatSim's conventional Monte Carlo (MC) engine and hybrid analytic-MC scatter simulator in a breast X-ray imaging setting. Since our work focuses on cone-beam geometry, validation results are provided for different setups around this geometry only. Scatter point spread functions, scatter intensity maps and scatter-to-primary ratios maps were computed. The effect of geometric set-ups, X-ray spectrum, as well as test object composition, size and shape were evaluated.

Our results were compared to previously published data, including experimentally assessed data and Monte Carlo derived scatter data.

3.2.1 PSF for Infinitely Wide Flat Phantoms

The experiment described below is a preliminary verification of the calculations concerning photons scattering and fluence estimation previously discussed in Section 2.5. To validate the Rayleigh and Compton photon scattering calculations within the Monte Carlo engine, simulated Point Spread Function (PSF) of scattered radiation was compared with the validated Monte Carlo engine SIERRA, developed by Boone *et al.* [199]. Point-spread functions were calculated for a limited set of beam energies and phantom thicknesses, and the results compared to published results [178].

Simulation Setup
To match the geometry used by Boone *et al.*, an X-ray pencil beam was shot from a point source at 650 mm from a flat panel detector surface, at normal incidence angle. A 50% fibroglandular equivalent phantom, extremely wide, with constant thickness and voxelized at 1 mm^3 voxel size, was positioned parallel to the detector surface with a 10 mm air gap. Figure 3-3 illustrates the simulated geometry.

One million photons with given initial energy were tracked inside the phantom and underwent Photoelectric, Rayleigh and Compton interactions. The scattered X-ray photon intensity spectrum, $I_{scatter}(E, i)$, incident on the detector was calculated using the hybrid analytic-MC approach, according to Equation 2.11. The scattered photons were detected and accumulated by a perfect energy-integrating detector at a given position of its surface. The resulted signal will be referred to as being obtained from the *hybrid* approach. For comparison, the same photons were tracked down to detector surface, and their energies deposited individually at their terminal position over the detector surface. The results will be referred to as being obtained from the *pure Monte Carlo* approach.

The spatial distribution of the detected scattered photons energy was translated into polar coordinates $E_{detected}(r, \theta)$, with origin at the incident primary photon position. The radial profiles were integrated over 2π and tallied into n increments of radius, at 1 mm spacing step (Figure 3-3b). Accounting for differences in the n annulus surfaces, the final PSF was calculated as

$$PSF(r_n) = \frac{\int_0^{2\pi} E_{detected}(r_n, \theta) d\theta}{\pi(r_n^2 - r_{n-1}^2)} \tag{3.3}$$

PSF were calculated for three different acquisition setups: i) a 20 mm thick phantom hit by a 20 keV beam, ii) a 80 mm thick phantom hit by a 30 keV beam and iii) a 40 mm thick phantom hit by a polychromatic spectra generate by a Molybdenum (Mo) anode at 26 kV tube voltage and 0.03 mm Mo filtration.

Results
Figure 3-4a illustrates the PSF calculated using the hybrid method (solid lines) and pure Monte

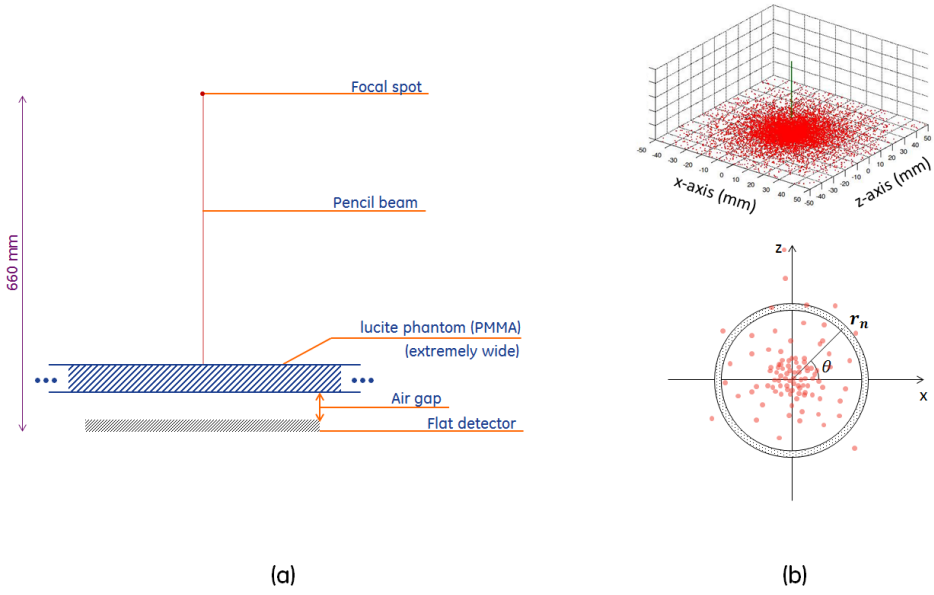

Figure 3-3: (a) Simulation setup for scattered radiation PSF validation; (b) illustration of scattered photons spatial distribution over the detector surface. The scattered photon energy is accumulated into n annulus surfaces, at step-wise increments of the radial distance r_n from the normally incident primary photons position

Carlo (dashed lines), as well as the reference data (circles) from previously validated Monte Carlo engine [199], for the three considered acquisition setups. From visual inspection, we observe good agreement between both hybrid and pure MC curves obtained with CatSim and the reference MC simulator.

It must be emphasized that since the results in Ref. [199] were not explicitly available (either numerically or electronically), the reference data points illustrated in Figure 3-4a were obtained by superposing magnified versions of the published curves over a high-resolution sampling grid. The errors during the sampling process were estimated to be below the differences observed between simulated and reference data. Unless otherwise specified, the same sampling process was used in the remainder of this chapter to retrieve data points from reference publications.

Figure 3-4b illustrates a qualitative comparison between the detected energy map, $E_{detected}(r, \theta)$, obtained with pure Monte Carlo and hybrid methods, while using the same input beam and the same number of photons (10^6). From the curves in Figure 3-4a and the maps Figure 3-4b we may notice that, for the same number of shot photons, the hybrid approach presents much smoother energy distributions and PSFs when compared to pure Monte Carlo approach.

Discussion

The objective of this experiment was to verify if photon transport calculations inside CatSim Monte Carlo hybrid engine agrees with the expected behavior predicted by Photoelectric, Compton and Rayleigh interaction models (cf. Annex A.2 for details on X-ray interactions with matter). We therefore assumed a limited set of X-ray spectra: two monochromatic beams at 20 and 30 keV, and one polychromatic spectra at typical mammography energy levels.

This experiment was also a preliminary step in the validation of Monte Carlo engine for absorbed radiation dose estimation, described in Section 3.3. Further indications on the quality of scattered radiation spreading over a flat detector, and for a wider range of acquisition conditions, are provided

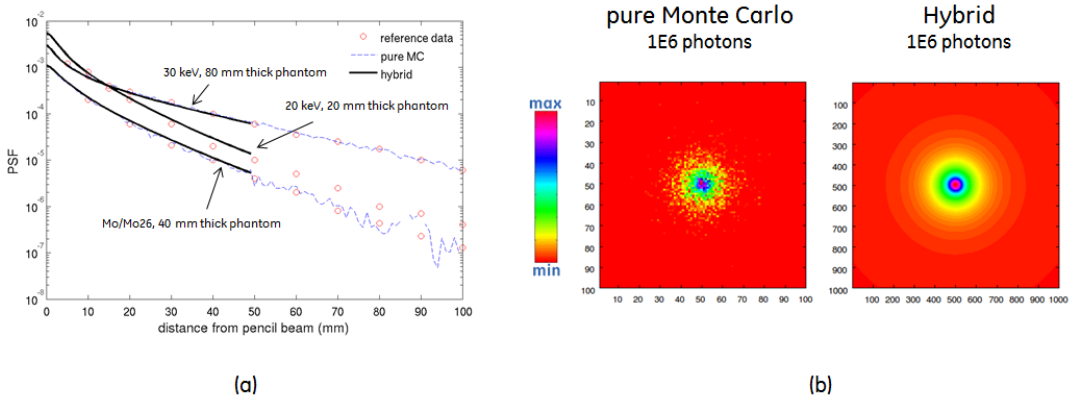

Figure 3-4: (a) CatSim PSF comparisons with reference; (b) Detected energy $E_{detected}$ on the detector surface, for pure Monte Carlo and Hybrid approaches

as follows.

3.2.2 Scatter and Scatter-to-Primary Ratios Profiles

In the second part of the scatter simulation module validation, signal intensity profiles, or *Scatter Intensity* profiles, generated from incident scattered radiation in an ideal blur-free detector, as well as Scatter-to-Primary Ratio (SPR) radiation profiles were simulated with hybrid analytic-MC method and compared to previously validated Monte Carlo engines. The experiment focused in verifying the accuracy of the simulated scatter intensity distribution over the flat detector, when different cone-beam breast CT geometries, input spectra, as well as different phantom sizes and composition are considered.

Table 3.3 summarizes the three previously published references chosen for the comparison, as well as the simulation parameters involved.

Simulation Setup
Following the description in Ref. [200], a cone-beam geometry illustrated in Figure 3-5a was assumed, with $SDD = 785\ mm$ and $SID = 415\ mm$. A $40 \times 30\ cm^2$ ideally sharp perfect energy-integrating detector, with 0.31 mm pixel pitch and equipped with 600 μm-thick CsI scintillator was considered. A 160 mm diameter, 240 mm wide homogeneous water phantom was centered at the system's center-of-rotation (COR) and voxelized into $2 \times 2 \times 2\ mm^3$ voxel size. The incident spectrum, emitted from a point source, was generated using the TASMIP model for a W anode with 120 kV tube voltage and filtered with 8 mm of Aluminum. Scatter signal intensity was

Table 3.3: References for Scatter and Scatter-to-Primary Ratios Profile validation

Reference	MC Engine	Geometry	X-ray Spectra	Cylindrical Phantom
Kyriakou et al. 2006[a]	ImpactMC	SDD/SID=785/415mm	W/Al 120 kV	Water / 16 cm
R. Bhagtani & TG. Schmidt, 2009[b]	GEANT4	SDD/SID=780/465mm	W/Al 80 KV, 50 keV	PMMA / 10, 14, 18 cm
Liu et al., 2005[c]	GATE (GEANT4)	SDD=910mm Air Gap = 15, 20, 25cm	W/Al 60 kV	50% fibroglandular/ 10, 12, 14 cm

[a] Ref. [200]
[b] Ref. [110]
[c] Ref. [113]

estimated using conventional Monte Carlo method with 10^9 photons and using the hybrid method with 10^6 photons.

Following the description in Ref. [110], a centered cone-beam geometry illustrated in Figure 3-5b was assumed[1], with $SDD = 780\ mm$ and $SID = 465\ mm$. A $40 \times 30\ cm^2$ ideally sharp photon-counting detector, with 100% detection efficiency and 0.394 mm pixel pitch was considered. Three 50% fibroglandular equivalent cylindrical phantoms with 10, 14 and 18 cm diameters and heights equal to 1.5 times their respective radius were simulated. Simulations for the 10 and 18 cm diameter phantoms were carried according to a W anode 80 kV spectrum generated using the TASMIP model and filtered with 3 mm of Aluminum, while scatter simulation for the 14 cm diameter phantom was carried for a 50 keV monochromatic X-ray beam. One million photos (10^6) were tracked in $2\times2\times2\ mm^3$ voxels, to generate scatter signal intensities over the detector. Scatter-to-Primary Ratio (SPR) maps over the detector, *i.e.*, the ratio between the signal generated from scattered photons only and the signal generated from primary photons only, were also calculated for each experimental condition. Primary signal intensities were calculated from analytic projections of each considered phantom.

Finally, following the description in Ref. [113], a shifted cone-beam geometry illustrated in Figure 3-5b was assumed, with $SDD = 910\ mm$. A $25 \times 20\ cm^2$ ideal blur-free energy-integrating detector, with 100% absorption efficiency and 2 mm pixel pitch was considered. Three 50% fibroglandular equivalent cylindrical phantoms with 10, 12 and 14 cm diameters and heights equal to 1.5 times their respective radius were simulated. The phantoms were positioned such as the cylinder's top cross-sectional plane was aligned with the COR. The incident spectrum, emitted from a point source, was generated using the TASMIP model for a W anode with 60 kV tube voltage and filtered with 1.5 mm of Aluminum. One million photos (10^6) were tracked in $2 \times 2 \times 2\ mm^3$ voxels, to generate scatter signal intensities and SPR maps over the detector when the 10, 12 and 14 cm phantom were positioned such as to leave 15, 20 and 25 cm air gaps from the detector for a fixed SDD value (*i.e.*, corresponding to the difference $SDD - SID$ values).

Results

Figure 3-6a shows the scatter intensity over the flat detector when hybrid and pure MC methods are used following the experiments carried in Ref. [200]. While employing 1000 times less photons, the hybrid method produces much smoother scatter intensity over the detector compared to pure MC method. Figure 3-6b shows the center profiles, perpendicular to the cylinder axis, for the hybrid and pure MC method, as well as the center scatter intensity from the reference. From visual inspection, very good agreement in the curves shape and intensity was found between CatSim simulations and the reference results.

Figure 3-7a shows the scatter intensity over the flat detector when the hybrid method is used, for different input spectra and phantom diameters, as described in the experiments of Ref. [110]. Figure 3-7b shows the center SPR profiles, perpendicular to the cylinder axis, for the three simulated setups, as well as the center SPR profiles from the reference. From visual inspection, very good agreement was found between CatSim simulations and the reference results.

SPR curves in Figure 3-7b are higher with increasing phantom size. The authors in Ref. [110] also observed that, for the same phantom size, SPR profiles are similar when considering a 50 keV monochromatic spectra and a W/Al 80 kV polychromatic spectra. This is because it exists an averaging effect on the energy-dependent scatter intensities of W/Al 80 kV spectra, giving similar results to a monochromatic beam energy equal to the polychromatic spectrum average energy, *i.e.*, approximately 50 keV in this case.

Figures 3-8 and 3-9 illustrate the dependency of scatter intensity and SPR with increasing phantom diameter (fixed air gap) and increasing air gap (fixed phantom diameter), respectively,

[1]Notice that the geometry adopted in Ref. [110] was based on the scatter experiments carried by Kwan *et al.* [114] in a table top prototype. Due to the lack of precise information in Ref. [114] about the phantom positionning with respect to the COR, it was assumed that the COR was aligned with the center of the flat detector

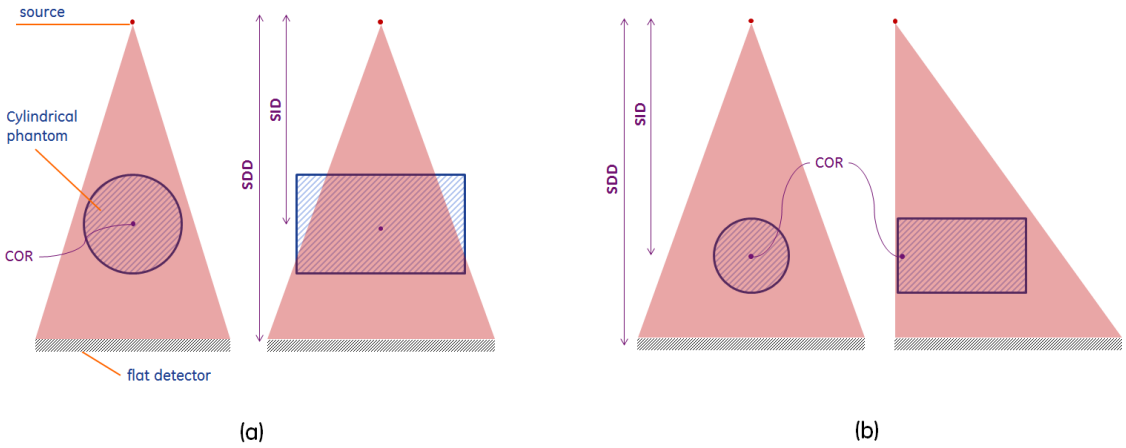

Figure 3-5: Simulated cone-beam geometries used for scatter simulation validation, according to (a) Ref. [200] and Ref. [110] and according to (b) Ref. [113]

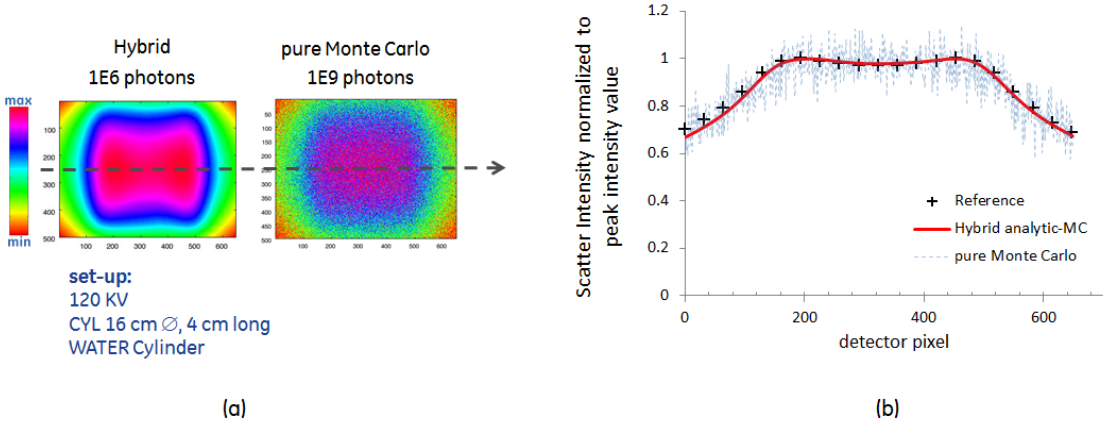

Figure 3-6: Scatter intensity profile comparison with Ref. [200]. (a) Scatter signal intensity over the detector surface using Hybrid and pure Monte Carlo approaches; (b) central profiles comparison with reference

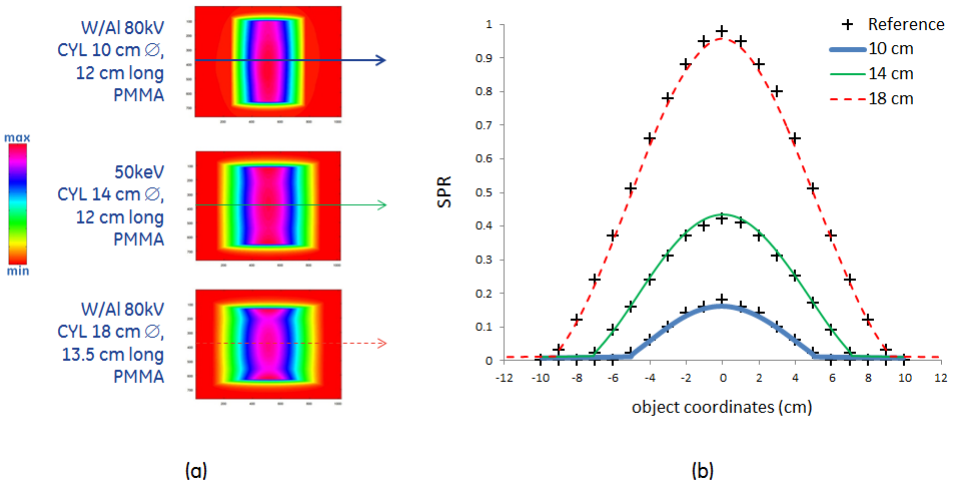

Figure 3-7: SPR profiles comparison with Ref. [110]. (a) Scatter Intensity over the detector surface using Hybrid method for W/Al 80 kV and 10 cm diameter phantom, monochromatic beam at 50 keV and 14 cm diameter phantom and W/Al 80 kV and 18 cm diameter phantom ; (b) central SPR profiles comparison with reference results

as described in the experiments carried in Ref. [113]. Both Scatter Intensity and SPR profiles displayed in Figures 3-8 and 3-9 are taken from a centered line perpendicular to the cylinder axis (coronal plane) and a centered line aligned with the cylinder axis (axial plane). The "bumps" or "discontinuities" in both scatter intensity and SPR profiles occurs at the frontier of the cylinder's edges and the air.

Figure 3-8 shows that, for a fixed geometry and the same number of shot photons, scatter intensity decreases with increasing phantom diameter while SPR increases with increasing phantom diameter. Figure 3-9 shows that, for a fixed phantom size, both scatter intensity and SPR decrease with the increasing air gap. From visual inspection, in both Figures 3-8 and 3-9 very good agreement was found between CatSim simulations and the reference results.

Discussion
The objective of this experiment was to evaluate the accuracy of scattered radiation spreading over a flat detector. For this experiment, we focused on assessing scatter intensity and scatter-to-primary ratios specifically for cone-beam breast CT geometries. Typical clinical input spectra (ranging from 60 to 120 kV tube voltage) and uncompressed breast phantom sizes (ranging from 10 to 18 cm in diameter) were considered.

To assess the performance of our pure MC and hybrid analytic-MC simulators, CatSim simulations were compared to three different Monte Carlo engines [110,113,200]. Since the actual data in Ref. [110,113,200] were not published, all conclusions were drawn solely through qualitative visual inspection between an approximate curve retrieved from the publications and those obtained with CatSim. A fair quantitative comparison would require access to the reference actual data, which was unfortunately not available.

3.2.3 Peak Scatter-to-Primary Ratio Values

Finally, in the last part of the scatter simulation module validation, maximum Scatter-to-Primary Ratio (SPR) values from simulated data were compared to SPR values previously published by

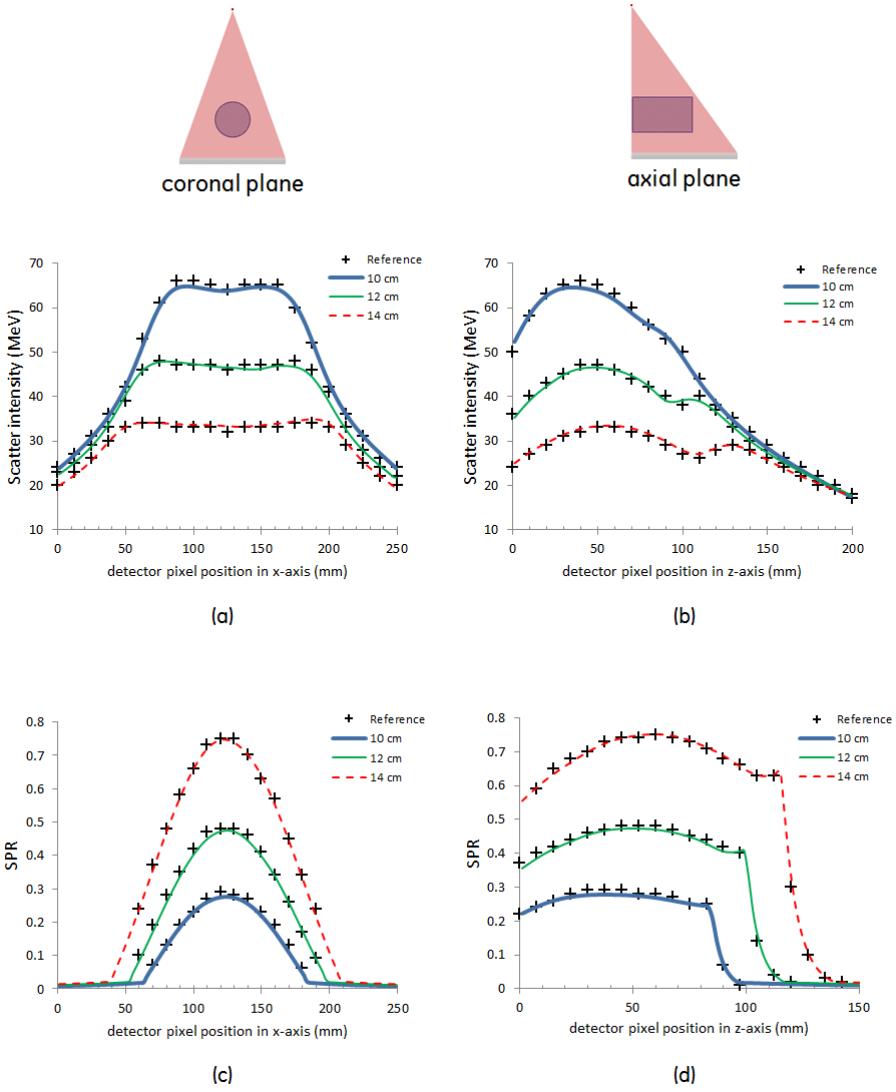

Figure 3-8: Scatter Intensity and SPR profile comparison with Ref. [113]. Dependency of Scatter Intensity and SPR with phantom diameter, for 15 cm air gap, using Hybrid method. (a),(b) Scatter Intensity over the detector surface taken along the coronal and axial planes, respectively; (c),(d) SPR over the detector surface taken along the coronal and axial planes, respectively

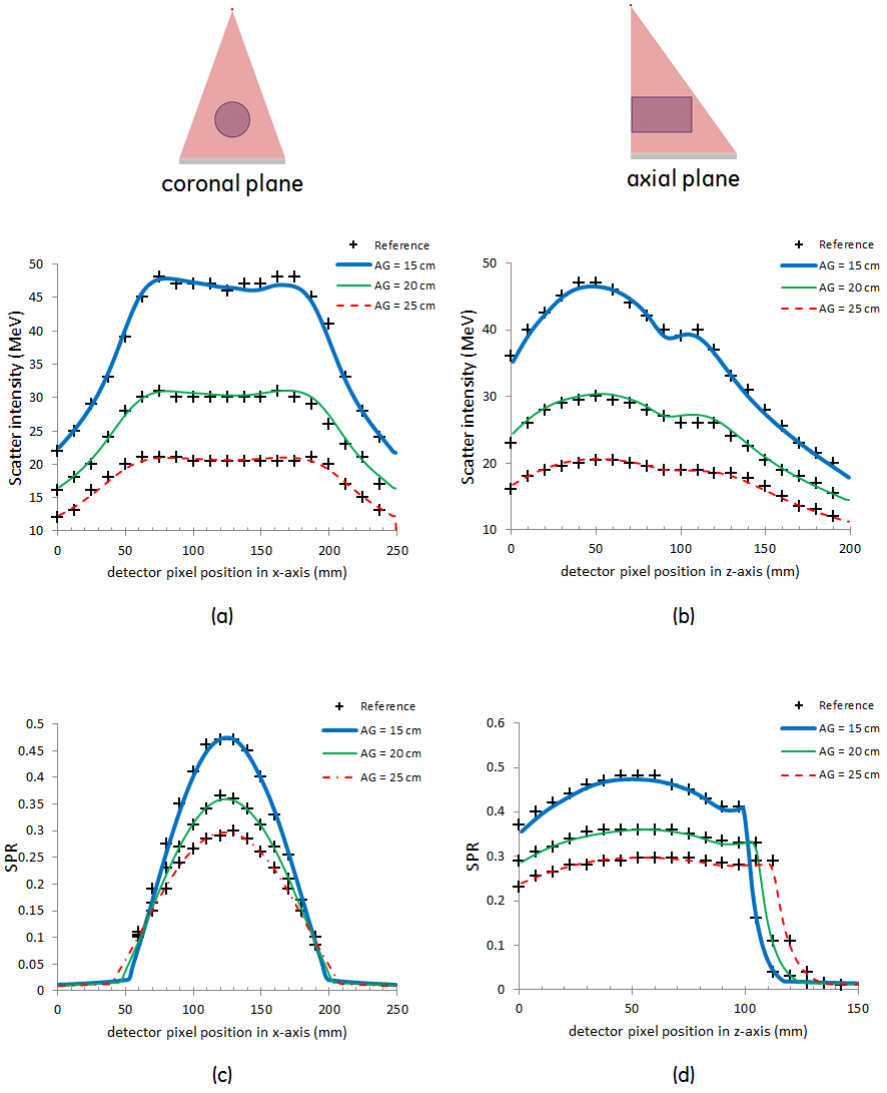

Figure 3-9: Scatter Intensity and SPR profile comparison with Ref. [113]. Dependency of Scatter Intensity and SPR with air gap, for the 12 cm diameter phantom, using Hybrid method. (a),(b) Scatter Intensity over the detector surface taken along the coronal and axial planes, respectively; (c),(d) SPR over the detector surface taken along the coronal and axial planes, respectively

Kwan *et al.* [114], measured on a table top cone-beam X-ray system. The experiment focused in verifying the quality of the simulated scatter intensity with respect to experimental data from a real X-ray system, while varying the input spectra and phantom sizes.

Simulation Setup

Similarly to the previous experiments, following the description in Ref. [114], a centered cone-beam geometry illustrated in Figure 3-5b was assumed, with $SDD = 780\ mm$ and $SID = 465\ mm$. A $40 \times 30\ cm^2$ ideal blur-free energy-integrating detector, with 100% efficiency and $0.394\ mm$ pixel pitch was considered. Three 50% fibroglandular equivalent cylindrical phantoms with 10, 14 and 18 cm diameters and heights equal to 1.5 times their respective radius were simulated. The incident spectrum, emitted from a point source, was generated using the TASMIP model for a W anode with 40, 60, 80 and 100 kV tube voltage and filtered with 3 mm of Aluminum. Two millions photos (2.0×10^6) were tracked in $2 \times 2 \times 2\ mm^3$ voxels, to generate scatter signal intensities over the detector. Maximum SPR values were estimated using mean per-pixel signal intensities on a region-of-interest at the center of primary-only projections and the mean per-pixel signal intensities on a region-of-interest at the center of scatter-only projections.

Results

Figure 3-10a illustrates maximum SPR values for the 14 cm diameter phantom as function of the tube voltage. Figure 3-10b illustrates maximum SPR values for 80 kV tube voltage as function of the phantom diameter. Figure 3-10c illustrates maximum SPR values for 80 kV tube voltage as function of the phantom diameter, but when the SDD value increases from 780 to 880 mm (*i.e.* air gap increasing from 315 to 415 mm, for a fixed SID value). Solid lines represent simulated data and squared markers represent measured data found in Ref. [114].

Figure 3-10a shows that peak SPR values decrease with increasing tube voltage. Figures 3-10b and 3-10c show that peak SPR increases with phantom size and decreases slightly (in this setup) with increasing air gap, as observed in the previous studies. From visual inspection, good agreement in the trends of both simulated and measured peak SPR values was found.

For a quantitative analysis, Figure 3-11a summarizes the results of Figures 3-10a, 3-10b and 3-10c into a scatter plot of measured peak SPR values found in Ref. [114] versus simulated peak SPR values. The solid line represents the linear regression of paired data, which showed coefficient of determination (R^2) equal to 0.9925. Residuals from the linear regression, which are shown in Figure 3-11b, are randomly dispersed around the null error line, confirming the goodness of the regression.

Discussion

The greater differences in peak SPR values were found for 80 and 100 kV tube voltages (respectively 0.06 and 0.08 absolute errors in Figure 3-10a). In order to explain this behavior, we emphasize that the authors in reference Ref. [114] suggested a correction to the TASMIP model by adding Aluminum such as to meet the actual X-ray tube half value-layer. However, due to the lack of details in Ref. [114], in this experiment such correction was not performed, which might explain the differences in SPR values for high tube voltages. Nonetheless, simulation results demonstrated good agreement in the trends of peak SPR values, with less than 5% error after linear regression correction.

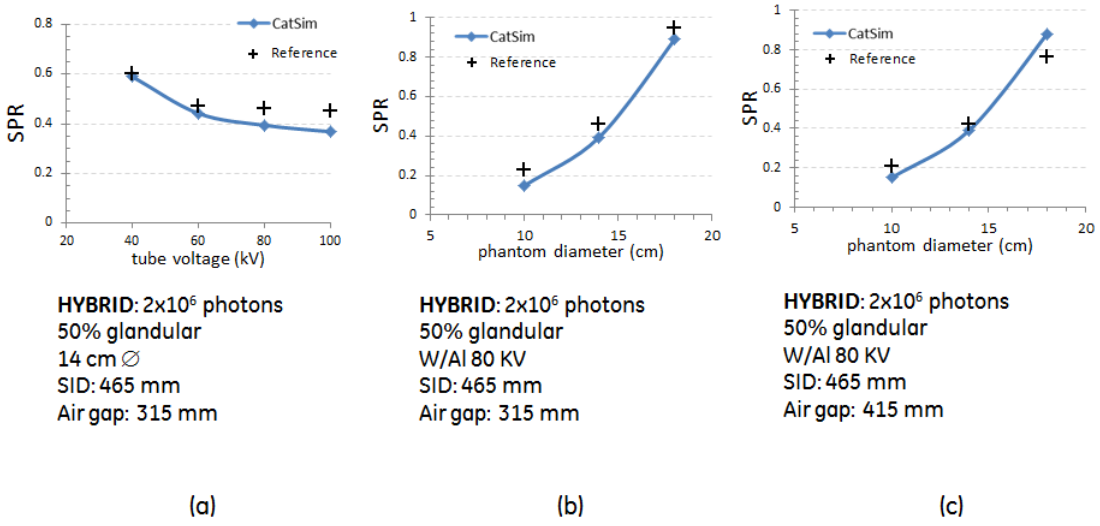

Figure 3-10: Maximum SPR value comparison with Ref. [114]. (a) Maximum SPR values as function of tube voltage; (b)-(c) Maximum SPR profiles as function of phantom diameter for 315 mm and 415 mm air gap, respectively. Solid lines represent SPR results simulated with CatSim, while markers represent published SPR measurements found in Ref. [114]

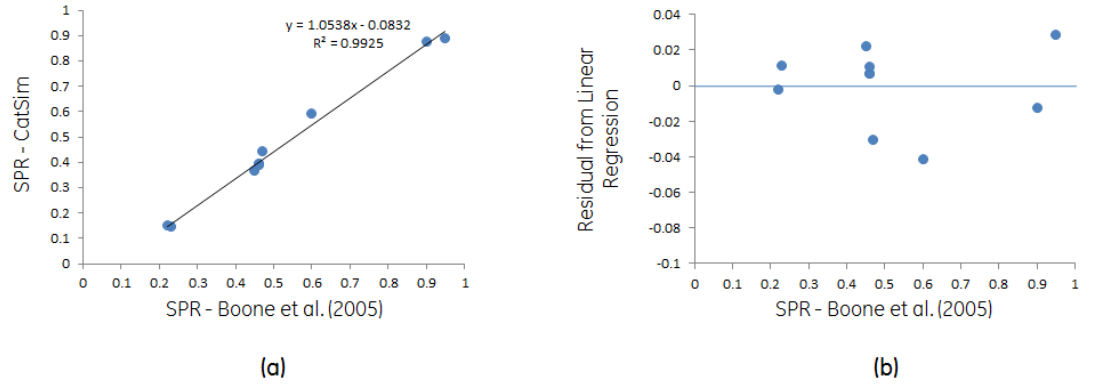

Figure 3-11: Scatter plot of reference vs simulated peak SPR values found in Figure 3-10

3.3 Glandular Dose Simulation Validation

Absorbed dose simulation using CatSim's MC engine was validated with previously published results for a conventional mammography geometry and a breast CT geometry. The Figure-of-Merit for dose simulation validation was the Normalized Glandular Dose (DgN) coefficients. DgN values have been previously defined as conversion factors between Air Kerma and Average Glandular Dose (AGD), *i.e.*, the total radiation dose deposited in the breast fibroglandular tissue only.

3.3.1 Conventional Mammography Geometry

Simulation Setup
Monochromatic DgN coefficients calculated with CatSim were compared to DgN coefficients published by Boone *et al.* [160]. The latter were obtained using the validated Monte Carlo engine SIERRA, developed by the same research group [199].

Figure 3-12 illustrates the simulated geometry. To match the geometry used by Boone *et al.*, a flat X-ray detector was placed 65 cm away from a point source. A half-cylinder phantom modeling the compressed breast in a cranial-caudal (CC) view, with 8.5 *cm* radius and either 2, 4 and 6 *cm* thicknesses, was positioned such as to leave a 1.2 *cm* air gap between the phantom and the detector surface. The half-cylinder was composed of 50% and 100% homogeneous fibroglandular equivalent materials. A skin layer of 4 mm encapsulated the half-cylinder. To account for possible photon backscattering from the patient body, a chest wall was modeled as a very large object with same composition as the irradiated breast.

Monte Carlo simulations were carried with incident photon energies ranging from 16 to 50 keV, using 2 keV steps. One million photons undergoing Rayleigh, Compton and photoelectric interactions were tracked in $2 \times 2 \times 2$ mm^3 voxels. The energy absorbed by the homogeneous fibroglandular equivalent breast tissue was tallied and corrected to account for the fibroglandular part of the breast only [189]. As suggested by Wilkinson and Heggie [190], this correction was applied at each photon interaction by weighting any eventual energy deposition with a scaling factor G_f. Finally, DgN values translating the AGD per unit of exposure at the breast entrance surface can be calculated following Equation 2.18, defined in Section 2.6.

Results
Figures 3-13a and 3-13b show scatter plots comparing monochromatic DgN values calculated using CatSim's MC engine with reference DgN values found in Ref. [160]. For this experiment only, reference data points were calculated from a nonlinear fit model with coefficients published in Ref. [160].

Figure 3-13a illustrates results for the 2 cm and 6 cm thick 50% fibroglandular equivalent phantoms. Figure 3-13b illustrates results for the 4 cm and 6 cm thick 100% fibroglandular equivalent phantoms. The solid lines represent the linear regression of paired data, with coefficient of determination (R^2) displayed beside each line. A very good agreement was found between CatSim results and the reference publication, with coefficient of determination R^2 greater than 0.99.

Figures 3-13c and 3-13d show the DgN coefficients of Figures 3-13a and 3-13b, respectively, as function of the incident monochromatic beam energy. Below ∼10 keV, radiation dose is mainly absorbed by the skin and DgN values are close to zero. For energies higher than 10 keV, DgN values increase rapidly as function of energy due to the increased beam penetration and 2nd order scattering in the breast tissues. From ∼40 keV onwards DgN values increase slowly since most energy is transmitted through the phantom.

Discussion
In this study, DgN values were validated for a conventional mammography geometry. It must

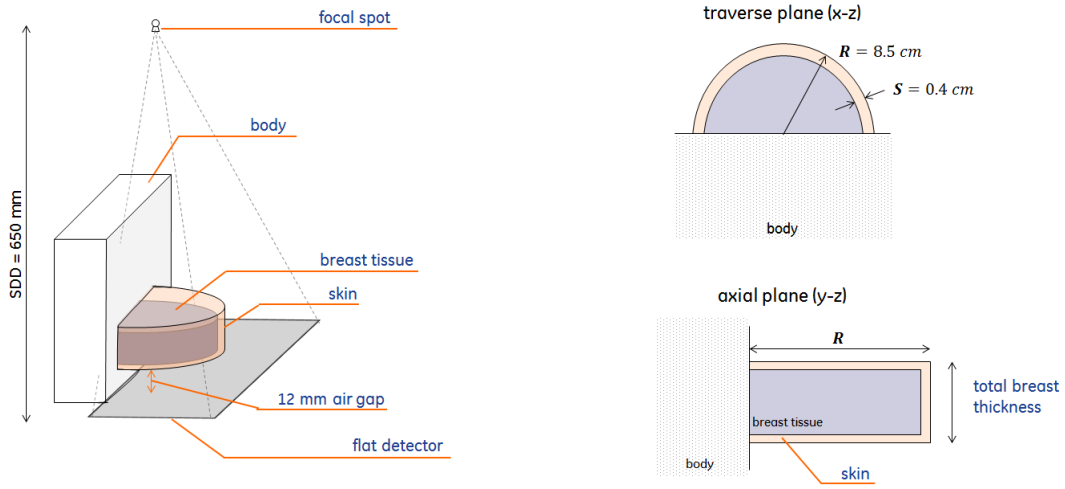

Figure 3-12: Simulated geometry used to validate DgN simulation with CatSim using conventional mammography geometry. This illustration was adapted from Ref. [160]

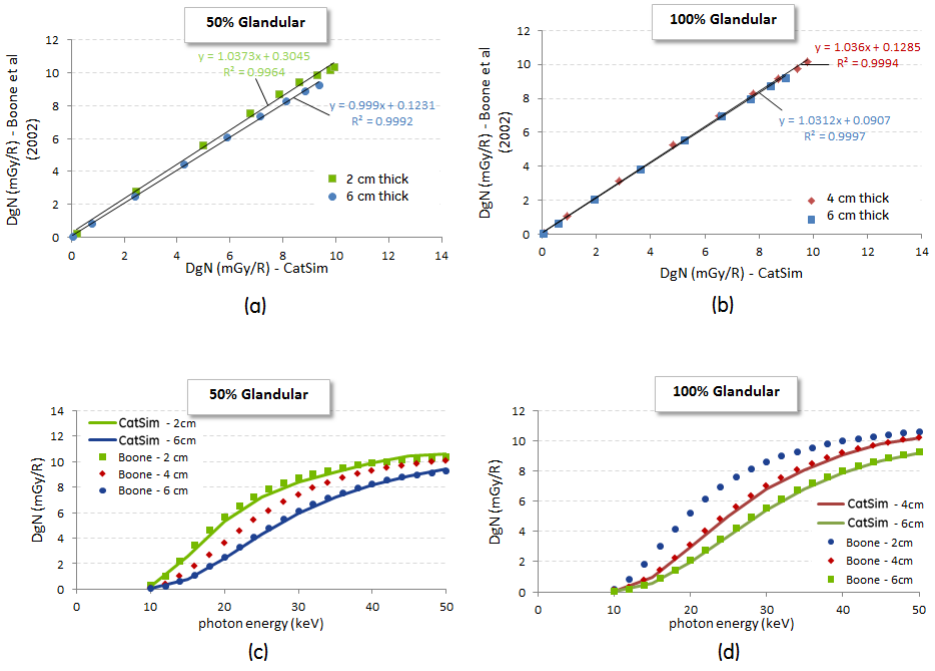

Figure 3-13: Results of glandular dose simulation validation for mammography geometry. (a)-(b) Scatter plot between DgN coefficient calculated with CatSim and the DgN coefficients published in Ref. [160]; (c)-(d) The same DgN coefficients as function of the incident monochromatic energy

be emphasized however that, for a digital breast tomosynthesis (DBT) acquisition, DgN values are likely to vary as function of the oblique incident angle. In a similar Monte Carlo study, Sechopoulos *et al.* [201] evaluated the absorbed dose as function of the oblique incidence angle α, using a relative glandular dose coefficient metric, $RGD(\alpha)$, with respect to DgN values obtained at 0° incidence. The authors reported that for a CC view, $RGD(\alpha)$ values decrease as low as 0.8 at $\alpha = 30°$, depending mainly on breast thickness and chest-wall to nipple distance. As a consequence, the mean RGD value over all angles $\mu_{RGD} = \sum_{\alpha=\alpha min}^{\alpha max} RGD(\alpha)$, varies from minimum 0.91 and maximum 0.97 values including all experimental conditions. Hence, the use of conventional mammography DgN values for DBT can overestimate the AGD by almost 10%.

In this PhD thesis research, unless otherwise stated, the investigations exploiting a DBT geometry assumed a 50% glandular 5 cm-thick breast with a chest-wall to nipple distance of $\sim 10\ cm$ in a CC view compression (cf. Section 2.3 for a description). In this case, and assuming an acquisition with total angular range of 25° (SenoClaire™, GE Healthcare; Chalfont St Giles, UK), μ_{RGD} values reported by Sechopoulos *et al.* would entail approximately 2% decrease in total AGD, with respect to a conventional mammography incidence. Since this small error does not significantly impact the Figures-of-Merit under evaluation, DgN values obtained at 0° incidence were used in our work to estimate AGD in a DBT geometry.

3.3.2 Breast CT Geometry

Simulation Setup
Monochromatic DgN coefficients calculated with CatSim were compared to DgN coefficients reported previously by Thacker and Glick [112], in which GEANT3 software package[2] was used.

Figure 3-14a illustrates the simulated geometry. To match the geometry used by Thacker and Glick, a point source was positioned at 100 cm from a flat detector, such as to make a half-cone beam geometry. The breast was modeled as a 50% fibroglandular equivalent cylinder with three different diameters (10, 14 and 18 cm) and height equal to 1.5 times their radius. A 4 mm skin layer encapsulated the cylinder object, except at the top side. The cylinders' central axes were positioned at 60 cm from the source and such that the beam ray normal to the detector passed through the top of the cylinder. In order to account for possible backscattering from the body, the patient torso was modeled as a 30 cm diameter water cylinder, with long axis parallel to the beam's direction and placed directly next to the breast.

Monte Carlo simulations were carried with incident photons having energies ranging from 15 to 120 keV, at 5 keV step. One million photons undergoing Rayleigh, Compton and photoelectric interactions were tracked in $2 \times 2 \times 2\ mm^3$ voxels. DgN coefficients were calculated using Equation 2.18, translating the total AGD per unit of exposure at the system isocenter. The correction factor G_f was applied in the same manner as the previous section, such as to account for fibroglandular part of the 50% fibroglandular equivalent homogeneous mixture.

Results
Figure 3-15 shows the DgN coefficients calculated with CatSim MC engine, as well as the reference DgN coefficients found in Ref. [112], as function of the incident monochromatic energy, for the 10, 14 and 18 cm diameter phantoms. From visual inspection, very good agreement between simulated and reference DgN values can be observed for all three breast sizes.

Discussion
We have shown that the differences between previously published DgN values and DgN values simulated with CatSim's MC engine are in very good agreement.

[2] `http://wwwasd.web.cern.ch/wwwasd/geant/`

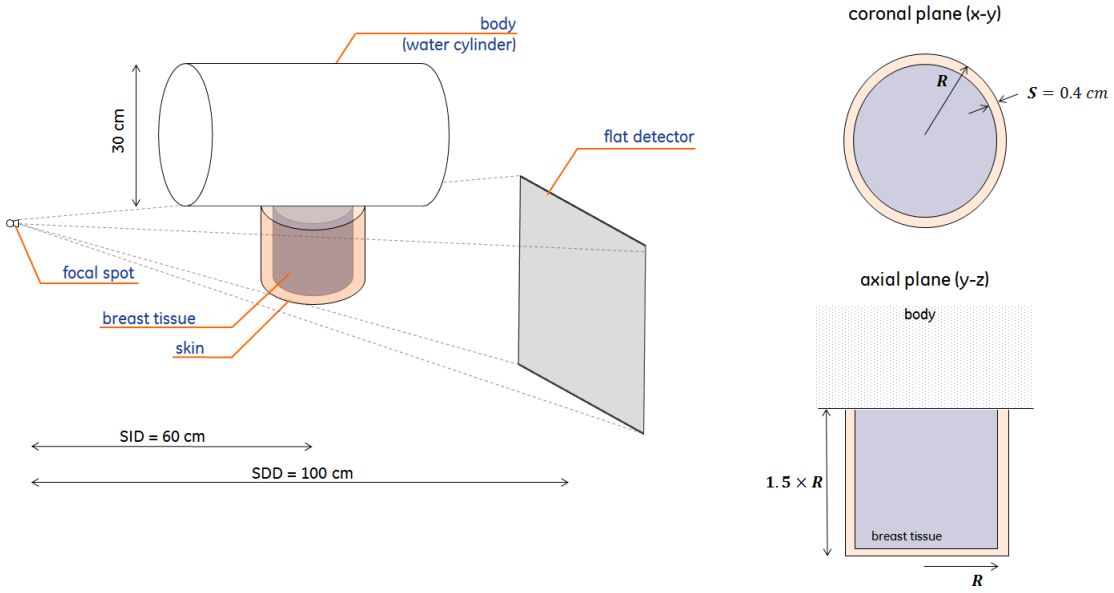

Figure 3-14: Simulated geometry used to validate DgN simulation with CatSim using a breast CT geometry set-up. This illustration was adapted from Ref. [112]

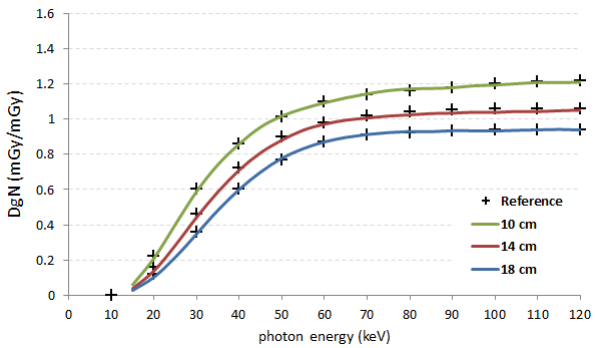

Figure 3-15: DgN coefficients calculated with CatSim as well as the DgN coefficients published in Ref. [112], as function of the incident monochromatic energy

Previously published DgN values were also obtained through MC simulation. To the best of our knowledge DgN values have not been validated yet through experiment. Nevertheless, the good match indicates that the AGD derived from the simulated DgN values we will calculate in Chapters 5, 6 and 7 will be comparable to values found in literature.

Differently from what reported in Ref. [112], in the present study, the spatial distribution of the deposited energy in the phantom was not assessed. This is because the purpose of our simulation was to ensure we can compute total AGD values comparable to those found in literature.

3.4 Detector Model Validation

As previously discussed, the investigations carried during this PhD thesis research and presented in the following chapters, have been mainly focused on noise-free blur-free detectors, *i.e.*, a detector that does not generate any kind of noise or blurring and for which quantum noise is the only random component. Since the model for signal and noise propagation defined in Equation 2.22 is a widely adopted model for such idealistic detectors, the validation experiments presented in this section were not focused in evaluating Figures-of-Merit (FOM) for an exhaustive set of input acquisition setups and geometries. The validation experiment aimed to validate the developed simulation chain and their individual modules and parameters, such as phantom projection, absorption efficiencies, conversion factors, energy-integration and Poisson-distributed quantum noise.

To validate the idealistic detection model, a series of experiments on three real X-ray systems were performed and reproduced in simulation. A GE Senographe® DS system and a GE Senographe® Essential mammography system (GE Healthcare; Chalfont St Giles, UK) using low-energy spectra, as well as a GE Innova™ Interventional Image Guided System (IGS) 620 (GE Healthcare; Chalfont St Giles, UK), using high-energy spectra, were considered. The experimental setups were reproduced in simulation, while considering the simplified cascade model for scintillator-based indirect conversion detectors, defined previously in Equation 2.25. By validating the signal and noise propagation in such detectors while considering straightforward acquisition setups and energy ranges that have been adopted throughout this PhD thesis research and typical for a contrast-enhanced breast X-ray imaging, it was assumed that signal and noise propagation in noise-free blur-free detectors would also be validated.

Various FOMs were assessed: detector pre-sampling Modulation Transfer Function (MTF), Noise Power Spectrum (NPS) and image descriptive statistics for stationary signals such as average and standard deviation of signal intensities, and consequent Signal-to-Noise Ratio (SNR).

For convenience, Equations 2.22 and 2.25, corresponding to signal and noise propagation in noise-free blur-free and indirect conversion detectors, respectively, are recalled below:

$$\begin{cases} \text{Eq. 2.22}: \; SI(i) = \kappa \sum\limits_{E \in \mathcal{E}} \xi(E) \mathcal{P}\left\{\eta(E) \cdot I_{inc}(E,i)\right\} \\ \\ \text{Eq. 2.25}: \; SI(i) = \mathcal{N}(0,\sigma_{DAS}) + G \cdot \mathcal{F}^{-1}\left\{\mathcal{F}\left\{\sum\limits_{E \in \mathcal{E}} E \cdot \mathcal{P}\Big(\eta(E) \cdot I_{inc}(E,i)\Big)\right\} H(f_u,f_v)\Pi(f_u,f_v)\right\} \end{cases}$$

where κ is a scaling factor for digital units, $\xi(E)$ is the detector conversion response, $\mathcal{P}\{\cdot\}$ denotes the Poisson distribution, $\eta(E)$ is a function translating an eventual energy-dependent efficiency in detecting photons, $I_{inc}(E,i)$ is the X-ray intensity spectrum incident over the detector element i and energy bins defined in the set $\mathcal{E}$, $\mathcal{N}(0,\sigma_{DAS})$ corresponds to the additive electronic noise modeled as a Gaussian distribution $\mathcal{N}(\mu,\sigma)$ with null average ($\mu = 0$) and standard deviation σ_{DAS}, G is the optical gain, $\mathcal{F}\{\cdot\}$ and $\mathcal{F}^{-1}\{\cdot\}$ denote respectively the direct and inverse Fourier transform operators, $H(f_u,f_v)$ and $\Pi(f_u,f_v)$ are respectively the optical spread and photodiode aperture transfer functions, with f_u and f_v corresponding to columns and rows directions, respectively, in the frequency domain.

3.4.1 Modulation Transfer Function

In order to evaluate CatSim's ability in emulating the spatial resolution of a given X-ray system and as a pre-requirement for the evaluation of noise propagation, we compared the pre-sampling MTF measured in X-ray projections acquired with a Senographe DS, Senographe Essential and Innova IGS620 systems and the pre-sampling MTF measured in X-ray projections simulated with CatSim.

Figure 3-16 illustrates the methodology used to implement the optical spreading in CatSim and perform the comparison of measured and simulated MTF. 1) X-ray projection images of a thin radio-opaque Tungsten sheet are acquired for each considered X-ray system; the MTFs are the calculated using the edge method and 2) the optical spread transfer function $H(f_u, f_v)$ are modeled using Lorentzian decay functions. 3) $H(f_u, f_v)$ is introduced CatSim acquisition chain (Equation 2.25). Using the same geometry adopted for the three experimental setups, X-ray projection images of a thin radio-opaque Tungsten sheet are simulated and the MTFs calculated using the edge method. Finally, 4) previously measured MTFs and simulated MTFs are compared. Further details on steps 1 to 4 are provided as follows.

Experimental Setup
The calculation of the MTF for each considered X-ray system was performed using the edge method and with aid of a software tool developed by Kao *et al.* [202].

X-ray projection images of a $100\mu m$-thick radio-opaque Tungsten sheet placed directly on the X-ray detectors were acquired. The Tungsten sheet was positioned such as to make a small angle ($\varphi \approx 3^{\circ}$) with respect to the detector elements matrix (Figure 3-17a). X-ray fluence spectra for Senographe DS and Senographe Essential systems were set for a Rhodium (Rh) anode with 28 kV tube voltage filtered with 0.25 mm of Rh and set to 20 mAs of exposure. The correspondent simulated X-ray fluence spectra were generated using the SpeXim model. X-ray fluence spectra for Innova IGS620 system was a Tungsten anode with 80 kV tube voltage, 80 mA tube current, 10 ms pulse width and filtered by 0.3 mm of Copper. The correspondent simulated X-ray fluence spectra were generated using the TASMIP model with additional 1.5 mm of Aluminum filtration to match the system's HVL.

The digital images were processed with the MTF tool described in Ref. [202] to obtain the pre-sampled MTF. Image processing include the detection of the edge angle, reprojection and sub-binning of the individual edge spread function (ESF) (Figure 3-17b) to obtain an oversampled ESF (Figure 3-17c). By differentiating the oversampled ESF, the Line Spread Function (LSF) was generated, and the absolute value of its Fourier transform originates the measured MTF, $MTF_{meas}(f)$ (in 1D only at this stage).

Estimation of the Optical Photon Spread Transfer Function $H(f_u, f_v)$
It was assumed that system's pre-sampled MTF, MTF_{pre}, is the concatenation of four responses functions: the focal spot emission pattern H_{fs}, the X-ray tube motion blur H_{motion}, the scintillator optical spread $H_{scint} = H(f_u, f_v)$ and the detector cell aperture transfer function $H_{ap} = \Pi(f_u, f_v)$. Hence, in the frequency domain, MTF_{pre} can be expressed as:

$$MTF_{pre}(f_u, f_v) = H_{fs}(f_u, f_v) \cdot H_{motion}(f_u, f_v) \cdot H(f_u, f_v) \cdot \Pi(f_u, f_v) \tag{3.4}$$

Since the gantry is static during the acquisition, $H_{motion}(f_u, f_v) = 1$. With the Tungsten sheet placed directly over the detector, the influence of the focal spot blur is almost null since the focal spot size is very small with respect to the source-to-detector distance and the object magnification is close to 1. As consequence, $H_{fs}(f_u, f_v) \approx 1$. Therefore, the optical spread transfer function $H(f_u, f_v)$, necessary for Equation 2.25, can be derived from the measured pre-sampled MTF,

$$MTF_{meas}(f) \xrightarrow[symmetry]{rotation} MTF_{pre}(f_u, f_v) \approx H(f_u, f_v) \cdot \Pi(f_u, f_v) \tag{3.5}$$

where we assume that $MTF_{meas}(f)$ is symmetric to rotation.

Assuming that the detector elements have the same pitch p and fill fraction a in both row and column directions, generating this way a sensitive surface centered in the element total surface (cf. Figure 2-10), the centered uniform aperture window in the spatial domain is translated into a

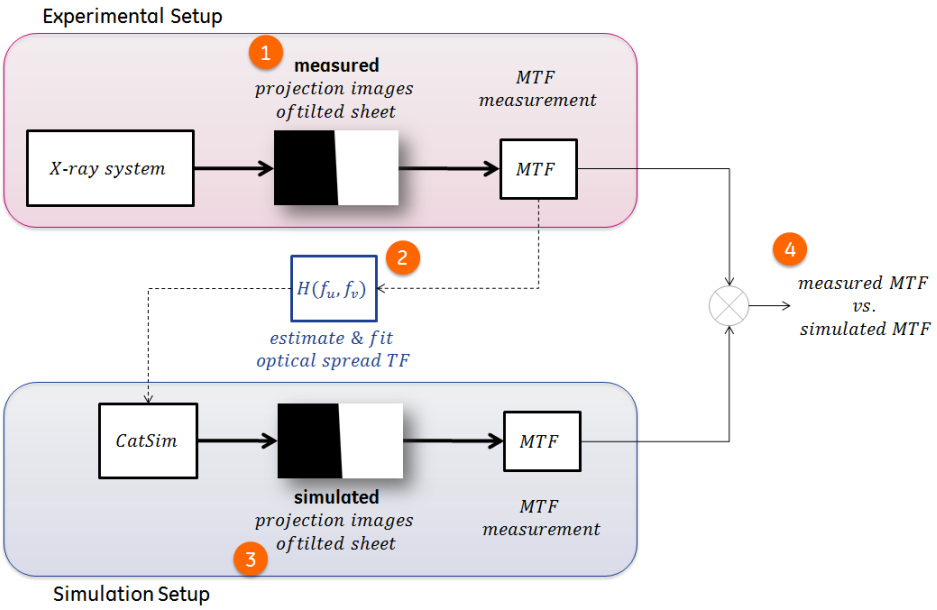

Figure 3-16: Illustration of methodology used to implement the optical spreading in CatSim and perform the comparison of measured and simulated MTFs

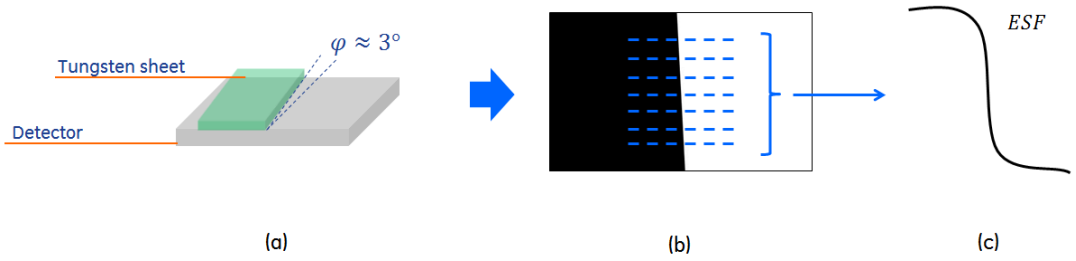

Figure 3-17: Illustration MTF estimation method. By projecting the (a) tilted radio-opaque slit over the detector we acquire an (b) edge image, which will be used to estimate the (c) oversampled ESF and the pre-sampling MTF

sinc function in the frequency domain. The measured optical spread transfer function is therefore found by

$$H(f_u, f_v) = \frac{MTF_{pre}(f_u, f_v)}{sinc(ap\pi f_u) \cdot sinc(ap\pi f_v)} \tag{3.6}$$

where f_u and f_v correspond to columns and rows directions, respectively, in the frequency domain.

Optical Photon Spread Transfer Function $H(f_u, f_v)$ Parametrization
In order to obtain a smoother and continuous model for $H(f_u, f_v)$, the measured $H(f_u, f_v)$ can be fitted using Lorentzian decay functions. In this case, it was assumed that $H(f_u, f_v)$ possesses a high-frequency (HF) component due to the crystalline shape of CsI scintillators, and a low-frequency (LF) component due to back-scattering and other long-range scattering (either X-ray or optical photons) [192–194]:

$$H(f_u, f_v) = \omega_H \frac{\zeta_{HF}}{\zeta_{HF} + f_u^2 + f_v^2} + (1 - \omega_H) \frac{\zeta_{LF}}{\zeta_{LF} + f_u^2 + f_v^2} \qquad , 0 \leq \omega_H \leq 1 \tag{3.7}$$

where ζ_{LF} and ζ_{HF} adjust the low- and high-frequency Lorentzians decay, respectively, and ω_H is a weight between both components ensuring the normalization of $H(f_u, f_v)$.

By fitting the measured optical spread function with the Lorentzian model of Equation 3.7, the full spatial resolution of given X-ray detector can be simulated at any given frequency $f = (f_u, f_v)$.

Simulation setup
Using the same geometry adopted for the experimental setup, primary photons were shot from a single point source and interacted with a simulated Tungsten sheet, with 3° tilt angle. Twenty-five (5×5) sample points were uniformly distributed over each detector element sensitive surface in order to avoid aliasing, with X-ray photon fluence spectrum calculated following Equation 2.20. According to Equation 2.25, the oversampled incident photon intensity spectrum was integrated and it's Fourier transform filtered by the previously measured and parametrized optical spread transfer function $H(f_u, f_v)$, as well as by the photodiode aperture transfer function $\Pi(f_u, f_v)$ defined by the detector element size and fill fraction. After inverse Fourier transform and decimation operations, the simulated images were used as input for the MTF calculation software, using the same process as for the experimental setup.

Results
Figure 3-18 shows the measured and simulated pre-sampling MTF for the three considered X-ray systems. The Nyquist frequency for the Senographe DS and Senographe Essential system is 5.0 mm^{-1} (pixel pitch $p = 100$ μm). The Nyquist frequency for the Innova IGS620 system is 2.5 mm^{-1} (pixel pitch $p = 200$ μm). From visual inspection, very good qualitative agreement is found between simulated and measured data is found, for all three MTF curves. Table 3.4 shows measured and simulated MTF values at 1, 1/2 and 1/4 fractions of the Nyquist frequency, for the three considered X-ray systems.

Table 3.5 summarizes the Lorentzian parameters for the optical Spreading Function $H(f)$ models, obtained from non-linear fitting (*Curve Fitting Toolbox™*, The MathWorks Inc.; Natick, MA, USA) with the associated fitting goodness.

3.4.2 Noise Power Spectrum

With pre-sampling MTF implementation verified above, noise propagation was assessed by the calculation of the Normalized Noise Power Spectrum (NNPS) in uniform X-ray images acquired with real X-ray systems and simulated with CatSim

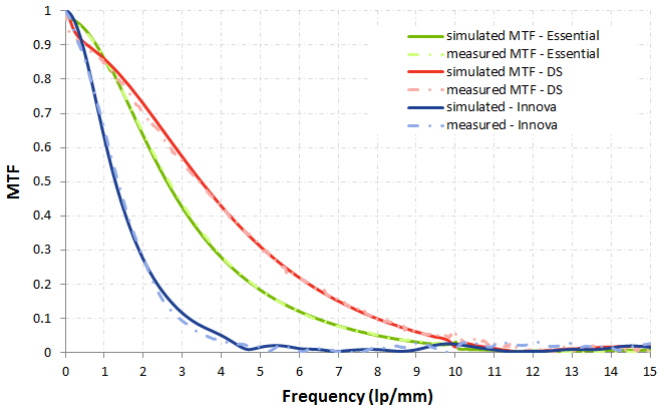

Figure 3-18: Measured and simulated Modulation Transfer Function (MTF) for the three considered X-ray systems

Table 3.4: Measured and simulated MTF values at 1/1, 1/2 and 1/4 fractions of the Nyquist frequency

X-ray System		**Fraction of Nyquist Frequency**		
		1/4	**1/2**	**1/1**
DS	meas	0.81	0.63	0.31
	CatSim	0.83	0.65	0.31
Essential	meas	0.81	0.53	0.18
	CatSim	0.81	0.52	0.18
Innova	meas	0.76	0.54	0.15
	CatSim	0.75	0.51	0.18

Table 3.5: Lorentzian parameters for the optical spreading function $H(f)$ models and associated fitting goodness, measured by the coefficients of determination (R^2)

Parameters	**DS**	**Essential**	**Innova IGS620**
ω_H	0.907	0.976	1
ζ_{HF}	21.895	8.547	1.44
ζ_{LF}	0.038	0.002	~ 0
R^2	0.995	0.999	0.98

For NNPS calculation, X-ray projection images of uniform phantoms are divided into N different 256×256 pixels Regions-of-Interest (ROI). The ROI positions are chosen such as to overlap by 128 pixels in the horizontal and vertical directions. The numbers of ROIs are obtained such as to cover a fraction of detector surface, usually close to the chest wall. Low-frequency variations in signal intensity due to Heel Effect and other photon fluence fluctuations were removed by subtracting $SI(u,v)$ from a reference image $SI_{ref}(u,v)$, which was one of the acquired uniform images

Finally, the 2D-NNPS can be calculated by using the following equation:

$$NNPS(f_u, f_v) = \frac{p^2}{256 \times 256 \cdot N \cdot \bar{SI}_N} \sum_N \left| \mathcal{F}\left\{ \frac{SI(u,v) - SI_{ref}(u,v)}{\sqrt{2}} \right\} \right|^2 \tag{3.8}$$

where p in the detector pixel pitch, N is the total number of ROIs, $\bar{SI}_N$ is the average per-pixel signal intensity calculated in the considered ROI, $\mathcal{F}\{\cdot\}$ denotes the direct Fourier transform operator and $\sqrt{2}$ corrects the noise added by the reference image.

Experimental setup

Figure 3-19 illustrates the experimental setup for NPS measurement, reproduced with the Senographe DS and Senographe Essential systems. The experimental setup was built to suppress as much as possible scattered radiation coming from the phantom.

The 2.7 mm PMMA breast compression paddle was set upside down, positioned as close as possible to the X-ray source. A 5 cm PMMA flat phantom was placed over the compression paddle, using the latter as support. This setup was chosen to leverage the increased air gap between the phantom and the detector, decreasing this way scattered X-rays incident on the detector surface. The X-ray detector was not equipped with bucky neither scatter grid.

In order to match Tube Yield values between experiment and simulation, Air Kerma measurements were performed in a separate setup and without any object in the X-ray beam path, similar to the illustration in Figure 3-1. A 6 cm^3 ionization chamber (RadCal® 10X6, RadCal Corporation; Monrovia, CA, USA) was place at 592 mm from the X-ray source, using a metallic support coupled to the detector surface. The collimator was set to 9×9 cm^2 FOV and the ionization chamber was positioned to be fully aligned with the beam's path.

Seven X-ray projection images were acquired using a Rhodium (Rh) anode with 30 kV tube voltage, 0.25 mm Rh filter thickness and 4.57 mAs. The images were cropped into 520×300 pixels images close to the chest wall. One out of the seven images was used as reference image, resulting in a total of 18 ROIs for NNPS calculation.

One-dimensional NNPS in the horizontal and vertical direction were obtained by averaging 14 central frequency bands on both sides of the u and v axes, respectively were averaged. The central axes were excluded to avoid a residual trend in signal background.

Simulation setup

The same geometric setup illustrated in Figure 3-19 was emulated using CatSim. Simulated X-ray fluence spectra for Rh anode with 30 kV tube voltage and 4.57 mAs were generated using SpeXim model. Primary photons only were shot from a single point source and interacted with the 2.7 mm PMMA paddle and the 5 cm PMMA flat phantom. The simulated photon fluences were set so as to match the experimentally measured photon fluences. The transmitted photons were detected by a 520×300 pixels flat detector with same QDE, optical gain G and A/D conversion factors as the real Senographe DS and Senographe Essential systems (cf. Annex B for details). More than ten projection images were simulated for each system, resulting in at least 30 ROIs for NNPS calculation. One-dimensional NNPS was calculated in the same manner as for the experimental data.

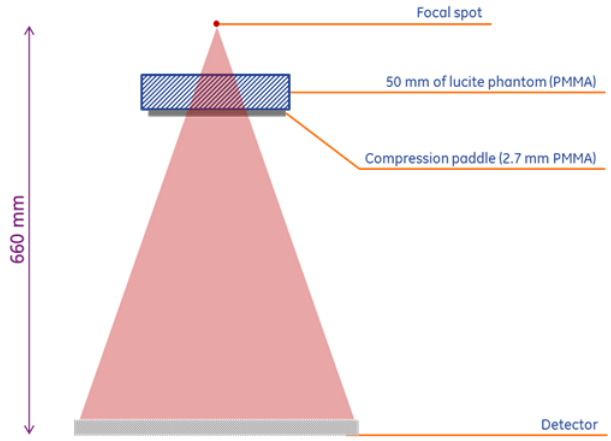

Figure 3-19: Experimental setup used in NPS validation

Optical spread transfer function $H(f_u, f_v)$ and photodiode aperture transfer function $\Pi(f_u, f_v)$ were included in the same way as for MTF measurements. Hence, the size of the detector matrix (520×300 pixels) was chosen to optimize simulation time and memory allocation, mainly due to the detector element oversampling.

Results
Figure 3-20 shows measured and simulated NNPS curves obtained for the GE Senographe Essential and Senographe DS systems. Very good agreement can be seen in the overall shape of both simulated and experimental data. A small difference can be seen at lower frequencies for the Senographe Essential system.

Figure 3-21 shows 1st and 2nd order statistics from a simulated image in comparison to an image acquired with the GE Senographe Essential. Figure 3-21 shows a good quantitative agreement between simulated and measured data.

3.4.3 Image Signal Descriptive Statistics

In order to assess the detector model accuracy and linearity in simulating signal intensity values, a descriptive statistical analysis of 1st and 2nd order was performed as function of the input X-ray spectra and exposure values. Per-pixel average and standard deviation of signal intensities, and the consequent Signal-to-Noise Ratio (SNR) values, were assessed on homogeneous phantoms for low-energy spectra on a Senographe DS system, as well as for high-energy spectra on an Innova IGS620 system.

Experimental Setup on GE Senographe DS (low energy)
Figure 3-22a illustrates the experimental setup for average SI measurement, reproduced with the Senographe DS system and emulated in simulation. The experimental setup was built to suppress as much as possible scattered radiation coming from the phantom.

The 2.7 *mm* PMMA breast compression paddle was set upside down and was positioned as close as possible to the X-ray source. A very wide 5 *cm*-thick PMMA flat phantom was placed over the compression paddle, using the latter as support. This setup was chosen to leverage the increased air gap between the phantom and the detector, decreasing this way scattered X-rays over the detector surface. For further scatter suppression, a three-step collimation setup was used. The collimators were thin steel plates including a single small circular hole, with 1, 2 and 5 mm

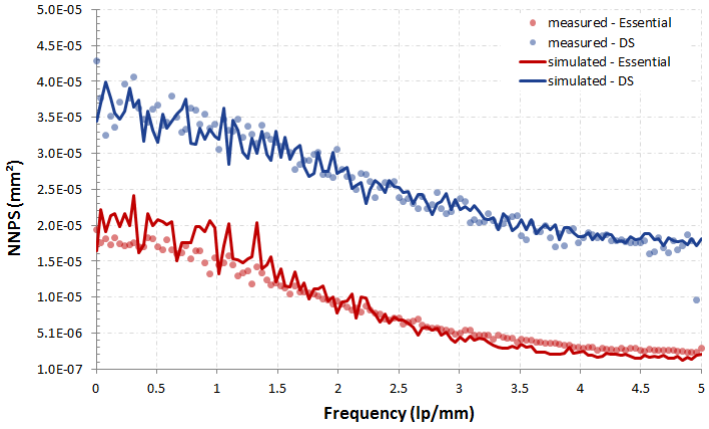

Figure 3-20: Measured and simulated Normalized Noise Power Spectrum (NNPS) for GE Senographe Essential and Senographe DS

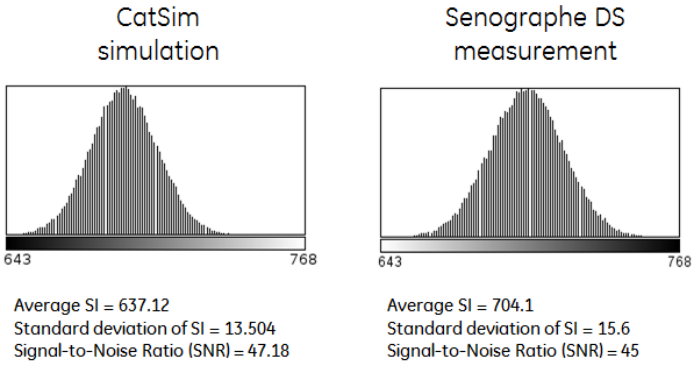

Figure 3-21: Histogram, 1st and 2nd order descriptive statistics and Signal-to-Noise Ratio (SNR) measured in simulated and experimental data obtained for NPS validation. Results are illustrated using ImageJ v1.47 (U.S. National Institutes of Health; Bethesda, MD, USA)

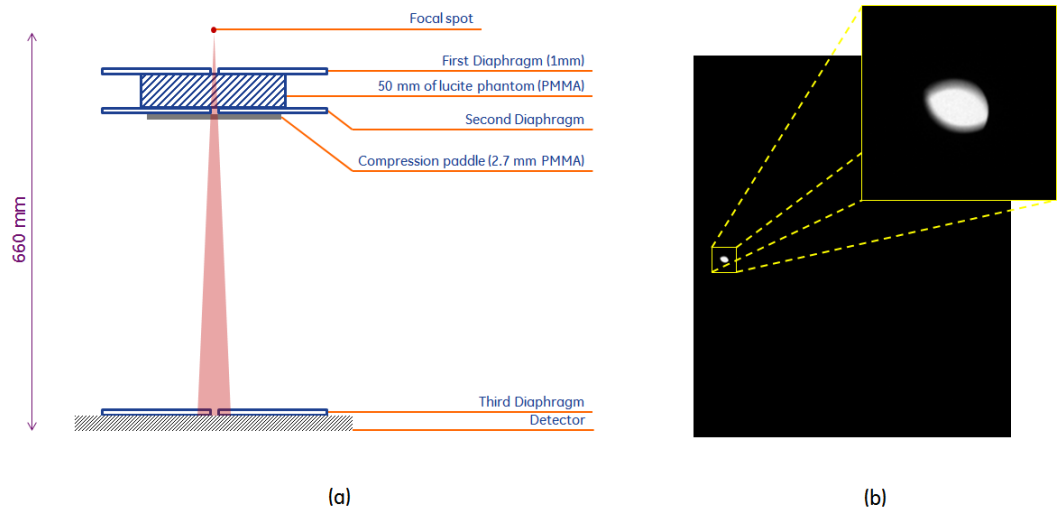

Figure 3-22: (a) Experimental setup illustration on GE Senographe DS used for SI validation; (b) the X-ray image obtained using the diaphragm; measurement were performed in a ROI inside the zone hit by photons

diameter, emulating different diaphragms. The 1 mm diaphragm was placed above the PMMA slab and the2 mm diaphragm directly below it. The 5 mm diaphragm was placed over the detector surface, which was not equipped with the bucky neither the scatter grid. All three diaphragms were aligned such that a small zone over the detector was freely hit by X-rays photons, almost all from primary radiation (cf. Figure 3-22b).

X-ray images were acquired at fixed 200 mAs exposure and for four combinations of anode/filter and tube voltage: Mo/Mo 26 kV, Mo/Mo 28 kV, Mo/Rh 28 kV and Rh/Rh 30 kV. The average per-pixel SI was measured in a circular region-of-interest (ROI) inside the region hit by primary photons, where SI values were rather uniform. In order to ensure lag and afterglow-free measurements, a time delay of several minutes was imposed between subsequent acquisitions. Gain map correction was turned off, leaving only offset and bad pixel correction functional.

In order to match Tube Yield values between experiment and simulation, Air Kerma measurements were performed in a separate setup and without any object in the X-ray beam path, similar to the illustration in Figure 3-1. A 6 cm^3 ionization chamber (RadCal® 10X6, RadCal Corporation; Monrovia, CA, USA) was place at 592 mm from the X-ray source, using a metallic support coupled to the detector surface. The collimator was set to 9x9 cm FOV and the ionization chamber was positioned to be fully aligned with the beam's path.

Simulation Setup (low energy)
The same geometric setup illustrated in Figure 3-22a was emulated using CatSim. Simulated X-ray fluence spectra for the Mo and Rh anode were generated using SpeXim model. Primary photons only were shot from a single point source, with matching photon fluence, and interacted with the 2.7 mm PMMA paddle and the 5 cm PMMA flat phantom. The transmitted photons were detected by flat detector with same QDE, optical gain G and A/D conversion factors as the real GE Senographe DS system (cf. Annex B for details). Neither blur nor noise were considered, since the FOM will only be sensitive to low-frequencies. Finally, the average SI was estimated in the simulated ROI, placed at same position with respect to the detector geometry.

Experimental Setup on GE Innova IGS620 (high energy)
Figure 3-23a illustrates the experimental setup for average SI, standard deviation and SNR mea-

surements, reproduced with the Innova IGS620 system and emulated in simulation. Once more, the experimental setup was built such as suppress as much as possible scattered radiation coming from the phantom.

A very wide 10 cm thick PMMA phantom was placed over the patient table at 720 mm from the source. The table and the phantom were positioned such as to leave only the phantom in X-ray beam path. The beam was collimated for a 5×5 cm^2 FOV over the detector, which leaves an approximate 2.5×2.5 cm^2 beam cross-section incident over the phantom. The collimation combined with the air gap between the phantom and the detector substantially decreases the detection of scattered radiation.

X-ray fluence was generated by the Tungsten anode with 0.3 mm-thick Copper filter and focal spot set to 0.6 mm. Different sets containing over than 30 X-ray images were acquired using the 30 frames-per-second fluoroscopy mode with 60, 80 and 100 kV tube voltages and 60, 80 and 100 mA tube currents. Beam pulse width was set to 10 ms. An additional image was acquired at 80 kV tube voltage and 40 mA tube current, and served as reference data for simulation.

The average per-pixel SI, the SI standard deviation as well as their ratio, *i.e.* the Signal-to-Noise Ratio (SNR), were measured in a circular region-of-interest (ROI) inside the 5×5 cm^2 region hit by primary photons, displaying uniform SI values (cf. Figure 3-23b).

Simulation Setup (high energy)
The same geometric setup illustrated Figure 3-23a was emulated using CatSim. Simulated X-ray fluence spectra for the W anode were generated using TASMIP model with additional 1.5 mm of Aluminum filtration to match the system's HVL. Primary photons only were shot from a single point source and interacted with the 10 cm PMMA flat phantom. The transmitted photons were detected by flat detector with same QDE, optical gain G and A/D conversion factors as the real Innova IGS620 system (cf. Annex B for details). For the sake of comparison, simulations were repeated with and without the blur generated by the optical quanta spreading inside the scintillator, to test the hypothesis that the FOMs are energy-independent.

In simulations, a scaling factor was calculated to match X-ray production of the Innova IGS620 tube with the TASMIP model. This scaling factor is necessary due to the possible mismatch in X-ray photon production efficiency of tube, differences in X-ray photon absorption efficiency of the detector when compared to nominal values (usually measured as the detector Conversion Factor (CF), in units of electrons per X-ray quanta), as well as other physical and geometrical factors. Hence, it scales the absolute photon counts to the right level which can be easily determined by forcing the simulated image noise to match the measured ones, for one phantom and one acquisition spectra. Additionally, the scaling factor for simulated blur-free detector is expected to be much higher than simulation including optical spreading. This is due mainly to the differences in the noise color modulation. Nevertheless, by analyzing the Innova IGS620 system pre-sampling MTF, it is expected that in both cases the FOMs are energy-independent and therefore behave accordingly.

In this validation experiment, the scaling factors were estimated using a reference acquisition at 80 kV and 40 mA. It is worth noting that even though such a scaling factor will lead to nearly perfect agreement between measurements and simulations at 80 kV, discrepancies are still expected for other tube voltage and tube current values, as a result of possible errors in the shapes of the spectra, and the varying spectrum-amplitude ratios of 80 kV to other tube voltage values.

Results
Figures 3-24a and 3-24b shows signal intensity profiles passing through the ROIs where 1st and 2nd order statistic measurements occurred, as previously illustrated in Figures 3-22b and 3-23b for the Senographe DS and Innova IGS620 experimental setups, respectively. The bottom row in Figures 3-24a and 3-24b shows a zoomed region where the influence of residual scattered radiation can be distinguished. A polynomial fit was applied on the data outside the 5×5 cm^2 FOV, *i.e.*, corresponding to scatter-only signals, in order to estimate the scatter signal inside the measurement

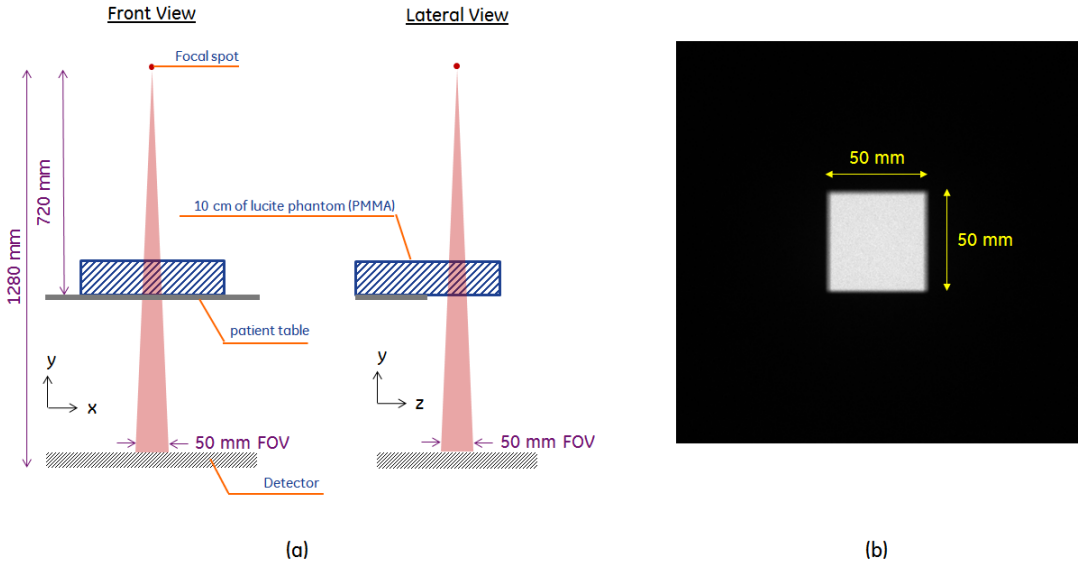

Figure 3-23: (a) experimental setup illustration on GE Innova IGS620 used for SI, noise and SNR validation; (b) the X-ray image obtained with 50×50 mm^2 collimation at the detector level; measurement were performed in a ROI inside the zone hit by photons

ROI. Good suppression of scattered radiation was seen in both experimental setups, with Scatter-to-Primary Ratios (SPR) values at $\sim$ 1% for GE Essential DS setup and $\sim$ 4% for GE Innova IGS620 setup.

Table 3.6 summarizes the measured and simulated average per-pixel SI for the Senographe DS experiment. Good quantitative agreement was seen, with maximum absolute error of 5.5%.

Table 3.6: Measured and simulated average per-pixel SI for the Senographe DS experiment

Spectrum	**Measured SI (counts)**	**Simulated SI (counts)**	**error (%)**
Mo/Mo 28kV 200 mAs	1958	1936	-1.12
Mo/Mo 26kV 200 mAs	1261	1224	-2.98
Mo/Rh 28kV 200 mAs	2432	2573	5.77
Rh/Rh 30kV 200 mAs	4421	4665	5.50

Figures 3-25a, 3-25b and 3-25c shows X-ray images obtained from measurement on the Innova IGS620 system, as well as blur-free simulation and simulation including optical spreading in the detector, respectively. They were acquired with the reference acquisition parameters: 80 kV and 40 mA. From visual inspection, we can observe a good similarity in background noise color between measurement and simulation including optical spreading.

Figures 3-26a, 3-26b and 3-26c shows measured and simulated average signal intensity, standard deviation and SNR, respectively, as function of the tube voltage and for 60, 80 and 100 mA tube currents. A good agreement can be seen in the trends of both measured and simulated values. Figures 3-27a, shows measured vs. simulated SNR values comprising all simulated conditions, with linear regression fit and coefficient of determination R^2 above 0.99. Figure 3-27b shows the relative error between simulated and measured SNR as function of the tube voltage, increasing up to $\sim$ 8% at 100 kV.

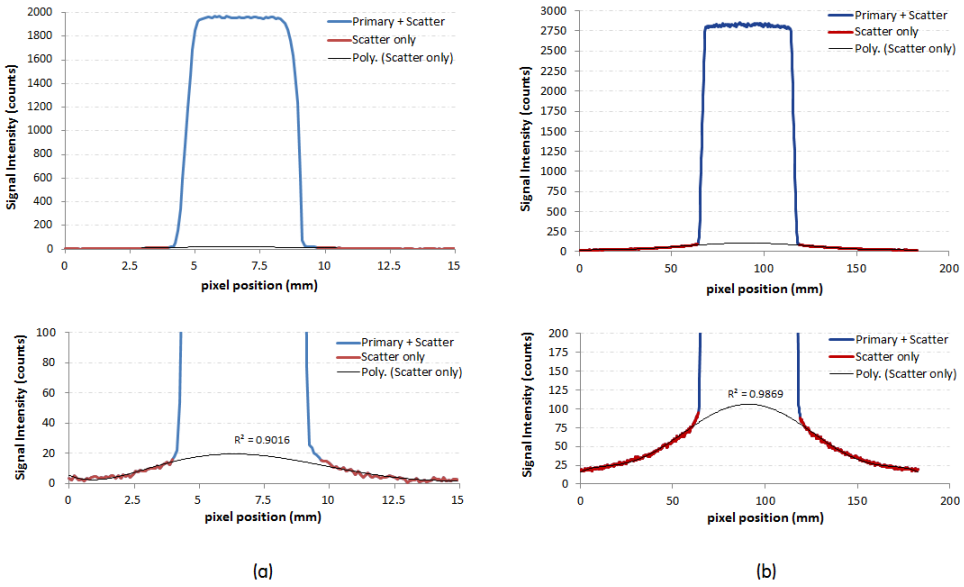

Figure 3-24: Measured primary and scatter signal profiles in (a) GE Senographe DS (cf. 3-22) and (b) GE Innova IGS620 (cf. 3-23) projection images; the bottom row shows a zoomed region of the graphs in the top row, showing a polynomial fit of scatter only signal; SPR was estimated at $\sim 1\%$ for GE Senographe DS setup and $\sim 4\%$ for GE Innova IGS620 setup

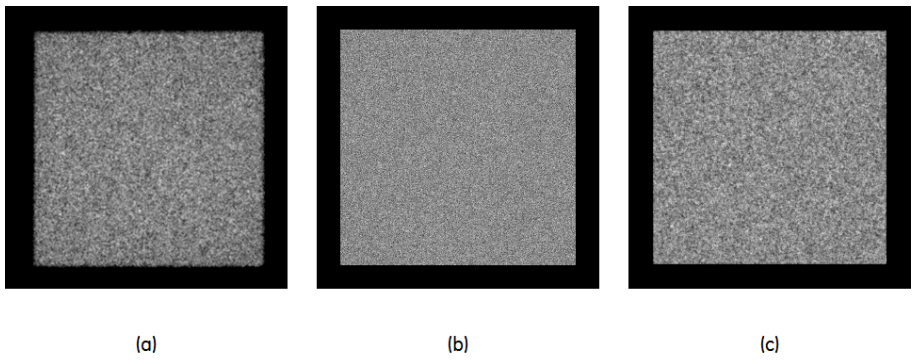

Figure 3-25: Innova IGS620 X-ray images obtained from (a) measurement and from simulations (b) without and (c) with blur from pre-sampling MTF; images were obtained for 80 kV and 40 mA setup

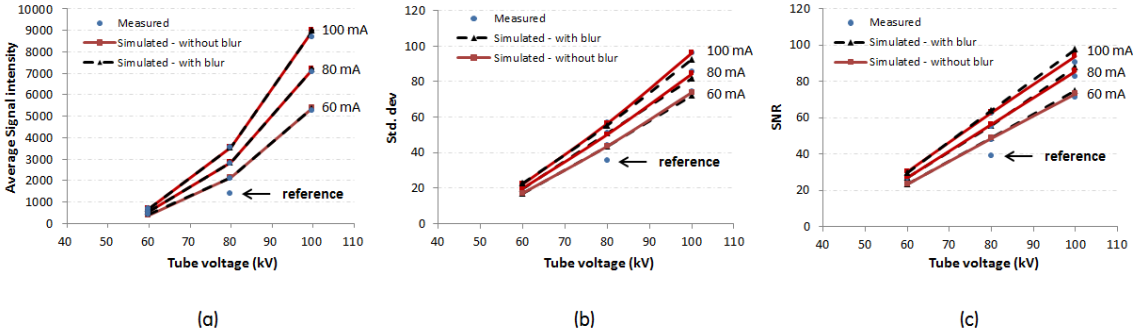

Figure 3-26: (a) Average signal intensity, (b) noise std. deviation and (c) SNR as function of the tube voltage and for 60, 80 and 100 mA tube currents. Measured data were obtained on the Innova IG620 system and simulated data was obtained with and without blur generated by the optical quanta spreading inside the scintillator

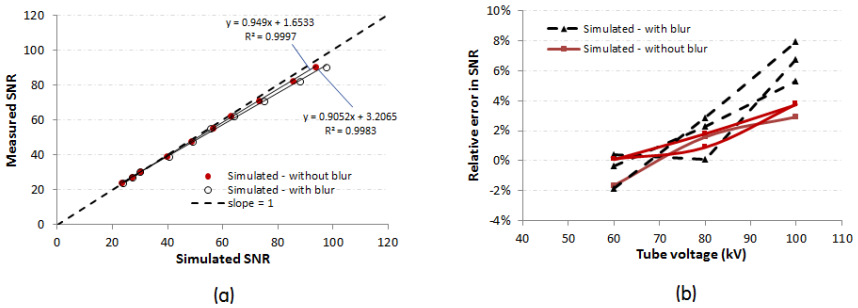

Figure 3-27: (a) Measured vs simulated SNR for all simulated conditions; (b) relative error of simulated vs measured values as function of the tube voltage. Measured data were obtained on the Innova IG620 system and simulated data was obtained with and without blur generated by the optical quanta spreading inside the scintillator

Discussion
In this section, a descriptive 1st and 2nd order statistical analysis of signal intensities was performed on X-ray images of homogeneous phantoms obtained acquired using low-energy spectra on a GE Senographe DS system, as well as high-energy spectra on a GE Innova IGS620 system.

For the high-energy experiment on Innova IGS620 system, the sufficiently wide ROI allowed to obtained precise measurements of per-pixel average and standard deviation of signal intensities, and the Signal-to-Noise Ratio (SNR) values. A good agreement can be seen in the trends of both measured and simulated values, with maximum $\sim 8\%$ error on the SNR. An approximate linear relationship in SNR error with the increasing tube voltage was observed ($R^2 > 0.99$), most likely due to differences in the X-ray fluence, which could be further calibrated.

For the low-energy experiment on Senographe DS system, only per-pixel average signal intensity was assessed. This is because our experimental setup did not provide homogeneous background noise inside the ROI and precise standard deviation measurements, due to the small aperture of the diaphragm. However, since the simulated NPS of Senographe DS system had good agreement with the real system, and assuming the good linearity observed in the Innova IGS620 experiment would also be found in Senographe DS simulation, we estimated that any difference in SNR could also be calibrated.

To conclude, we verified that the developed simulation chain modules agreed with real X-ray systems only for a limited set of acquisition configurations, but that covers the space of parameters used during the remainder of this PhD thesis investigation. Further investigations are nonetheless required in order to generalize our results to a wider set of acquisition configurations.

3.5 Conclusions

In this chapter, an extensive validation of the different CatSim modules described in Chapter 2 for a range of X-ray energies (10 to 80 keV), breast thicknesses (2 to 8-cm thick for compressed breasts, 10 to 18-cm diameter for uncompressed breast) and compositions expected in breast imaging was performed. The main objective was to provide sufficient evidence that the implemented simulation chain is capable to emulate realistic physical phenomena underlying an X-ray breast imaging system, especially digital breast tomosynthesis and dedicated breast computed tomography.

Validation of implemented simulation modules was performed by analyzing each step of a X-ray imaging chain: from the generation of X-ray photons, their interaction with matter and their absorption in flat panel detectors. Beam penetrating quality of low-energy X-ray spectrum models for Molybdenum and Rhodium anodes showed to be in agreement with the behavior of a typical mammography X-ray tube, with error below 2% on average. X-ray photon scattering simulation validation was performed for typical cone-beam breast geometries, and considering energy range and phantom sizes expected for CE-bCT. Monte Carlo based simulation of scattered photon intensity showed good qualitative agreement with previously reported results. Peak scatter-to-primary ratio values where within ∼5% error. Monte Carlo based estimation of absorbed average glandular dose were compared to previously published results and agreed within ∼4% error for both typical mammography and breast CT geometries. X-ray detector model was validated while considering the simplified cascade model for scintillator-based indirect conversion detectors. Detector spatial resolution (pre-sampling MTF) and Noise Power Spectrum (NPS) simulations qualitatively agreed to those of real X-ray imaging systems. Signal intensity and signal-to-noise ratio for low-energy spectra (Mo/Mo 26kV to Rh/Rh 30kV) agreed within ∼5% error when compared to a real X-ray mammography system, while signal intensity and signal-to-noise ratio for high-energy spectra (W/Al 60kV to W/Al 100 kV) agreed within ∼8% error when compared to a real X-ray fluoroscopy system.

In summary, we demonstrated that CatSim simulation chain is in good agreement, qualitatively and quantitatively, with respect to real X-ray imaging systems and previously published simulation and experimental results. We provided validation evidence through comparisons with experimentally obtained data or previously published data from other validated simulation platforms.

Chapter 4

Iodine-Enhanced Breast X-ray Imaging Framework

Spectral imaging originated from the limitation of single-energy imaging in differentiating tissues with different chemical composition but similar X-ray attenuation. Alternatively, any difference in X-ray attenuation due to changes in the tissue density may also be mistaken with differences due to changes in its chemical composition. There exists hence an ambiguity in single-energy imaging which limits tissue differentiation and classification. For example, in single-energy CT, when determining the amount of iodine enhancement of a soft tissue lesion the measured average CT number in a region-of-interest in that lesion will reflect not only the enhancement due to iodine, but also the underlying tissue. Therefore, the attenuation coefficients alone can hardly provide sufficient information on the fundamental properties of the tissue, nor on its absolute density, making it difficult to correlate measured signal intensities with pathologies [203]. To overcome this limitation, additional information is required.

Due to the energy dependency of the linear attenuation coefficients, materials can be differentiated in images acquired using different X-ray beam energies. By properly combining the acquired spectral data set, one can generate images where the contrast of a given material of interest with respect to all other materials in the imaged object is ultimately enhanced [204]. This is the main principle behind *spectral imaging*. When combined with vascular contrast agents, spectral imaging techniques lead to enhanced visibility of abnormal vascular development and cancerous lesions.

In this PhD thesis research, we leveraged a dual-energy imaging technique to generate selective iodine images. Different dual-energy recombination algorithms were used to optimize and compare the performance of iodinated contrast-agent-enhanced breast CT technique, while considering different dual-energy acquisition strategies and input spectra. In this chapter we introduce the basic concepts behind spectral imaging and selective iodine image generation.

In Sections 4.1 and 4.2, we introduce the basics of basis material decomposition and the main algorithm used to generate material selective images. In Section 4.3, a brief overview on the different methods allowing to obtain dual-energy data is also provided. In Section 4.4 the framework which will serve as basis for the dual-energy iodine imaging application, specifically design for the dual-energy Contrast-Enhanced Digital Breast Tomosynthesis (CE-DBT) and dual-energy Contrast-Enhanced breast CT (CE-bCT) geometry setups studied in this PhD thesis research work, is presented. Image and projection-based decomposition algorithms, implemented to obtain enhanced iodine uptake in recombined dual-energy images, are described. A material decomposition calibration method is proposed to ensure optimal recombined iodine-equivalent images during CE-bCT acquisition parameters optimization discussed in Chapter 5.

4.1 Basis Material Decomposition

Representation of Attenuation Coefficients
The attenuation coefficients of each material in an object, $\mu(\mathbf{r}, E)$, as function of energy E and at position $\mathbf{r}$ in its volume, may be decomposed as:

$$\mu(\mathbf{r}, E) = a_1(\mathbf{r})\psi_1(E) + a_2(\mathbf{r})\psi_2(E) + \dots a_M(\mathbf{r})\psi_M(E) \tag{4.1}$$

where $\psi_m(E)$ are known energy-dependent basis functions and $a_m(\mathbf{r})$ translate the local quantities of $\psi_m(E)$, for $m = 1, 2, \cdots, M$ basis.

The functions ψ_m must be chosen so they can represent the energy-dependent behavior of all materials inside the volume. Therefore, the most generic representation is to decompose $\mu(\mathbf{r}, E)$ into the energy-dependent mass or linear attenuation coefficient functions of all *basis materials* composing the object [205, 206]. In this case, $a_m(\mathbf{r})$ represents the density distribution of the basis material m at position $\mathbf{r}$ in its volume. This is the main representation behind *material separation* and will be adopted as the main method throughout this PhD thesis.

Alternative representations of the attenuation coefficients have also been proposed. For instance, in a two-basis setup ($M = 2$), Alvarez and Macovski [204] used the fact that most of the atomic interactions occurring in CT energy range are Photoelectric and Compton events (cf. Annex A.2) and described both phenomena according to energy-dependent functions $\psi_{photo}(E)$ and $\psi_{compton}(E)$. For Photoelectric effect they assumed a $1/E^3$ dependency, while for the Compton effect the Klein-Nishina equation was used. If a material has a K-edge in the energy range of interest, a third term $a_{edge}(\mathbf{r})\psi_{edge}(E)$ must be included in Equation 4.1 [205, 207–209], which will describe the behavior of the absorption edge. When multiple K-edges are present, each adds a unique corresponding basis function.

4.2 Spectral Imaging

Spectral Imaging at M Energies and M Unknown Materials
One of the applications in spectral or multi-energy imaging is to obtain M images in which signal intensities are proportional to the quantities of each $m = 1, 2, \cdots, M$ basis materials inside an object. For this purpose, the object is imaged using M different X-ray spectra and the materials composing the object are differentiated by analyzing their differences in X-ray attenuation. This material decomposition can be performed either in the reconstruction domain, hereafter referred to as *image domain*, or in the *projection domain*.

In the image domain, we typically choose $\psi_m(E) = \mu_m(E)$ and $a_m(\mathbf{r}) = f_m(\mathbf{r})$, respectively the linear attenuation coefficient of basis material m at energy E and its volume fraction at position $\mathbf{r}$. Following Equation 4.1, we can write the measured attenuation volumes $\tilde{\mu}(\mathbf{r})$ as:

$$\tilde{\mu}(\mathbf{r}) = \bar{\mu}_1 f_1(\mathbf{r}) + \bar{\mu}_2 f_2(\mathbf{r}) + \cdots + \bar{\mu}_M f_M(\mathbf{r}) \tag{4.2}$$

where $\bar{\mu}_m$ is the effective linear attenuation coefficient of basis material m calculated at the effective energy of a given input spectrum.

In the projection domain, we typically choose $\psi_m(E) = (\mu/\rho)_m(E)$ and $a_m(\mathbf{r}) = \rho_m(\mathbf{r})$, respectively the linear mass attenuation coefficient of basis material m at energy E and its local effective density at position $\mathbf{r}$. Following Equation 4.1 and disregarding X-ray scattering, we can write the measured log-projection $\tilde{p}(i)$ at detector element i as:

$$\tilde{p}(i) = -ln \int_0^\infty w(E) \cdot exp\left[\delta_1(i)\left(\frac{\mu}{\rho}\right)_1(E) + \delta_2(i)\left(\frac{\mu}{\rho}\right)_2(E) + \cdots + \delta_M(i)\left(\frac{\mu}{\rho}\right)_M(E)\right] dE \tag{4.3}$$

where $\delta_m(i) = \int \rho_m(\mathbf{r})dl$ is the projected area density (in g/cm^2) of basis material m, dl is the incremental chord length of the beam path between the X-ray source s and the detection element i, and $w(E)$ is a normalized spectral weight [131, 210] or system weighting function [211] defined as:

$$w(E) = \frac{I_{net}(E)\xi(E)\eta(E)}{\int_0^\infty I_{net}(E)\xi(E)\eta(E)dE} \tag{4.4}$$

where $I_{net}(E, i)$ is the X-ray intensity spectrum generated by the X-ray source s and towards the detection element i, $\xi(E)$ is the detector conversion response and $\eta(E)$ is a function translating an eventual energy-dependent efficiency in detecting photons.

Under no further assumption, the problem of spectral imaging is then to invert a system of equations based on M measurements similar to Equation 4.2 (for an image-based decomposition) or Equation 4.3 (for an projection-based decomposition), and recover a unique solution to the local quantities $f_m(\mathbf{r})$ or $\delta_m(i)$ of each basis materials. The solutions $f_m(\mathbf{r})$ or $\delta_m(i)$ are hereafter referred to as *material-equivalent images* or *material-equivalent projections*, respectively, as their intensity values are proportional to the quantity of material m.

In the case of monochromatic input spectra, both Equations 4.2 and 4.3 are linear combinations of the local quantities $f_m(\mathbf{r})$ or $\delta_m(i)$, and can be solved by algebraic inversion of a linear system of equations. In the case of polychromatic input spectra, Equation 4.2 is still linear but $\tilde{\mu}(\mathbf{r}) < \sum_{m=1}^{M} \bar{\mu}_m f_m(\mathbf{r})$, due to beam hardening. On the other hand, Equation 4.3 is no longer linear and requires more complex calculations to invert the system of equations.

The accuracy of the inversion of both image and projection domain decomposition system of equations is directly related to the singularity of their Jacobian matrices[1] [204, 212]. In general, a nonzero Jacobian determinant is sufficient to perform material separation. For monochromatic spectra this is achieved by using M different X-ray beam energies. For polychromatic spectra, this is achieved by using M different spectra. In both cases, the higher the distance and smaller the overlap among the M different input spectra, the better conditioned the system of equations will be, resulting in more accurate solutions of $f_m(\mathbf{r})$ or $\delta_m(i)$ and less sensitivity to quantum noise.

Material Separation in the Image Domain

Image-based decomposition is performed after tomographic reconstruction. It is a straightforward approach that does not require the same acquisition geometry for all M spectral measurements. Each m-th projection data is treated independently until they are reconstructed. Spatial correlation among the M reconstructed volumes is then achieved and basis decomposition is performed to obtain the material-equivalent images $f_m(\mathbf{r})$ (Equation 4.2).

For an accurate material separation, beam hardening effects must be corrected. *Beam hardening* occurs because the images are acquired using polychromatic X-ray beams. In CT, beam hardening can cause inaccurate reconstructed attenuation coefficients due to intensity cupping, shading, or streak artifacts. If not corrected, signal intensity in measured attenuation volumes $\tilde{\mu}(\mathbf{r})$ deviates from the true material attenuation at position $\mathbf{r}$, resulting in incomplete material separation, residual texture from the complementary materials and jeopardized quantification.

There exists an extensive number of beam-hardening correction (BHC) methods to independently correct the M acquisitions. In water-based correction [213,214], attenuation values displace-

[1] The Jacobian matrices of both image and projection domain decomposition system of equations, respectively J_{img} and J_{proj}, for M materials and M energies, are defined as:

$$J_{img} = \begin{pmatrix} \partial\tilde{\mu}_1/\partial f_1 & \partial\tilde{\mu}_1/\partial f_2 & \cdots & \partial\tilde{\mu}_1/\partial f_M \\ \partial\tilde{\mu}_2/\partial f_1 & \partial\tilde{\mu}_2/\partial f_2 & \cdots & \partial\tilde{\mu}_2/\partial f_M \\ \vdots & \vdots & \ddots & \vdots \\ \partial\tilde{\mu}_M/\partial f_1 & \partial\tilde{\mu}_M/\partial f_2 & \cdots & \partial\tilde{\mu}_M/\partial f_M \end{pmatrix} \quad \text{and} \quad J_{proj} = \begin{pmatrix} \partial\tilde{p}_1/\partial\delta_1 & \partial\tilde{p}_1/\partial\delta_2 & \cdots & \partial\tilde{p}_1/\partial\delta_M \\ \partial\tilde{p}_2/\partial\delta_1 & \partial\tilde{p}_2/\partial\delta_2 & \cdots & \partial\tilde{p}_2/\partial\delta_M \\ \vdots & \vdots & \ddots & \vdots \\ \partial\tilde{p}_M/\partial\delta_1 & \partial\tilde{p}_M/\partial\delta_2 & \cdots & \partial\tilde{p}_M/\partial\delta_M \end{pmatrix}$$

ment due to beam-hardening is partially compensated by remapping the measured log-projection values $\tilde{p}(i)$ based on known water attenuation characteristics:

$$\tilde{p}_{corrected}(i) = \sum_{l=0}^{N_{BHC}} c_l^{BHC} \left[\tilde{p}(i)\right]^l \tag{4.5}$$

where N_{BHC} is typically between 2 and 5 (depending on the object size). The coefficients c_l^{BHC} are found through *a priori* calibration by performing least squares minimization with Equation 4.5 for known log-projection values of a homogeneous water phantom. Theoretically, any homogeneous material could be used and correction accuracy increases if they better represent the imaged object (*e.g.* soft-tissue). The corrected projections are then reconstructed and linearly combined to generate the material equivalent images. Since CT values displacement is corrected with respect to a single material, there may still be a significant variation in CT values if materials with very different effective atomic number (Z_{eff}) are present (*e.g.* iodine, bone and metallic clips). Nonetheless, the correction might be sufficient if such materials are present at low concentrations.

The use of *bowtie filters* provides similar results to water-based correction, since they also perform an intrinsic linearization of CT values. Bowtie filtration provides uniform hardening of the X-ray beam across the detector field of view, minimizing cupping artifacts and decreasing corresponding deviation in CT numbers due to beam hardening. This approach is particular suitable for dedicated breast CT geometry because the uncompressed pendant breast presents a highly symmetrical geometry [141]. However, for a good performance the shape of the bowtie filter must match the imaged object.

Maaβ*et al.* [215] suggested to extend Equation 4.2 to a nonlinear version using a high-order polynomial combination of measured attenuation volumes. Such method requires a pre-calibration step based on known object templates and minimization of the differences between the reconstructed material-selective images and the templates. Although significantly more precise than the previous two methods, its real implementation could be very time consuming if multiple input spectra are considered.

These pre-correction methods partially correct for the cupping artifacts and attenuation inaccuracy in the individual projection images, but the resulting reconstructed images might still not be fully quantitative.

Material Separation in the Projection Domain

Projection-based decomposition is performed before tomographic reconstruction. It requires that the same acquisition geometry of all M spectral measurements. The system of equations based on measured log-projection images is inverted to calculate the material projections δ_m (Equation 4.3), which are subsequently reconstructed to obtain material density volumes, $\rho_m(\mathbf{r})$.

Since X-ray spectrum polychromaticity is foreseen in the nonlinear log-projection decomposition of Equation 4.3, beam hardening is automatically taken into account. The accuracy in the inversion of the system of equations based on Equation 4.3 will dictate the quality of beam hardening correction.

A straightforward way to invert Equation 4.3 was proposed by Alvarez and Macovski [204,216]. It relies on expanding the nonlinear log-projection equation 4.3 into a Taylor series of high order polynomial combination of the basis functions [216], or in its inverse form, expressing the basis functions as a high order polynomial combination of the measured log-projections [205, 217]. The coefficients of the Taylor series can be found by empiric calibration, using least squares minimization of known values of δ_m. Typically, 2nd or 3rd order polynomials with crossed terms are sufficient to account for beam hardening. However, if calibration is performed with the noisy projection data (*e.g.* in a real X-ray system), fluctuations in the calculated coefficient and consequent inaccuracy in material separation are expected.

Look-up table methods have been also proposed [206,218], in particular to address the fluctuations of polynomial coefficient calibration in the presence of high quantum noise levels and image artifacts. The look-up table maps a limited set of measured low-noise log-projections $\{\tilde{p}_1, \tilde{p}_2, \cdots, \tilde{p}_M\}$ into a set of material projections $\{\delta_1, \delta_2, \cdots, \delta_M\}$, and any intermediate values can found by bilinear interpolation. The image volume data sets reconstructed from the material projections are free of beam hardening artifacts. Although the decomposition process is fast, stable and easy to implement, the generation of tables can be time consuming depending on the desired accuracy.

Iterative methods minimizing the error of the spectral measurement with the expected attenuation coefficients have also been proposed [211,219]. They can be incorporated in the flow process of know iterative reconstruction algorithms and benefit from noise regularization and artifact management.

In contrary to image-based methods, projection-based decomposition enables for exact beam hardening correction and therefore superior material separation accuracy and quantification.

Spectral Imaging at $M-1$ Energies and M Unknown Materials

The decomposition of M unknown materials using $M-1$ different X-ray spectra involves an *underdetermined* system of equations, for which an external assumption or *a priori* information must be included as the M-th equation.

For most biological materials and contrast agents involved in X-ray imaging, we can assume that the sum of the volumes of the M constituent materials equals the volume of the mixture [220]. In image-based decomposition, volume conservation constraint is written as:

$$f_1(\mathbf{r}) + f_2(\mathbf{r}) + \cdots + f_M(\mathbf{r}) = 1 \tag{4.6}$$

In the projection domain, Equation 4.6 can be reinterpreted by integrating both sides over the incremental chord length dl in the X-ray beam path, and obtain:

$$\frac{\delta_1(i)}{\bar{\rho}_1} + \frac{\delta_2(i)}{\bar{\rho}_2} + \cdots + \frac{\delta_m(i)}{\bar{\rho}_m} = T(i) \tag{4.7}$$

where the material projections $\delta_m(i)$ are normalized by the density ρ_m of material m in its pure state and $T(i)$ is total object length (or thickness) in the X-ray beam path from the source s and the detector element i.

Spectral Imaging with K-edge

K-edge imaging involves performing material decomposition with one or multiple materials containing K-shell binding energy in the energy range of the M input spectra. Typical K-edge materials explored in diagnostic X-ray energy range are iodine (33.2 keV), barium (37.4 keV) and gadolinium (50.2 keV). In this PhD thesis investigations we concentrated on iodine imaging.

Selective iodine imaging can be performed either by exploring the K-absorption discontinuity of iodine (at least one out of the M input X-ray spectra straddling 33.2 KeV), or without exploring the discontinuity (all M X-ray spectra below or above 33.2 keV). The first option is however more accurate, with superior cancellation of noniodine materials and is less sensitive to quantum noise. This is because the K-edge discontinuity drastically increases the Jacobian matrices partial derivatives with respect to iodine ($\partial\tilde{\mu}/\partial\mu_{iodine}$ or $\partial\tilde{p}/\partial\delta_{iodine}$) if the X-ray spectra have mean energy above the iodine K-edge. This entails in a better conditioned problem when compared to non-K-edge decomposition.

Riederer and Mistretta [217] demonstrated that since the Photoelectric and Compton interactions account for almost all X-ray photon attenuation in diagnostic X-ray energy range, the use of three energy measurements is necessary and sufficient to distinguish iodine from any other material, provided that the beam energies straddle only the K-edge of iodine and no other element K-edge.

In a three-beam setup, material decomposition is therefore performed by describing the attenuation coefficient discontinuity as an independent term $a_{edge}(\mathbf{r})\psi_{edge}(E)$ in Equation 4.1. This can be performed either by decomposition the attenuation coefficients into Photoelectric, Compton and iodine K-edge basis functions [205, 207–209], or by decomposition into three basis materials attenuation coefficients: one with low Z_{eff} (emulating the predominantly Compton interactions), one with high Z_{eff} (emulating predominantly Photoelectric interactions) and iodine (describing its K-edge) [205, 206, 221].

In a two-beam (or dual-energy) setup, iodine K-edge imaging based on Photoelectric, Compton and iodine K-edge basis functions decomposition cannot be performed, since we only dispose of two spectral measurements. However, iodine K-edge imaging can be performed if based on basis material attenuation coefficient decomposition combined with an additional volume conservation hypothesis (Equation 4.6), which acts as the third equation. Accordingly, a system with three equations can be solved as long as only three materials are present ($M = 3$). This is the main principle behind *dual-energy three-material decomposition.*

Dual-energy three-material decomposition is exploited in Contrast-Enhanced Spectral Mammography (CESM) in which iodine is separated from adipose and fibroglandular tissues and volume conservation among the three materials is approximately held [16, 92, 198]. It has also been the baseline to generate iodine-equivalent images for dual-energy Contrast-Enhanced Digital Breast Tomosynthesis (CE-DBT) and dual-energy Contrast-Enhanced breast CT (CE-bCT) applications investigated in this PhD thesis research. Further details on their implementation are provided in Section 4.4.

4.3 Acquisition Strategies to Obtain Dual-Energy Data

To obtain two spectral data sets, different acquisition strategies have been previously proposed. These methods can be distinguished into two families, depending on where the energy separation is performed: at the source, by using different input spectra, or at the detector using so-called energy-resolved (or energy-discriminating) detectors.

In the first family of methods, one way to obtain different input spectra is by using dual source (DS) systems with two independent, synchronized and specific source-detector couples. Due to data truncation constraints, spectral material decomposition is commonly performed in the image domain, usually combined with water-based beam hardening correction algorithms. The first clinical DS CT scanner was introduced in 2006 [222], and acquired dual-energy data at 80 kV/140 kV LE/HE tube voltage combination (SOMATOM® Definition, Siemens Healthcare; Forchheim, Germany). The main advantage of this setup is that both source-detector couples can be operated independently with respect to voltage and current settings, and benefit from dedicated filtration for improved spectral separation, such additional Tin filter (Sn) typically used at 100 kV/Sn140 kV in the second generation DS CT scanners (SOMATOM® Definition Flash, Siemens Healthcare; Forchheim, Germany) [223]. However, the presence of a second X-ray tube induces additional scatter in the first detector and vice versa. Unfortunately, these supplementary photons cannot be completely suppressed by anti-scatter grids [224] and will degrade signal-to-noise ratio in both LE and HE projection images. An illustration of typical DS CT acquisition geometry and spectra are provided in Figure 4-1a.

Another dual-energy acquisition technique is to use a single source (SS) system, with spectral separation being achieved by alternating tube voltages and filtration. The most straightforward way to generate dual-energy data in a SS system is to first perform a full patient or target-volume scan with a LE spectrum, switch the acquisition parameters, and then perform another full scan with a HE spectrum [220]. Although this method suffers today from patient motion artifacts and consequent spatial resolution degradation due to long time interval between LE and HE scans, it does offer the benefit of requiring little additional hardware compared to single-energy applications and is therefore a relatively low cost solution for an additional dual-energy implementation. Furthermore, it allows to adjust tube voltage and tube current for better dose distribution between LE and HE acquisitions. In order to increase the temporal resolution, it is preferable to acquire dual-energy data while "switching" LE and HE spectra between two consecutive projection views. Two categories emerged: systems which perform slow and fast spectral switching.

Slow switching systems are easier to implement and the hardware often enables to change both X-ray tube voltage and filter between two consecutive acquisition views. This is the case of clinically available contrast enhanced mammography systems (SenoBright™, GE Healthcare; Chalfont St Giles, UK) and a number of dual-energy contrast-enhanced digital breast tomosynthesis prototypes based on energy-integrating detectors [95, 96, 225, 226]. With exposure time intervals in the order seconds, slow switching acquisition techniques greatly reduces patient motion artifacts compared to non-switching techniques [22].

Alternatively, single source *fast switching* CT scanners became clinically available in late 2000's with the introduction of the GE Discovery™ CT750 with GSI™ (GE Healthcare; Milwaukee, Wisconsin, USA). The GSI™ technology applies rapid 80 kV/140 kV tube voltage switching ($0.3 - 0.5$ ms interval between images), using a single filtration is available. This method, also named *Fast kVp switching*, allows for very good temporal resolution and nearly perfect spatial correlation between two consecutive acquisition views[2]. Achieving fast KV switching acquisitions requires however solutions to several technical challenges: high-detector frame rates, electronic systems capable of reading out two to three times more projection data, low electronic noise and afterglow, inclusion of the spectrum rise/fall profiles in the acquisition view integration period [227], flexibility in X-ray flux generation at both LE and HE spectra to enable dose efficiency optimiza-

[2] In reality, LE and HE projection data between two consecutive view angles are commonly spatially interpolated before recombination, such as to fully align the projections [219]

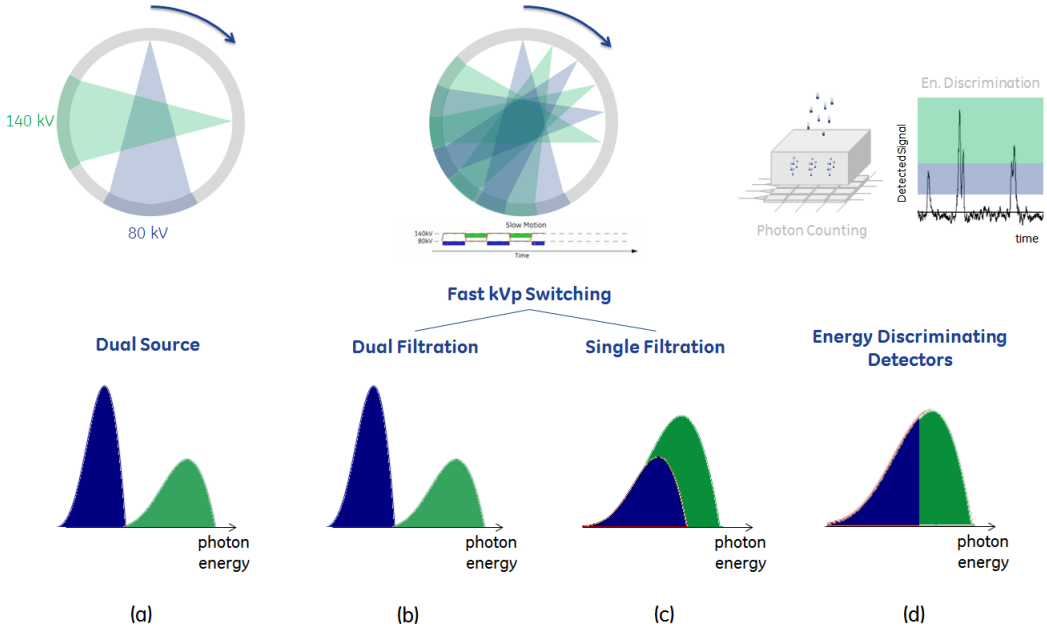

Figure 4-1: Illustration of four main acquisition strategies to obtain dual-energy data: (a) Dual Source, (b) Fast kV Switching with dual filtration, (c) Fast kV switching with single filtration and (d) single source system with energy-discriminating photon-counting detector. A representation of their typical low-energy (LE) and high-energy (HE) spectra is also provided

tion, and so on. Accordingly, an easier alternative for fast switching scans is to keep tube voltage constant and alternate filtration to enhance spectral separation. This acquisition technique was proposed by Mistretta *et al.* [228] for iodine absorption-edge fluoroscopy by the means of a rotating filter wheel composed of different material segments. A similar approach for breast imaging was proposed by Carton *et al.* [23]. The authors studied a dual-energy CE-DBT acquisition using a photon counting detector and a multi-slit scanning system. LE and HE images were acquired by differentially filtering the X-ray beam incident on adjacent linear detector slits, using alternating Tin and Copper filtration and fixed 49 kV tube voltage.

A fast kV switching technique with rotating filter, *i.e.* alternating simultaneously tube voltages and filtration, is a technological challenge and has not yet been implemented in clinical practice for dual-energy imaging. It would allow however for a substantial gain in spectral separation and a potential increase in image quality. In this PhD thesis research, this technique is studied in a theoretical framework, which could be implemented in the future. Illustrations of typical SS kV switching CT acquisition with dual and single filtration are provided in Figures 4-1b and 4-1c, respectively.

The second family of methods relies on performing spectral separation during the detection process, using so-called energy-resolved detectors. This type of detector has been developed in two ways. The first, relies on a sandwich detector with two photo-sensitive layers [220, 229, 230] with energy-discrimination occurring as function of its depth. The first layer is a thin scintillator coupled to a photodiode, and detects mainly low-energy photons. The transmitted photons reach a second layer composed of a thicker scintillator and another photodiode, which detects the remaining photons (mainly with high energy). This technology was recently introduced in clinical dual-energy CT (IQon Spectral CT, Royal Philips; Eindhoven, The Netherlands). The energy discrimination in this type of detector is however limited due to the large amount of spectral superposition between the high and low energy measurements [220]. Another technique relies on detectors with energy discriminant capabilities using photon counting technology. Energy resolution is provided by the

measurement of individual photons energy and its association to pre-defined *energy bins*. The main limitation of this technique is that it requires high temporal resolution in order to detect individual photon events. Otherwise, a possible misinterpretation of two consecutive incident photons as being a single event occurs, known as *photon pile-up*. Figures 4-1d illustrates a photon-counting implementation and the separation of a single acquisition spectra into two energy bins.

Both techniques provide excellent spatial registration and temporal resolution between LE and HE energy projection data, which makes them more suitable for projection-based decomposition. However, by construction, energy-discrimination through photon counting is preferable for material decomposition problem requiring minimal superposition. In breast X-ray imaging, dual-energy system prototypes based on energy-discriminating detectors have been implemented for CESM [18, 231], CE-DBT [25], and more recently for dual-energy breast CT with K-edge contrast agent [140, 141] and without contrast-agent enhancement [131]. In 2013, a dual-energy mammography system based on photon-counting technology was made available in clinical practice for breast density measurements (MicroDose SI, Royal Philips; Eindhoven, The Netherlands), while contrast-enhancement is still under investigation. Although encouraging results for breast CT applications using current photon technology have been recently shown, count rate, spectral response and energy resolution are still challenges for an actual K-edge breast imaging implementation.

In summary, both families of dual-energy acquisition methods present advantages and drawbacks on their implementation, such as data truncation, tube power requirements, spectral separation, temporal resolution, patient motion artifact and so on. Table 4.1 summarizes the characteristics, advantages and limitations of different dual-energy acquisition strategies discussed in this section.

In order to find the best acquisition strategies for dual-energy Contrast-Enhanced Breast CT, in this PhD thesis research work, four different dual-energy acquisition strategies were considered: dual source and fast KV switching with a single filtration are considered as state-of-the-art techniques for dual-energy acquisitions; fast kV switching with dual filtration, as well as the exploitation of photon-counting energy-discriminating detectors are considered as promising techniques, which could be available in the future. These techniques are investigated in a theoretical framework, *i.e.* disregarding up-to-date technical limitations (*e.g.*, temporal resolution, patient motion artifacts, data truncations, ...) while making idealistic hypothesis to the X-ray source and detector performances. Further details are provided in Section 5.4. The four candidate acquisition strategies for CE-bCT are summarized in Figures 4-1a to 4-1d.

Table 4.1: Characteristics, advantages and limitations of different acquisition strategies to obtain dual-energy data

Acq. Strategy	**Constructor**	**Application**	**Characteristics**	**Pros**	**Cons**
Dual Spin	Toshiba	CT	Two rotations Helical acquisition	Cost effective w/ little development Good spectral separation Customizable dose repartition	Delay for kV switching Large motion artifacts Poor temporal resolution
Dual-Source	Siemens	CT	2 source-detector pairs at 90° 2 individual filtrations	Better spectral separation Customizable dose repartition	Asynchronous projections Cross-scatter Cost of 2 imaging chains
Fast kVp Switching (Single Filtration)	GE	CT, RAD	Single source w/ single filter	Good temporal resolution Less costly with one source	No mA nor dose modulation Poor spectral separation Thermal constraints
Slow kVp Switching (Dual Filtration)	GE	CESM	Single source w/ dual filter	Better spectral separation Customizable dose repartition	Delay for kV switching
Dual-Layer Detector	Philips	DE-DM*, CT, RAD	Detector sensitive to 2 energy bins	Perfect temporal resolution Dual-Energy "always on"	Dose repartition predicted by the detector Poor spectral separation
Photon-Counting Detector w/ Energy Discrimination	GE, Hologic Philips	DXA DE-DM*	Signal proportional to photon energy	Perfect temporal resolution Ultra low dose scans Multi-energy imaging	Pile-up, charge sharing Technology still very costly Requires high frame rate

CT – Computed Tomography

RAD – conventional digital Radiography

CESM – Contrast-Enhanced Spectral Mammography

DE-DM – Dual-Energy Digital Mammography

DXA – Dual-energy X-ray Absorptiometry

*without contrast-agent

4.4 Iodine-Enhanced Breast X-ray Imaging

In this PhD thesis research, we leveraged a dual-energy three-material decomposition approach to generate selective iodine images.

Dual-energy three-material decomposition for iodine contrast-agent enhanced breast X-ray imaging consists in acquiring two spectrally separated datasets, using low-energy (LE) and high-energy (HE) spectra, and decompose them into three different basis materials: adipose tissue, fibroglandular tissue and the injected iodinated contrast agent. It involves therefore solving the system of equations based on Equations 4.2 (for an image-based decomposition) or Equation 4.3 (for an projection-based decomposition) with three unknowns (the quantity of each material) and two measurements (the LE and HE data). Therefore, a third equation is included by assuming a volume conservation constraint among the three materials. In order to achieve high image contrast and low-dose levels, we were interested in dual-energy acquisition leveraging the iodine K-absorption edge, *i.e.* with LE and HE spectra having mean energies that straddle the iodine K-shell binding energy.

For both CE-bCT and CE-DBT geometries investigated in this PhD thesis, the goal of iodine K-edge imaging is to invert a system of equations for $f_{iodine}(\mathbf{r})$ and obtain *iodine-equivalent* slice images. Notice that signal intensities in iodine-equivalent images are proportional to the quantity of iodine inside each voxel. Accordingly, the volumetric iodine concentration in each voxel can be estimated by multiplying $f_{iodine}(\mathbf{r})$ with the iodine density in its pure state ($\bar{\rho}_{iodine} \approx 4.93\ g/cm^3$).

4.4.1 Dual-Energy Recombination for CE-DBT

In this thesis, dual-energy recombination for CE-DBT has been performed using a projection-based algorithm previously developed by Puong *et al.* [226]. In this algorithm, the LE and HE log-projections p_{LE} and p_{HE}, respectively, are decomposed into material-equivalent projections $\delta_m(i)$, using 2nd polynomial with crossed terms, as suggested by Alvarez and Macovski [204, 216], to account for beam hardening originated from polychromatic acquisitions:

$$\delta_m(i) = \sum_{l=0}^{N}\sum_{k=0}^{N} c_{l,k} \left[p^{LE}(i)\right]^l \left[p^{HE}(i)\right]^k \qquad m = \text{adipose, gland, iodine} \tag{4.8}$$

where $N = 2$ is the order of the polynomial. The coefficients $c_{l,k}$ are found by simulation, using least squares minimization of known values of δ_{iodine}, while assuming a constant breast thickness T in the X-ray beam path between the source and all detector elements i (Equation 4.7).

Reconstructed iodine-equivalent images (or volumes) are subsequently calculated by reconstructing the iodine-equivalent projections δ_{iodine}:

$$f_{iodine}(\mathbf{r}) \approx \mathcal{R}\left\{\frac{\delta_{iodine}(i)}{\bar{\rho}_{iodine}}\right\} \tag{4.9}$$

where $\mathcal{R}\{\cdot\}$ is a linear reconstruction method and $\bar{\rho}_{iodine}$ is the density of iodine in its pure state. In this PhD research work, Filtered BackProjection (FBP) was the standard reconstruction algorithm for CE-DBT data.

It must be emphasized that due to limited angular sampling in CE-DBT acquisition, the reconstructed iodine-equivalent images $f_{iodine}(\mathbf{r})$ are only proportional to the actual volume fraction of iodine. Hence, it does not allow to calculate the local iodine volumetric concentration at position $\mathbf{r}$ in the breast volume. The limited iodine quantification in CE-DBT is discussed in Chapter 6.

4.4.2 Dual-Energy Recombination for CE-bCT

As stated in the introductory chapter, one of the objectives of this PhD thesis is to optimize dual-energy acquisition spectra for CE-bCT, while comparing the performance of different dual-candidate acquisition strategies in their ability to provide optimal iodine detectability with minimum background texture and cupping artifacts. This study is described in Chapter 5.

When designing an optimization study considering a large range of X-ray spectra, it is expected that certain combinations of input LE and HE spectra might not provide good material separation, especially those presenting significant spectral overlap due to poor filtration and with similar tube voltage values. As discussed in Section 4.2, dual-energy three-material decomposition may become for these cases an ill-conditioned problem due to lack of spectral separation and consequent Jacobian matrix singularity. Under such conditions, the dual-energy system of equations (cf. Equation 4.2 and 4.6) becomes more sensitive to variations in signal intensity (*e.g.* due to quantum noise or calibration error), ultimately leading into uncorrected cupping artifacts and poor background texture cancellation in the iodine-equivalent images.

To allow for a fair comparison between the different acquisition strategies when a large range polychromatic acquisition spectra are considered, we propose in this section a material decomposition calibration procedure for CE-bCT as a consistent way to determine the optimal recombination parameters for any given input LE and HE spectra, and independently of the decomposition domain. The calibration objective is *not* to find the exact solution for the dual-energy three-material system of equations, but rather to find a solution which gives the best image quality in terms of minimal cupping and maximum texture cancellation in iodine-equivalent images. If the resultant iodine-equivalent image is free of cupping and residual texture, we ensure that any signal attributed to iodine uptake is, in fact, proportional to the iodine concentration. The accurate iodine concentration value can be found *a posteriori* through further calibration.

Image Domain

For image-based decomposition, the implementation is straightforward. The measured LE and HE log-projections $\tilde{p}_{LE}$ and $\tilde{p}_{HE}$, respectively, were first corrected for beam-hardening by linearizing CT values with respect to a reference material, using a 3rd order polynomial fit, as suggested by Kachelrieβ *et al.* [214]. The chosen reference material was the adipose tissue, since it is the material with greater proportion in the breast volume.

The corrected LE and HE sinograms were afterwards reconstructed by FBP reconstruction to generate LE and HE effective attenuation coefficients volumes $\tilde{\mu}^{LE}(\mathbf{r})$ and $\tilde{\mu}^{HE}(\mathbf{r})$. The latter were subsequently used to invert the linear system of equations based on Equations 4.2 and 4.6. Since the system of equations is linear, we can produce iodine-equivalent images as a linear combination of the attenuation coefficient volumes:

$$f'_{iodine}(\mathbf{r}) = (1 - |w_{img}|) \cdot \tilde{\mu}^{LE}(\mathbf{r}) + w_{img} \cdot \tilde{\mu}^{HE}(\mathbf{r}) \qquad (image - based) \tag{4.10}$$

where $f'_{iodine}(\mathbf{r})$ is an offset and scaled version of the true iodine volume fraction $f_{iodine}(\mathbf{r})$ and w_{img} is a weighting factor.

The image-based algorithm steps are illustrated in Figure 4-2.

Projection Domain

For projection-based decomposition, the LE and HE log-projections p_{LE} and p_{HE} were decomposed into material-equivalent projections δ_m using a 3rd order polynomial with crossed terms, as suggested by Alvarez and Macovski [204, 216] (Equation 4.8, with $N = 3$). The material projections were then reconstructed by FBP to generate material density volumes $\rho_m(\mathbf{r})$, for $m \in \{adipose, gland, iodine\}$.

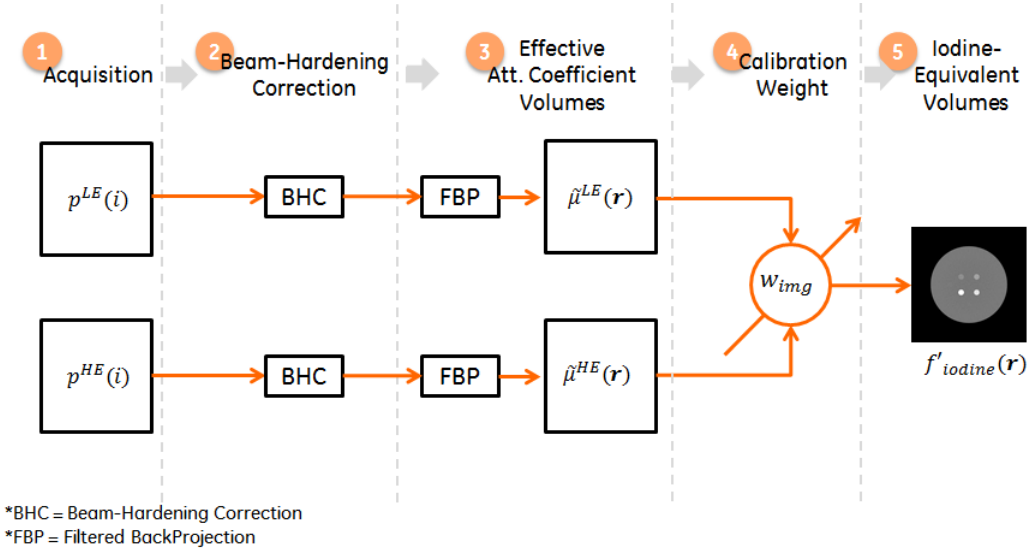

Figure 4-2: Flowchart of image-based decomposition

As proposed by Mendonça *et al.* [232], the production of material-selective images in a dual-energy three-material decomposition setup can be divided in two steps. First, cupping-free synthetic mono-chromatic attenuation images $\tilde{\mu}^{LE}(\mathbf{r})$ and $\tilde{\mu}^{HE}(\mathbf{r})$ can be generated at any given energy by inserting the reconstructed densities of two support basis materials, $\rho_1(\mathbf{r})$ and $\rho_2(\mathbf{r})$ into Equation 4.1, with $\psi_m(E) = (\mu/\rho)_m(E)$ and $a_m(\mathbf{r}) = \rho_m(\mathbf{r})$ [204]. The support basis materials must be chosen such as to approximately represent the energy-dependent attenuation behavior of all materials inside the imaged object. Secondly, as in the image-based decomposition method, $\tilde{\mu}^{LE}(\mathbf{r})$ and $\tilde{\mu}^{HE}(\mathbf{r})$ can be used to invert the system of equations based on Equations 4.2 and 4.6 and produce iodine-equivalent images.

Since both the generation of synthetic mono-chromatic images and the image-based dual-energy system of equations are linear processes, in this PhD thesis investigation we propose to combine them into a single equation and produce iodine-equivalent images directly from the material density volumes of adipose tissue and iodine:

$$f'_{iodine}(\mathbf{r}) = (1 - |w_{proj}|) \cdot \rho_{iodine}(\mathbf{r}) + w_{proj} \cdot \rho_{adipose}(\mathbf{r}) \qquad (projection - based) \qquad (4.11)$$

where $f'_{iodine}(\mathbf{r})$ is an offset and scaled version of the true iodine volume fraction $f_{iodine}(\mathbf{r})$ and w_{proj} is a weighting factor. Adipose tissue was chosen to approximately represent the energy-dependent attenuation of all soft-tissues inside the breast.

The projection-based algorithm steps are illustrated in Figure 4-3.

Equations 4.10 and 4.11 are written in a normalized way with terms of $(1 - |w|)$ and w. This was done such as to maintain the same range of weight values for the different input spectra to be considered during the optimization.

It must be emphasized that the weighting factors w_{img} and w_{proj} depend solely on the input LE and HE spectrum pair, *i.e.* they are independent of the imaged object. Hence, the calibration procedure described as follows has as objective to estimate and register the optimal weighting factors w_{img} and w_{proj} associated to every LE and HE spectrum pair considered in a look-up

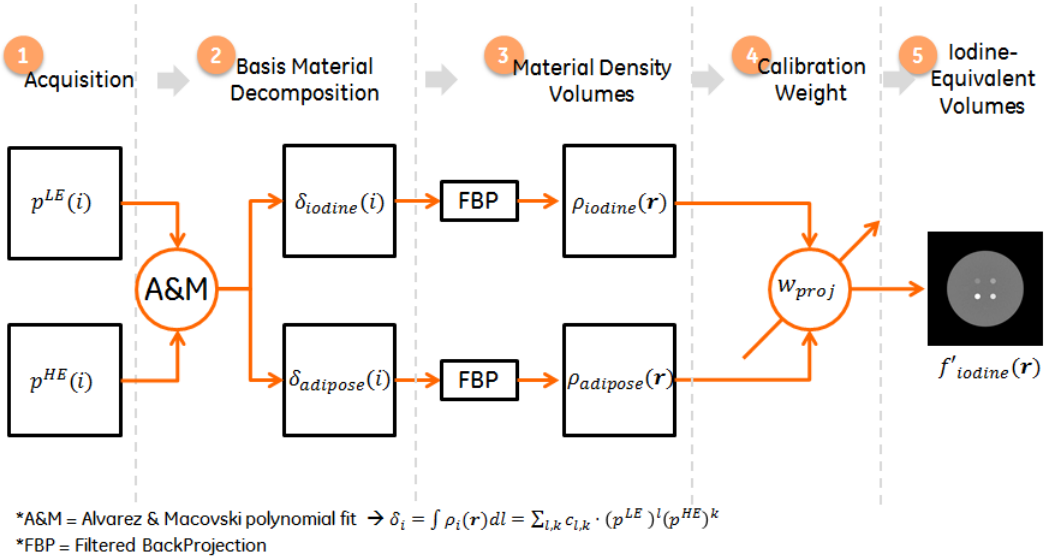

Figure 4-3: Flowchart of projection-based decomposition. Chosen basis material were iodine and adipose tissue

table.

Despite the similarities between image-based and projection-based approaches, a fundamental difference relies on the fact that the high-order polynomial transformation in Equation 4.8 takes into account the beam-hardening effect during the polychromatic projection. In this case, it is expected that projection-based decomposition provides better iodine quantification and non-iodine materials residual texture cancellation.

Breast Phantom and Calibration Procedure

As previously stated, the objective of iodine selective imaging is to obtain iodine-equivalent images with minimal residual texture from other materials in the imaged object. Accordingly, any remaining signal in these images should be proportional to the quantity of iodine in each voxel. Hence, we define the optimal weighting factors w_{img} and w_{proj} that best cancel the Signal Intensities (SI) of every material other than iodine inside the iodine-equivalent volume $f'_{iodine}(\mathbf{r})$.

A cylindrical phantom with similar diameter as the target imaged breast size and composed of adipose tissue was used as calibration phantom. It contained sixteen cylindrical fibroglandular inserts, oriented with the main cylinder axis and distributed at various radial positions, as illustrated in Figure 4-4a. The many radial positions allow to measure fibroglandular tissue contrast to background at different positions in the cylindrical phantom, ultimately enabling to assess intensity cupping.

LE and HE projections of the calibration phantom were simulated and used as input for either image or projection-based decompositions described above, to generate iodine-equivalent volumes $f'_{iodine}(\mathbf{r}, w)$ as function of the weighting factors w_{img} and w_{proj}, respectively.

The more intuitive way to find the weighting factor w_{img} and w_{proj} ensuring the best texture cancellation is to minimize the contrast of every fibroglandular insert with respect to their respective surrounding background. However, in the presence of important cupping artifact, minimizing the local contrast could converge to a local minimum where texture is ultimately not cancelled. Moreover, ensuring cupping-free images would also ensure SI values proportional to the iodine quantity independently of the position $\mathbf{r}$ in the volume. Hence, to account for any residual cupping, a Figure-of-Merit for texture cancellation taking into account the signal difference between

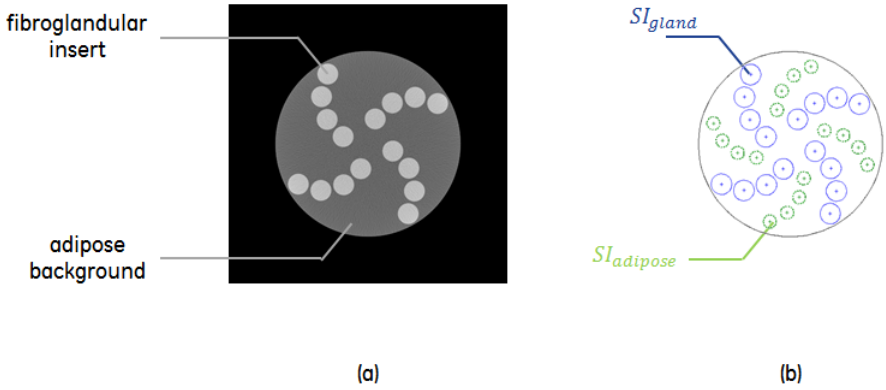

Figure 4-4: Phantom used in *a priori* calibration method for optimal dual-energy CE-bCT recombination

ROIs composed of both fibroglandular and adipose, at different positions in the volume, is needed.

Let $\mathcal{G}$ be the set of ROIs inside the *fibroglandular* inserts and SI_{gland} their individual mean per-pixel SI measured in the iodine-equivalent volume $f'_{iodine}(\mathbf{r})$, as illustrated in Figure 4-4b. Let also $\mathcal{A}$ be the set of ROIs on the *adipose* tissue background and $SI_{adipose}$ their individual mean per-pixel SI measured in the iodine-equivalent volume $f'_{iodine}(\mathbf{r})$, as illustrated in Figure 4-4b. Accordingly, the optimal weighting factors w_{img} or w_{proj} are defined as the weight w minimizing:

$$w_{img}, w_{proj} = \arg\min_{w}\{ \sum_{l,k} |SI_l(w) - SI_k(w)|^2 \}, \qquad l,k \in \mathcal{G} \cup \mathcal{A} \tag{4.12}$$

where $SI_l(w)$ and $SI_k(w)$ are found using Equation 4.10 or 4.11.

Figures 4-5a and 4-5b illustrate an example on the variation of the expression $\sum_{l,k} |SI_l - SI_k|^2$ with the weighting factor w, in image-based and projection-based algorithms, respectively. Optimal weighting factor w_{img} and w_{proj} are found at minimum expression value.

The calibration procedure was performed *a priori* to the actual optimization study. The optimal weighting factors w_{img} and w_{proj} were calculated for every LE and HE spectrum pairs considered during optimization and registered in a look-up table.

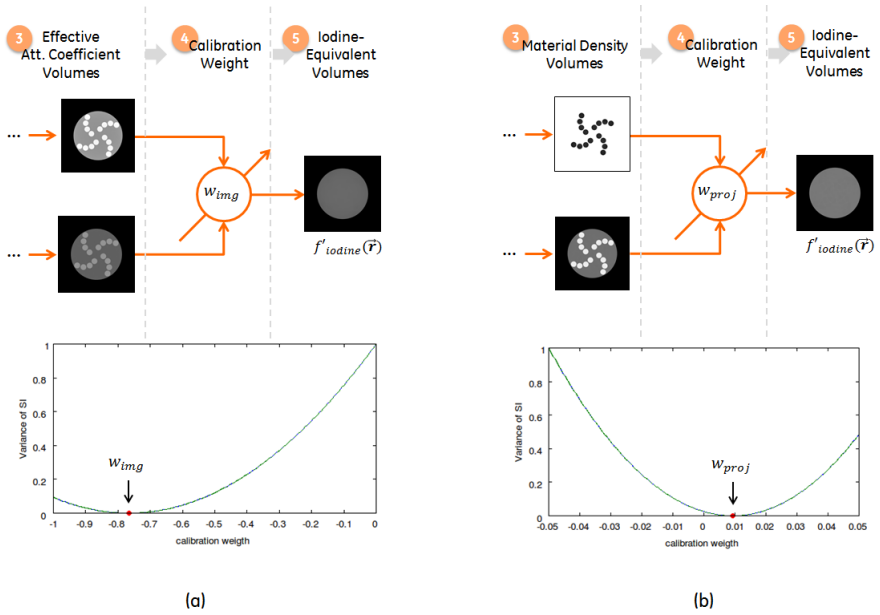

Figure 4-5: Illustration of calibration weighting for image and projection-based recombination

4.5 Discussion

In this chapter, the basic concepts behind spectral imaging and material separation were introduced. The production of selective material images were discussed when M different spectral data are decomposed into M material images (determined system of equations) and when $M-1$ different spectral data are decomposed into M material images (undetermined system of equations). Both image-based and projection-based decomposition approaches were described. Material decomposition with one or multiple materials containing K-shell binding energy in the energy range of the M input spectra were also discussed. A brief overview on the different state-of-the-art acquisition strategies used to obtain dual-energy data was also provided.

For the investigations carried in the remainder of this PhD thesis, an iodine K-edge breast imaging framework and the specific algorithms implemented to obtain iodine-enhanced images in dual-energy CE-DBT and dual-energy CE-bCT setups were described. For CE-DBT, a projection-based algorithm previously developed by Puong *et al.* [226] was implemented. For CE-bCT, both image-based and projection-based methods were implemented. The image-based recombination algorithm was based on the linear recombination of water-based corrected LE and HE attenuation volumes, while projection-based recombination algorithm was based on Alvarez and Macovski [204,216] high-order polynomial recombination of LE and HE projection data. For all methods, we assumed the composition of every unit of volume in the breast to be an ideal solution composed of adipose, fibroglandular tissues and iodine. To allow a fair comparison between different state-of-the-art acquisition strategies, proposed in Chapter 5 as candidate design options to obtain dual-energy data in a dedicated breast CT setup, we proposed a material decomposition calibration procedure as a consistent way to determine the optimal recombination parameters for any given input LE and HE spectra and independently to decomposition domain (images or projections).

In this PhD thesis, in order to solve the underdetermined problem of three-material separation with two spectral measurements, a volume conservation hypothesis was made. However, the assumption is not always verified. For example, whenever mixing salt and water, the volume of the mixture is not equal to the sum of the individual volumes of salt and water. Alternative methods based on the decomposition of mass fractions ω_m were proposed [233, 234]. Accordingly, a mass

conservation assumption could be written as:

$$\omega_1(\mathbf{r}) + \omega_2(\mathbf{r}) + \omega_3(\mathbf{r}) = 1 \tag{4.13}$$

In such methods, the material decomposition described by Equation 4.1 is written using $\psi_m(E) = (\mu/\rho)_m(E)$ and $a_m(\mathbf{r}) = \omega_m(\mathbf{r})$, where $(\mu/\rho)_m(E)$ is the energy-dependent mass attenuation coefficient of material m. More sophisticated approaches aiming to derive the density of a mixture based on models for the excess free energy of a mixture [235], were also proposed. However, the added accuracy of both mass conservation and excess free energy models are negligible in applications involving the biological materials and contrast agents expected for breast imaging, where volume conservation assumption is approximately held.

In the presented image-based decomposition algorithm, measured low and high energy volumes $\tilde{\mu}^{LE}(\mathbf{r})$ and $\tilde{\mu}^{HE}(\mathbf{r})$, respectively, are linearly recombined to form iodine equivalent images $f_{iodine}(\mathbf{r})$. To reduce beam-hardening artifacts and achieve better background tissue cancellation, $\tilde{\mu}^{LE}(\mathbf{r})$ and $\tilde{\mu}^{HE}(\mathbf{r})$ were corrected for beam-hardening by linearizing CT values with respect to a reference material, using a high-order polynomial fit [214]. Maaβ et al. [215] has proposed an alternative empirical calibration using high-order polynomial combination of the measured CT values for image-based decomposition. The method relies on the observation that, without the crossed terms in Alvarez and Macovski decomposition, high-order polynomial combination of LE and HE data can also be performed in the image-domain. In this case we would have:

$$a_m(\mathbf{r}) = \sum_{l=0}^{N}\sum_{k=0}^{N} c_l \left[\tilde{\mu}^{LE}(\mathbf{r})\right]^l + c_k \left[\tilde{\mu}^{HE}(\mathbf{r})\right]^k \tag{4.14}$$

where $a_m(\mathbf{r})$ is the local quantities of material m and the coefficients c_l and c_k can be found by calibration, using least squares minimization of known values of $a_m(\mathbf{r})$, usually obtained from an *a priori* calibration [236]. Naturally, this requires a linear reconstruction algorithm. Although the method was develop to decompose two-materials using dual-energy data and generate synthetic monochromatic images, we could have envisioned to apply it to the iodine K-edge imaging problem described in this chapter.

Since in this PhD thesis research we have been manipulating simulated data, Alvarez and Macovski [204, 216] polynomial approach was chosen for projection-based material decomposition. This allowed for faster calculation and little stability problems (*e.g.* fluctuations in the calculated coefficient and consequent inaccuracy in material separation) during spectral optimization. In a real case scenario however, photon starvation and other non-linear imaging artifacts could lead polynomial fit approaches to erroneous decomposition. Elsewhere, look-up table methods were proposed [206, 218] for dual-energy imaging in order to address the instability of polynomial surfaces, particularly in the presence of high noise and image artifacts. Furthermore, these methods could, in theory, be conceived such as to better handle the K-edge discontinuity. Another way proposed in literature to decompose dual-energy data is by using iterative methods [211, 219]. They present the possibility of being incorporated in an iterative reconstruction algorithm workflow and benefit from noise regularization and artifact management. Both look-up table and iterative approaches deserve further investigation to evaluate their potential in better handling real CE-bCT data.

Additionally, under the idealistic hypothesis of this study, beam hardening correction through linearization of CT numbers or polynomial decomposition in the projection domain did not took into account the variations of signal intensity in a given detector element other than the attenuation of the basis materials. However, the presence of Heel effect, bowtie filtration, X-ray scatter and non-homogeneous detector efficiency would deviate signal intensities in projection images from the values expected in the fitted model. In this case, one solution is to consider a family of fit models which depends on the detector element position, or alternatively on each X-ray beam path from the source s to element i. For example, in projection-based decomposition case, the material

projection $\delta_m(i)$ could be calculated as:

$$\delta_m(i) = \sum_{l=0}^{N}\sum_{k=0}^{N} \underbrace{\mathcal{C}_{l,k}(i)}_{\text{position-dependent}} \cdot \underbrace{c_{l,k}\left[p^{LE}(i)\right]^{l}\left[p^{HE}(i)\right]^{k}}_{\text{std. decomposition model}} \tag{4.15}$$

where the coefficients $\mathcal{C}_{l,k}(i)$ depend on the detector element i. In practice, they could be estimated by concatenating the effect of different phenomena:

$$\mathcal{C}_{l,k}(i) = c_{l,k}^{Heel}(i) \cdot c_{l,k}^{bowtie}(i) \cdot c_{l,k}^{scatter}(i) \cdot c_{l,k}^{\eta}(i) \cdots \tag{4.16}$$

In summary, with a validated simulation platform and the iodine-enhanced breast X-ray imaging framework described in this chapter, we achieve the basis for the ongoing improvements aimed at optimizing the performance of Dual-Energy CE-bCT and comparing its performance with Dual-Energy CE-DBT, *i.e.* the main objectives of this PhD thesis research work. Both topics are discussed in the following chapters.

Chapter 5

Spectral Optimization of Dual-Energy Contrast-Enhanced Breast CT

As described in Chapter 1, in the past decade much effort has have been oriented towards the optimization of single-energy (SE) breast CT image quality, in particular to improve the detectability of fibroglandular tissue and microcalcifications. Optimization studies on dual-energy (DE) breast CT have been limited to the improvement of spatial resolution as well as masses and microcalcification detectability in non-contrast-agent-enhanced breast images using energy-weighting recombination techniques [109, 131, 141, 237]. Little investigation on dual-energy recombination techniques for contrast-agent and tumor angiogenesis enhancement in a dedicated breast CT setup has been performed, with main contributions from Shikhaliev *at al.* [129,130,140]. This research group adopted Gadolinium-based contrast agent, since the minimum photon energy sensitive to the CZT detector (26 keV), prevented from exploring the iodine K-edge (33.2 keV), due to low X-ray quanta detected in the small energy bin ($25 - 33.2\ keV$). As far as we know, by the beginning of this PhD thesis research, no further studies had been carried to assess the feasibility of dual-energy recombination for iodine-enhanced breast CT technique.

In a 3D dual-energy X-ray imaging system framework, the main components and parameters in the imaging chain impacting dose-dependent detectability can be classified into two main groups: 1) energy-independent components defining spatial resolution and noise propagation (*e.g.* system topology, acquisition orbit, detector noise characteristics, reconstruction and post-processing methods) and 2) energy-dependent parameters (*e.g.* breast tissue attenuation, scattered radiation, detector energy-dependent efficiencies, DE acquisition parameters and recombination algorithm).

The first group of parameters influencing image quality has been intensively studied for single-energy breast CT. In particular, the effect of system topology [119–123], acquisition orbit [118, 136, 137], detector efficiency [123, 129, 130, 135] and reconstruction algorithms [133, 134, 238] on the detectability of fibroglandular tissue and microcalcifications have been object of investigation. They will not be further discussed in this chapter.

The second group of parameters is within the main topic of this chapter. Herein, we focus on the evaluation and the optimization of energy-dependent parameters impacting the image quality of dual-energy Contrast-Enhanced breast CT (CE-bCT). The study was performed through the assessment of dose-dependent detectability of vascular contrast agent in simulated iodine-equivalent images, as well as the dose-dependent detectability of fibroglandular tissue and microcalcifications in simulated morphological images.

In this chapter, design factors impacting X-ray system spatial resolution and energy-independent noise propagation were disregarded. Accordingly, idealistic hypothesis for the source and detector

efficiency were made, and a linear reconstruction algorithm was adopted. In this framework, the energy-dependent parameters influencing image quality and subject of the optimization studies of this chapter were identified by analyzing the energy-dependent terms of the equation describing the formation of X-ray images (cf. Annex A for further details on the principles of X-ray image formation):

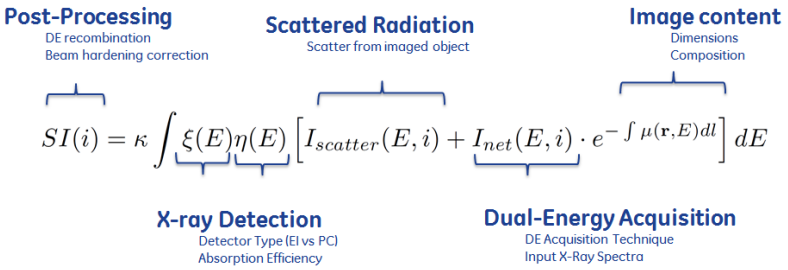

where κ is a scaling factor, $\xi(E)$ is the detector conversion response, $\eta(E)$ is a function translating an eventual energy-dependent efficiency in detecting photons, $I_{net}(E,i)$ is the X-ray intensity spectrum generated by the X-ray source s and towards the detection element i (calculated from the fluence $S_{net}(E,i)$ and the detector element surface), $\mu(\mathbf{r},E)$ is the linear attenuation coefficient of the imaged breast at energy E and position $\mathbf{r}$ in its volume, dl is the incremental thickness of the traversed breast in the path $s-i$ and $I_{scatter}(E)$ is the X-ray intensity spectrum incident over the detector element surface resulting from photon scattering (estimated from Monte Carlo simulations).

In Section 5.1, the critical factors to image quality and optimization criteria translating the key clinically relevant factors for breast cancer diagnosis, staging and therapy follow-up are defined. In Section 5.2, a detailed description on the simulated cone-beam CT geometry and parameters used throughout this chapter is provided. In Section 5.3, low-energy (LE) and high-energy (HE) monochromatic spectra and average glandular dose distribution between the LE and HE acquisitions are optimized. In Section 5.4, the optimal monochromatic spectra are used as a first approximation for the optimal acquisition parameters in a polychromatic source scenario. Different dual-energy acquisition strategies are considered and individually optimized (dual-source, dual kVp, energy-discriminating detector, ...). In order to have a glimpse on the impact of their practical implementation constraints in the optimization results, the performance of the different acquisition strategies is compared in Section 5.5. Finally, in Section 5.6, a spectral optimization study considering different columnar structured Cesium Iodide (CsI) scintillators thicknesses and, as consequence, energy-dependent absorption efficiencies is performed.

In all these experiments, X-ray scatter was disregarded. As shown by Glick *et al.* [163] and as confirmed in the experiments presented in Annex C, image quality degradation (in terms of contrast-to-noise ratio) due to X-ray scattering has little energy-dependency and would not have significant influence on the optimization studies of this chapter.

5.1 Optimization Critical-to-Quality Factors

As briefly described in Chapter 1 and mathematically formalized in Chapter 4, spectral techniques for iodine-enhanced breast X-ray imaging enable to obtain functional iodine-enhanced images in which the signal intensity is proportional to the quantity of iodine in breast tissues. These images provide functional information on breast vascularity and highlight breast tumor angiogenesis. In the case of a dedicated breast CT, the iodine-equivalent images are tomographically reconstructed slices of the breast, with signal intensities proportional to the volumetric iodine concentration inside each unit of volume. An optimal dual-energy system is therefore the one which provides the best image quality in iodine-equivalent images while minimizing the total radiation dose delivered to the patient.

In addition to functional images, it is also of great interest to provide additional morphologic images which are spatially correlated to the functional images. They provide complementary morphologic information on the mammary gland and eventual cancerous lesions, allowing to depict asymmetrical breast tissues and density differences between the two breasts, architectural distortions, unenhanced masses, microcalcifications clusters and other typical and relevant mammographic findings during breast cancer screening. The morphological images can be defined as either the reconstructed LE or HE volumes, or in some cases be found by an optimal combination of LE and HE data[1].

Accordingly, we define the Dual-Energy Contrast-Enhanced breast CT (CE-bCT) application as the technique which, departing from two spectrally separated acquisitions, provides an iodine-equivalent volume containing functional information on tumor angiogenesis, as well as a morphologic volume containing morphological information on the mammary gland, masses and microcalcifications. The iodine-equivalent volume is obtained from the recombination of low-energy (LE) and high-energy (HE) acquisitions. The morphologic volume is defined as the tomographic reconstructed LE volume. The process in summarized in Figure 5-1.

[1]When LE and HE acquisitions have sufficient spatial correlation (either on image or projection domain), they can also be recombined into a morphologic volume in which the detectability of fibroglandular tissue is optimal. In spectral CT literature, this process is often referred as *Energy Weighting* for soft-tissue [129, 131, 237, 239] and can be used, in the present three-material decomposition problem, to enhance fibroglandular tissue depiction or mask the iodine-uptake, as in Virtual Unenhanced CT techniques [232, 240, 241]. Energy-Weighting for breast morphologic image was not addressed in this PhD thesis research.

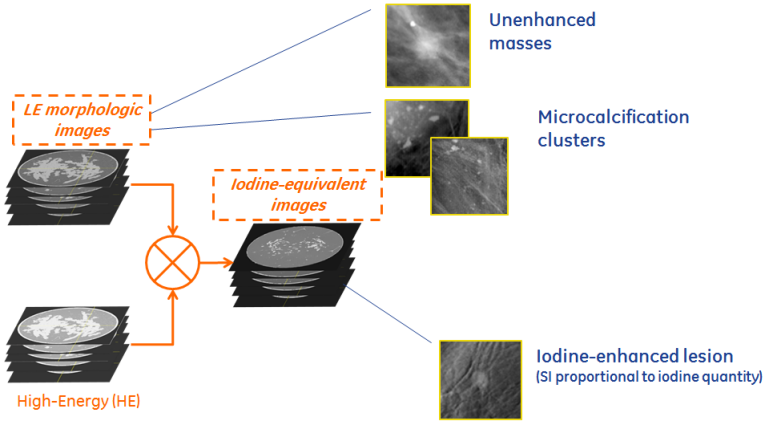

Figure 5-1: Optimization *Critical-to-Quality* (CTQ) factors

5.1.1 IQ Assessment in Recombined Iodine-Equivalent Images

Given the medical application just described, in this chapter the quality of recombined iodine-equivalent images was evaluated through the detectability of iodine-enhanced lesions as well as the detectability of the residual background texture (*i.e.* the anatomical noise). Image quality is therefore optimal when maximizing the detectability of iodine uptake while ensuring optimal cancellation of the residual texture (cancellation of the background texture caused by soft tissue differential attenuation).

Spatial resolution effects on detectability are out of the scope of this chapter. Therefore, Contrast-to-Noise Ratio (CNR) was chosen as the metric to assess iodine uptake detectability in a given region of interest. CNR has been shown to be a measure of detectability under specific experimental conditions [242, 243].

Dose-Dependent Iodine Detectability
Contrast-to-noise ratio per pixel between iodine-enhanced breast tissue and the background normalized to the square root of the total AGD (CNRD) was used as the figure of merit for dose-dependent iodine detectability in the iodine-equivalent images f_{iodine}:

$$CNRD_{iodine-bg} = \frac{SI_{iodine} - SI_{bg}}{\sigma_{bg}\sqrt{AGD_{LE+HE}}} \tag{5.1}$$

where SI_{iodine} and SI_{bg} are respectively the mean per-pixel signal intensity (SI) in an iodine-enhanced region of interest (ROI) and a non-iodine enhanced neighboring background ROI, σ_{bg} is the standard deviation of the SI in the non-iodine enhanced neighboring breast background ROI and AGD_{LE+HE} is the sum of AGD delivered during LE and HE acquisitions (AGD_{LE} and AGD_{HE}, respectively).

To assess background texture cancellation in iodine-equivalent images f_{iodine}, CNRD values between non-iodine-enhanced fibroglandular and adipose tissue were calculated as:

$$CNRD_{texture} = \frac{SI_{gland} - SI_{adipose}}{\sigma_{adipose}\sqrt{AGD_{LE+HE}}} \tag{5.2}$$

where SI_{gland} and $SI_{adipose}$ are the mean per-pixel SI in a ROI containing unenhanced fibroglandular and adipose tissues, respectively, and $\sigma_{adipose}$ is the standard deviation of the SI in an ROI containing adipose tissue.

Cupping artifact in the reconstructed iodine-equivalent images f_{iodine} was quantified as another quality metric. Cupping was estimated as the difference in mean per-pixel SI between circular ROIs at the breast phantom center position, SI_{center}, and the phantom's edge, SI_{edge}, normalized by the contrast between the iodine-enhanced ROI and the unenhanced background ROI (Equation 5.1):

$$cupping(\%) = 100 \times \frac{SI_{edge} - SI_{center}}{SI_{iodine} - SI_{bg}} \tag{5.3}$$

Iodine Concentrations Expected in Clinical Practice
The target iodine concentrations to be detected were calculated assuming typical injection protocols of contrast-enhanced CT and mammography [97,244,245], *i.e.* a contrast agent with concentration[2] C_{agent} = 270 to 370 $mg\ I/mL$, injected at d = 1.0 to 1.5 mL/kg of body weight. By assuming

[2]values are based on commonly used non-ionic iodinated contrast media: iopromide 300 and 370 (Ultravist®, Bayer Health Care Pharmaceuticals; Berlin, Germany); iodixanol 270 and 320 (Visipaque®, GE Healthcare; Chalfont St Giles, UK); iohexol 270, 300, 320 and 350 (Omnipaque®, GE Healthcare; Chalfont St Giles, UK); iopamidol 300 and 370 (Isovue®, Bracco Diagnostics Inc.; Princeton, NJ, USA)

complete dissolution of iodine in the patient's body volume, we calculated the minimum iodine concentration expected in clinical practice:

$$C_{lesion,min} = \frac{\text{mass of iodine}}{\text{patient volume}} = \frac{C_{agent} \cdot d \cdot M}{1000 \cdot M/\rho_{tissue}} \approx 0.27 \ - \ 0.5 \ mg/cm^3 \tag{5.4}$$

where M is the patient body weight.

Using similar reasoning, the maximum iodine concentration would be achieved when the injected contrast agent is concealed within the patient's blood only. In this case, for an average patient with $M = 70\ kg$ and $V = 5\ L$ of blood, we have:

$$C_{lesion,max} = \frac{\text{mass of iodine}}{\text{patient blood volume}} = \frac{C_{agent} \cdot d \cdot M}{V} \approx 4.2 \ - \ 7.7 \ mg/cm^3 \tag{5.5}$$

Target Iodine-Enhanced Lesion Size and Concentration
For the remainder of this PhD thesis, we consider a 2 mm diameter lesion as the minimum lesion size to be detected in a contrast-enhanced breast imaging setup. We assume 2 mm to be the smallest tumor size for which the angiogenesis phenomenon manifests (cf. Section 1.1 for details on breast anatomy and cancer development).

Additionally, from Equations 5.4 and 5.5 above, we consider 0.5 mg/cm^3 and 5.0 mg/cm^3 as the minimum and maximum iodine uptakes expected in clinical practice, respectively.

Measurement of Detectability for the Target Iodine-Enhanced Lesion
As a measure of detectability for the target iodine-enhanced lesion, effective CNR (CNR_{eff}) between lesion contrast uptake and a homogeneous background in recombined iodine-equivalent images f_{iodine} was calculated for a given AGD level, as defined by Rose [246, 247]:

$$CNR_{eff} = \frac{SI_{iodine} - SI_{bg}}{\sigma_{bg}} \times \sqrt{\text{lesion area in pixels}} \tag{5.6}$$

where SI_{iodine} and SI_{bg} are respectively the mean per-pixel SI in an iodine-enhanced region of interest (ROI) and a non-iodine enhanced neighboring background ROI, and σ_{bg} is the standard deviation of the SI in the non-iodine enhanced neighboring breast background ROI. Rose's threshold for minimum lesion depiction is achieved for CNR_{eff} values above 5.

For an average-sized breast (5 cm-thick compressed breast, corresponding to a 14 cm diameter uncompressed breast [162]), we considered a practical AGD operating point at 3 mGy, which corresponds approximately to the screening AGD for a two-view breast using the AOP[3] Contrast mode of GE Senographe® Essential system [248]. Note that 3 mGy is about half the radiation dose accepted by the European Union[4] and the American College of Radiology (ACR) guidelines for two-view mammography screening. Moreover, it is likely that CE-bCT will not be used for screening examinations but rather for diagnosis purposes. Therefore, higher AGD levels may be acceptable.

5.1.2 IQ Assessment in LE Morphologic Images

The quality of morphologic images was evaluated through the detectability of unenhanced fibroglandular tissue in adipose background as well as the detectability of microcalcifications in fibroglandular background. As before, the criterion used to assess the detectability in a given region of interest was the Contrast-to-Noise Ratio (CNR) per pixel. Image quality in morphological images

[3] AOP – Automatic Optimization of Parameters for exposure control system
[4] EUREF – European Guidelines for Quality Assurance in Breast Cancer Screening and Diagnosis

is therefore optimal when maximizing CNR values between fibroglandular and adipose tissues, as well as CNR values between microcalcification and fibroglandular tissue.

In this PhD thesis, eventual differences in contrast between healthy fibroglandular tissue and tumors were not considered. Although Johns and Yaffe [249] showed slight differences in linear attenuation coefficients between fibroglandular and tumor tissues, it remains unclear whether tumors can actually be detected by contrast differences in morphologic breast CT images [107], at least not without the aid of vascular contrast agents, as previously demonstrated by Prionas *et al.* [138]. Moreover, using Johns and Yaffe attenuation coefficients, Chen and Ning [104] demonstrated in a spectral optimization study that maximum CNRD values for carcinoma and fibroglandular inserts embedded in a 50% fibroglandular background are found at 32 and 31 keV, respectively, *i.e.* with only 1 keV difference. Hence, for the optimizations studies of this chapter, we assumed the measurement of fibroglandular tissue depiction as a good first approximation for unenhanced breast masses detectability in LE morphologic images.

Microcalcification and Mass Detectability

CNRD between microcalcifications and fibroglandular tissue, $CNRD_{\mu Cal-gland}$, and between fibroglandular and adipose tissues, $CNRD_{gland-adipose}$, were used as Figures-of-Merit assessing respectively microcalcification and mass tissue detectability in the LE morphologic images:

$$\begin{cases} CNRD_{\mu Cal-gland} = \dfrac{SI_{\mu Cal} - SI_{gland}}{\sigma_{gland}\sqrt{AGD_{LE+HE}}} \\ CNRD_{gland-adipose} = \dfrac{SI_{gland} - SI_{adipose}}{\sigma_{adipose}\sqrt{AGD_{LE+HE}}} \end{cases} \tag{5.7}$$

where $SI_{\mu Cal}$, SI_{gland}, $SI_{adipose}$ are the means per-pixel SI in an ROI containing unenhanced microcalcifications, fibroglandular and adipose tissues, respectively, and σ_{gland} and $\sigma_{adipose}$ are the standard deviation of the SI in fibroglandular and adipose tissues, respectively.

5.2 Cone-Beam Breast CT Acquisition Geometry

In this chapter, a cone-beam breast CT topology similar to that described by Boone *et al.* [103] was adopted as the main geometry and starting point for all simulations. With the woman in prone position, the uncompressed breast was modeled as a cylinder with diameter D and height equal to three-quarters of its diameter ($3D/4$) [162]. The cylinder's central axis was positioned at 46 cm from the source and such that the beam ray normal to the detector passed through the top of the cylinder. Figure 5-2 illustrates and summarizes the cone-beam topology.

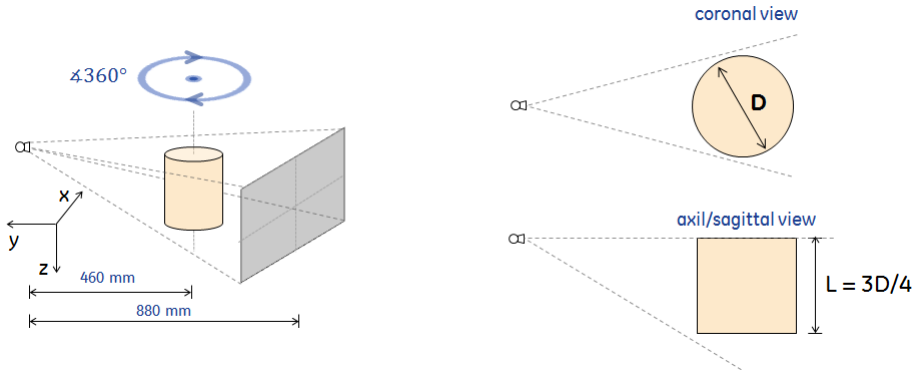

Figure 5-2: Cone-Beam CT geometry used in dual-energy CE-bCT spectra optimization

The source was considered an isotropic emitting point, positioned at 88 cm from a flat detector, such as to make a half cone-beam geometry. The detector pixel pitch was set to 776 μm (4x4 binning), with total matrix size chosen to be wide enough to accommodate the irradiated phantom in its FOV. As previously discussed, a throughout evaluation of the detector technology impact on DE-bCT image quality is not in the scope of this PhD thesis research. Hence, unless otherwise specified, the flat detector was considered to be a perfect detector, with perfect efficiency in collecting and transforming X-ray photons into electronic signal, without suffering from optical scattering or spectral distortions inherent of its technology (either energy-integrating or photon-counting). For more information on X-ray detector technologies and performances, we refer the reader to the work of Yaffe and Rowlands [250] (digital radiography), or Yaffe and Mainprize [251] (digital mammography).

The acquisitions were simulated assuming a "step-and-shoot" mode, and the time interval for one view integration is considered for exposure calculation (*i.e.*, mAs values). The X-ray tube and the detector rotated over a full angular sampling range of the object (360°). Tube voltage switching during rotation was assumed to be ideally performed, *i.e.* with instantaneous transition between LE and HE tube voltage values.

Between three and six hundred analytical projections were simulated for each LE and HE scans, depending on the phantom size. Tomographic reconstruction was carried with the standard Filtered BackProjection (FBP) algorithm, with an ideal ramp filter and distance-driven interpolation [252], to obtain 512×512 coronal images with 0.41×0.41 mm^2 pixel size, and 1 mm slice thickness. Detection element and voxel sizes, as well as the number of projections views have no energy-dependent impact on dose-dependent detectability. They were chosen to keep simulation time manageable and to provide good noise estimation at all considered spectra.

As shown by Glick *et al.* [163], X-ray scattering in a single-energy acquisition has a moderate effect on absolute lesion CNR value. However, the authors showed that CNR degradation has little energy-dependency. In Ref. [163], this result was illustrated for a full cascade system analysis of a 600 μm-thick CsI:Tl-based flat detector, including optical spreading, K-fluorescence, energy-dependent QDE, and other inefficiencies. This observation was verified to be also valid for the

cone-beam CT geometry exploited in this PhD thesis research work. A detailed study is described in the Annex C (cf. Figure C-4c and C-5 for an illustration of the impact of scattered radiation on CNR as function of the monochromatic beam energies, with additional published data from Ref. [163]). Accordingly, we assumed henceforth that X-ray scattering has little effect on spectra optimization for dual-energy CE-bCT, and was therefore further disregarded.

5.3 Monochromatic Spectra Optimization

In this section, simulations are performed to optimize the low-energy (LE) and high-energy (HE) monochromatic spectra and the average glandular dose (AGD) repartitioning between the LE and HE acquisitions to obtain optimally enhanced iodine and morphological images. The analysis is performed for small, average and large 50% fibroglandular equivalent breast phantoms, containing iodine-enhanced inserts, as well as inserts with various fibroglandular equivalent compositions, representing masses, and calcium hydroxyapatite, emulating calcifications.

Monochromatic spectra optimization is a preliminary step in our study. It provides a first approximation on the design of optimal acquisition parameters in a polychromatic spectra scenario, where it is desirable to generate low and high-energy polychromatic spectra with effective energies as close as possible to optimal monochromatic energy pairs. Polychromatic optimization will be discussed in Section 5.4.

5.3.1 Optimization Method

Breast Phantom and X-ray Image Simulation
The cone-beam CT geometry described in Section 5.2 and illustrated in Figure 5-2 was simulated. Three 50% fibroglandular equivalent cylindrical phantoms with diameter D measuring 10, 14 and 18 cm and heights equal to three-quarters of their diameter ($3D/4$) were simulated to mimic small, average and large uncompressed breasts, when the woman is in prone position [162]. Although a 50% fibroglandular assumption does not represent the average breast density [253], for this preliminary monochromatic study, the 50-50 hypothesis allowed to verify that our results are in agreement with previously published investigations (glandular dose estimation [112], scattered radiation [114, 163], mass and microcalcification detectability [116], ...). Eight 10 mm diameter spherical inserts emulating 0, 25, 75 and 100% fibroglandular equivalent tissues as well homogeneous mixtures of 50% fibroglandular tissue and 0.5, 1.0, 2.5 and 5.0 mg/cm^3 of iodine, were distributed in the horizontal plane at mid-depth of the cylinder (cf. Figure 5-3a). An iodine concentration of 0.5 mg/cm^3 was assumed to be the minimum iodine concentration expected clinically if a typical injection protocol of contrast-enhanced mammography is considered (cf. Section 5.1). A CaHA (calcium hydroxyapatite) sphere, simulating microcalcifications composition, was positioned at the cylinder's axis but at a different height.

X-ray projections and tomographic reconstruction were simulated as described in Section 5.2. Simulated low and high energy volumes $\tilde{\mu}^{LE}(\mathbf{r})$ and $\tilde{\mu}^{HE}(\mathbf{r})$, respectively, were recombined using the dual-energy image-based recombination algorithm for three-material decomposition problem described in Chapter 4, such as to produce iodine-equivalent slice images, $f_{iodine}(\mathbf{r})$.

Figure 5-3b illustrates a scatter plot representing the SI in the HE and LE reconstructed images. SI from non-iodine enhanced breast tissue and iodine-enhanced breast tissue are distributed around the linear fit $\mathcal{L}_1$ and $\mathcal{L}_2$ respectively. The angle θ between $\mathcal{L}_1$ and $\mathcal{L}_2$ can be used to evaluate material separation and breast tissue cancellation in the iodine-equivalent images. In literature, studies have used θ as a Figure-of-Merit for spectra optimization [254,255], especially when contrast and average signal intensities are difficult to measure, *e.g.* in iodine-bone separation [256]. It can be in some cases normalized by a given definition of noise and provide signal-to-noise ratio as metric. In this investigation however, we assessed θ only as reference metric.

AGD was estimated using the Monte Carlo simulator described in Section 2.6. Two millions photons (2×10^6) undergoing Rayleigh, Compton and photoelectric interactions were tracked in $2 \times 2 \times 2\ mm^3$ voxels. The deposited energy was tallied and corrected to account for the glandular part of the breast only [189, 190]. AGD was calculated in mGy and normalized to 1 mGy of air kerma at the isocenter, forming Normalized Glandular Dose (DgN) coefficients. Since the spectral optimization is independent of the total AGD, mAs values were adjusted to provide an ad hoc total AGD of 100 mGy to avoid any artifacts attributed to a lack of quanta (*e.g.* streaks).

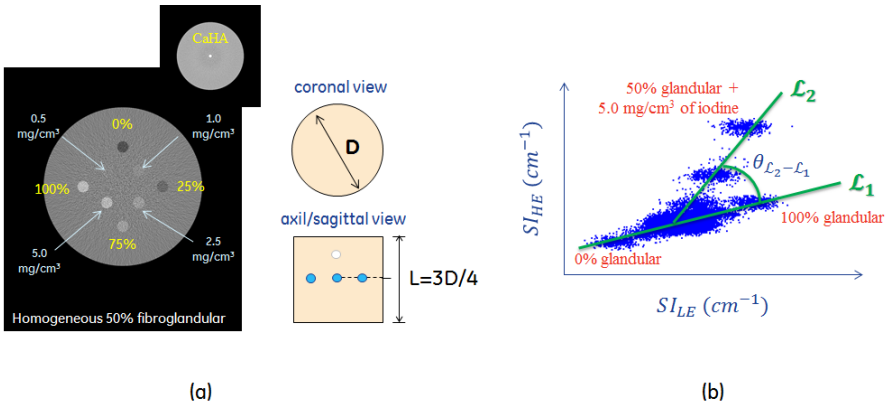

Figure 5-3: (a) Slice of the cylindrical phantom containing different inserts used for dual-energy CE-bCT spectra optimization; (b) example of scatter plot between the signal intensity in HE vs LE images

Optimization Criteria

As described in Section 5.2, CNRD between iodine-enhanced breast tissue and unenhanced background breast tissue ($CNRD_{iodine-bg}$) was used as the figure of merit for dose-dependent iodine detectability in the iodine-equivalent images $f_{iodine}(\mathbf{r})$ and was calculated following Equation 5.1.

Assuming quantum noise only, the standard deviations of the SI in LE and HE images are inversely proportional to $\sqrt{AGD_{LE}}$ and $\sqrt{AGD_{HE}}$, respectively (Poisson distribution). Let $\tau = AGD_{LE}/AGD_{LE+HE}$ be the LE dose allocation ratio, *i.e.*, the fraction of the total AGD allocated to the LE image. It can be derived that:

$$\sigma_{bg}^2 \propto \frac{A}{AGD_{LE}} + \frac{B}{AGD_{HE}} \longrightarrow CNRD_{iodine-bg}^2 \propto \frac{\tau(1-\tau)}{(B-A)\tau + A} \tag{5.8}$$

where A and B are proportionality constants. Equation 5.8 shows that $CNRD_{iodine-bg}$ is independent of the total AGD and depends only on the AGD_{LE}/AGD_{HE} repartitioning [257].

CNRD between microcalcifications and fibroglandular tissue, $CNRD_{\mu Cal-gland}$, and between fibroglandular and adipose tissues, $CNRD_{gland-adipose}$, were respectively used as figures of merit assessing microcalcification and mass detectability in the LE morphologic images. They were calculated as described by Equation 5.7.

Since monochromatic X-ray beams only are considered, projections images are free from the effects of beam-hardening. Moreover, assuming primary X-ray photons only, no cupping was introduced from scattered radiation. Therefore, reconstructed iodine-equivalent images are cupping-free and the dual-energy recombination provides perfect texture cancellation.

5.3.2 Research Space and Data Analysis

$CNRD_{iodine-bg}$ was calculated in the iodine-equivalent volume for beam energies varying from 20 to 80 keV, at 5-10 keV steps and at 1 keV step near the iodine K-absorption edge (33.2 keV). For each LE and HE X-ray beam pair, LE dose allocation ratio was varied between 20% and 80% at 5-10% steps. $CNRD_{iodine-bg}$ was evaluated as a function of the LE dose allocation ratio τ. Optimal LE dose allocation ratio, τ_{opt}, *i.e.* maximizing $CNRD_{iodine-bg}$ was identified for each LE/HE pair.

Figure 5-4 illustrates the simulated Normalized Glandular Dose (DgN) coefficients as function of the X-ray beam energy, for the 10, 14 and 18 cm diameter phantoms. In the energy range

considered for the spectra optimization, DgN values are very low before 20 keV since most photons are stopped at the breast periphery. They increase rapidly after 20 keV due to the higher beam penetration and higher scatter production. Finally, DgN values increase slowly at higher energies, since most energy is transmitted through the phantom and the absorbed dose increases at the same pace as the Air Kerma.

To ensure the best image quality in recombined iodine-equivalent images, $CNRD_{\mu Cal-gland}$ and $CNRD_{gland-adipose}$ were computed for τ_{opt}. As a consequence, the LE/HE spectra pairs accounting simultaneously for maximum $CNRD_{iodine-bg}$, $CNRD_{\mu Cal-gland}$ and $CNRD_{gland-adipose}$ ensure the best trade-off in image quality for both iodine-equivalent and morphologic images.

Figure 5-5a illustrates for three different energy pairs, $CNRD_{iodine-bg}$ as function of LE dose allocation ratio τ. Figure 5-5b and 5-5c illustrates $CNRD_{\mu Cal-gland}$ and $CNRD_{gland-adipose}$, respectively, as function of LE dose allocation ratio τ. A squared root dependency was found since $CNRD_{\mu Cal-gland}$ and $CNRD_{gland-adipose}$ as function of $\sqrt{\tau}$.

A 2nd degree polynomial (for $CNRD_{iodine-bg}$) and a squared root function (for $CNRD_{\mu Cal-gland}$ and $CNRD_{gland-adipose}$) were used to the fit all simulated data as a function of LE dose allocation ratio. This entailed in a better estimation of the optimal LE dose allocation ratio τ_{opt} and the corresponding CNRD values. For all experimental conditions, fitness coefficients (R^2) values were larger than 0.95.

5.3.3 Optimal Spectra and Dose Allocation

Optimal Spectra and Dose Allocation for Iodine Uptake Depiction
Figures 5-6a, 5-7a and 5-8a show the optimal LE dose allocation ratio, τ_{opt}, i.e. providing maximum CNRD in iodine-equivalent images, as a function of LE and HE pairs for 10 cm, 14 cm and 18 cm diameter phantoms, respectively. Optimal LE dose allocation ratio, τ_{opt}, varies around 50% for a large range of LE and HE pairs, and is in general higher for thicker phantoms. Optimal LE dose allocation ratio increases rapidly for LE smaller than $\sim$ 25 keV, such as to compensate the lack of transmitted quanta, and decreases slowly with increasing HE values.

Figures 5-6b, 5-7b and 5-8b show $CNRD_{iodine-bg}$ at τ_{opt}, as a function of LE/HE pairs and for all phantom diameters. $CNRD_{iodine-bg}$ was computed considering an iodine-enhanced lesion containing 5.0 $mg\ I/cm^3$. This choice was meant to ensure accurate CNRD estimation for all simulation points, especially in the presence of low lesion contrast and high quantum noise. For all phantom diameters, $CNRD_{iodine-bg}$ is higher for LE and HE pairs just below and above the iodine K-edge, than for LE and HE pairs with energies farther away from the iodine K-edge discontinuity.

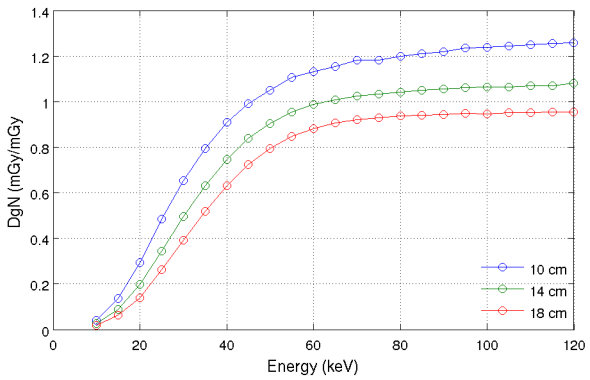

Figure 5-4: DgN coefficients as function of the incident monochromatic beam energy for the 10, 14 and 18 cm diameter phantoms

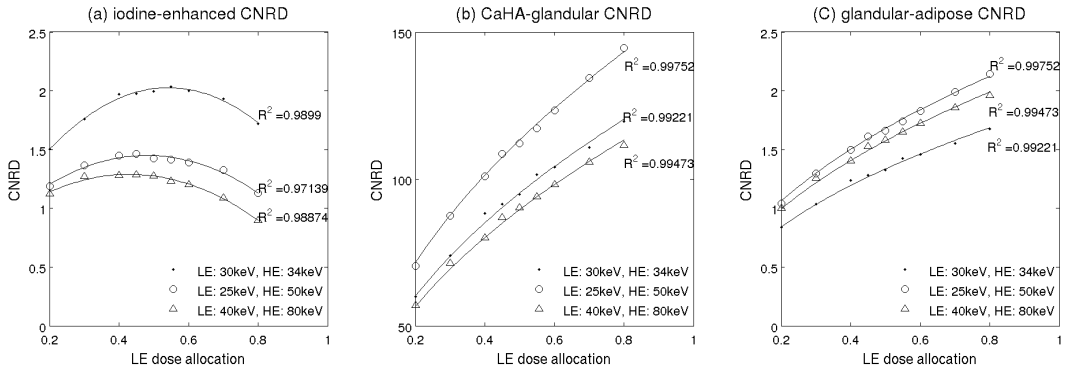

Figure 5-5: Illustration of (a) $CNRD_{iodine-bg}$, (b) $CNRD_{\mu Cal-gland}$ and (c) $CNRD_{gland-adipose}$ as function of LE dose allocation ratio τ. Markers represent simulated data; solid lines represent 2nd degree polynomial or squared root function fits

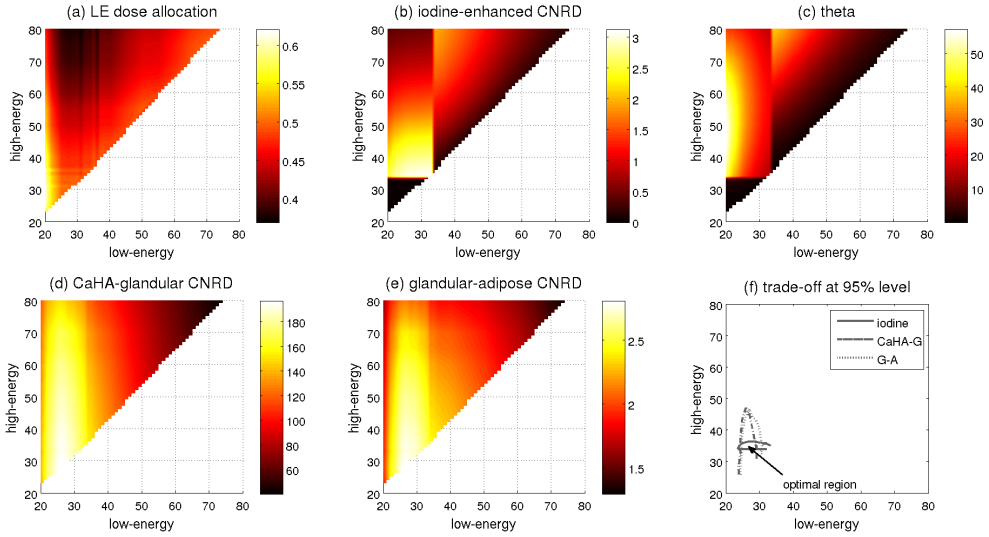

Figure 5-6: Monochromatic spectra optimization results for 50% fibroglandular-equivalent 10 cm diameter phantom. (a) Optimal LE dose allocation ratio τ_{opt}; (b) $CNRD_{iodine-bg}$ at τ_{opt}; $CNRD_{iodine-bg}$ computations were performed for iodinated lesions with 5 $mg\ I/cm^3$; (c) resulting angle θ; (d) $CNRD_{\mu Cal-gland}$ and (e) $CNRD_{gland-adipose}$ at τ_{opt}; (f) isocontours within which $CNRD_{iodine-bg}$ (iodine), $CNRD_{\mu Cal-gland}$ (CaHa-G) and $CNRD_{gland-adipose}$ (G-A) exceed 95% of their maxima

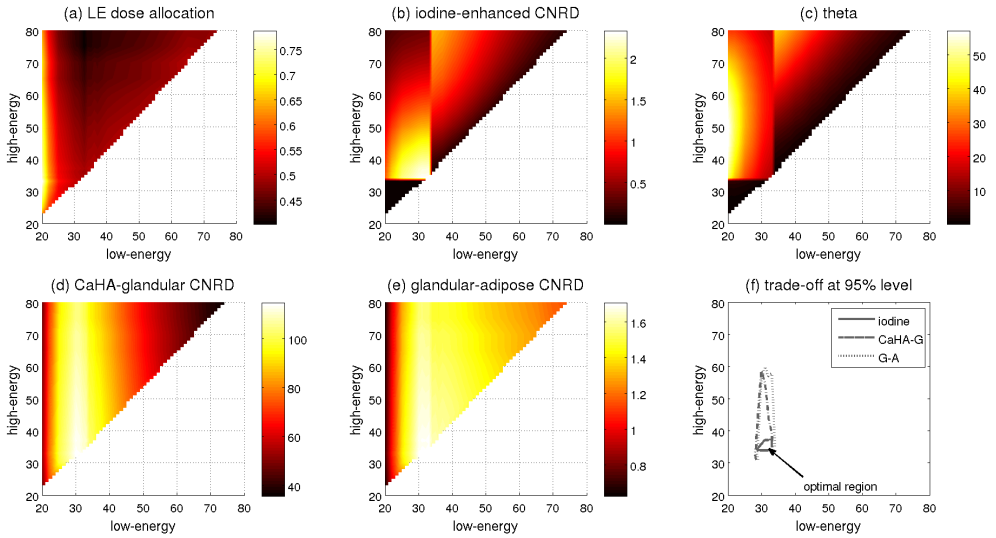

Figure 5-7: Monochromatic spectra optimization results for 50% fibroglandular-equivalent 14 cm diameter phantom. (a) Optimal LE dose allocation ratio τ_{opt}; (b) $CNRD_{iodine-bg}$ at τ_{opt}; $CNRD_{iodine-bg}$ computations were performed for iodinated lesions with 5 $mg\ I/cm^3$; (c) resulting angle θ; (d) $CNRD_{\mu Cal-gland}$ and (e) $CNRD_{gland-adipose}$ at τ_{opt}; (f) isocontours within which $CNRD_{iodine-bg}$ (iodine), $CNRD_{\mu Cal-gland}$ (CaHa-G) and $CNRD_{gland-adipose}$ (G-A) exceed 95% of their maxima

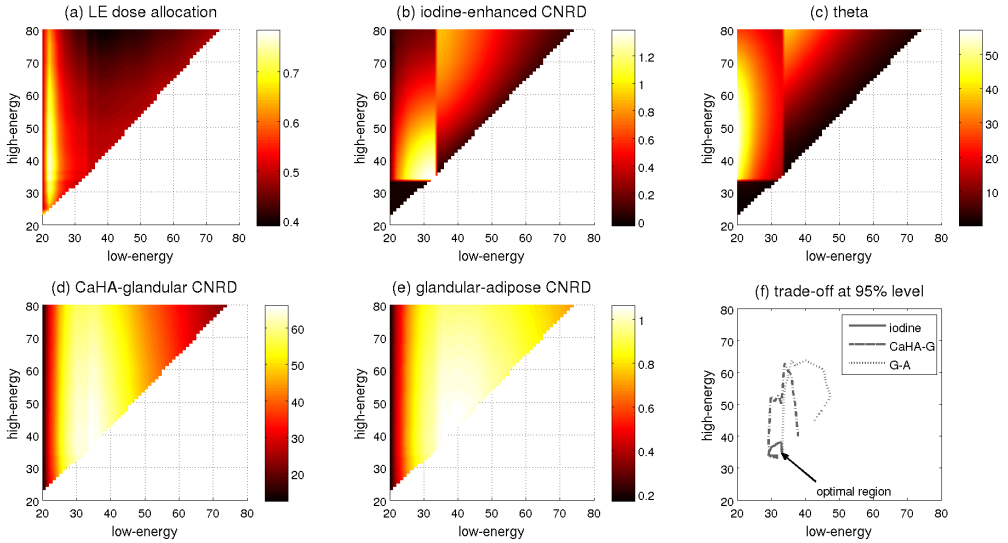

Figure 5-8: Monochromatic spectra optimization results for 50% fibroglandular-equivalent 18 cm diameter phantom. (a) Optimal LE dose allocation ratio τ_{opt}; (b) $CNRD_{iodine-bg}$ at τ_{opt}; $CNRD_{iodine-bg}$ computations were performed for iodinated lesions with 5 $mg\ I/cm^3$; (c) resulting angle θ; (d) $CNRD_{\mu Cal-gland}$ and (e) $CNRD_{gland-adipose}$ at τ_{opt}; (f) isocontours within which $CNRD_{iodine-bg}$ (iodine), $CNRD_{\mu Cal-gland}$ (CaHa-G) and $CNRD_{gland-adipose}$ (G-A) exceed 95% of their maxima

For small, average and large diameter phantoms, maximum $CNRD_{iodine-bg}$ values are obtained at 33keV/34keV LE/HE pairs.

Figures 5-6c, 5-7c and 5-8c show the angle θ, as a function of LE/HE pairs. Notice that since the reconstructed images are free from beam-hardening, θ is independent of the phantom diameter. Similar to $CNRD_{iodine-bg}$ results, θ is higher for LE and HE pairs below and above the iodine K-edge, respectively. In this energy range, θ increases with decreasing LE beam energy, and is maximum for ∼50 keV HE beam energy. Therefore, optimal LE and HE beam energies based on $CNRD_{iodine-bg}$ and θ evaluation does not coincide, mainly because θ does not takes into account image noise.

Optimal Spectra and Dose Allocation for μCal and Mass Depiction

Figures 5-6d, 5-7d and 5-8d show $CNRD_{\mu Cal-gland}$ calculated in the morphologic images at τ_{opt}. Figures 5-6e, 5-7e and 5-8e show $CNRD_{gland-adipose}$ calculated in the morphologic images at τ_{opt}. For average and large diameter phantoms, $CNRD_{\mu Cal-gland}$ and $CNRD_{gland-adipose}$ are characterized by a broad maximum as a function of LE, although the values decline rapidly for small LE values. Maximum $CNRD_{\mu Cal-gland}$ and $CNRD_{gland-adipose}$ values for small, average and large diameter phantoms are obtained for the LE ranges summarized in Table 5.1. These results are concordant with a previously published optimization study carried by Weigel *et al.* [116], in which optimal monochromatic spectra for single-energy morphologic bCT images were evaluated.

Optimal Trade-Off for Iodine-Equivalent and Morphological Images

Figures 5-6f, 5-7f and 5-8f show the isocontour lines of $CNRD_{iodine-bg}$, $CNRD_{\mu Cal-gland}$ and $CNRD_{gland-adipose}$ at 95% of their maximum value, for all investigated LE/HE pairs. Based on the intersection of the isocontours, 27keV/34keV, 30keV/34keV and 33keV/34keV LE/HE pairs were found to provide a good compromise in performance for iodine, microcalcification and mass detectability in small, average and large diameter phantoms, respectively. For these LE/HE spectrum pairs, τ_{opt} was approximately equal to 50%.

As a measure of detectability for the target iodine-enhanced lesion (2 mm diameter, 0.5 mg/cm^3 iodine uptake) in a homogeneous background (cf. Section 5.1 and Equation 5.6), effective CNR (CNR_{eff}) between lesion contrast uptake and a homogeneous background was calculated as defined by Rose [246, 247] using $CNRD_{iodine-bg}$ values at a given AGD level. For the 14 cm diameter phantom, we consider 3 mGy AGD comparable to the screening AGD for a two-view breast of average thickness (AOP Contrast mode on GE Senographe® Essential system, for a 5 cm-thick PMMA). In this case, for the acquisition geometry considered in this chapter (cf. Section 5.2) and if a Hamming apodization function is included to the reconstruction ramp filter[5], we obtain at optimal LE and HE beam energies $CNR_{eff} \approx 5.1$, *i.e.* just above the Rose's detectability threshold of 5.

Table 5.1 summarizes the optimal acquisition spectra for all phantom sizes.

Table 5.1: Summary of optimal monochromatic acquisition spectra for different 50% fibroglandular-equivalent phantom diameters. Energy values were estimated using the isocontour lines of CNRD surfaces, plotted in Figures 5-6f, 5-7f and 5-8f. The results are based on 50% glandular phantoms and CNRD values computed relative to the 5 mg/cm^3 iodine-enhanced lesion

	Iodine Imaging			**CaHA-Gland.**	**Gland.-Adipose**
Phantom Diam. (cm)	LE/HE En. Pair (keV)	AGD repart. LE/HE	CNRD	Optimal LE (keV)	Optimal LE (keV)
10	33/34	49/51%	3.13	25–27	25–29
14	33/34	50/50 %	2.38	28–32	30–34
18	33/34	51/49%	1.41	30–38	34–44

[5]The ideal ramp alone would generate unrealistic noise levels, due to high-frequency signal amplification

5.3.4 Discussion

This section illustrated the optimal monochromatic spectra for dual-energy subtraction cone-beam breast CT. Under the assumptions of primary monochromatic X-rays and a perfect energy-integrating noise-free blur-free detector, the monochromatic LE and HE spectra and the AGD repartitioning between the LE and HE acquisitions providing optimally enhanced iodine-equivalent and morphological images were presented.

Under the hypothesis of this study, to obtain maximum iodine detectability in iodine-equivalent images, LE and HE spectra need to bracket the iodine K-edge and an approximate 50%-50% AGD repartitioning between the LE and HE is required for all breast thicknesses. For microcalcification and mass depiction in morphologic images, optimal LE levels were found to be close to those optimizing the iodine-equivalent images, demonstrating the feasibility, in terms of spectra, of a bCT system capable to provide both functional and morphological information. In this case, a trade-off in image quality between iodine-equivalent and morphologic images can be achieved.

The results presented in this section were found using a perfect energy-integrating detector, *i.e.* with 100% absorption efficiency at all energy levels, and can be considered as a first approximation of optimal parameters independently of the detector type (energy-integrating or photon-counting). However, if a CsI-based scintillator with finite thickness is used, an energy-dependent reduction on its absorption efficiency is expected, which might ultimately affect the optimal parameters found in this section assuming a perfect detector. The effect of CsI thickness on optimal X-ray spectra for contrast-enhanced dual-energy bCT will be described in Section 5.6. Similarly, photon-counting detectors are likely to have energy-dependent CNRD degradation, due to spectral distortions caused by photon pile-up, which might also affect the optimal parameters found for a perfect detector. In order to evaluate the best approach, further studies and an exhaustive comparison of both detector types under more realistic scenarios for breast CT applications are required.

Spectral optimization was carried out with a high AGD level (*i.e.* 100 mGy) to prevent photon starvation at the detector level (especially for the very low LE beams) and thus to obtain accurate CNRD estimations. A practical operating point however would be at 3 mGy for average-sized breasts, which corresponds to dose levels comparable to the screening AGD for a two-view breast with average thickness, as discussed in Section 5.1. In this case, with optimal LE and HE beam energies for the 14 cm diameter 50% fibroglandular equivalent phantom and a Hamming-windowed ramp filter, we showed that $CNR_{eff} \approx 5.1$, *i.e.* just above the Rose's detectability threshold of 5. Operation with a higher spatial resolution would therefore require either an increase in the total delivered AGD (*e.g.* to diagnostic levels) or the implementation of more advanced reconstruction algorithms and denoising schemes. A preliminary detectability study at low-dose levels is presented further on in Chapter 7.

5.4 Polychromatic Spectra Optimization

In order to develop a dual-energy technique for breast CT geometry, in which the iodine K-edge discontinuity is explored and the total delivered radiation dose is minimal, a polychromatic spectra optimization is performed. Four different dual-energy acquisition strategies are proposed as candidates for CE-bCT, and are individually assessed in terms of iodine-equivalent image quality.

First, the four hypothetical acquisition strategies under consideration are presented. The image quality metrics and the optimization methodology are then described. Finally, the four acquisition strategies are each optimized and their performance with respect to the image quality metrics presented as function of the acquisition parameters.

Their performance is compared subsequently in Section 5.5.

5.4.1 Candidate Acquisition Strategies for DE-bCT

As discussed in Chapter 4, to obtain the two poly-chromatic spectral data sets for Dual-Energy acquisitions, different methods have been proposed. They can be separated into two main families of methods. The first performs spectral separation by using different input spectra. This is typically achieved either by using dual-source systems with independent spectrum filtration and two X-ray detectors [224], or by using a single source with alternating tube voltages and/or spectrum filtration and a single X-ray detector [198,216,258]. The second main family of methods relies on performing spectral separation during the detection process, by using independent post-patient filtration such as the "sandwich" detectors [229, 259] or, more recently, through photon-counting with energy-resolved capabilities [260]. Both families of methods present advantages and drawbacks on their implementation, such as the quality of spectral separation, data truncation artifacts, tube power requirements and other engineering constraints. Their specific characteristics can, in a certain way, be translated into different levels of image quality.

The four candidate dual-energy acquisition strategies considered in the poly-chromatic spectra optimization study of this section were simulated as if they were obtained by the acquisition techniques defined below:

1. **Dual-Source with Dual Filtration (DS-DF):** refers to a system with two independent source-detector couples, linked to the same acquisition gantry and shifted for example by a 90° angle. One source-detector couple acquires LE data with an individual tube voltage, filter material, filter thickness and exposure; the other source-detector couple acquires HE data with a different set of tube voltage, filter material, filter thickness and exposure. Due to data truncation constraints, spectral material decomposition is commonly performed in the reconstructed image domain (slices). The detector is assumed to integrate photon energy to generate signal intensities. DS-DF strategy is illustrated in Figure 4-1a.

2. **Single-Source with Dual Filtration (SS-DF):** refers to a single source-detector couple, with any given method allowing to switch between HE and LE spectra, for example through kV and rotating filter switching. If tube voltage and filter switching are performed fast enough between low and high energy acquisitions, material decomposition can be performed in the projection domain. The detector is assumed to integrate photon energy to generate signal intensity. SS-DF strategy geometry is illustrated in Figure 4-1b.

3. **Single-Source with Fast kV Switching (SS-FkV):** refers to a single source-detector couple, with a single flat filter and any given method allowing to switch between two tube voltages. With fast kV switching between LE and HE acquisitions, projection domain decomposition is commonly used. The detector is assumed to integrate photon energy to generate signal intensity. SS-FkV strategy geometry is illustrated in Figure 4-1c.

4. **Single-Source with Energy-Resolved Photon-Counting (SS-PC):** refers to a single source-detector couple, with a single flat filter and equipped with an energy-resolved detector, which response to the incoming spectra is separated into low and high-energy bins. The latter are separated by an energy threshold set at 33 keV, *i.e.* approximately at the iodine K-shell binding energy (33.2 keV). By construction, low and high-energy projection images are perfectly correlated, making of this technique the most suitable for decomposition in the projection domain. The detector is assumed to count photons to generate signal intensity. SS-PC strategy geometry is illustrated in Figure 4-1d.

Design of Polychromatic Spectra
In Section 5.3, it was demonstrated that, for an perfect energy integrating detector, the monochromatic energy pair providing a good compromise in performance for iodine, microcalcification and mass detectability, for an average-sized breast (14 cm diameter) with 50% fibroglandular composition, is approximately 30 keV and 34 keV. Hence, for a real X-ray tube it seems reasonable, as first approximation, to generate low and high-energy poly-chromatic spectra with mean energies as close as possible to 30 and 34 keV. These results are used herein to design the optimal acquisition parameters in a polychromatic spectra scenario.

For DS-DF and SS-DF techniques, both with dedicated and independent LE and HE filtration, spectrum optimization was performed using X-ray fluence spectra generated from a Tungsten anode and filtered with either Tin (Sn) or Copper (Cu), producing low-energy and high-energy images respectively. The choice of the filter materials was a trade-off between maximizing spectral quality, *i.e.*, producing LE and HE spectra with minimal spectral overlap and average energies as close as possible to 30 and 34 keV, as well as practical considerations such as the availability and durability of high purity foil filters with homogeneous thickness. For SS-FkV and SS-PC techniques, both with a single filtration, spectrum optimization was performed using X-ray fluence spectra generated from a Tungsten anode and filtered with Copper (Cu), producing both low-energy and high-energy images. X-ray spectra for the Tungsten anode were generated using the TASMIP model [261].

5.4.2 Optimization Method

Dual-Energy Recombination
As discussed in the theoretical framework of spectral imaging (cf. Chapter 4, Section 4.4), in order to obtain iodine-equivalent images with no residual texture nor cupping, LE and HE spectra must have minimal spectral overlap and minimal trespassing over the iodine K-edge. However, in light of the polychromatic spectra designed for this study, it is expected that certain combinations of input LE and HE spectra will hardly meet these conditions, especially those which are poorly filtered and with similar tube voltages. In these cases, three-material decomposition may become an ill-conditioned problem due to lack of spectral separation and the Dual-Energy system of equations (cf. Equations 4.2 and 4.3 in Chapter 4) becomes unstable, ultimately leading into an important cupping artifacts and poor background texture cancellation in the iodine-equivalent images.

In this optimization study, the dual-energy three-material decomposition framework combined with the *a priori* calibration procedure developed in Chapter 4 are used as recombination algorithm to obtain iodine-equivalent images. As previously demonstrated, for both image and projection-based recombination, the solution of the system of equations above can be written as:

$$\begin{cases} f'_{iodine}(\mathbf{r}) = (1 - |w_{img}|) \cdot \tilde{\mu}^{LE}(\mathbf{r}) + w_{img} \cdot \tilde{\mu}^{HE}(\mathbf{r}) & (image - based) \\ f'_{iodine}(\mathbf{r}) = (1 - |w_{proj}|) \cdot \rho_1(\mathbf{r}) + w_{proj} \cdot \rho_2(\mathbf{r}) & (projection - based) \end{cases}$$

where $f'_{iodine}(\mathbf{r})$ is an offset and scaled version of the true iodine volume fraction $f_{iodine}(\mathbf{r})$ and the weighting factors w_{img} and w_{proj}, depending solely on the input LE and HE spectrum pairs, were previously calculated and stored in a look-up table.

Breast Phantom and X-ray Image Simulation

The phantom used for optimization was a 14 cm diameter cylinder phantom composed of adipose tissue and containing different cylindrical inserts, oriented parallel to the main cylinder axis, as illustrated in Figure 5-9a. Eight sets of cylindrical inserts of different compositions were placed at three different radial positions (cf. Figure 5-9b), totaling 24 cylindrical inserts. Sets 1 to 4 correspond to 0, 25, 75 and 100% fibroglandular equivalent tissues. Sets 5 to 8 correspond to homogeneous mixtures of 100% fibroglandular tissue and 0.5, 1.0, 2.5 and 5.0 mg/cm^3 of iodine, under volume conservation constraint (cf. Figure 5-9c). All inserts had the same diameter, which was chosen such as to generate a phantom with total Volume Breast Density (VBD)[6] equal to 12.5%, which represents the average density of a 14 cm diameter breast, as shown by Huang *et al.* [169].

As in the monochromatic optimization study of Section 5.3, the log-projections p_{LE} and p_{HE} (for image-based recombination), the material projections δ_{iodine} and $\delta_{adipose}$ (for projection-based recombination), as well as their respective tomographic reconstructed volumes, were simulated as described in Section 5.2.

AGD was calculated by first estimating the Normalized Glandular Dose (DgN) coefficients for a homogeneous 12.5% fibroglandular equivalent cylinder, with monochromatic input beams ranging from 10 to 80 keV. Using the input polychromatic spectral fluence as weights, AGD can be expressed as:

$$AGD = \int DgN(E) S_{net}(E) \lambda(E) dE \tag{5.9}$$

where $S_{net}(E)$ is the filtered X-ray fluence spectrum (number of photons per unit of area, mm^{-2}) at energy E and measured at the isocenter, and $\lambda(E)$ is an energy-dependent factor converting photon fluence to Air Kerma (radiation units per number of photons crossing a unit of area, $mGy \cdot mm^2$). Since the spectral optimization is independent of the total AGD, mAs values were adjusted to provide an ad hoc total AGD of 100 mGy to avoid artifacts attributed to a lack of quanta (*e.g.*, streaks). As in Section 5.3, we define $\tau = AGD_{LE}/AGD_{LE+HE}$ as the LE dose allocation ratio, *i.e.*, the fraction of the total AGD allocated to the LE image.

Optimization Criteria

As described in Section 5.2, CNRD between iodine-enhanced breast tissue and unenhanced background breast tissue ($CNRD_{iodine-bg}$) was used as the figure of merit for dose-dependent iodine detectability in the iodine-equivalent images $f_{iodine}(\mathbf{r})$. Except for the SS-PC technique,

[6]The Volumetric Breast Density (VBD) is defined as the volume fraction of fibroglandular tissue with respect to the total breast volume

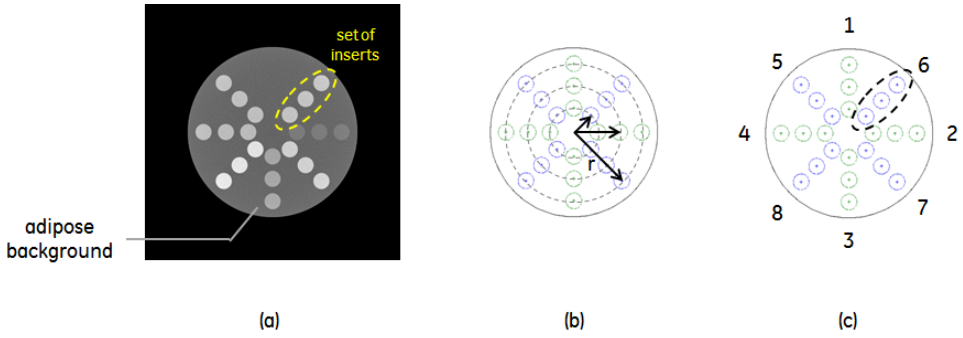

Figure 5-9: Computational breast phantom used for polychromatic spectra optimization

$CNRD_{iodine-bg}$ was evaluated in iodine-equivalent images following Equation 5.1 and as a function of the LE dose allocation ratio τ. Optimal LE dose allocation ratio, τ_{opt}, *i.e.*, maximizing $CNRD_{iodine-bg}$ was identified for each LE/HE spectrum pair. For the SS-PC technique, $CNRD_{iodine-bg}$ was evaluated for each input spectrum, since dose allocation between LE and HE bins is dictated by the input spectrum and the energy threshold.

Background texture cancellation and cupping artifact in iodine-equivalent images $f'_{iodine}(\mathbf{r})$ were calculated as a secondary quality metric, as described respectively by Equations 5.2 and 5.3 defined in Section 5.1.

For projection-based decomposition, the coefficient of determination, R^2, of Alvarez and Macovski's polynomial fit (cf. Equation 4.8) was tracked as an additional support quality metric for material decomposition goodness. Low R^2 values translate an ill-conditioned inversion problem and can be used to evaluate how well the spectral conditions for material separation were satisfied (cf. Section 4.4 for further details). The coefficient of determination of Alvarez and Macovski's polynomial fit are noted as $R^2_{A\&M}$, in order to differentiate it from other fit goodness measurements during the data analysis.

In this section, microcalcifications and mass detectability were not assessed. We believe that for a fair optimization of morphological images quality obtained from the different acquisition strategies, spatial resolution properties due to practical implementation constraints and the possibility of performing dual-energy recombination for enhanced breast morphology depiction should be assessed. However, as previously discussed, both topics are not in the scope of this chapter. They require more complex assessment of detectability, and cannot be evaluated by CNR evaluations alone, as previously suggested by Kalluri *et al.* [131]. Hence, for the remainder of this chapter, we will focus solely on the assessment of iodine contrast agent uptake in recombined iodine-equivalent images.

5.4.3 Research Space and Data Analysis

Input Acquisition Parameters
Table 5.2 summarizes the input parameters considered in the optimization.

For DS-DF and SS-DF techniques, tube voltage for LE spectra was varied from 30 to 60 kV, at 5 kV steps, while the Sn filter thickness was varied from 0.03 to 0.30 mm, at 0.03 mm steps. Tube voltage for HE spectra was varied from 40 to 80 kV, at 5 kV steps, while the Cu filter thickness was varied from 0.05 to 0.50 mm, at 0.05 mm steps. LE dose allocation ratio τ was varied from 20 to 80%, at 5-10% steps.

For the SS-FkV technique, tube voltage was varied from 30 to 80 kV, at 5 kV steps, while the Cu filter thickness was varied from 0.05 to 0.50 mm, at 0.05 mm steps. LE dose allocation ratio τ was varied from 20 to 80%, at 5-10% steps.

For the SS-PC technique, tube voltage was varied from 40 to 80 kV, at 5 kV steps, while the Cu filter thickness was varied from 0.05 to 0.50 mm, at 0.05 mm steps. The energy threshold for the discriminating detector was set to 33 keV. Hence, the lower bound of 40 kV tube voltage for DS-PC technique intended to enable two energy bins that straddle the iodine-K-edge.

Lower and upper limits of tube voltage values were chosen such as to mainly consider LE spectra with average energy below the iodine K-edge and HE spectra with average energy above the iodine K-edge. The choice of lower and upper limits of filter thickness was a trade-off in realistic aspects of dose, tube power and commercial availability, as well as concerns on image quality (minimum detector signal level) and exposition of patient skin to very low-energy X-ray photons.

The first row in Figure 5-10 illustrates the filtered fluence spectra incident over the imaged phantom, $S_{net}(E)$, for different tube voltages and using the Sn filter with 0.03, 0.15 and 0.3 mm thickness. The second row in Figure 5-10 illustrates the input fluence spectra $S_{net}(E)$, for different tube voltages and using the Cu filter with 0.05, 0.25 and 0.5 mm thickness. A normalization in

Table 5.2: Summary of input parameters for each acquisition technique considered in the polychromatic spectra optimization

Technique	Anode/Filter	Parameters	Recomb. Method
DS-DF	LE: W/Sn HE: W/Cu	30 – 60 kV 0.03 – 0.3 mm Sn τ = 20 – 80% 40 – 80 kV 0.05 – 0.5 mm Cu τ = 20 – 80%	image-based
SS-DF	LE: W/Sn HE: W/Cu	30 – 60 kV 0.03 – 0.3 mm Sn τ = 20 – 80% 40 – 80 kV 0.05 – 0.5 mm Cu τ = 20 – 80%	projection-based
SS-FkV	W/Cu	LE: 30 – 60 kV, τ = 20 – 80% HE 40 – 80 kV, τ = 20 – 80% 0.05 – 0.5 mm Cu	projection-based
SS-PC	W/Cu	40 – 60 kV 0.05 – 0.5 mm Cu En. threshold = 33 keV	projection-based

arbitrary units was applied to obtain optimal illustration of the considered spectra, in all KV ranges. It is only for purpose of illustration.

Figure 5-11 illustrates the correspondent polychromatic normalized glandular dose coefficients [160], DgN_{poly}[7], as function of the X-ray tube voltage for three different Sn and Cu filtrations considered in the spectra optimization, corresponding to minimum, average and maximum considered filter thickness values. Both Sn and Cu-filtered spectra, DgN_{poly} increases monotonically with tube voltage and filter thickness. While the three Cu-filtered DgN_{poly} curves as function of the tube voltage presents are approximately parallel to each other, differences in Su-filtered DgN_{poly} values substantially decreases for tube voltage values between 45 and 55 kV, becoming nearly independent of filter thickness. This is due to the presence of Sn K-shell absorption edge at 29.2 keV.

Concerning the recombination methods, for DS-DF technique, the iodine-equivalent images $f'_{iodine}(\mathbf{r})$ were obtained through image-based recombination of LE and HE effective attenuation coefficients volumes $\tilde{\mu}^{LE}(\mathbf{r})$ and $\tilde{\mu}^{HE}(\mathbf{r})$, using previously calculated optimal weight w_{img}. For SS-DF, SS-FkV and SS-PC techniques, $f'_{iodine}(\mathbf{r})$ was obtained through projection-based recombination of material density volumes $\rho_{iodine}(\mathbf{r})$ and $\rho_{gland}(\mathbf{r})$, using previously calculated optimal weight w_{proj}.

Data Analysis

The goal of spectral optimization is summarized in maximizing $CNRD_{iodine-bg}$ while varying up to five unknown parameters (LE tube voltage, LE filter thickness, HE tube voltage, HE filter

[7] $$DgN_{poly} = \frac{\int DgN(E)S_{net}(E)\lambda(E)dE}{\int S_{net}(E)\lambda(E)dE}$$

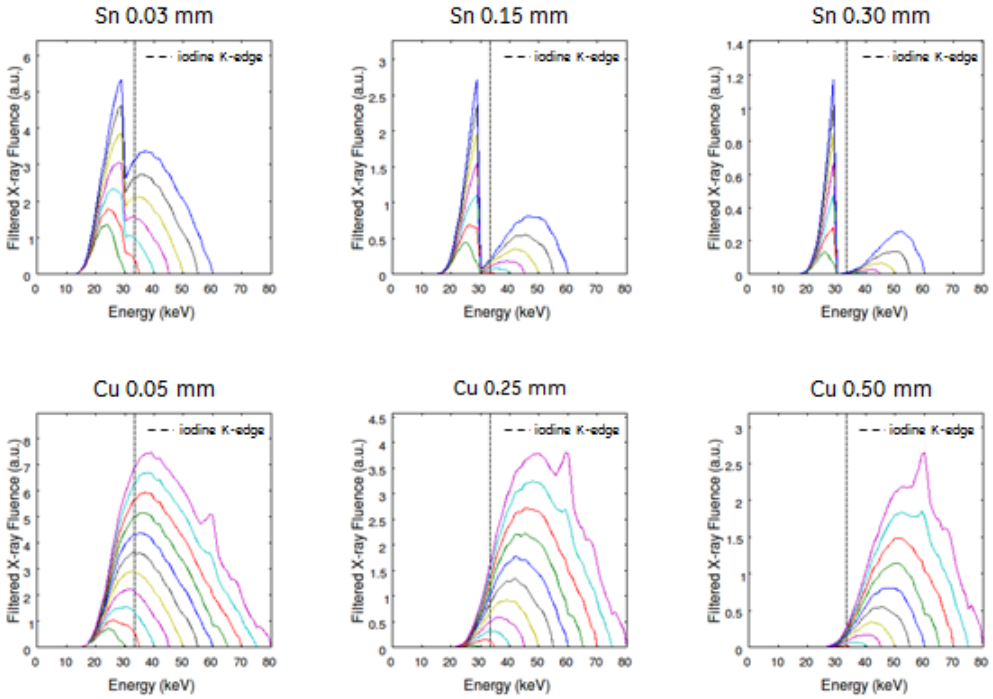

Figure 5-10: Input spectra $S_{net}(E)$ for W/Sn and W/Cu anode/filter combinations, for different tube voltages and filter thicknesses. The vertical dashed lines indicate the iodine K-edge (33.2 keV). A normalization in arbitrary units was applied to obtain optimal illustration of the considered spectra, in all KV ranges

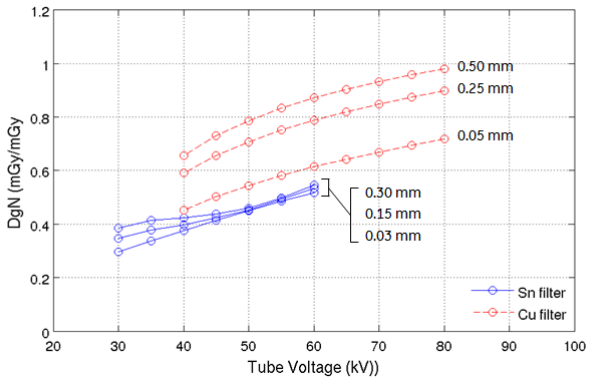

Figure 5-11: Polychromatic DgN coefficients as function of the tube voltage for 12.5% fibroglandular-equivalent cylindrical phantoms. Solid lines correspond to incident spectra filtered with Tin (Sn), while dashed lines correspond to incident spectra filtered with Copper (Cu)

thickness and dose repartition between LE and HE acquisitions), depending on the acquisition strategy.

For the DS-DF and SS-DF techniques, the optimization was designed as a 5D problem. In order to analyze the simulated data, the optimization problem was analyzed as a concatenation of a 1D optimization problem (over the LE dose allocation ratio), followed by a 2D optimization problem (over the tube voltages), followed by another 2D optimization problem (over the filter thicknesses). For the SS-FkV technique, the optimization was designed as a 4D problem, since only one filter is implemented. The optimization was in this case carried as for the DS-DF and SS-DF techniques, but considering only the case when LE filter thickness is equal to HE filter thickness. For the SS-PC technique, the optimization was designed as a 2D problem maximizing $CNRD_{iodine-bg}$ as function of the tube voltage and filter thickness.

For a general data analysis framework, the 5D optimization problem was sub-divided in three steps. Firstly, to obtain optimal LE dose allocation ratios, 2nd degree polynomials were fit to the $CNRD_{iodine-bg}$ values as function of LE dose allocation ratio τ. At this step, we observed that the coefficient of determination (R^2) values were larger than 0.95, for all LE and HE tube voltages and filter thicknesses. This step enables decreasing the optimization problem by one dimension.

Secondly, to obtain optimal LE and HE tube voltages as function for each pair of LE and HE filter thicknesses, $CNRD_{iodine-bg}$ values found at optimal LE dose allocation ratio, τ_{opt}, were plotted as function of the LE and HE tube voltages. A locally weighted smoothing fit function (*loess*, robust, span: 25%) was implemented using Matlab (*Curve Fitting Toolbox™*, The MathWorks Inc., Natick, MA, USA) in order to better estimate the optimal parameters. Figure 5-12 illustrates a series of $CNRD_{iodine-bg}$ smoothed surfaces, for SS-DF strategy, as function of LE and HE tube voltages, and when LE and HE filter thicknesses increases from minimum to maximum values (marks indicate maximum $CNRD_{iodine-bg}$ values for each surface).

Finally, optimal input acquisition parameters (LE dose allocation ratio τ, LE tube voltage and HE tube voltage) and the correspondent optimized criteria ($CNRD_{iodine-bg}$) and the secondary FOMs ($CNRD_{texture}$ and *cupping*(%)) were analyzed as function of the LE and HE filter thicknesses.

For projection-based decomposition, in order to expose and penalize outliers from ill-conditioned spectral separation, all simulated data during fit and surface smoothing operations originated were heavily weighted by the $R^2_{A\&M}$ values.

5.4.4 Optimal Acquisition Parameters for Iodine Uptake Depiction

Table 5.3 summarizes the lower and upper limits of optimal input parameters (LE and HE tube voltage, and LE dose allocation ratio) and optimal Figures-of-Merit (iodine detectability, texture cancellation and cupping magnitude) relative to the 5 $mg\ I/cm^3$ iodine-enhanced lesion, for all four considered dual-energy acquisition strategies. As in Section 5.3, dose-dependent iodine detectability was evaluated by assessing $CNRD_{iodine-bg}$ values relative to the 5 $mg\ I/cm^3$ iodine-enhanced lesion. This choice was meant to ensure accurate CNRD estimations for all simulation points, especially in the presence of low lesion contrast and high quantum noise. Accordingly, $CNRD_{texture}$ and *cupping*(%) were also computed relative to the 5 $mg\ I/cm^3$ iodine-enhanced lesion.

Below we provide a more detailed description on the optimization results for each acquisition strategy. All optimal surfaces presented below, were smoothed using Matlab's locally weighted smoothing fit function (*loess*, robust, span: 25%), with R^2 values highlighted at the bottom of each figure.

Optimal Acquisition Parameters for DS-DF technique

Figures 5-13a, 5-13b and 5-13c illustrate the optimal input parameters, LE tube voltage, HE tube voltage and the LE dose allocation ratio respectively, as function of the LE and HE filter thicknesses.

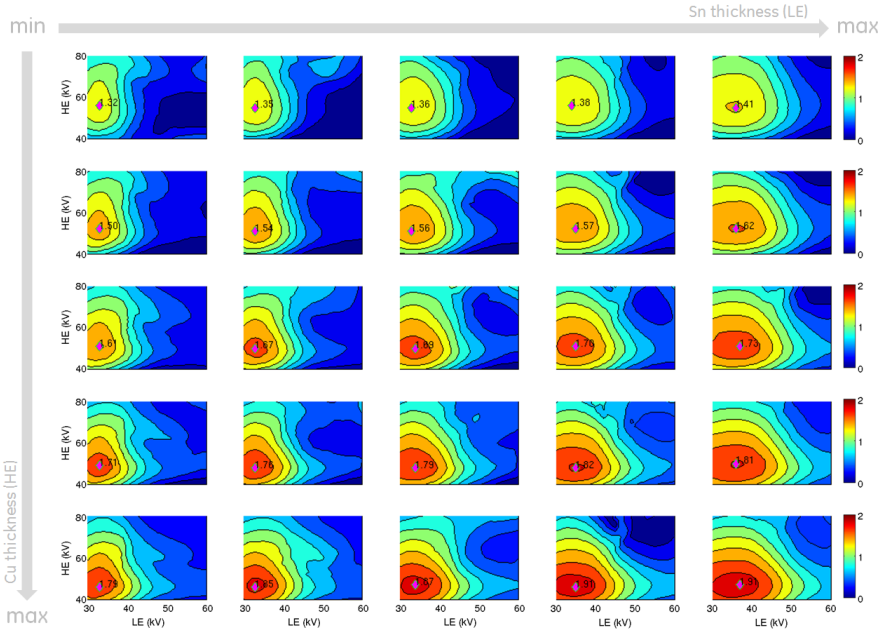

Figure 5-12: Illustration of iodine CNRD at optimal LE dose allocation ratio for SS-DF acquisition strategy, as function of LE and HE tube voltages, and when Sn and Cu filter thicknesses vary from the minimum to maximum studied values. Marks indicate maximum $CNRD_{iodine-bg}$ values for each surface.

Table 5.3: Lower and upper limits of optimal input parameters and optimal Figures-of-Merit for the unconstrained polychromatic spectra optimization, per considered dual-energy acquisition strategy and for all filter thicknesses. The results are based on a 12.5% glandular 14 cm diameter phantom and computed relative to the 5 mg/cm^3 iodine-enhanced lesion

	Optimal Input Parameters			**Optimal Figures-of-Merit**		
Technique	**LE tube voltage(kV)**	**HE tube voltage(kV)**	**LE dose alloc. ratio τ**	$CNRD_{iodine-bg}$	$CNRD_{texture}$	$cupping(\%)$
DS-DF	30 – 35	48 – 58	47 – 51%	1.4 – 2.0	0 – 0.06	-0.5 – 1.8
SS-DF	33 – 36	47 – 55	48 – 53%	1.3 – 1.9	-0.025 – 0.045	-0.5 – 2.8
SS-FkV	28 – 32	47 – 55	48 – 50%	1.35 – 1.85	-0.035 – -0.045	-1 – 0.5
SS-PC	-	40 – 80	-	0.4 – 2.6	-0.01 – 0.06	0 – -2.5

(*) Correspond to the range tube voltage values considered for all filter thicknesses

Maximum $CNRD_{iodine-bg}$ values for SS-PC are found between 40 and 45 kV, and with little influence of the filter thickness

Figures 5-13d, 5-13e and 5-13f illustrate the output FOMs, $CNRD_{iodine-bg}$, $CNRD_{texture}$ and *cupping*(%) respectively, calculated at optimal LE and HE tube voltages and optimal LE dose allocation ratio, τ_{opt}, and as function of the LE and HE filter thicknesses.

Optimal LE tube voltage varies between 30 and 35 kV, approximately increasing with the LE filter thickness. Optimal HE tube voltage decreased from 58 to 48 kV with increasing HE filter thickness. Optimal LE dose allocation ratio was found to be approximately 50%. Optimal $CNRD_{iodine-bg}$ values for the 5 $mg\ I/cm^3$ lesion were found to vary between approximately 1.4 and 2.0, increasing with LE and HE filters thicknesses. HE filter thickness showed to have a larger influence on $CNRD_{iodine-bg}$ values, as can be remarked by the approximately horizontal contour lines. $CNRD_{texture}$ values varied between 0 and 0.06, *i.e.* up to $\sim$ 3.5% of the 5 $mg\ I/cm^3$ lesion contrast. Cupping artifact was found to be within -0.5 and 1.8 % of the 5 $mg\ I/cm^3$ lesion contrast.

In sum, optimal input parameters for the DS-DF technique generate LE and HE spectra that bracket the iodine K-edge with approximate 50% dose repartitioning. Moreover, optimal LE and HE spectra draw nearer to the iodine K-edge with the increasing filter thickness, converging to the theoretical monochromatic limit found in the Section 5.3. Results showed that "water-based-like" correction for image-based decomposition produced negligible beam-hardening, with residual texture and cupping magnitude below 0.5 $mg\ I/cm^3$, *i.e.* the minimal iodine-enhanced lesion uptake we aim to detect.

Optimal Acquisition Parameters for SS-DF technique

Figures 5-14a, 5-14b and 5-14c illustrate the optimal input parameters, LE tube voltage, HE tube voltage and the LE dose allocation ratio respectively, as function of the LE and HE filter thicknesses. Figures 5-14d, 5-14e and 5-14f illustrate the output FOMs, $CNRD_{iodine-bg}$, $CNRD_{texture}$ and *cupping*(%) respectively, calculated at optimal LE and HE tube voltages and optimal LE dose allocation ratio, τ_{opt}, and as function of the LE and HE filter thicknesses.

Optimal LE tube voltage remained between 33 and 36 kV, slightly increasing with the LE filter thickness. Optimal HE tube voltage varies between 47 to 55 KV. Optimal LE dose allocation ratio was found to be approximately 50%. Optimal $CNRD_{iodine-bg}$ values for the 5 $mg\ I/cm^3$ lesion were found to vary between approximately 1.3 and 1.9, increasing with both filters thicknesses. As for the DS-DF technique, HE filter thickness showed to have a larger influence on $CNRD_{iodine-bg}$ values. $CNRD_{texture}$ values varied between -0.025 and -0.045, *i.e.* up to $\sim$ 2.8% of the 5 $mg\ I/cm^3$ lesion contrast. Cupping artifact was found to be within -0.5 and 2.8 % of the 5 $mg\ I/cm^3$ lesion contrast.

As for the previous technique, optimal input parameters for the SS-DF technique also favor LE and HE spectra that closely bracket the iodine K-edge with approximate 50% dose repartitioning. However, the use of projection-based decomposition slightly decreased $CNRD_{iodine-bg}$ values when compared to DS-DF results. This result is concordant with previously published studies comparing image and projection-based energy-weighting for morphologic breast CT imaging [131, 237]. The decrease in CNRD is most likely due to the complex noise propagation in high order terms of the decomposition equation (cf. Equation 4.8 in Section 4.4). Texture cancellation and cupping magnitude were also below 0.5 $mg\ I/cm^3$, though no substantial difference was found when compared to image-based decomposition implemented for the DS-DF technique.

Optimal Acquisition Parameters for SS-FkV technique

The solid lines in Figures 5-15a, 5-15b and 5-15c illustrate the optimal input parameters, LE tube voltage, HE tube voltage and the LE dose allocation ratio respectively, as function of the LE and HE filter thicknesses. Figures 5-15d, 5-15e and 5-15f illustrate the output FOMs, $CNRD_{iodine-bg}$, $CNRD_{texture}$ and *cupping*(%) respectively, calculated at optimal LE and HE tube voltages and optimal LE dose allocation ratio, τ_{opt}, and as function of the filter thickness.

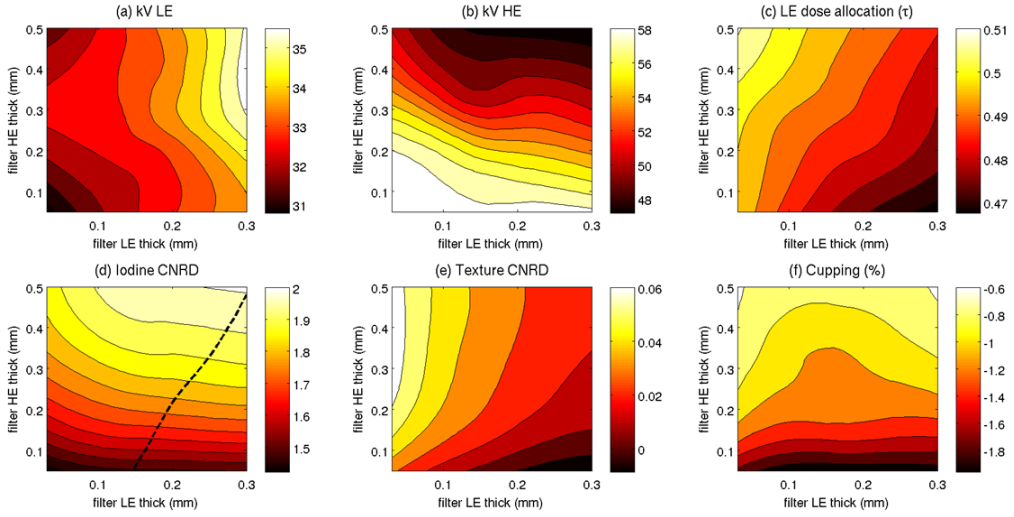

Figure 5-13: Optimization results for DS-DF technique as function of the LE and HE filter thicknesses. In the first row, the optimal input parameters: (a) LE tube voltage, (b) HE tube voltage and (c) LE dose allocation ratio. In the second row, the output FOM: (d) $CNRD_{iodine-bg}$, (e) $CNRD_{texture}$ and (f) $cupping(\%)$, calculated at optimal input parameters. The dashed line in (d) indicates the set of input parameters where the same tube power is required for LE and HE acquisitions. The results are based on a 12.5% glandular 14 cm diameter phantom and computed relative to the 5 mg/cm^3 iodine-enhanced lesion

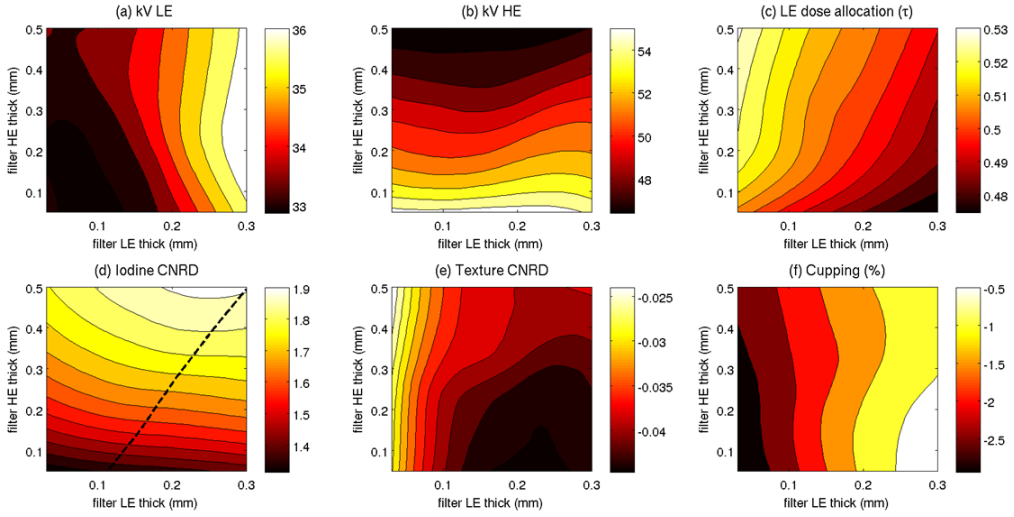

Figure 5-14: Optimization results for SS-DF technique as function of the LE and HE filter thicknesses. In the first row, the optimal input parameters: (a) LE tube voltage, (b) HE tube voltage and (c) LE dose allocation ratio. In the second row, the output FOM: (d) $CNRD_{iodine-bg}$, (e) $CNRD_{texture}$ and (f) $cupping(\%)$, calculated at optimal input parameters. The dashed line in (d) indicates the set of input parameters where the same tube power is required for LE and HE acquisitions. The results are based on a 12.5% glandular 14 cm diameter phantom and computed relative to the 5 mg/cm^3 iodine-enhanced lesion

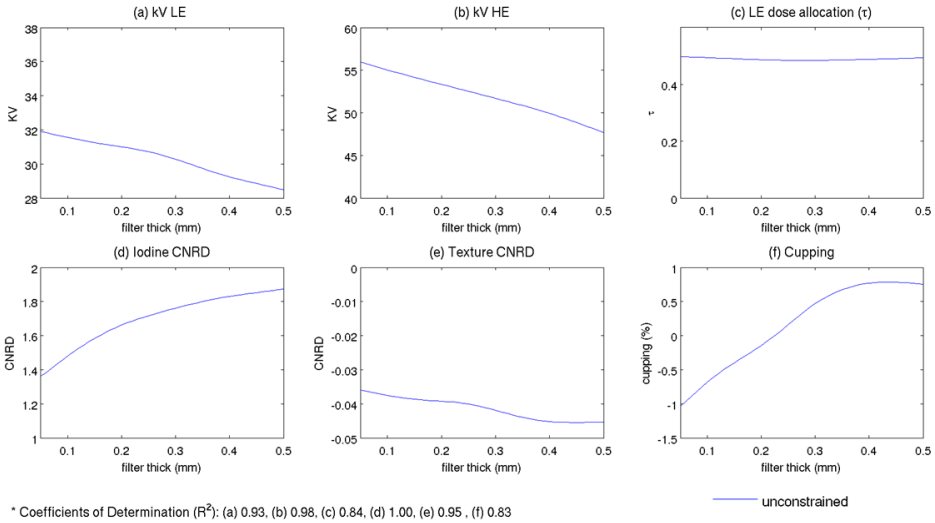

Figure 5-15: Optimization results for SS-FkV technique as function of the filter thickness. In the first row, the optimal input parameters: (a) LE tube voltage, (b) HE tube voltage and (c) LE dose allocation ratio. In the second row, the output FOM: (d) $CNRD_{iodine-bg}$, (e) $CNRD_{texture}$ and (f) $cupping(\%)$, calculated at optimal input parameters. The results are based on a 12.5% glandular 14 cm diameter phantom and computed relative to the 5 mg/cm^3 iodine-enhanced lesion

Optimal LE tube voltage decreased from 32 and 28 kV with increasing LE filter thickness, while optimal HE tube voltage decreased from 55 to 47 kV with the increasing HE filter thickness. Optimal LE dose allocation ratio remained between 48 and 50% for all filter thicknesses. Optimal $CNRD_{iodine-bg}$ values for the 5 $mg\ I/cm^3$ lesion increased from approximately 1.35 to 1.85 with increasing filter thickness. $CNRD_{texture}$ values varied between -0.035 and -0.045, *i.e.* up to $\sim 2.5\%$ of the 5 $mg\ I/cm^3$ lesion contrast. Cupping artifact was found to be within -1 and 0.5 % of the 5 $mg\ I/cm^3$ lesion contrast.

In sum, when compared to the previous two techniques, optimal input parameters for the SS-FkV technique also favor LE and HE spectra that closely bracket the iodine K-edge with approximate 50% dose repartitioning. However, the SS-FkV technique presented lower optimal LE tube voltage values, which aimed to decrease the spectral overlap with the HE spectra. Moreover, both optimal LE and HE tube voltages decreases with increasing filter thickness. Although the spectral overlap entailed in a slightly lower $CNRD_{iodine-bg}$ values when compared to DS-DF and SS-DF techniques, residual texture and cupping artifact were also below 0.5 $mg\ I/cm^3$.

Optimal Acquisition Parameters for SS-PC technique

Figures 5-16a, 5-16b and 5-16c illustrate the output FOMs, $CNRD_{iodine-bg}$, $CNRD_{texture}$ and $cupping(\%)$ respectively, as function of the tube voltage and filter thickness.

In the range of the two input parameters, $CNRD_{iodine-bg}$ values for the 5 $mg\ I/cm^3$ lesion were found between 0.4 and 2.6, with broad maxima between 40 and 45 kV tube voltage and with little influence of the filter thickness in this energy range. $CNRD_{texture}$ values varied between -0.01 and 0.06, *i.e.* up to $\sim 5\%$ of the 5 $mg\ I/cm^3$ lesion contrast, and also presented minimum values at regions of low tube voltages and large range of filter thicknesses. Cupping artifact remained within 0 and -2.5 % of the 5 $mg\ I/cm^3$ lesion contrast.

Differently from the previous three techniques, optimal $CNRD_{iodine-bg}$ values decrease with filter thickness. This is because the increasing filtration hardens the input spectra and decreases the dose allocated to the LE bin, with no significant change in its mean energy. In addition, although

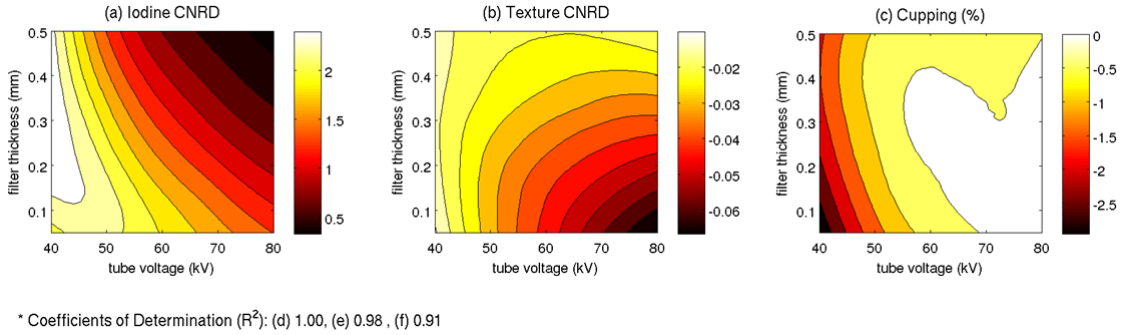

Figure 5-16: Optimization results for SS-PC technique as function of the tube voltage and filter thickness: (a) $CNRD_{iodine-bg}$, (b) $CNRD_{texture}$ and (c) $cupping(\%)$, calculated at optimal input parameters. The results are based on a 12.5% glandular 14 cm diameter phantom and computed relative to the 5 mg/cm^3 iodine-enhanced lesion

the energy-discriminating detector provided perfect spectral separation between LE and HE bins, no significant difference was observed in texture cancellation or cupping correction quality when compared to the previous non-discriminating techniques.

5.4.5 Discussion

In the second step of CE-bCT acquisition parameter optimization, X-ray fluence spectra generated from a Tungsten anode and filtered with Tin (Sn, K-edge: 29 keV) and Copper (Cu) were chosen to provide LE and HE spectra with effective energies close to optimal monochromatic beam energies found previously. Four dual-energy acquisition strategies were considered: i) Dual Source Dual Filtration (DS-DF, 2 sources, 2 kVs and 2 filters), Single Source Dual Filtration (SS-DF, 1 source, 2 kVs and 2 filters); iii) Single Source with Fast kV Switching (SS-FkV, 1 source, 2 kVs and 1 filter); and iv) Single Source with energy-resolved Photon-Counting detector (SS-PC, 1 source, 1 kV, 1 filter). Point source and 100% efficient blur-free detector assumptions were made for all considered strategies.

Optimization results showed that for all four acquisition strategies, there exists a given set of LE and HE tube voltages and filter thickness which provides minimum cupping artifact (in absolute, up to $\sim$ 3% of 5.0 $mg\ I/cm^3$ lesion contrast, which represents $\sim$ 0.15 $mg\ I/cm^3$ in terms of iodine concentration) and minimum residual texture (in absolute, up to $\sim$ 5% of 5.0 $mg\ I/cm^3$ CNRD, which represents 0.25 $mg\ I/cm^3$ in terms of iodine concentration). $CNRD_{iodine-bg}$ values for the 5 $mg\ I/cm^3$ lesion varied between approximately 1.35 and 2.6, depending on the acquisition strategy.

In general, optimal LE tube voltages increased with LE filter thickness while optimal HE filter thickness decreased with HE filter thickness. This behavior can be seen as a tendency to optimize LE and HE spectra average energies and the amount of spectral overlap. Higher thickness values make LE and HE spectra narrower, which allows to increase or decrease their mean energies closer to 33.2 keV (iodine K-edge), approaching monochromaticity and providing optimal lesion contrast and noise weighting. It also minimize the overlap between both spectra, therefore avoiding undesired uncorrelated noise from the complementary spectral image. These two factors contribute to increase CNRD in the recombined iodine-equivalent images. Therefore, as expected, we observed that $CNRD_{iodine-bg}$ systematically increased when increasing the LE and HE filter thicknesses.

In this section, microcalcifications and mass detectability were not assessed. We assumed that a fair comparison of morphological images quality from the different acquisition strategies, spatial resolution constraints and dual-energy recombination for enhanced breast morphology depiction

must be assessed. As demonstrated by Kalluri *et al.* [131], the assessment of CNR alone as measurement of detectability for microcalcifications might be misleading. For instance, this research group showed in a simulation study [262] that Signal-to-Noise Ratio (SNR) of microcalcifications imaged with optimal weighting using a CZT based photon-counting detector was 30–40% higher than with a CsI based energy-integrating detector [262]. However, the same research group showed in a subsequent detectability study with human observers, that the percentage improvement of the average Area Under ROC curve was 21–23%. In summary, further comparison studies using human observers or mathematical observer models are necessary to understand the effect of each acquisition strategy on microcalcification and mass detectability in morphologic breast CT images.

In summary, under the assumption of this study, we showed that through a careful choice of acquisition parameters (Table 5.3) all four candidate strategies were able to provide recombined iodine-equivalent images with cupping artifacts and residual texture below 0.5 $mg\ I/cm^3$ contrast levels, *i.e.* the minimum iodine concentration expected in clinical practice if a typical injection protocol of contrast-enhanced mammography is considered (cf. Section 5.1). One could use the curves presented above as preliminary guidance towards the optimal acquisition parameters of one's acquisition strategy of interest. It is expected however, each system will impose engineering challenges for their actual implementation. In order to a have glimpse on the impact of their practical design constraints in the optimization results, the performance of the different acquisition strategies is compared in the next section.

5.5 Performance Comparison Between Candidate Dual Energy Acquisition Strategies

The four candidate acquisition strategies optimized in the last section perform spectral separation in different manners. In particular, they differ in the way low and high-energy data are obtained while the system gantry rotates around the breast. Accordingly, their practical implementation may impose substantial engineering constraints and ultimately impact image quality. For instance, in the last section we demonstrated that iodine detectability (in terms of contrast-to-noise ratio) increases monotonically with LE and HE filter thickness, therefore converging to the ideal monochromatic beam scenario. However, an increase in the filter thickness would also demand an increase in X-ray tube power required in order to deliver the desired X-ray fluence. This may impose a severe constraint when designing the dual-energy acquisition systems.

In this section, in order to compare the performance of the four candidate acquisition strategies, we impose a constant tube power constraint between LE and HE acquisitions and re-run polychromatic optimization framework discussed in the previous section. The new constrained optimization concentrated once again in maximizing iodine detectability ($CNRD_{iodine-bg}$) while reducing cupping and residual texture ($CNRD_{texture}$).

5.5.1 Comparison Methodology

To compare the four candidate acquisition strategies, three main technological assumptions were sequentially combined to build one single constraint to the optimization.

First, as described in section 5.2, we assumed the acquisitions to be performed in a "step-and-shoot" mode with instantaneous displacement (infinite speed) between two consecutive view angles (*i.e.* without tube motion-induced blur). For each view, the X-ray source emits continuously and integration time interval is used for exposure calculation (*i.e.* mAs values).

Secondly, any tube voltage switch was assumed to be performed ideally, *i.e.* with instantaneous transition between consecutive values, and LE and HE photon fluences were assumed to be detected during the same amount of time (in other words, with a fixed detector frame rate). Therefore, the idealistic tube voltage waveforms for each acquisition strategy are illustrated in Figure 5-17a. DS-DF strategy has independent and continuous LE and HE acquisitions during the gantry rotation. The same is observed for the SS-PC strategy, although only one tube voltage is required. For SS-DF and SS-FkV strategies, LE and HE acquisitions are intercalated during the gantry rotation. Hence, in a real case scenario, LE and HE projection data between two consecutive gantry angles are typically spatially interpolated before recombination [219, 263]. The different waveforms would impact the system spatial resolution due to tube motion. However, once again spatial resolution was not considered to have an energy-dependent impact on the Figures-of-Merit of spectral optimization and LE and HE acquisitions were assumed to have perfect spatial correlation. This setup is also preferable to keep simulation time manageable.

Third, besides the consequences on spatial resolution, the different considered waveforms would also require different X-ray tube powers to achieve the same photon flux and radiation dose. For instance, as illustrated in Figure 5-17a, single-source designs would require twice the frame rate of dual-source designs and twice the tube power for the same delivered dose. Therefore, knowing that iodine detectability increases with LE and HE filter thickness, differences in tube power design can be used as substantial differentiator in each acquisition strategy performance. X-ray tube power was therefore the independent constraint variable for this comparison study.

Tube Power Constraint Definition
X-ray tube design can be a complex problem and power requirements have been previously used as a constraint for dual-energy spectra optimization [219, 264].

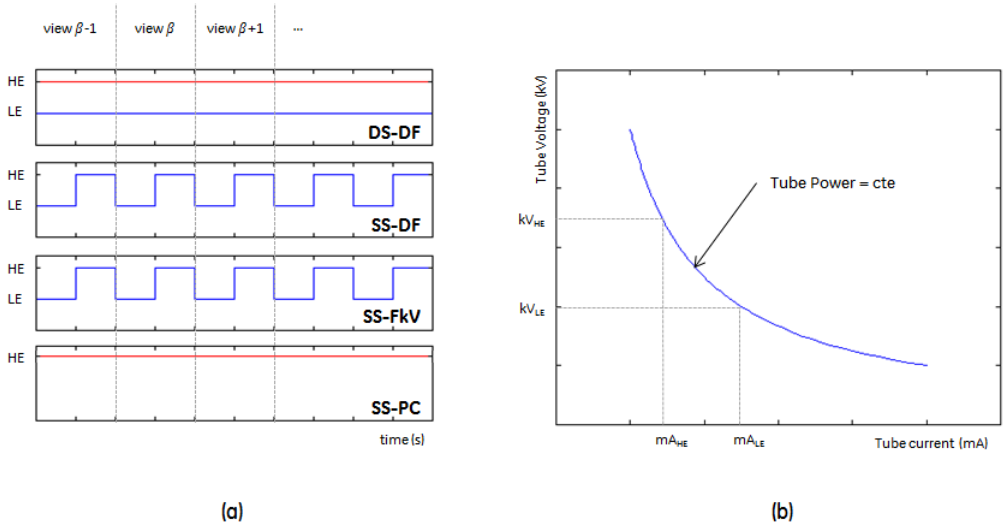

Figure 5-17: (a) Ideal square tube voltage waveform for each acquisition strategy, at fixed detector frame rate; (b) relationship between LE and HE tube voltage and current, for a fixed tube power

In a dual-energy CT setup, both a *constant mA* and *constant power* model for tube power design have been reported [219, 264]. In the *constant mA* model the tube current is the same for all tube voltages, while in the *constant power* model the product of the tube current and tube voltage is fixed for all kV. The *constant mA* is technically easier to implement in fast kV switching techniques, since in terms of tube design it is easier to keep the mA constant during kV switching. This is the case of current clinical dual-energy fast kV switching systems [241, 265, 266] with which iodine-enhanced and synthetic monochromatic imaging is performed using GE Discovery™ CT750HD system equipped with GSI™ technology at 80kV/140kV body scans with approximately constant 600mA (GE Healthcare; Chalfont St Giles, UK). On the other hand, imposing a constant mA constraint to a dual source system goes against the main advantage of this technique, *i.e.* the possibility of independent design of X-ray tubes for LE and HE acquisitions. Therefore, for a fair comparison and since a constant power assumption can be considered the theoretical limit of a X-ray tube behavior, we adopted the *constant power* constraint as a mean for comparison. We assumed that for a constant tube power and fixed detector frame rate, tube voltage and tube current are inversely proportional, as illustrated in Figure 5-17b.

For simplicity and to be free of other assumptions on the acquisition protocol, tube power values for the different acquisition techniques were calculated as function of the acquisition parameters and normalized by the total AGD and acquisition time, such as:

$$P_N = \frac{\text{tube voltage} \times \text{tube current} \times \text{acq. time}}{\text{AGD}} \tag{5.10}$$

where P_N is the normalized tube power in units of $kW \cdot s \cdot mGy^{-1}$ or J/mGy. Tube power calculation took into account the waveforms in Figure 5-17a.

5.5.2 Optimal Acquisition Parameters from Constrained Optimization

In practical terms, the constrained optimization in summarized in restraining the space of parameters of the previous unconstrained optimization to a limited set of points in which the same tube power is required between LE and HE acquisition. In the special case of the SS-PC technique (which has a single input spectrum), the problem is summarized in identifying maximum

$CNRD_{iodine-bg}$ values as function of the X-ray tube power. For each acquisition strategy, optimal input parameters and optimal Figures-of-Merit are then described as function of a single independent variable, the normalized tube power P_N.

Table 5.4 summarizes the lower and upper limits of optimal input parameters (LE and HE tube voltage, and LE dose allocation ratio) and optimal Figures-of-Merit (iodine detectability, texture cancellation and cupping magnitude) for the *constant power* polychromatic spectra optimization. For an easier comparison, the lower and upper limits found with the unconstrained optimization (Table 5.3) are also presented. Below we provide a more detailed description on the optimization results for each acquisition strategy under *constant power* constraint.

Table 5.4: Lower and upper limits of optimal input parameters and optimal Figures-of-Merit for the unconstrained and *constant power* polychromatic spectra optimizations, per considered dual-energy acquisition strategy and for all filter thicknesses. The results are based on a 12.5% glandular 14 cm diameter phantom and computed relative to the 5 mg/cm^3 iodine-enhanced lesion

	Optimal Input Parameters			**Optimal Figures-of-Merit**		
Technique	**LE tube voltage (kV)**	**HE tube voltage (kV)**	**LE dose alloc. ratio τ**	$CNRD_{iodine-bg}$	$CNRD_{texture}$	$cupping(\%)$
			UNCONSTRAINED OPTIMIZATION RESULTS			
DS-DF	30 – 35	48 – 58	47 – 51%	1.4 – 2.0	0 – 0.06	-0.5 – 1.8
SS-DF	33 – 36	47 – 55	48 – 53%	1.3 – 1.9	-0.025 – 0.045	-0.5 – 2.8
SS-FkV	28 – 32	47 – 55	48 – 50%	1.35 – 1.85	-0.035 – -0.045	-1 – 0.5
SS-PC	-	40 – 80 (*)	-	0.4 – 2.6	-0.01 – 0.06	0 – -2.5
			CONSTANT POWER OPTIMIZATION RESULTS			
DS-DF	33 – 35	48 – 58	∼48%	1.4 – 2.0	0.01 – 0.02	-0.5 – 1.8
SS-DF	33 – 36	47 – 55	∼48%	1.3 – 1.9	∼0.04	-2.0 – -1.0
SS-FkV	35 – 37	40 – 55	15 – 20%	1.05 – 1.15	-0.02 – 0	-1.25 – 0.25
SS-PC	-	40 – 65	-	1.7 – 2.6	-0.01 – 0.05	-0.5 – -2.0

(*) Correspond to the range tube voltage values considered for all filter thicknesses
Maximum $CNRD_{iodine-bg}$ values for SS-PC are found between 40 and 45 kV, and with little influence of the filter thickness

DS-DF and SS-DF Strategies

For both DS-DF and SS-DF strategies, optimal input parameters and Figures-of-Merit found under constrained optimization can be illustrated in the surfaces of Figures 5-13 and 5-14, presented in the unconstrained optimization of Section 5.4.

For DS-DF and SS-DF techniques, the dashed lines in Figures 5-13d and 5-14d, respectively, represent $CNRD_{iodine-bg}$ values for which the correspondent optimal acquisition parameters entail equal tube power requirement between LE and HE acquisitions. The direction of increasing tube power in the dashed lines coincides with the direction of increasing LE and HE filter thickness. The optimal LE and HE tube voltages and optimal LE dose allocation ratio can be found by projecting this line over the other surfaces in Figures 5-13 and 5-14.

For both techniques, it was found that $CNRD_{iodine-bg}$ increases with increasing tube power. This is because the increasing available tube power allows for heavier filtration, higher LE tube voltages and lower HE tube voltages. Together, they entailed in smaller spectral overlap, higher proximity to the iodine K-edge and consequently better iodine separation from unenhanced breast tissue. The *constant power* constraint only slightly affect the lower and upper limits of optimal input parameters and optimal Figures-of-Merit compared to the unconstrained optimization results (Table 5.4). This is because both systems allow for complete tuning of LE and HE tube voltages, filter thicknesses and AGD repartitioning, and as consequence, to found a set of parameters entailing the same tube power between LE and HE acquisitions.

SS-FkV Strategy
The dashed lines in Figures 5-18a to 5-18e illustrate the optimization results when the *constant power* constraint is applied to space of acquisition parameters.

Optimal LE tube voltage varied between 35 and 37 kV. Optimal HE tube voltage decreased from 55 to 40 kV with the increasing filter thickness. Optimal LE dose allocation ratio dropped from 50% to approximately 15% after applying the *constant power* constraint. Optimal $CNRD_{iodine-bg}$ values slightly increases with filter thickness, ranging between 1.05 and 1.15. $CNRD_{texture}$ values varied between -0.02 and 0, *i.e.* up to $\sim$ 1.8% of the iodine-enhanced lesion contrast. Cupping artifact was found to be within -1 and 0.5 % of the 5 $mg\ I/cm^3$ lesion contrast.

In sum, the *constant power* constraint drastically reduces performance of the SS-FkV technique. The decrease in LE dose allocation ratio (50 to 15% after applying the constraint) greatly affected iodine-enhanced lesion detectability, with an approximate 40% drop in maximum $CNRD_{iodine-bg}$ values (from 1.85 to 1.1 after applying the constraint). Moreover, differently from DS-DF and SS-DF techniques, iodine detectability was almost independent of the tube power. Nonetheless, residual texture and cupping magnitude remained in the same order of magnitude of the unconstrained optimization results.

SS-PC Strategy
For SS-PC technique, since only one X-ray spectrum is required, the problem is summarized in identifying maximum $CNRD_{iodine-bg}$ values as function of the X-ray tube power. This was performed by analyzing the results of the unconstrained optimization presented in the Section 5.4.

Figure 5-19a illustrates contour plots of normalized X-ray tube power, P_N, required by the SS-PC technique, as function of the tube voltage and filter thickness. A dashed line is drawn to represent the maximum $CNRD_{iodine-bg}$ values found for each tube power level in the contour plot. The correspondent $CNRD_{iodine-bg}$ values can be found in Figure 5-19b, where the same line is draw. Figure 5-19b shows that $CNRD_{iodine-bg}$ increases with the available tube power, ranging from 1.7 to 2.6. Optimal tube voltage decreases from 65 to 40 kV, while filter thickness increases from 0.05 to 0.23 mm. Notice that maximum $CNRD_{iodine-bg}$ values are bound to the lower limit of filter thickness values.

Residual texture detectability ($CNRD_{texture}$) and cupping magnitude can be found by projecting the dashed line in Figure 5-19b over the surfaces in Figures 5-16b and 5-16c, presented Section 5.4. Better texture cancellation is observed with increasing tube power, whereas cupping magnitude increases from -0.5 to 2.0%, due to lower tube voltages and increased beam hardening.

5.5.3 Iodine-Equivalent Image Quality Performance Comparison

Figure 5-20a summarizes the optimal $CNRD_{iodine-bg}$ values found with the constant power assumption for each candidate acquisition technique, as function of the normalized tube power P_N. The dark dashed line illustrates the theoretical limit for $CNRD_{iodine-bg}$, obtained with optimal monochromatic spectra (LE/HE pair at 33/34 keV, with 50% dose repartitioning). The SS-PC technique showed highest $CNRD_{iodine-bg}$ curve, while SS-FkV showed lowest $CNRD_{iodine-bg}$ curve, due to the high tube power required by LE acquisitions. Moreover, $CNRD_{iodine-bg}$ values are almost independent of the input tube power. DS-DF and SS-DF techniques showed intermediate performance in $CNRD_{iodine-bg}$ values.

To have a more practical view of the differences between the four strategies, Contrast-to-Noise Ratio (CNR) per pixel between contrast uptake and the background in recombined iodine-equivalent images were calculated for a particular set of acquisition design parameters. CNR values were subsequently translated into an effective CNR (CNR_{eff}), as defined by Rose [246, 247], as a measurement of detectability for the target iodine-enhanced lesion (2 mm diameter, 0.5 mg/cm^3 iodine uptake) in a homogeneous background (cf. Section 5.1 and Equation 5.6). Rose's threshold for minimum lesion depiction is achieved for CNR_{eff} values above 5.

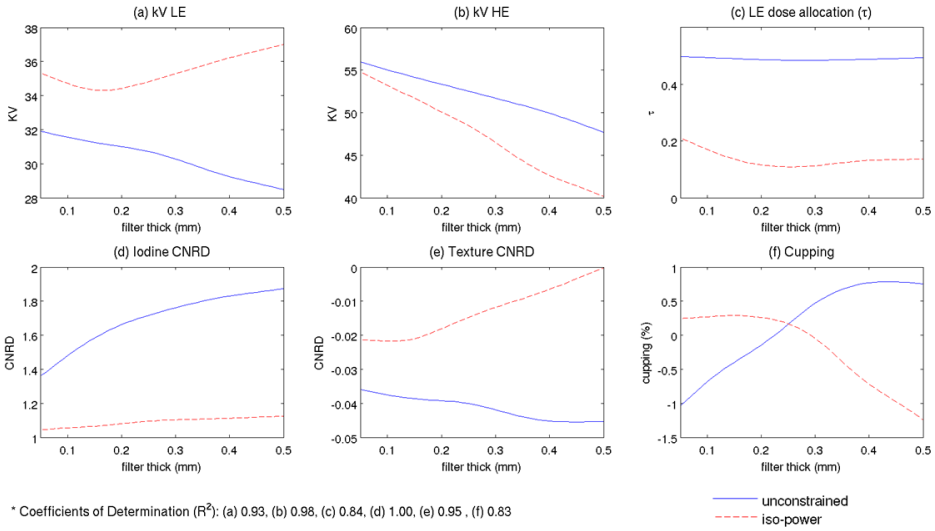

Figure 5-18: Optimization results for SS-FkV technique as function of the filter thickness when *constant power* constraint is applied. In the first row, the optimal input parameters: (a) LE tube voltage, (b) HE tube voltage and (c) LE dose allocation ratio. In the second row, the output FOM: (d) $CNRD_{iodine-bg}$, (e) $CNRD_{texture}$ and (f) $cupping(\%)$. Solid lines indicate the optimization results for the unconstrained optimization, while dashed lines indicate the optimization results when the *constant power* constraint is applied during the choice of τ_{opt}. The results are based on a 12.5% glandular 14 cm diameter phantom and computed relative to the 5 mg/cm^3 iodine-enhanced lesion

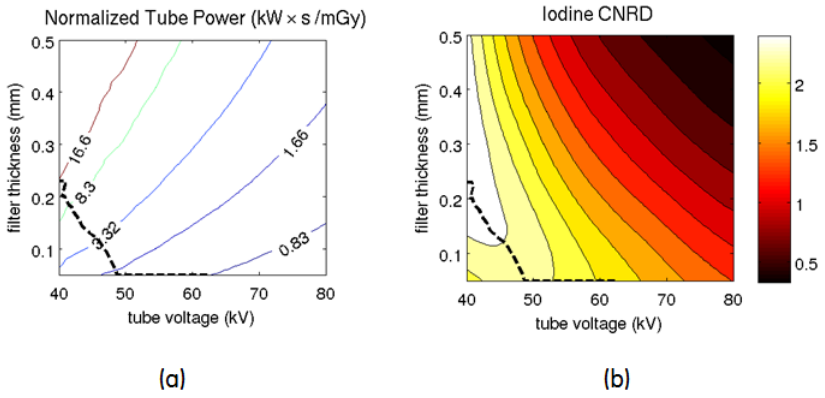

Figure 5-19: Optimization results for SS-PC technique as function of the tube voltage and filter thickness, when *constant power* constraint is applied. (a) Normalized tube power in $kW \times s/mGy$ and (b) correspondent optimal $CNRD_{iodine-bg}$. Dashed line corresponds to the maximum $CNRD_{iodine-bg}$ values found for each tube power level in Fig. (a)

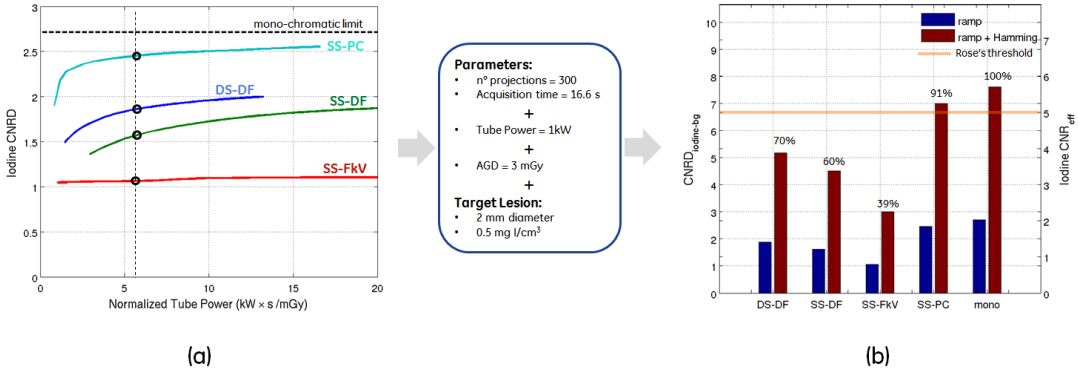

Figure 5-20: Results of the comparison between the four considered dual-energy strategies for the 12.5% glandular 14 cm diameter phantom. (a) Optimal $CNRD_{iodine-bg}$ relative to the 5.0 mg/cm^3 iodine-enhanced lesion, as function of the normalized tube power P_N. The dark dashed line illustrate the theoretical limit obtained with optimal monochromatic spectra; (b) $CNRD_{iodine-bg}$ (left ordinate axis) and correspondent CNR_{eff} (right ordinate axis) of a 2 mm diameter 0.5 mg/cm^3 iodine-enhanced lesion, when considering 300 projections acquired in 16.6 seconds and using a 1kW tube power delivering 3 mGy AGD. The ratio of CNR values with respect to the monochromatic limit is indicated in percentage

We assumed a full breast scan with three hundred projections per LE and HE spectra, acquired in a total acquisition time of 16.6 seconds. This time interval was has been used for single-energy acquisitions with the cone-beam breast CT topology published by Boone *et al.* [103], chosen as the reference geometry for this chapter. Lindfors *et al.* [127] showed that 16.6 seconds has been well tolerated by patients with a single breath hold. Optimal LE and HE acquisition parameters were chosen such as to require 1 kW tube power, since it reflects the nominal X-ray tube power of the reference cone-beam breast CT geometry [103]. This value is also very similar to typical nominal tube powers implemented in state-of-the-art mammography and digital breast tomosynthesis systems. AGD was set at 3 mGy, which corresponds approximately to the screening AGD for a two-view average-sized breast (AOP Contrast mode on GE Senographe® Essential system, for a 5 cm thick PMMA thickness [248]). Finally, in order to attenuate the unrealistic noise level generated by the ideal ramp filter (due to high-frequency signal amplification), CNR_{eff} was also calculated when a Hamming apodization function is included.

Table 5.5 summarizes the optimal input parameters entailing in 1 kW tube power and the corresponding optimal Figures-of-Merit (iodine detectability, texture cancellation and cupping magnitude). For comparison, we included optimal Figures-of-Merit when optimal monochromatic spectra are considered.

Figure 5-20b, shows the $CNRD_{iodine-bg}$ and correspondent CNR_{eff} of a 2 mm diameter 0.5 mg/cm^3 iodine-enhanced lesion, for each acquisition strategy and under the assumption just described. CNR_{eff} values for DS-DF, SS-DF, SS-FkV and SS-PC were respectively at 70%, 60%, 39% and 91% of the theoretical monochromatic limit. When the Hamming apodization filter is included, only SS-PC technique and the monochromatic implementation presented CNR_{eff} values above Rose's detectability threshold of 5.

5.5.4 Discussion

Under the same hypothesis of ideal, X-ray point source and a 100% efficient blur-free detector, in this section we imposed a constant tube power constraint to the polychromatic optimization frame-

Table 5.5: Optimal input parameters and optimal Figures-of-Merit for LE and HE polychromatic spectra requiring 1 kW tube power, per considered dual-energy acquisition strategy and for the theoretical monochromatic limit. The results are based on a 12.5% glandular 14 cm diameter phantom and computed relative to the 5 $mg\ I/cm^3$ iodine-enhanced lesion

	Optimal Input Parameters			**Optimal Figures-of-Merit**		
Technique	**LE Spectra**	**HE Spectra**	**LE dose alloc. ratio τ**	$CNRD_{iodine-bg}$	$CNRD_{texture}$	$cupping(\%)$
Mono	33 keV	34 keV	50%	2.75 (100%)	0	0
DS-DF	34 kV 0.24 mm Sn	52 kV 0.30 mm Cu	48%	1.89 (70%)	0.02	-0.95
SS-DF	34 kV 0.17 mm Sn	51 kV 0.18 mm Cu	50%	1.61 (60%)	-0.04	-1.20
SS-FkV	34 kV 0.14 mm Cu	52 kV 0.14 mm Cu	14%	1.07 (39%)	-0.02	0.29
SS-PC	-	42 kV 0.17 mm Cu	-	2.47 (90%)	-0.02	-1.88

work previously discussed in order to compare the performance of the four dual-energy acquisition strategies under evaluation in this chapter.

Comparison results between different dual-energy acquisition strategies under a *constant power* constraint revealed that iodine K-edge imaging with both ideal energy-discriminating and non-discriminating detectors, and with both image-based and projection-based recombination is feasible in terms of background texture cancellation and cupping artifact magnitude, which showed to be below the minimum target iodine-enhanced lesion concentration (0.5 $mg\ I/cm^3$). Under the idealistic hypothesis of detector performance, dual-energy acquisitions leveraging a photon-counting energy-discriminating detector (SS-PC) showed highest iodine uptake CNRD, due to the perfect spectral separation and proximity of LE and HE bins mean energies to the optimal monochromatic beam energies. On the other hand, the DE acquisitions with a single source/filter pair (SS-FkV) showed lowest iodine CNRD, mainly due to the high tube power required by LE acquisitions. Techniques applying dedicated filtration for LE and HE acquisitions (DS-DF and SS-DF) showed intermediate performance.

To have a more practical view of the differences between the four strategies, the effective CNR (CNR_{eff}), as defined by Rose [246, 247], was calculated as a measurement of detectability for the target 2 mm diameter 0.5 mg/cm^3 iodine-enhanced lesion. Under a particular set of acquisition assumptions (2 sets of 300 projections acquired in 16.6 seconds with a 1kW tube power constraint and entailing total 3 mGy AGD), the SS-PC technique was the only technique presenting CNR_{eff} levels above Rose's detectability threshold.

In this section, idealistic hypothesis for the detectors efficiencies were made. Under these conditions, the photon-counting (PC) energy-discriminating detector outperformed the non-discriminating techniques based on energy integration (EI). This result has been observed in previous optimization studies for full body dual-energy CT [267]. In literature, it has been shown however that current energy-discriminating capability of PC detectors are far from ideal (due mainly to photon pile-up and spectral distortions) and that state-of-the-art dual kV methods based on EI scintillators are still competitive with current PC-based dual-energy systems [140, 264, 267]. It must also be emphasized, that the performance of PC detectors relative to EI detector would most probably depend on the imaging task, as indicated by Wang *et al.* [268]. In light of the optimal acquisition parameters presented for the PC implementation and their tendency to narrow the optimal X-ray spectra around the iodine-K-edge for increased CNR performance, we estimate that count rate, spectral response and energy resolution are still challenges for an actual K-edge breast imaging

implementation. Although encouraging results for breast CT applications using current PC technology have been recently shown [140], further detector performance improvement may reveal the potential benefits of energy-discrimination and its clinical applications.

A Copper-filtered Fast kV switching (SS-FkV) technique was implemented in this section. Comparison between unconstrained and *constant power*-constrained optimization results revealed that the high tube power required by LE acquisition substantially decreased SS-FkV technique performance, with an approximate 40% drop in maximum $CNRD_{iodine-bg}$ values (from 1.85 to 1.1 after applying the *constant power* constraint). One possible solution is to replace the filter material from Copper to Aluminum, since both materials provide comparable X-ray spectrum shape and beam qualities, though Aluminum has nearly 30 times smaller attenuation coefficient. In a previous optimization study for single energy breast CT, Weigel *et al.* [116] showed that a Copper filtration provides slightly better contrast-to-noise ratio values when compared to an Aluminum filtration. Nonetheless, given the significant performance handicap found in our results, an Aluminum-based filtration would be fairly justified.

In this optimization study, other simplification assumptions were made. For instance, acquisitions were assumed to be performed in a "step-and-shoot" with instantaneous displacement between two consecutive view angles and therefore without introducing blur from tube motion. Additionally, a square waveform with ideal transitions in LE and HE tube voltages were assumed. If however a pulsed X-ray source with continuous rotation is considered, with no particular change to kV transitions, as long as the duty cycle (or pulse width) is the same for both LE and HE acquisitions, the optimal acquisition parameters for each candidate technique shall not change with respect to a "step-and-shoot" mode. A simple example is to assume that during one frame rate, the pulse width decreases by a factor 2 while the mA increases by a factor 2, while maintaining mAs product constant. Any change in pulse width between LE and HE acquisition can be compensated by changes in LE dose allocation ratio. Future analysis on the impact of more realistic sinusoidal tube voltage waveforms on spectral separation and iodine detectability degradation in a dual-energy breast CT setup is subject for further investigation.

In summary, if current X-ray detector technology is considered, we expect techniques with dual filtration (DS-DF and SS-DF) to be the best choice for an actual dual-energy CE-bCT implementation. Dual-source techniques are simpler to implement but probably more costly, since they require two acquisition chains. Single-source techniques are based on a single acquisition chain, but require a more complex management of tube voltage and filter switching. Although our results showed comparable performance between DS-DF and SS-DF techniques in terms of iodine uptake CNRD, the impact of cross-scatter, lag, tube voltage waveforms and other inefficiencies on image quality, as well the account for engineering trade-offs and constraints of a real dual-energy implementation could reveal further indications on the best technology path for CE-bCT. Additionally, since both ideal implementation of DS-DF and SS-DF techniques showed insufficient performance for target iodine-enhanced lesion detectability, further study on pre- and post-processing techniques for noise reduction would be beneficial before their real implementation. In this PhD thesis, a preliminary detectability study at low-dose levels leveraging two post-processing techniques dedicated for dual-energy imaging is presented further on in Chapter 7 and intends to partially address this question.

While the impact of realistic models for PC detector's energy-dependent inefficiencies have been studied elsewhere for dual-energy image quality optimization [264, 268, 269], no study has been dedicated to the energy-dependent imaging quality performance of scintillator-based EI detector while considering its energy-dependent absorption efficiency. In the next section, a preliminary study on the impact of CsI scintillator thickness on optimal dual-energy acquisition spectra for iodine K-edge breast imaging is performed.

5.6 Impact of CsI-Scintillator Thickness on Optimal Spectra

Columnar structured cesium iodide (CsI) scintillators doped with Thallium (Tl) have been widely used for digital breast X-ray imaging since last decade. Several publications have investigated their imaging performance at typical X-ray spectra for conventional digital mammography, digital breast tomosynthesis and dedicated breast computed tomography [123, 270–272]. So far, no study has been dedicated to the energy-dependent imaging performance of CsI as a function its thickness for dual-energy applications.

In this section, the impact of CsI scintillator thickness on the optimal spectra for dual-energy breast imaging combined with an iodine-based contrast agent is investigated. A new spectra optimization is performed to assess contrast-to-noise ratio between iodine-enhanced and unenhanced tissue normalized to the square root of the average glandular dose, while considering different quantum detection efficiencies.

In a first approach we considered monochromatic spectra. The optimization framework of Section 5.3 was therefore leveraged in this section.

5.6.1 Energy-Dependent Absorption Efficiency

As discussed in Chapter 2, for energy-integrating detectors equipped with scintillators, the energy-dependent absorption efficiency, $\eta(E)$, can be approximated as:

$$\eta(E) = 1 - e^{\mu_{scint}(E)t_{scint}(i)} \tag{5.11}$$

where $\mu_{scint}(E)$ is the linear attenuation coefficient at energy E of a continuous and homogeneous scintillator material and $t_{scint}(i)$ is the oblique thickness of the scintillator at detector element i. For simplicity, X-ray beam obliquity was disregarded in $\eta(E)$ calculation since it would entail only small differences in signal intensities for small incident angles [195].

Figure 5-21 shows $\eta(E)$ as a function of incident photon energy for three CsI thicknesses and for the perfect energy-integrating detector with $\eta(E) = 1$. It can be seen that $\eta(E)$ increases with scintillator thickness and all curves show discontinuities at the K-edges of Cs (36 keV) and I (33.2 keV), due to the sudden increase in their attenuation coefficients.

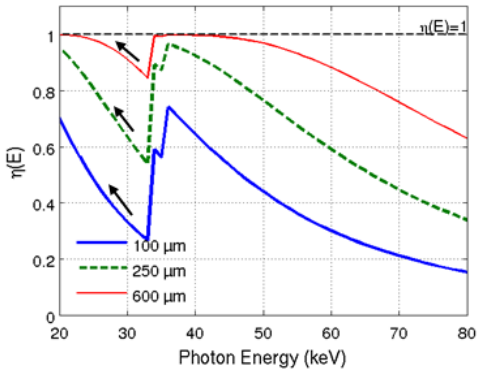

Figure 5-21: Absorption efficiency $\eta(E)$ as function of incident photon energy E for 100, 250 and 600 μm CsI thicknesses

5.6.2 Optimization Framework

The same optimization framework described in Section 5.3 was considered.

The cone-beam CT geometry with parameters described in Section 5.2 was simulated. Three 50% fibroglandular equivalent cylindrical phantoms with 10, 14 and 18 cm in diameter simulated small, average and large uncompressed breasts. They contained spherical inserts emulating homogeneous mixtures of 50% fibroglandular tissue and 0.5, 1.0, 2.5 and 5.0 mg/cm^3 of iodine (cf. Figure 5-3a, in Section 5.3).

Contrast-to-Noise-Ratio per pixel between iodine-enhanced breast tissue and background breast tissue normalized to the square root of the total AGD, $CNRD_{iodine-bg}$, was used as the Figure-of-Merit for the detectability of iodine in iodine-equivalent images.

$CNRD_{iodine-bg}$ was calculated for LE and HE beam energies pairs varying from 20 to 80 keV. For each LE and HE X-ray beam pair, LE dose allocation ratio was varied between 20 and 80%. $CNRD_{iodine-bg}$ was evaluated as a function of the LE dose allocation ratio τ.

Optimal LE and HE beam energies and optimal LE AGD allocation ratio, τ_{opt}, were identified for t_{scint} equal to 100, 250, 400, 600 and 780 μm and compared to the results obtained in Section 5.3, where a perfect energy-integrating detector with $\eta(E) = 1$, regardless of the energy value, was considered.

Below, we provide the optimal LE and HE beam pairs and optimal LE AGD allocation ratio entailing in maximum $CNRD_{iodine-bg}$ values as function of the CsI scintillator thickness and the phantom diameter.

5.6.3 Optimal Spectra and Dose Allocation for Iodine Uptake Depiction

For all experimental conditions of this section, results showed similar trends in optimal LE dose allocation ratio and $CNRD_{iodine-bg}$ as function of the LE and HE X-ray beam pairs when compared to results with a perfect energy-integrating detector, described in Section 5.3. $CNRD_{iodine-bg}$ was higher for LE and HE pairs just below and above the iodine K-edge, than for LE and HE pairs with energies farther away from the iodine K-edge discontinuity (cf. Figures 5-6, 5-7 and 5-8). Therefore, for simplicity, we did not present all the curves as function of the CsI scintillator thickness.

Figure 5-22a, 5-22b and 5-22c show optimal LE energies, optimal LE dose allocation ratio τ_{opt}, and the corresponding $CNRD_{iodine-bg}$ values for all studied CsI thicknesses and for the perfect energy-integrating detector. Figures 5-22a and 5-22b shows that optimal LE values increase as a function of CsI thickness, while τ_{opt}, decreases as a function of CsI thickness. Optimal LE energies and optimal LE dose allocation ratio for the perfect energy-integrating detector converge to 33 keV and $\sim 50\%$, respectively, discussed in Section 5.3, when CsI thickness increases.

For all studied cases, optimal HE beam energy occurs just above the K-edges of I or Cs (range 34 to 36 keV). Figure 5-22c shows that optimal $CNRD_{iodine-bg}$ increases monotonically with increasing scintillator thickness and converges to $CNRD_{iodine-bg}$ obtained with the perfect energy-integrating detector. Due to differences in the phantom thickness and since CNRD in independent of dose, for a fixed CsI thickness $CNRD_{iodine-bg}$ decreases with increasing phantom diameter. For an average sized breast, $CNRD_{iodine-bg}$ increases from 64% to 95% of the $CNRD_{iodine-bg}$ obtained with the perfect energy-integrating detector, when passing from a 100 to 600 μm thick CsI layer.

5.6.4 Discussion

Under the assumptions of primary mono-energetic X-rays and an energy-integrating noise-free blur-free detector with the same absorption efficiency at all incident beam angles, it was shown

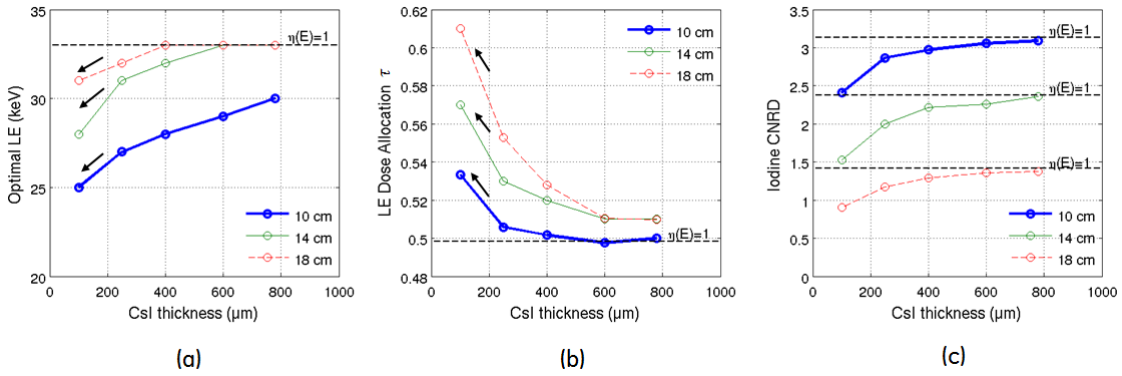

Figure 5-22: (a) Optimal LE, (b) optimal AGD allocation ratio τ_{opt} and (c) optimal $CNRD_{iodine-bg}$ as a function of the CsI scintillator thickness. The results are based on 50% glandular phantoms and CNRD values computed relative to the 5 mg/cm^3 iodine-enhanced lesion

that optimal LE and optimal LE dose allocation ratio vary up to 25% with CsI layer thickness and that optimal iodine CNRD monotonically increases with increasing scintillator thickness. It was observed that optimal LE values increase as a function of CsI thickness while optimal LE dose allocation ratio decreases as a function of CsI thickness. This trend can be seen as compensation for the loss in absorption efficiency for energies values just below the iodine K-edge (cf. black arrows in Figures 5-21, 5-22a and 5-22b). Moreover, we found that the variations in optimal LE values are more expressive as the breast size decreases, while variations in LE dose allocation ratio are more expressive as the breast size increases.

Results were shown for a cone-beam breast CT geometry, for which the breast is not compressed during imaging (10 to 18 cm in diameter). By extrapolating the trends in our results to breast sizes in the order of magnitude of compressed breasts (2 to 8 cm-thick) and CsI scintillator thickness used in digital mammography and digital breast tomosynthesis (100 – 250 μm-thick), we provide preliminary evidence to why previously found optimal spectra for dual-energy Contrast-Enhanced Mammography (CESM) and dual-energy Contrast-Enhanced Digital Breast Tomosynthesis (CE-DBT) do not bracket the K-edge of iodine as closely as expected. For instance, Puong *et al.* found that optimal LE and HE beam energies in a CESM setup with 5 cm-thick phantom and 100 μm-thick CsI are 20 and 34 keV, with 40% LE dose allocation ratio [257]. The same research group found that optimal LE and HE beam energies in a CE-DBT setup with 5 cm-thick phantom and 100 μm-thick CsI are 19 and 36 keV, with 51% LE dose allocation ratio [226]. Although the trends in our results are aligned with those found in previously published data, the optimization framework leveraged in this section should be extended to actual CESM and CE-DBT geometries and CsI thickness, in order to disclose the optimal monochromatic spectra dependency on detector efficiency.

In this section, simplified assumptions on X-ray image generation were made. A point source, emitting mono-energetic X-ray beams was assumed. Although the adoption of polychromatic spectra would degrade iodine uptake detectability, our results can be used as a preliminary detectability evaluation for polychromatic X-ray beams with average energy coincident with the studied monochromatic energies.

Idealistic hypothesis for the detector model were also made. Optical glare, the scatter of optical photons within the phosphor layer of the detector, and its degrading effect on the detector pre-sampling MTF were disregarded. Our results showed that CNRD increases with increasing scintillator thickness. However, it is known that the detector pre-sampling MTF degrades with increasing scintillator thickness, especially at high-frequency components. A blur-free assumption would in this case be interesting to evaluate iodine uptake detectability through low-frequency

metrics such as CNRD, but would possibly be insufficient for the assessment of iodine uptake morphology and other Figures-of-Merit sensible to high-frequency variations in signal intensity.

X-ray beam obliquity was not taken into account when computing $\eta(E)$. By geometric calculation, it can be demonstrated that oblique X-ray beam incidence entails up to $\sim$5% increase in t_{CsI} values (at the largest obliquity, for the largest phantom) and, as consequence, $\sim$ 3% average increase in $\eta(E)$. In cross-sectional images reconstructed at the phantom's mid-depth, differences in lesion CNRD values would be below 1% and, therefore, with imperceptible impact on the results presented above. Further studies including more realistic detector models will provide better understanding on the impact of different CsI scintillators on iodine uptake detectability and characterization.

In summary, several research papers on optimizing LE and HE X-ray spectra for dual-energy contrast-enhanced iodine breast imaging found counter-intuitive results; optimal spectra do not bracket the K-edge of iodine as closely as expected. Our work presents preliminary evidence that optimal X-ray spectra strongly depend on detector scintillator thickness. Detector energy-dependent absorption inefficiencies should therefore be taken into account when designing X-ray imaging systems for spectral applications.

5.7 Conclusions

In this chapter, under the assumptions of scatter free and perfect energy-integrating noise-free blur-free detector, a spectral optimization study was performed aiming to reveal the dual-energy acquisition strategy and acquisition parameters maximizing the performance of CE-bCT technique in the depiction of contrast-agent uptakes in recombined iodine-equivalent images, as well as the depiction of masses and microcalcifications in LE morphological images.

Through a monochromatic spectra optimization study, we found that to obtain optimal iodine detectability in recombined dual-energy images, LE and HE spectra need to closely bracket the iodine K-edge (33.2 keV) and an approximate 50%-50% average glandular dose repartitioning between LE and HE exposures is required. Moreover, optimal LE values optimizing masses and microcalcifications are close to those optimizing iodine uptake detectability. These results demonstrate the feasibility, in terms of spectra, of a CE-bCT system capable to provide both functional and morphological information. The effective CNR (CNR_{eff}), as defined by Rose [246,247], was also calculated as a measurement of detectability for the target 2 mm diameter 0.5 mg/cm^3 iodine-enhanced lesion, at 3 mGy average glandular dose (approximately the screening AGD for a two-view average-sized breast using the AOP[8] Contrast mode of GE Senographe® Essential system). Using optimal input parameters for the 14 cm diameter 50% fibroglandular equivalent phantom, we showed that CNR_{eff} is slightly above Rose's detectability criterion.

Using the monochromatic optimization results as first approximation to design LE and HE polychromatic spectra, a second optimization study was performed. Four dual-energy acquisition strategies, based on state-of-the-art dual-energy system designs, were considered as potential candidates for dual-energy CE-bCT and individually optimized. Optimization results showed that through a careful choice of acquisition parameters (Table 5.3) all four candidate strategies were able to provide recombined iodine-equivalent images with cupping artifacts and residual texture below 0.5 $mg\ I/cm^3$ contrast levels, *i.e.* the minimum iodine concentration expected in clinical practice if a typical injection protocol of contrast-enhanced mammography is considered (cf. Section 5.1).

In order to a have glimpse on the impact of their practical design constraints, the performance of the four acquisition strategies was compared under a *constant tube power* constraint for the LE and HE acquisitions. We showed that a dual-energy implementation leveraging an ideal photon-counting energy-discriminating detector showed highest iodine uptake detectability, in terms of per-pixel CNR, due to perfect spectral separation and proximity of LE and HE bins mean energies to the optimal mono-chromatic beam energies. On the other hand, DE acquisitions with a single source/filter pair showed lowest detectability, due to the high tube power required by LE acquisitions. Non-discriminating techniques applying dedicated filtration for LE and HE acquisitions showed intermediate performance. The effective CNR (CNR_{eff}) was also calculated as a measurement of detectability for the target 2 mm diameter 0.5 mg/cm^3 iodine-enhanced lesion. Under a particular set of acquisition assumptions (2 sets of 300 projections, acquired within 20 seconds with a 1kW tube power constraint and entailing 3 mGy AGD), the photon-counting energy-discriminating technique was the only technique presenting CNR_{eff} levels above Rose's detectability criterion.

Finally, a monochromatic spectral optimization study considering different CsI layer thicknesses and, as consequence, different energy-dependent absorption efficiencies, was performed. In this study we showed that optimal spectra do not bracket the K-edge of iodine as closely as expected. In fact, optimal LE beam energy and optimal LE dose allocation ratio varied up to 25% with CsI layer thickness. Variations in optimal LE beam energy and dose allocation ratio act as compensation for the loss in absorption efficiency for energies values just below the iodine K-edge, whenever the CsI layer thickness vary. If the trends in our results are extrapolated to breast sizes in the order of magnitude of compressed breasts and CsI scintillator thickness used in digital mammography, we can provide preliminary evidence to why previously found optimal spectra

[8] AOP – Automatic Optimization of Parameters for exposure control system

for dual-energy Contrast-Enhanced Mammography (CESM) and dual-energy Contrast-Enhanced Digital Breast Tomosynthesis (CE-DBT) do not bracket the K-edge of iodine as closely as expected [226, 257]. We also showed that optimal iodine uptake CNRD monotonically increases with increasing scintillator thickness. However, it is known that the detector pre-sampling MTF degrades with increasing scintillator thickness, especially at high-frequency components, due to the spreading of optical quanta in the scintillator. Nonetheless, if the optical spreading transfer function can be estimated, the blur introduced in the pre-sampling MTF might be corrected through post-processing techniques for resolution restoration [251, 273].

In this chapter, a throughout evaluation of topological parameters, detector technology and other energy-independent system design parameters impact on CE-bCT image quality was not in the main objectives. In reality, energy-independent system design components defining spatial resolution and noise propagation have been intensively studied for single-energy cone-beam breast CT acquisitions. In particular system topology [119–123], acquisition orbit [118, 136, 137] and reconstruction algorithms [133, 134, 238] impact on the detectability of fibroglandular tissue and microcalcifications have been investigated. Assuming linearity and stationarity of first- and second-order statistics, it was assumed that these results can be extrapolated to describe spatial resolution and noise propagation in the dual-energy imaging framework studied in this chapter.

A noise-free blur-free detector was assumed in all optimization studies. A positive consequence is that the derived optimal parameters and feasibility conclusions could be used as *a priori* information for future studies on real X-ray systems. However, although photon-counting energy-discriminating detectors showed, in theory, better detectability results during our optimization study, further investigations taking into account more realistic photon-counting detectors models are necessary to evaluate their degradation effect in image quality and the impact on iodine uptake detectability. In particular, the high detector frame rates and low incident quanta necessary for minimal photon pile-up, as well as energy-dependent inefficiencies such as spectrum tailing and energy resolution [264, 268], impose substantial constraints to the photon-counting model and affect its energy discriminating ability in dual-energy imaging setups.

In summary, we provided in this chapter an extended overview on the dual-energy acquisition parameters (monochromatic and polychromatic) and acquisitions strategies maximizing image quality in recombined dual-energy CE-bCT images. With knowledge of the optimal parameters for CE-bCT and CE-DBT, in the next chapter, we compare their potential to accurately depict and localize tumors, as well as to provide accurate quantitative information on contrast uptake morphology and concentration, at radiation dose levels comparable to a two-view mammogram.

Chapter 6

Quantitative Comparison Between CE-bCT and CE-DBT

As discussed in Chapter 1, CE-DBT and CE-bCT are two potential candidates for providing accurate quantitative information on breast lesions' location, morphology, and functional information. This chapter aims to perform a preliminary comparison between CE-DBT and CE-bCT in their ability to provide quantitative information at low radiation dose levels. For a fair comparison, we consider optimal acquisition parameters for CE-DBT and CE-bCT maximizing the depiction of contrast-agent uptake in recombined iodine-equivalent images. Optimal dual-energy acquisition parameters for CE-DBT have been previously assessed and are available in literature [17–26]. For CE-bCT, an optimization study aiming to reveal the dual-energy acquisition parameters maximizing iodine detectability was presented in Chapter 5.

In the comparison studies described in this chapter, reconstructed CE-DBT and CE-bCT images of respectively compressed and uncompressed breast phantoms were simulated using optimal dual-energy acquisition parameters. The breast phantoms contained lesions of different sizes, shapes and iodine concentrations, enabling to compare both CE-DBT and CE-bCT topologies with respect to the ability to accurately detect and characterize contrast-enhanced lesions through localization, morphology, and the associated contrast uptake. In Section 6.1, the effect of CE-DBT and CE-bCT topologies on 3D lesion extent estimation precision is investigated. In Section 6.2, the quantitative accuracy of both topologies on the estimation of local quantities of iodine is compared. For a more complete evaluation of both system potentials, in Section 6.3, a mesh-based anthropomorphic breast model with mathematically defined anatomical structures is exploited in a reader preference study aiming to assess and compare the depiction and characterization of embedded iodine-enhanced lesions of different sizes, shapes and iodine uptakes.

In all comparison studies, average glandular dose (AGD) was similar to AGD for two-view mammography. Moreover, in order to keep simulation time manageable and without any significant effect on the Figures-of-Merit defined in this chapter, primary mono-energetic X-rays and perfect energy-integrating noise-free blur-free detectors were assumed.

6.1 Iodine-Enhanced Lesion 3D Extent Estimation in CE-bCT vs CE-DBT

As a first step in the assessment of breast CT potential benefits in comparison to breast tomosynthesis, the quantitative accuracy of CE-DBT and CE-bCT in term of 3D lesion extent was investigated through theoretical modeling. At this point, lesion detectability was not considered and simulations were performed without noise. In this case, only the systems' geometry, angular sampling, and reconstruction algorithm are assumed to impact quantification accuracy.

Previously described cone-beam topologies and acquisition techniques were compared. For CE-DBT, a topology similar to a CE-DBT prototype based on a GE Senographe® DS system (GE Healthcare; Chalfont St Giles, UK) using a dual-energy (DE) subtraction technique was investigated [274]. For CE-bCT, a cone-beam topology similar to that published by Boone et al. [127] using a dual-energy (DE) subtraction was investigated.

6.1.1 Breast Phantoms and X-ray Image Simulation

Figure 6-1 illustrates the investigated CE-DBT and CE-bCT topologies and phantoms. Table 6.1 summarizes the model parameters to simulate the CE-DBT and CE-bCT implementations. Two 50% fibroglandular equivalent mathematical phantoms were simulated. For CE-DBT, a 5 cm thick half-cylinder was used to mimic the breast under compression, while for CE-bCT a 14 cm diameter cylinder was used to mimic the same breast without applying compression and with the patient in prone position [162]. Spherical lesions with 2 to 20 mm diameters and 0.5, 1.0, 2.5 and 5.0 mg/cm^3 iodine concentrations were embedded in the phantoms. They were positioned at three distances from the chest wall side of the detector, in order to assess the effect of the cone-beam artifact on 3D lesion extent (especially in the cone direction – z-axis).

To evaluate the impact of CE-DBT limited depth resolution, in addition to spherical lesions we also considered lesions with ellipsoidal shape, with major axis aligned with the system depth direction (y-axis). Different ellipsoid eccentricities were considered while varying the traverse diameter length (y-axis) and keeping the conjugate diameter (x-z plane direction) constant at the nominal spheres diameter (2 to 20 mm). The lesion eccentricity index ϵ was defined as:

$$\epsilon_{y,xz} = \frac{Y}{X} = \frac{Y}{Z} \tag{6.1}$$

where X, Y, Z are the true lesion dimensions in x-, y- and z-axis directions, respectively.

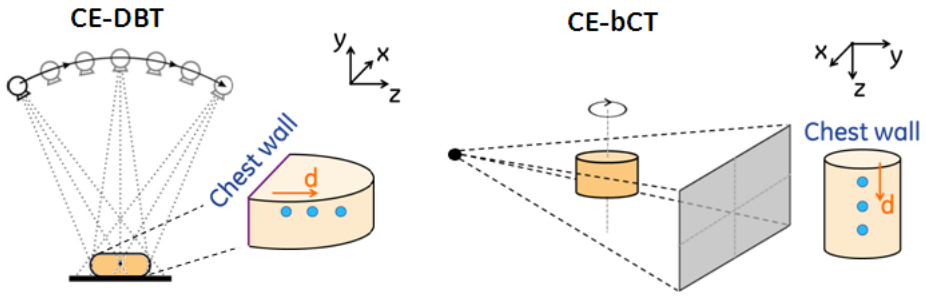

Figure 6-1: CE-bCT and CE-DBT topologies and phantom configurations for quantitative comparison studies of Sections 6.1 and 6.2. Iodine-enhanced lesions were positioned along the rotation axis, at distance d from the chest wall side of the detector.

Table 6.1: Parameters used to simulate the CE-bCT and CE-DBT implementations in the investigations of Sections 6.1 and 6.2

Model parameters		CE-DBT	CE-bCT
Spectrum	Mono-energetic	20 & 34 keV	30 & 34 keV
	Total AGD	3 mGy	
	Dose ratio (LE/HE)	50/50%	
Geometry	Mag (SDD/SID)	660mm / 620mm	880mm / 460mm
	no. of projections	15 & 40°range	300 & 360°range
Phantom		Thickness: 5 cm	Diameter: 14 cm
	Composition	50 % fibro-glandular equivalent	
	Lesions	Diameter: 2, 5, 10, 15, 20 mm Iodine concentration: 0.5, 1.0, 2.5,5.0 mg/cm^3 Distance from chest wall: 20, 45, 70 mm	
Flat detector	Pixel size	0.100 mm	0.394 mm
Reconstruction	Method	FBP	FBP
	Voxel size	$0.1 \times 0.1 \times 1.0\ mm^3$	$0.410 \times 0.410 \times 0.410\ mm^3$

Perfect energy-integrating detectors that do not generate any kind of noise or blurring were assumed. X-ray projections were simulated using mono-energetic X-ray beams, assuming primary X-rays only. For CE-DBT, a projection-based dual-energy recombination technique was used to generate iodine-equivalent projection images. Tomographic reconstruction of the iodine projections was subsequently performed using a Filtered Backprojection (FBP), with a filter designed following the methodology described in [275], to obtain reconstructed iodine images parallel to the detector array with 1 mm spacing and an in-plane voxel pitch of 0.1 mm. For CE-bCT an image-based dual-energy recombination technique was considered, due to its easier implementation and since projection-based recombination with monochromatic spectra would lead to the exact same results (cf. Chapter 4 for more details on projection-based and image-based dual-energy recombination). LE and HE projection images were reconstructed by FBP, using a ramp filter and a 0.410 mm isotropic voxel size, such as to avoid spatial distortions caused by apodizing filter and anisotropic voxels, respectively. The reconstructed LE and HE attenuation volumes were then recombined into an iodine-equivalent volume. Details on image and projection domain dual-energy recombination techniques for CE-DBT and CE-bCT are provided in Section 4.4.

6.1.2 Lesion Extent Estimation and Quantitative Analysis Method

Automatic Lesion Extent Estimator

Lesion extent was evaluated independently in the x, y, z directions (Figure 6-1), using the reconstructed iodine images for CE-DBT and CE-bCT and an automatic estimator, $\mathcal{A}$. The estimator is defined as the maximum of the convolution of a 1D profile through the lesion's center of mass (COM), f, with a sliding rectangle function, h, with varying width D_W. For example, $\tilde{D}$ in the x-direction was computed as:

$$\tilde{D} = \arg\max_{D_W}\{f(x) * h(x)\}, \quad \text{with} \quad h(x) = \begin{cases} 1/D_W & ,|x| \leq D_W/2 \\ -1/(N - D_W) & ,\text{elsewhere} \end{cases} \tag{6.2}$$

where N is the length of $h(x)$.

Figures 6-2a and Figure 6-2c illustrate two lesion profiles $f(x)$, respectively, a sharp and a blurred rectangular window with $D_{true} = 80\ pixels$, as well as the sliding rectangular window $h(x)$ and the calculated convolutions $f(x) * h(x - \Delta x)$, with maximum value identified by the red circles. By convolving $f(x)$ with sliding windows with different widths D_W, the curves in Figures 6-2b and 6-2d are obtained. They illustrate the calculated values of the expression $max\{f(x) * h(x, D_W)\}$

in Equation 6.2 as function of the window width D_W. The estimated lesion extent $\tilde{D}$ is the width W for which the expression is at its maximum value (red circles).

Notice that there exists a small difference $\Delta\tilde{D}$ in the estimated lesion extent, as shown in Figures 6-2b and 6-2d. This is due to the blurring present in one of the lesion profiles. This is a simple illustration on how blurring due to the system's MTF is introduced. Since in a real scenario the system MTF can be estimated, a deconvolution could be performed in order to achieve more accurate estimations. In this investigation however, this is performed by the linear regression calibration.

The difference between $\tilde{D}$ and D_{true}, *i.e.* the true lesion dimension, was minimized through linear regression:

$$D_{true} = \underbrace{\alpha \cdot \tilde{D} + \beta}_{\text{estimation of } D_{true}} + \varepsilon \tag{6.3}$$

where α and β are calibration parameters and ε is the residual error. The coefficients α and β were obtained by linear regression using a subset of simulated images with known lesions sizes. The regression was repeated for each axis direction separately and included all lesion diameters, positions and iodine concentrations. In this case, no hypothesis is made on the system's MTF, and the estimated extent is the best possible estimation within the limits of the estimator $\mathcal{A}$ (*e.g.* the choice of a rectangular sliding window, instead of a blurred one).

Figure 6-3 summarizes the steps during automatic lesion extent assessment.

Multivariable Full Factorial Analysis
Since digital detectors are not shift invariant, the imaged lesion size depends on its alignment with respect to the sampling grid. Therefore, the simulations were repeated by shifting the lesions' COM by sub-voxel values in all three directions. The large obtained dataset ($>$ 1000 simulated lesions) allowed to calculate the residual error's mean, $\hat{\varepsilon}$, and standard deviation, σ_ε, in lesion extent estimation. Since $\hat{\varepsilon}$ tends towards zero due to calibration regression (Equation 6.3), only lesion size estimation precision was characterized through the assessment of σ_ε.

A full factorial experiment was designed to understand the impact of iodine concentration, lesion diameter and position (the independent variables) on the measurement precision, described by σ_ε (the observations). A general linear equation with crossed terms describes the interactions within the model:

$$\sigma_\varepsilon = a_0 + a_s X_s + a_p X_p + a_c X_c + a_{sp} X_s X_p + \ldots + a_{spc} X_s X_p X_c \tag{6.4}$$

where X_s, X_p and X_c represent lesion size, position and iodine concentration values, respectively. Statistical hypothesis tests were applied to verify the statistical significance of each factor in the model. The level of significance for the p-values was set at 0.05. The data analysis was performed using Minitab® Statistical Software (v12, Minitab Inc.; Conventry, UK).

6.1.3 Effect of CE-bCT vs CE-DBT Topologies

The obtained results indicate that the linear regression fit is adequate to estimate D_{true}; R^2 values were found to be larger than 0.999 (t-test, $p < 0.001$) for all axes and both topologies, except for the y-direction in CE-DBT ($R^2 = 0.79$). Figure 6-4a shows the calibration of the automatic estimator for CE-DBT depth-direction. Assuming that the reconstructed volume is limited to the 5 cm phantom thickness (blue diamond markers), the automatic estimator is unable to differentiate lesions $> 15mm$ in diameter positioned at mid-depth in the phantom. Due to CE-DBT's limited

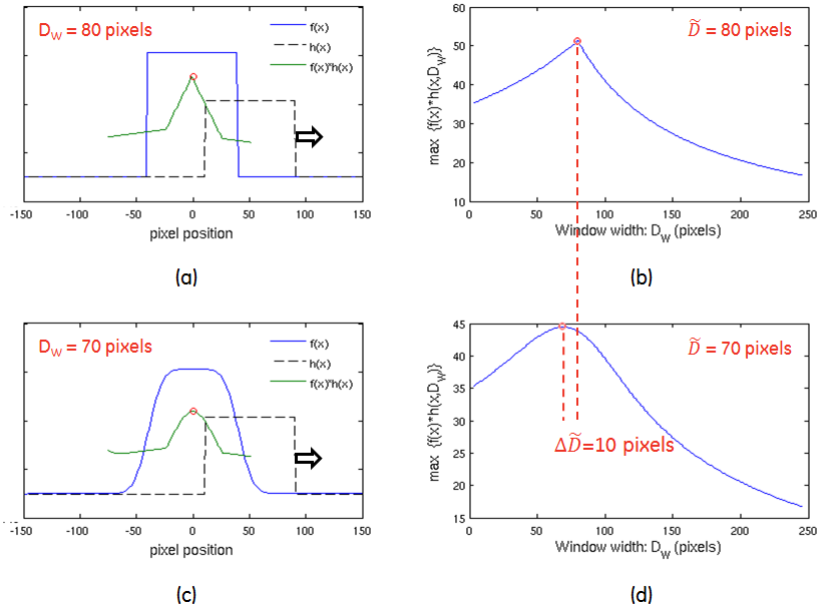

Figure 6-2: Illustration of 3D lesion extent estimation. (a)-(c) Examples of two different lesion profiles $f(x)$ with $D_{true} = 80\ pixels$, the sliding rectangular window $h(x)$ and the convolution $f(x) * h(x - \Delta x)$; (b)-(d) calculated values of the expression $max\{f(x) * h(x, D_W)\}$ for increasing window width D_W. The red circles in all graphs indicate the estimated lesion extent

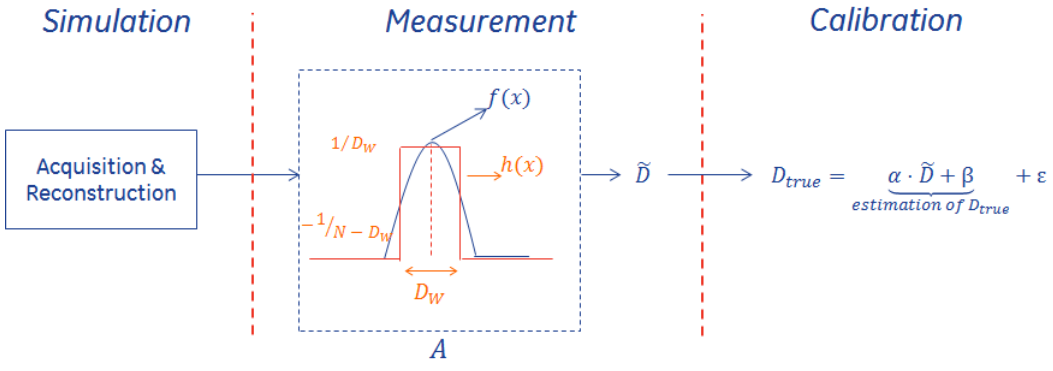

Figure 6-3: Method for automatic lesion extent assessment; $\mathcal{A}$ represents the automatic estimator, $f(x)$ and $h(x)$ a 1D lesion profile and the rectangle window function in the x direction

depth resolution in the y-direction, lesions appear ∼3 times larger in that direction[1]. This is illustrated in Figure 6-4b, where a reconstructed coronal slice (y-x plane) passing through the center of a 20 mm diameter spherical lesion is shown. To assess the precision to estimate lesion dimension in the y-direction, the analysis was repeated with 10 cm thick phantoms and lesions positioned at mid-depth (red circle markers in Figure 6-4a). This resulted in an improved fit in the y-direction ($R^2 > 0.995$, t-test, $p < 0.001$) without affecting the original calibration parameters in the x- and z-direction.

Figure 6-5a summarizes the overall precision in spherical lesion diameter estimation; for both topologies σ_ε is shown for the x-, y- and z- directions. For CE-DBT, the precision to estimate lesion diameter in the in-plane direction is about twice the in-plane voxel dimension (0.1 mm), while the precision in the y-axis direction is about half the spacing between reconstructed slices. For CE-bCT the precision to estimate lesion dimension is similar in all three axes directions; the precision is approximately half the voxel dimension (0.410 mm).

Figure 6-5b summarizes the factorial analysis experiment; for both topologies, σ_ε is shown as a function of each independent variable (lesion concentration, lesion diameter and distance from chest wall) and for the x-, y- and z -directions. Figure 6-5b highlights σ_ε variations for the independent variables who showed statistically significant effect on σ_ε (p-values smaller than 0.05), while leaving transparent those who did not presented enough statistical significance. In CE-DBT, measurement precision is affected by the true lesion diameter in the three directions (t-test, p-values, 0.001, 0.064, and 0.001 for the x-, y- and z-direction respectively) and by the lesion's iodine concentration only in the depth-direction (t-test, $p = 0.029$). The magnitude of these effects is however smaller than the voxel dimensions, in all three directions. No statistically significant effect on σ_ε as function of the lesion position was found. In CE-bCT, measurement precision is only affected by the true lesion diameter (t-test, $p < 0.001$). Again, the magnitude of this effect is smaller than the voxel dimension. No statistically significant effect on σ_ε as function of the lesion iodine concentration and position was found for CE-bCT.

Effect of Lesion Eccentricity

Figure 6-6 illustrates the effect of CE-bCT and CE-DBT topologies in the estimation of ellipsoidal lesion extent in the depth direction. Figure 6-6 shows the average measured ellipsoidal lesion eccentricity $\tilde{\epsilon}_{y,xz}$ versus true lesions eccentricity $\epsilon_{y,xz}$ for both CE-bCT and CE-DBT, considering all iodine concentrations and x-z plane diameters (except 2 mm diameter lesions, since low $\epsilon_{y,xz}$ values entail in measurement imprecision due to topology spatial resolution limits). Bars indicate one standard deviation. The ideal curve is also illustrated by the unit slope (dashed line). For CE-DBT, lesion extent estimation in y-axis is poorly correlated with its true values, while CE-bCT presented nearly perfect correlation.

6.1.4 Discussion

This section focused on the quantitative comparison of a cone-beam CE-bCT and a cone-beam CE-DBT topology in the assessment of iodine-enhanced lesion 3D extent. To assess lesion extent in the reconstructed slices, a calibrated automatic estimator was proposed. Without quantum noise, this estimator was shown to be robust to all simulated lesions and a factorial experiment demonstrated the effect of lesion size, position and iodine concentration on estimation precision.

In the absence of noise, the results showed that CE-DBT and CE-bCT precision to estimate lesion dimension was similar in the in-plane direction, while CE-bCT was superior to estimate lesion dimension in the depth direction. This result was expected, despite the larger voxel size of

[1]It must be emphasized that the 3-fold magnification factor is strictly dependent on DBT acquisition topology, as a direct consequence of incomplete data sampling (cf. Annex A.5 for more details on angular sampling effect on Radon transform and tomographic reconstruction); it should vary with DBT total angular span and the implemented acquisition orbit

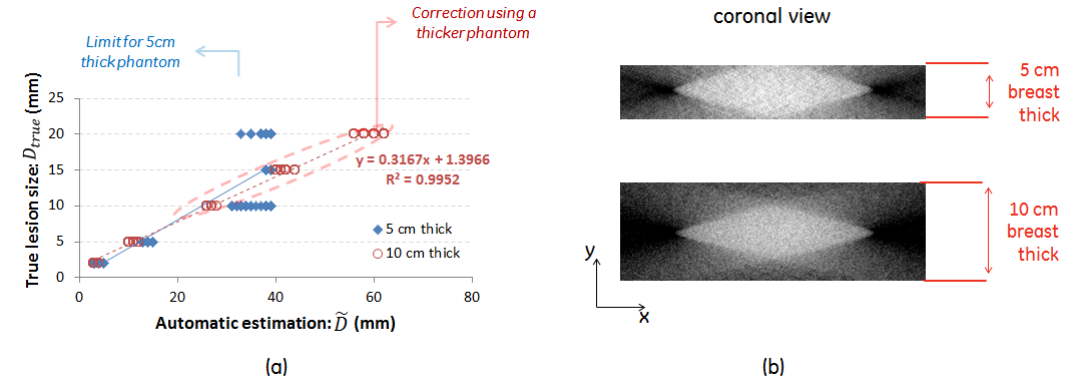

Figure 6-4: Reconstructed lesion magnification in the CE-DBT depth-direction, due to limited angular span acquisition; (a) Automatic estimator calibration for CE-DBT depth-direction when a 5 cm-thick (blue diamond markers) and 10 cm-thick (red circle markers) phantoms are considered. We can note that estimation precision in the y-axis decreases with the lesion diameter; (b) Reconstructed coronal slice (y-x plane) crossing the center of a 20 mm diameter spherical lesion inside 5 cm and 10 cm-thick phantoms

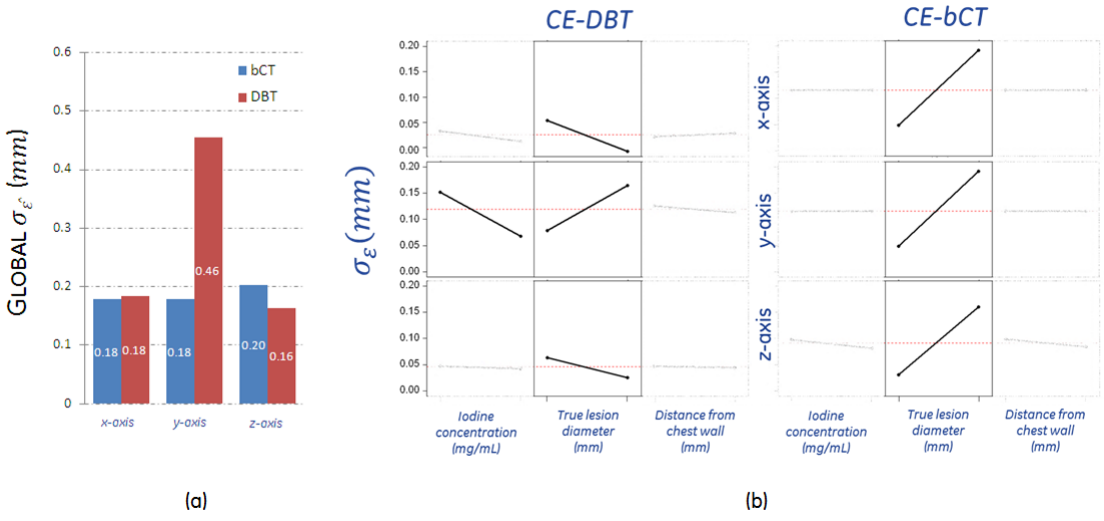

Figure 6-5: Results of 3D lesion estimation precision comparison between CE-bCT and CE-DBT. (a) Overall precision to estimate lesion diameter with CE-DBT and CE-bCT by evaluating the standard deviation, σ_ε, of the residual errors, ε, in the three axis directions; (b) Main effect of independent variables on lesion extent estimation precision. Highlighted σ_ε variations correspond to the independent variables who showed statistically significant effect on σ_ε (p-values < 0.05), while transparent variations correspond to those who did not

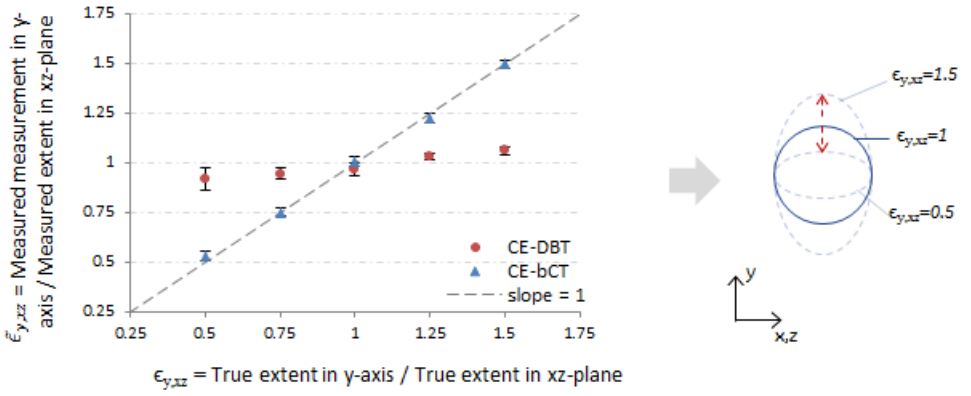

Figure 6-6: Measured vs true ellipsoidal lesions eccentricity in both CE-bCT (solid line) and CE-DBT (dot-dashed line), as well as the ideal behavior illustrated by the unit slope (dashed line)

the CE-bCT images, because CE-bCT is characterized by an inherently isotropic spatial resolution, while CE-DBT has limited resolution in the depth direction (y-axis).

A multifactorial analysis demonstrated that the precision to estimate lesion dimension was affected by lesion size and iodine concentration for CE-DBT, and only by lesion dimension for CE-bCT. If instead an ellipsoidal shape, with major axis aligned with the system depth direction is considered, the automatic estimator reveals that for CE-DBT, the estimated extent in the y-axis is poorly correlated with its true values. For CE-bCT, estimated lesion extent in the y-axis was perfectly correlated with the true extent in the same axis (cf. Figure 6-6). Hence, we can conclude that any attempt to measure lesion extent in CE-DBT depth direction is far from accurate. Moreover, introducing *a priori* knowledge from extent measurement in the focus plane would entail in misleading results, since measurement in-plane and depth direction measurement are poorly correlated.

The simulation studies of this section were performed without any source of noise. Although not demonstrated here, we tested the simulation setup described in this section in the presence of quantum noise correspondent to a 3 mGy average glandular dose. In this scenario, the automatic estimator was shown to be inefficient for lesions with low CNR. In addition, the efficiency of the estimator with respect to the human observer (*i.e.* the radiologist) was has not been investigated. Other methods based on image segmentation have been developed to highlight the contour of breast lesions in morphologic DBT [276–278] and bCT [279–281] setups. They are often cross-validated with manually-drawn lesion outlines in the presence of noise and provide good correlation with the human observer. If combined to a calibration procedure using known lesion sizes, they could all be instrumented to assess the acquisition topology effect on iodine-enhanced lesion 3D extent. In Section 6.3 that follows, a study including human observers is described to properly assess the accuracy and precision of lesion extent estimation in the presence of noise.

The results presented in this section are a first step in the comparison of CE-DBT and CE-bCT for their quantitative performance. By assuming an ideal monochromatic point source, primary only X-rays and perfect energy-integrating detectors, we only assessed the impact of CE-DBT and CE-bCT topologies. The framework proposed in this section could be used to further compare dual-energy CE-DBT and CE-bCT systems while accounting for additional and/or more realistic physical phenomena in the image simulation chain, and evaluate their individual impact on 3D lesion extent estimation accuracy and precision. Inclusion of more a realistic imaging chain could reveal further differences between CE-bCT and CE-DBT performances.

6.2 Iodine Uptake Quantification in CE-bCT vs CE-DBT

As discussed in Chapter 1, imaging techniques combined with intravenous contrast agents have been developed to highlight breast tumor angiogenesis. In breast imaging, the measurement of vascular density associated to pathogenic angiogenesis can provide additional diagnostic information [33], for example on its association with invasive breast cancers [34–36] and its aggressiveness [37–39]. Therefore, the ability to quantify intravenous vascular contrast agents uptakes in the breast could be a useful clinical information.

In this section, the effect of CE-DBT and CE-bCT topologies on iodine uptake quantification estimation accuracy is investigated.

6.2.1 Breast Phantoms and X-ray Image Simulation

The analytical breast phantoms and X-ray image simulation framework described in Section 6.1 were leveraged for iodine uptake assessment (Figure 6-1 and Table 6.1). Both spherical lesions with 2 to 20 mm diameters and ellipsoidal lesion shapes, elongated along CE-DBT depth-direction (y-axis), were embedded in the phantoms at three distances from the chest wall side of the detector. Iodine concentrations of 0.5, 1.0, 2.5 and 5.0 $mg\ I/cm^3$ were considered.

The simulations were repeated without quantum noise and with quantum noise corresponding to a total average glandular dose (AGD) equal to 3 mGy, with 50/50% AGD repartitioning between LE and HE acquisitions.

6.2.2 Figure-of-Merit for Iodine Quantity Estimation

As discussed in Chapter 4, iodine-equivalent images produced from dual-energy three-material decomposition have, in theory, signal intensities (SI) proportional to the quantity of iodine per unit of volume. However, in the presence of beam-hardening, scattered radiation and other artifacts, SI values may deviate from its expected value. Nonetheless, if a proper decomposition method is implemented, the relative intensity of iodine uptake with respect to its background is proportional to local iodine quantities, despite absolute SI values having no particular physical meaning. Image contrast is therefore a better suited metric to estimate iodine quantities than direct SI measurements.

Iodine-enhanced lesion-to-background contrast, C, was used as metric for iodine uptake quantity in recombined iodine-equivalent images:

$$C = SI_{iodine} - SI_{bg} \tag{6.5}$$

where SI_{iodine} and SI_{bg} are, respectively, the average per-pixel SI in an iodine-enhanced region of interest (ROI) and a non-iodine enhanced neighboring background ROI. SI_{iodine} and SI_{bg} were computed in the reconstructed slices centered at the lesion's COM.

To account for the different signal intensity scaling of the CE-DBT and CE-bCT reconstruction algorithms, the absolute lesion contrast-to-background, C, was normalized to the absolute lesion contrast-to-background of a reference lesion: a 10 mm diameter reference lesion, positioned at 20 mm from the chest wall side of the detector and with the same iodine concentration as the lesion under consideration. We define therefore a relative lesion-to-background contrast metric, C_{rel},

$$C_{rel} = \frac{SI_{iodine} - SI_{bg}}{SI_{iodine}^{10mm} - SI_{bg}} \tag{6.6}$$

Notice that C_{rel} is independent of lesion iodine concentration.

6.2.3 Effect of CE-bCT vs CE-DBT Topologies on Quantification Accuracy

Fig. 6-7 shows average C_{rel} values as a function of spherical lesions diameter and position in the phantom. For CE-DBT, C_{rel} is greatly affected by lesion diameter, with an approximate linear relationship for lesion diameters between 5 and 20 mm, and a larger drop for the 2 mm diameter lesion. For CE-bCT, C_{rel} is almost constant for lesion diameters between 5 and 20 mm. For the 2 mm diameter lesion, C_{rel} values were a slightly lower than 1. In this case, for both CE-DBT and CE-bCT, measurement accuracy was affected by the voxel dimension. For CE-DBT and CE-bCT the cone-beam artifact has only a small effect on C_{rel}; for lesions positioned further away from the chest-wall side C_{rel} decreases up to 1% and 5% for CE-DBT and CE-bCT, respectively.

Figure 6-7 shows mean (unfilled markers) and standard deviation (error bars) in C_{rel} values for CE-DBT and CE-bCT, when quantum noise at 3 mGy AGD is added to the simulations. Average C_{rel} values were found very similar to those obtained for simulations without noise. For CE-DBT, standard deviation remains constant with increasing lesion size, while for CE-bCT, standard deviation decreases with increasing lesion size. For lesions > 10 mm in diameter, CE-bCT was more precise than CE-DBT.

Effect of Lesion Eccentricity

Figures 6-8a and 6-8b show relative contrast C_{rel} as function of the lesion eccentricity $\epsilon_{y,xz}$ (Equation 6.1) for CE-bCT and CE-DBT, respectively. For CE-DBT, C_{rel} increases with both lesion eccentricity and lesion diameter in the x-z plane. For CE-bCT, C_{rel} is practically independent of lesion dimension for all three axes directions when lesion size extends the voxel size, but slightly decreases when the lesion diameter is smaller than 5 mm.

6.2.4 Discussion

This section focused on the quantitative comparison of a cone-beam CE-bCT and a cone-beam CE-DBT topology in the assessment of iodine uptake estimation accuracy. Relative image contrast between iodine-enhanced lesions and background breast tissue was used as figure of merit translating local quantities of iodine in recombined iodine-equivalent images. Relative image contrast showed very good agreement with and without quantum noise, but may have a different behavior when applying more advanced reconstruction algorithms.

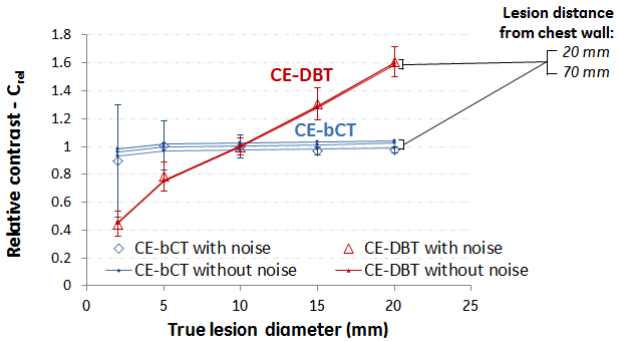

Figure 6-7: C_{rel} as a function of lesion diameter, for lesions positioned at different distances from the chest wall. For CE-DBT, C_{rel} is 60% higher for 20 mm diameter lesions than for 10 mm lesion, while for CE-bCT C_{rel} is almost independent of lesion diameter.

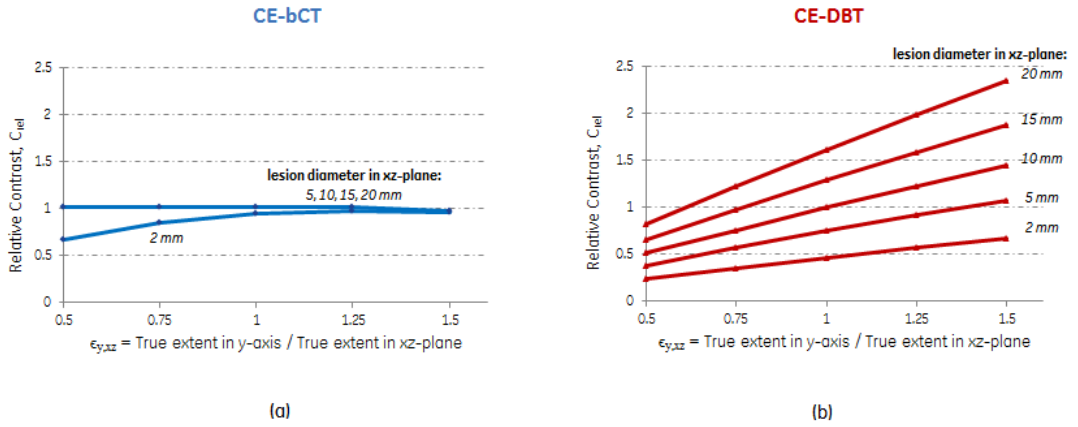

Figure 6-8: C_{rel} as function of the ellipsoid depth-direction eccentricity for (a) CE-bCT and (b) CE-DBT, for different x-z plane diameter values

For CE-DBT, our results show that lesion contrast-to-background increases with lesion diameter. As suggested previously, relative image contrast can be used to estimate the iodine area density when the appropriate transformation is known. Since contrast in CE-DBT depends on lesion size (Figure 6-7), one could say that the accuracy of iodine concentration estimation can be improved by including the estimated lesion diameter as *a priori* information. This conclusion was also drawn by Hill *et al.* [95] in an experimental study on iodine contrast agent kinetics CE-DBT. However, when analyzing lesion contrast-to-background for ellipsoidal lesions, we showed that C_{rel} depends not only on lesion diameter as seen in the in-focus image plane, but also depends on its depth extent (Figure 6-8). As a consequence, any calibration procedure to correct topologic aspects of CE-DBT acquisition and accurate estimate iodine quantities should take both in-plane and depth lesion extent into account. It must be emphasized however that a spherical assumption might be sufficient for certain lesion types (well circumscribed round-like masses such as cysts, fibroadenoma, rim-enhancements, metastasis, ...) and any residual error in iodine concentration estimation could possibly be negligible depending on the clinical task. Further studies are required to better understand the clinical needs in terms of accuracy of iodine uptake quantification.

For CE-bCT, our results show that lesion contrast-to-background is almost independent of spherical lesion diameter and ellipsoid lesion eccentricity. This result was expected since CE-bCT reconstructed images are obtained from a full angular sampling of the imaged breast. Deviations on expected values were found, in principle, for lesion diameters below 5 mm, since it approaches CE-bCT image resolution and jeopardizes ROI averaging metrics. Nonetheless, it remains clear that CE-bCT outperforms CE-DBT in iodine quantification tasks.

Cone-beam showed to have little effect on iodine uptake quantification for both CE-bCT and CE-DBT topologies. These results were found using monochromatic X-ray beams. If polychromatic beams are considered only a slight decrease is expected. Indeed, as long as LE and HE acquisition parameters are chosen among the optimal parameters found in Section 5.4, cupping and residual background should include respectively up to ~ 0.15 and ~ 0.25 $mg\ I/cm^3$ variation in iodine concentration estimation, which are below the minimum target iodine concentration of 0.5 $mg\ I/cm^3$ considered in this PhD thesis research work.

6.3 Iodine-Enhanced Lesion Detectability and Characterization in CE-bCT vs CE-DBT: a Human Observer Study

In this section, a mesh-based computational breast model with mathematically defined anatomical structures is used to assess and compare the depiction and characterization of embedded iodine-enhanced lesions of different sizes, shapes and iodine concentrations. A detailed description of the anthropomorphic breast phantom is provided in Section 2.3.

Simulated reconstructed iodine-equivalent CE-DBT and CE-bCT images were shown to three different readers, who scored the quality of iodine-enhanced lesion depiction and the characterization in a Likert scale. Statistical analysis for sensitivity and specificity was performed for the different acquisition geometries. A detailed comparison study on the performance of CE-DBT versus CE-bCT was then performed, which is the main goal of this investigation.

6.3.1 Image Database

An image database containing one hundred and forty-four $5 \times 5 \times 5$ cm^3 CE-DBT Volumes-of-Interest (VOI) and one hundred and forty-one $5 \times 5 \times 5$ cm^3 CE-bCT VOIs were extracted from simulated iodine-equivalent images of compressed and uncompressed meshed-based anthropomorphic phantoms embedded with enhanced lesions of different morphologies, sizes and injected iodine concentrations. Two anatomical background types were considered; they were classified as being representative ACR 2 and ACR 3 textures, through visual inspection of low-energy projection images by Dr. Clarisse Dromain (radiologist at Gustave Roussy – former IGR; Villejuif, France).

The compressed breast phantom thickness for CE-DBT topology was 5 cm-thick, while the uncompressed breast phantom for CE-bCT had 14 cm diameter close to the chest wall, mimicking the same breast without applying compression and with the patient in prone position [162]. Both compressed and uncompressed phantoms had, on average, approximately 7% Volumetric Breast Density (VBD)[2], which is similar to density values found for an average breast size [169]. The skin was on average 3 mm thick.

Five types of lesions were simulated, classified according to their overall shape, margin and internal enhancement:

- **Round Homogeneous:** round mass-like lesions, with smooth margin and homogeneous internal iodine enhancement
- **Rim Enhancement:** round mass-like lesions, with smooth margin and peripheral iodine-enhancement (seen as bright rim is radiographic images)
- **Irregular:** mass-like lesions with irregular shape, margin in an intermediate class between smooth and spiculated, and homogeneous internal iodine enhancement
- **Linear Enhancement:** non-mass-like enhancement along a "line", following the growth direction of a given lactiferous duct
- **Spiculated:** essentially round nucleus, with spiculated margin randomly distributed around the nucleus towards all three axes and homogeneous internal iodine enhancement

For Round Homogeneous, Rim Enhancement, Irregular and Spiculated lesions, two equally populated sets of lesions were simulated: one with ∼5 mm diameter and the other with ∼10 mm diameters. For Linear Enhancement lesions, their largest extent ranged from ∼9 to 26 mm. Iodine-enhanced images with no embedded lesion contrast uptake were also considered. Figure 6-9 illustrates the five lesion types.

[2]The Volumetric Breast Density (VBD) is defined as the volume fraction of fibroglandular tissue with respect to the total breast volume

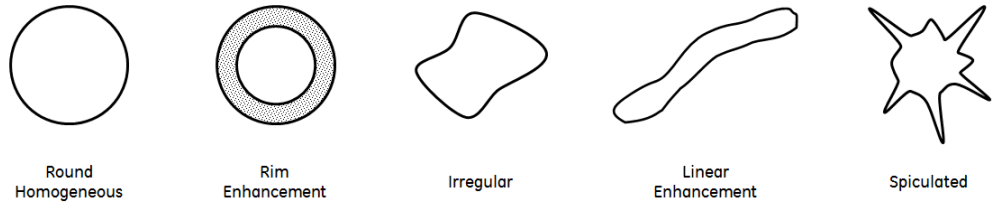

Figure 6-9: Illustration of the five iodine-enhanced lesion types considered in the human observer study. Lesions were classified according to their overall shape, margin and internal enhancement

The chemical composition of every object inside the phantom was based on the definitions of *skin*, *adipose tissue* and *fibroglandular tissue* by Hammerstein *et al.* [159]. More precisely, adipose compartments and adipose columns in the skin were emulated as Hammerstein's *adipose tissue* material. Copper's ligament, lactiferous ducts, fibroglandular tissue and unenhanced lesions were emulated as Hammerstein's *fibroglandular tissue* material. The skin convex envelope and the nipple were emulated as Hammerstein's *skin* material. With the injection of the contrast agent, we assumed that only the fibroglandular tissue and the lesions take contrast. Their final chemical composition is that of fibroglandular tissue homogeneously mixed with a given iodine concentration under a volume conservation constraint.

The simulated lesions were enhanced with 0.5, 1.0, 2.0 and 4.0 $mg\ I/cm^3$. As described in Section 5.1, an iodine concentration of 0.5 mg/cm^3 was chosen to be the minimum iodine concentration expected clinically in the embedded lesion, if a typical injection protocol of contrast-enhanced mammography is considered (cf. Equation 5.4 in Section 5.1). Moreover, it was assumed that the fibroglandular tissue constituting the mammary gland was also enhanced by the contrast agent, as evidenced in previous clinical studies [282]. A contrast uptake of 0.2 $mg\ I/cm^3$ in the fibroglandular tissue was considered.

Table 6.2 summarizes the total number of studied cases per acquisition geometry, considering all sizes, the four iodine concentrations and the two background glandularities.

Table 6.3 summarizes the parameters used to simulate low-energy (LE) and high-energy (HE) projection images in CE-DBT and CE-bCT implementations. CE-DBT images were simulated using the topology of a CE-DBT prototype based on the GE Senographe® DS mammography systems (GE Healthcare; Chalfont St Giles, UK), as described in Section 6.1. For CE-bCT, the same cone-beam topology described in Section 5.2 was simulated. As discussed in Chapter 5, this choice of topologic parameters provided contrast-to-noise ratio values above Rose's detectability criterion [246, 247] for a 2 mm diameter 0.5 mg/cm^3 iodine-enhanced lesion in an average-sized breast and with dose levels comparable to a two-view mammogram.

Table 6.2: Total number of simulated lesion types for the human observer study, per acquisition geometry

Lesion Type	**CE-DBT**	**CE-bCT**	**Total**
No Lesion	36	39	**75**
Round Homogeneous	24	24	**48**
Rim Enhancement	24	24	**48**
Irregular	24	24	**48**
Linear Enhancement	12	6	**18**
Spiculated	24	24	**48**
Total	**144**	**141**	**284**

For both topologies, perfect energy-integrating detectors that do not generate any kind of noise or blurring were assumed. X-ray projections were simulated assuming primary X-rays only.

Table 6.3: Parameters used for CE-DBT and CE-bCT implementations in the human observer study

Model Parameters		CE-DBT	CE-bCT
Acquisition	Mono-energetic	20 & 34 keV	30 & 34 keV
	Total AGD	1.86 mGy	3.72 mGy
	Dose ratio (LE/HE)	50/50%	50/50%
Geometry	Mag (SDD/SID)	660mm / 620mm	880mm / 460mm
	no. of projections	9 (25˚range)	300 (360˚range)
	Detector element size	0.100 mm	0.776 mm
Reconstruction	Method	FBP	FBP
	Filter	Ref. [275]	Ramp + Hamming
	Voxel size	$0.1 \times 0.1 \times 1.0\ mm^3$	$0.410 \times 0.410 \times 0.410\ mm^3$
DE Recomb		projection-based	image-based

No compression paddle was emulated in this study. For CE-DBT, total AGD was kept at 1.86 mGy, corresponding to the dose delivered in clinical practice for a one-view contrast-enhanced mammography exam (SenoBright™ , GE Healthcare; Chalfont St Giles, UK). For CE-bCT, AGD was kept at 3.72 mGy, *i.e.* twice the dose used for a single view SenoBright™ acquisitions. This choice was made assuming that the clinical protocols for CE-DBT would require two views (*e.g.*, one CC and one MLO), while a single CE-bCT acquisition would provide complete 3D information about the breast and the enhanced-lesions. It must be emphasized that, in terms of detectability, this hypothesis favors CE-bCT, though there is no proof to this day that a 2-view CE-DBT protocol is statistically better than a 1-view protocol. Nonetheless, in theory, a 2-view CE-DBT protocol provides more accurate information on lesion morphology and localization than a 1-view protocol. There exists hence a trade-off between lesion detectability and availability of morphologic and localization information.

Figure 6-10a and 6-10b illustrate the lesion embedding process for CE-DBT and CE-bCT. Examples show reconstructed HE images for both considered background types, with and without an embedded lesion. The final recombined iodine-equivalent images are also shown, where we distinguish the enhancement of lesion contrast as well as the 0.2 $mg\ I/cm^3$ uptake in the fibroglandular background.

Figure 6-11 shows examples of simulated iodine-equivalent images containing the different lesion types considered in the study. For CE-DBT, the in-focus plane crossing the lesion center is shown. For CE-DBT, the three orthogonal planes crossing the lesion centers are shown.

6.3.2 Observers

Three readers individually reviewed the random sequence of 284 images comprising the different topologies.

Reader 1 (R1) is a radiologist with over 15 years' experience in medical imaging and specialized in diagnostic and interventional imaging of gastrointestinal, neuroendocrine and breast tumors. Reader 1 has experience with full-body CT, MRI, conventional radiography and mammography images review. Reader 1 is also actively involved in pre-clinical research investigations on contrast-enhanced mammography and CE-DBT.

Reader 2 (R2) is a radiologist with over 10 years' experience in medical imaging, specialized in oncologic and breast imaging, and possesses a doctorate degree in Medicine for his/her research on brain tumor malignancy evaluation in perfusion MRI. Reader 2 has experience with full-body CT, MRI, ultrasound and mammography images review.

Reader 3 (R2) is a senior research engineer at GE Healthcare, with doctorate degree on Signal

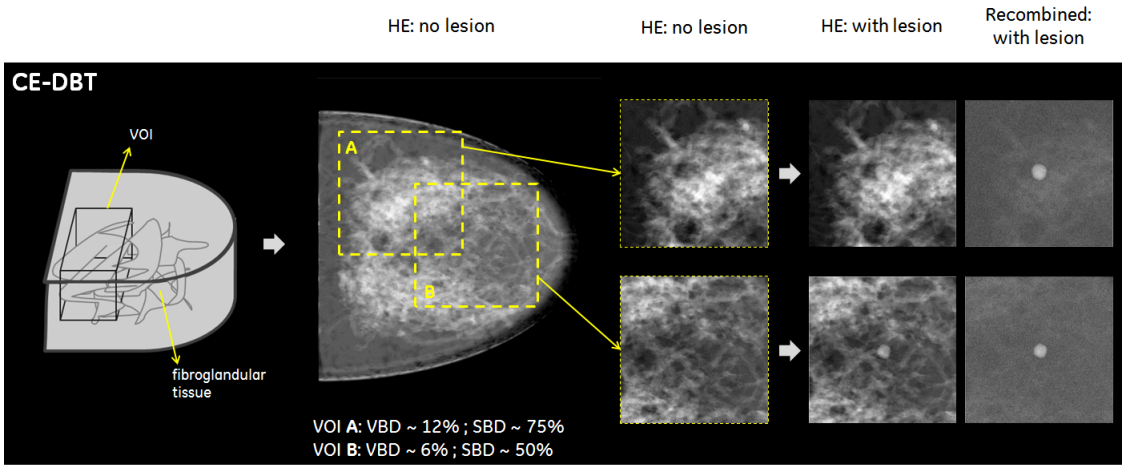

(a)

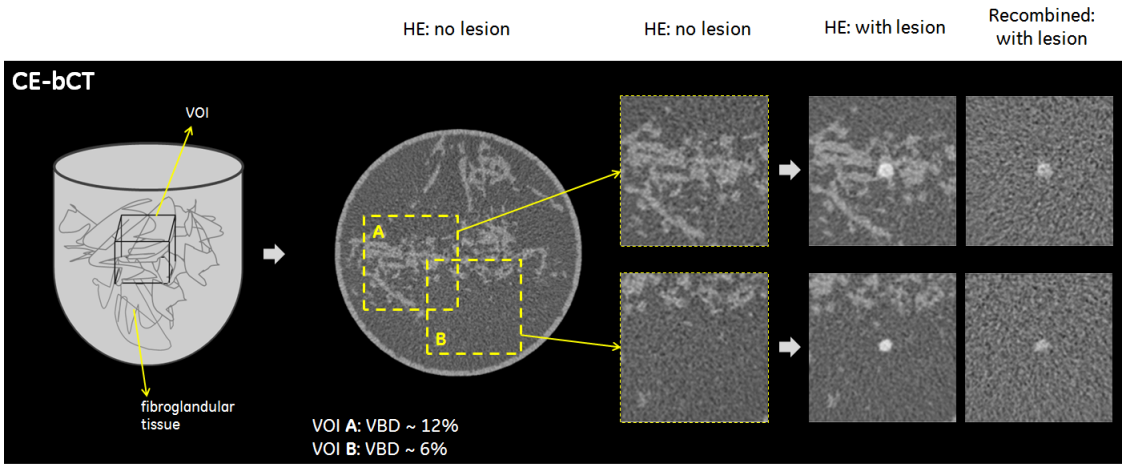

(b)

Figure 6-10: Illustration of volume-of-interest (VOI) cropping to form (a) CE-DBT and (b) CE-bCT region-of-interest used for review. Two different background were considered: (**A**) classified as ACR 3 (heterogeneously dense), and (**B**) classified as ACR 2 (presence of some fibroglandular tissue). Average volumetric breast density (VBD) and surface breast density (SBD)[4] values are presented for the two background

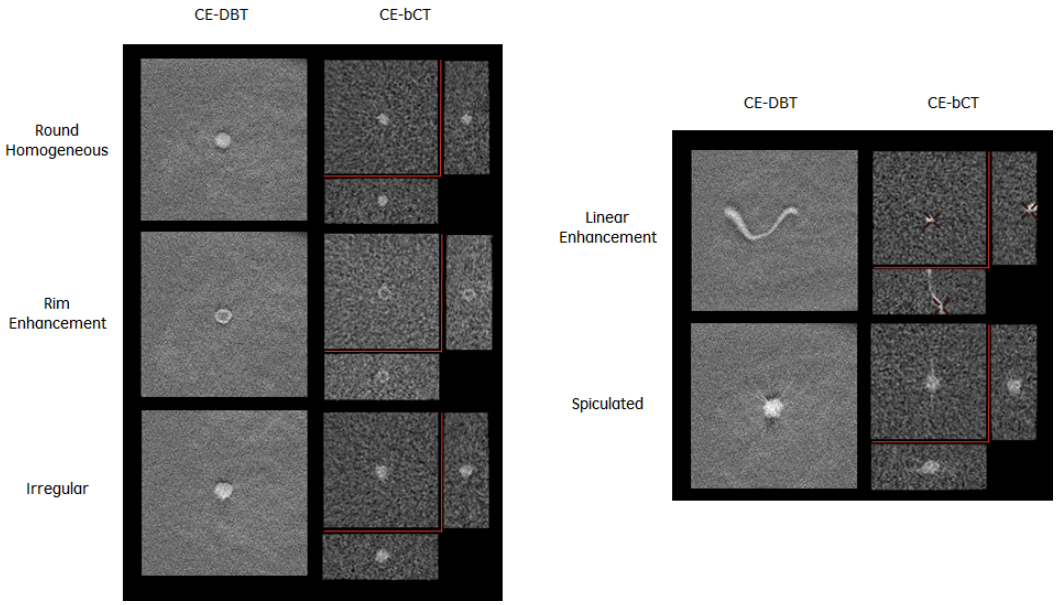

Figure 6-11: Examples recombined iodine-enhanced images for each topology and for each considered lesion type. Lesions had 2.0 $mg\ I/cm^3$ uptake while the fibroglandular background had 0.2 $mg\ I/cm^3$ uptake

and Image Processing for his/her research on automatic detection of masses in DBT. Reader 3 has accumulated over 8 years of experience in developing and evaluating iterative reconstruction algorithms for morphologic DBT and dual-energy CE-DBT.

6.3.3 Viewing Conditions

CE-DBT images were stored for display on a Seno Advantage™ Workstation (v4.4, GE Healthcare; Chalfont St Giles, UK), equipped with high-resolution (5M pixels) grayscale portrait monitors (SMD 21500 G, Siemens AG; Munchen, Germany), which were calibrated for review in a dark room. CE-DBT slices were presented at fixed resolution. The mouse or the keyboard could be used to alter the window/level, to zoom in, to change the position in the 3D CE-DBT stack, perform extent measurement and to signify the beginning end of the review phase.

CE-bCT images were stored for display on an Advantage Workstation™ (v4.5, GE Healthcare; Chalfont St Giles, UK) equipped with Volume Viewer software (GE Healthcare, Chalfont St Giles, UK) and calibrated for review in a dark room. Readers had simultaneous access to axial, sagittal, coronal and oblique planes. Access to window/level, zoom and measurement tools was also granted through the mouse or the keyboard. Additionally, the *MIP* (Maximum Intensity Projection) and *Average* slice tools were also available, since they are common tools used by radiologist during the review of other fully 3D methods such as MRI and full-body CT [283–286]. Accordingly, the reconstruction of CE-bCT volumes at isotropic resolution would allow to better exploit the fully 3D topology by analyzing *MIP* and *Average* of any "thicker" oblique plane, potentially enhancing lesion depiction and characterization.

During review, both CE-DBT and CE-bCT images were displayed in stand-alone. No constraints on viewing distance (typical distance was $\approx$ 40-50 cm) or on viewing time were imposed. All cases were displayed once and in random order, mixing both CE-DBT and CE-bCT images. The order in which the cases were displayed was different for each reader. To reduce effects of reader fatigue, a 10 minutes pause was introduced after each 50 minutes of reading session.

The readers had *a priori* knowledge on the acquisition geometry used to generate the image being reviewed. They were also informed that all lesions were approximately localized at the center of the VOI.

6.3.4 Preference Study Questionnaire

A review questionnaire based on ACR-BIRADS for CE-MRI was defined to study the readers' confidence during image review. The questionnaire is summarized in Table 6.4.

For each presented ROI, six questions were asked to the readers. The questions regarded lesion detectability (Q1), characterization (Q3,Q5,Q7,Q9) and 3D extent (Q11). For each questions, except Q11, the reader was also asked to provide a degree of confidence in his answers, using five-point Likert items where 1 represents "not at all confident", 2 represents "not so confident", 3 represents "moderately confident", 4 represents "very confident" and 5 represent "extremely confident". In total, eleven items composed the questionnaire, which is summarized in Table 6.4.

Table 6.4: Review questionnaire based on ACR-BIRADS and used to assess the readers confidence

QUESTIONNAIRE	
About lesion detectability	
Q1	Is there a lesion in the center of the ROI? (YES = 1 / NO = 0)
Q2	How confident are you about that? *
About lesion characterization	
Q3	This lesion is a mass? (YES = 1 / NO = 0)
Q4	How confident are you about that? *
Q5	The shape of the mass is: round = 1 / oval = 2 / irregular = 3 ?
Q6	How confident are you about that? *
Q7	The margin of this mass is : smooth = 1 / irregular = 2 / spiculated = 3 ?
Q8	How confident are you about that? *
Q9	The internal mass enhancement is: homogenous = 1 / rim = 2 ?
Q10	How confident are you about that? *
About lesion extent	
Q11	What is the largest lesion dimension?
*** Degrees of Confidence (Likert Scale)**	
	Not at all confident = 1
	Not so confident = 2
	Moderately confident = 3
	Very confident = 4
	Extremely confident = 5

Q1/Q2 referenced to the presence or absence of a lesion. If the answer is positive, Q3/Q4 specified if the actual lesion was a mass-like or non-mass-like lesion, respectively. For mass-like lesions only, the reader was asked to specify the morphological characteristics of the lesion, such as the overall shape (Q5/Q6), its margin allure (Q7/Q8) and its internal enhancement (Q9/Q10). Notice that it exists a hierarchical dependency between the different questions, which was taken into account in the statistical analysis.

Table 6.5 summarizes a contingency table classifying each simulated lesion type by the possible

answers to questions Q1 to Q9, with respect to their true value (or **"Gold"**). Although all simulated mass-like lesions were approximately round, in order to assess an eventual distortion in the reconstructed lesion shape (*e.g.* due to the acquisition geometry and angular sampling), for Q5 the readers could also characterize the mass-like lesions as having an "oval" or "irregular" shapes.

Table 6.5: Contingency table of reader answers as function of their true value, $Gold(\cdot)$

Lesion Type	**Gold(Q1)** (existence)	**Gold(Q3)** (mass)	**Gold(Q5)** (shape)	**Gold(Q7)** (margin)	**Gold(Q9)** (int enhanc)
Empty	0	-	-	-	-
Round Homogeneous	1	1	1	1	1
Rim Enhancement	1	1	1	1	2
Irregular	1	1	1	2	1
Linear Enhancement	1	0	-	-	-
Spiculated	1	1	1	3	1

6.3.5 Reader Training

Before starting the real image review session, the experimental course was explained by means of an additional subset of VOIs. The database was explained including the morphologic characteristics of the lesions under study (different types, sizes, iodine concentrations) and the two ACR background types.

The questionnaire was detailed to the reviewers, who were also instructed to use the full Likert scale. The reviewers were told they had to detect, characterize and assess lesion size. For that, reviewers were explained how to handle the mouse and the keyboard, to scroll between slices, perform window/level and zoom adjustments, handle *MIP* and *Average* slice tools for CE-bCT, and how to alternate between the different cases.

6.3.6 Statistical Analysis

For each reader and each acquisition geometry, a contingency table of each question by its true value (gold) and by its Likert score was built. An overall Sensitivity (Se) and Specificity (Sp) per reader and per acquisition geometry was then calculated. To compare the different geometries, a summary measurement translating the "Majority Opinion" among the three readers was calculated for questions Q1, Q3, Q5, Q7, Q9 and then compared to their gold value.

As previously stated, answers to Q5, Q7 and Q9 depend on having previously characterized the lesion as a mass (Q3), which in turn depends on having previously detected the lesion (Q1). Accordingly, in order to study the sensitivity and specificity of the majority opinion for Q3, only the samples for which *all three readers* agreed on Q1 (*i.e.*, a "unanimity opinion") were considered. Likewise, to study the majority opinion for Q5, Q7 and Q9, only the samples for which all three readers agreed on both Q1 and Q3 were considered. Notice that this hierarchical selection process could potentially decrease the samples size, ultimately affecting statistical strength.

For each acquisition geometry and each question, the agreement among the three readers was studied by analyzing the distribution of Likert items per reader, as well as by calculating Cohen's Proportion of Overall Agreement (p_o) and Kappa coefficients (κ_C) [287] as statistical measurements of interobserver agreement. To interpret Kappa coefficients magnitude, Landis and Koch [288] have proposed different ranges of values for κ_C with respect to the degree of agreement among readers. Although Landis-Koch benchmark scale is widely adopted [289], its interpretation was based on their empirical results and opinions. A more general representation was proposed by Fleiss *et al.* [290], where Kappa values below 0.40 or so may be taken to represent poor agreement, values

between 0.40 and 0.75 may be taken to represent fair to good agreement, and greater than 0.75 or so may be taken to represent excellent agreement beyond chance. Both Landis-Koch and Fleiss interpretations for Kappa magnitude are summarized in Table 6.6.

Table 6.6: Classification of reader agreement strength proposed by Landis and Koch [288], and Fleiss *et al.* [290]

Kappa	**Landis and Koch (1977)**	**Kappa**	**Fleiss *et al.* (2003)**
0.81–1.00	excellent	0.75–1.00	excellent
0.61–0.80	substantial	0.41–0.75	fair to good
0.41–0.60	moderate		
0.21–0.40	fair		
0.00–0.20	slight	< 0.40	poor
< 0	poor		

To study lesion detectability and characterization, for each acquisition geometry and each question, the sensitivity and specificity of the majority opinion versus the "Gold" was calculated. A multivariable logistic model was used in order to test the samples characteristics (iodine concentration, true lesion extent and background texture) effect on sensitivity and specificity. Especially for the study of Q5 (shape), an additional variable translating the degree of ovality (or eccentricity) of the simulated lesion was incorporated to the logistic model. The eccentricity index ϵ was defined as:

$$\epsilon_{x,z} = \frac{X}{Z} \tag{6.7}$$

where X and Z are the true lesion dimensions in x- and z-axis directions, respectively. The eccentricity index $\epsilon_{x,z}$ was translated into a symmetric variable, by taking $|\log(\epsilon_{x,z})|$. A null $|\log(\epsilon_{x,z})|$ value reflects a round shape, whereas values further away from zero reflect ellipsoidal shapes. Two classes of rather round, $\{0.9 < \epsilon_{x,z} < 1.11\}$, and rather oval, $\{\epsilon_{x,z} < 0.9\} \cup \{\epsilon_{x,z} > 1.11\}$, forms were considered.

Also for Q5, majority agreement analysis was performed using Gold(Q7) as an additional variable, to explore the hypothesis that simulated lesions with smooth margins ("round homogeneous lesions" and "round rim-enhancement lesions") would be associated with a better sensitivity.

To study the lesions extent measurement (Q11), a continuous variable defined as the median extent measurement value between the three readers was calculated as a summary measure for each sample. For this study, only the samples for which all three readers agreed in Q1 were considered (unanimity opinion in lesion depiction). For each acquisition geometry, the difference of the median measure for Q11 and the true lesion largest extent (*i.e.*, a measurement error) was examined with a Bland-Altman plot against the true lesion largest extent. The variation of the measurement error was examined with a multivariable linear model according to the acquisition geometry and the simulations characteristics (iodine concentration, true lesion extent and background texture).

6.3.7 Results - Part I: Preference Scale Usage and Interobserver Agreement

Interobserver Preference Distribution on Lesion Detectability Task
Figure 6-12 illustrates the Likert scale frequency distribution for Q1 (lesion existence) per acquisition geometry and per observer answer. The answers of all three readers were mainly concentrated in high confidence items (4 and 5, cf. Table 6.4), summing up at least 70% of the sample. The distribution is separated for each reader. A tendency of decreasing confidence of each reader can be observed when passing from CE-DBT to CE-bCT. This trend is also observed for questions Q3/Q4, Q5/Q6, Q7/Q8 and Q9/Q10 (for simplicity their individual graphs are not displayed; an average behavior as function of each question is provided below).

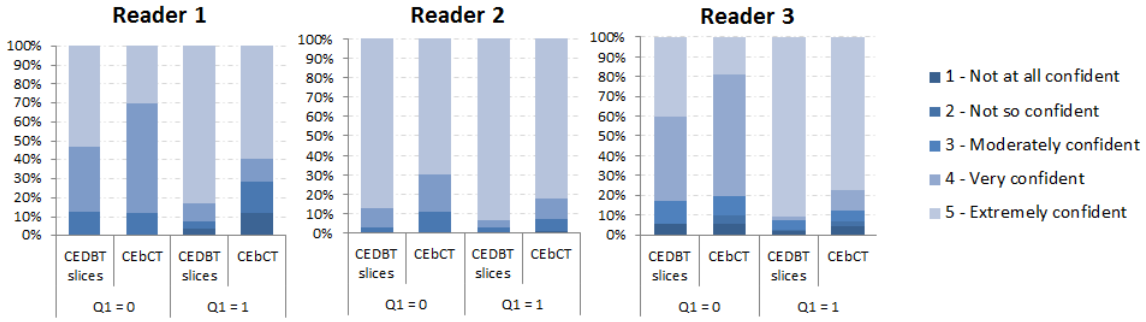

Figure 6-12: Likert scale for Q1/Q2 (lesion existence) when Gold(Q1) is 0 (lesion not present) and 1 (lesion present), per individual readers and per acquisition geometry

Figure 6-13a and Figure 6-13b shows the Sensitivity (Se) and Specificity (Sp) of lesion detection task (Q1), per acquisition geometry and per reader. Lesion detection sensitivity was slightly lower for CE-bCT. Specificity greatly varied among the three readers, most probably due to the different confidence behavior observed in Figure 6-12. The statistical analysis of sensitivity and specificity are presented further on.

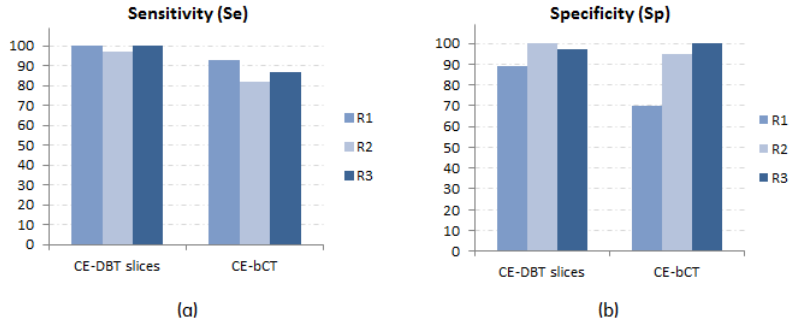

Figure 6-13: (a) Sensitivity and (b) Specificity of each reader in lesion detectability task (Q1), per acquisition geometry

Interobserver Preference Distribution on Lesion Characterization Task
Figure 6-14 illustrates the average Likert scale values, ±1 standard deviation, for questions Q2, Q4, Q6, Q8 and Q10. The average scores are given per acquisition geometry and per reader. Reader 3 showed an evident distinct confidence behavior compared to Readers 1 and 2. Reader 3 presented

lower average confidence for all acquisition geometries but increased standard deviation, which denote a better exploitation of the Likert scale.

Due to the hierarchical process in lesion characterization task, Sensitivity (Se) and Specificity (Sp) for questions Q2, Q4, Q6, Q8 and Q10, as function of the acquisition geometry were studied through majority agreement analysis and are discussed as follows.

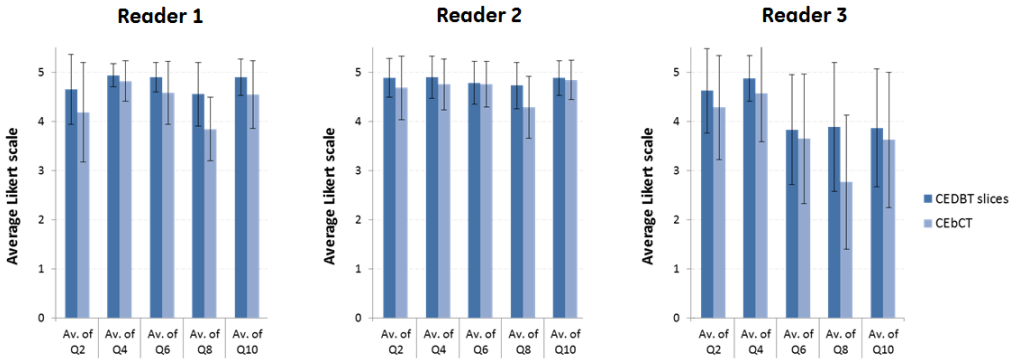

Figure 6-14: Average Likert scale values for all questions, per individual reader, and independently of the characterization answers (Q1, Q3, Q5, Q7 and Q9). The bars illustrate ±1 standard deviation of mean values

Interobserver Agreement

Figure 6-15 shows the Cohen's Kappa coefficients, κ_C (bar plots, left ordinate axes) and the Proportion of Overall Agreement, p_o (lines, right ordinate axes), for questions Q1, Q3, Q5, Q7 and Q9, and for each pairwise test between readers: 'R1 vs R2', 'R1 vs R3' and 'R2 vs R3'. Figure 6-15a and 6-15a show results obtained respectively from CE-DBT and CE-bCT data samples. Error bars indicate 95% confidence interval in Kappa coefficient calculations, obtained from z statistics with significance level for p-values set at 0.05. All calculated κ_C values presented p-values smaller than 0.05, except the two κ_C values indicated by arrows in Figure 6-15.

According to Table 6.6, for Q1, Kappa coefficients indicate excellent agreement among readers during CE-DBT images review ($\kappa_C > 0.87$, $p_o = 100\%$), and good agreement for CE-bCT ($\kappa_C > 0.51$, $p_o = 100\%$). For Q3, Cohen's equation fails to calculate κ_C values, since it exists perfect overall agreement ($p_o = 100\%$) and imbalanced marginal answers among the possible categories[5]. For Q5, taking into account the same Kappa calculation issues as Q3, Reader 1 and Reader 2 presented excellent agreement between themselves ($\kappa_C = 1$, $p_o = 100\%$), but smaller agreement with Reader 3 ($p_o > 70\%$). For Q7, excellent agreement during CE-DBT images review was observed among the three readers ($\kappa_C > 0.75$, $p_o > 70\%$). However, for CE-bCT, while Readers 1 and 2 presented excellent agreement between themselves ($\kappa_C = 1$, $p_o = 100\%$), they poorly agreed with Reader 3 ($\kappa_C < 0.21$, $p_o < 51\%$). The differences observed between Reader 3 and Readers 1 and 2 could be somewhat anticipated, since Reader 3 demonstrated different confidence behavior in Q5 and Q7, when compared to Readers 1 and 2 (Figure 6-14). For Q9, excellent agreement was observed among the readers during both CE-DBT and CE-bCT images review ($\kappa_C > 0.85$, $p_o = 95\%$).

[5]This problem has been referred to in literature as the 'Kappa paradox', and occurs in the presence of imbalanced number of answers among the possible categories. In this case, very low values of Kappa may not necessarily reflect low rates of overall agreement, for instance, in the presence of high p_o values. Feinstein and Cicchetti [291, 292] discussed the main issues in the 'Kappa paradox' and how to address them. This requires, however, a more complex analysis on the study design, increased number of samples and recursive reader training. To maintain a simple approach, this subject is out of scope of this PhD thesis and is envisioned to be addressed in future work.

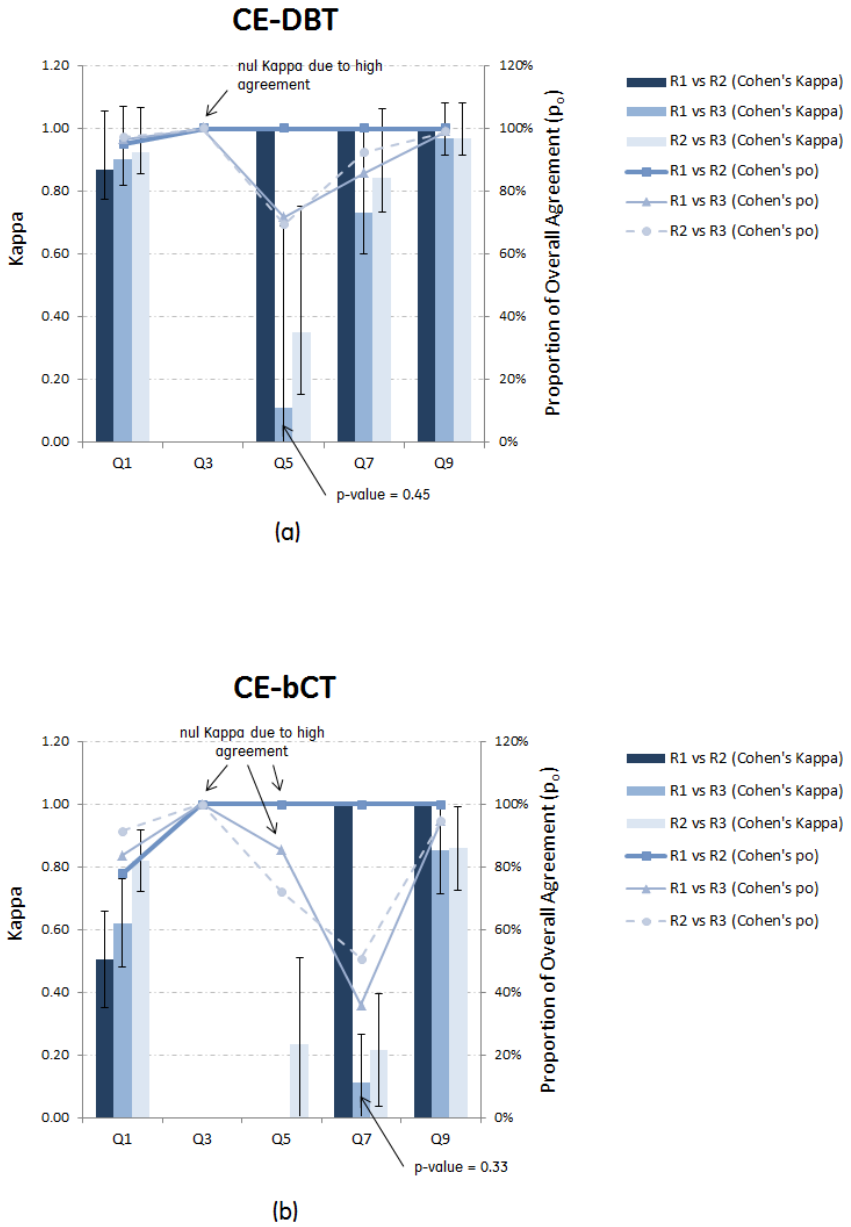

Figure 6-15: Interobserver agreement in (a) CE-DBT and (b) CE-bCT data. Bar plots indicate Cohen's Kappa coefficients, κ_C (left ordinate axes), and lines indicate the Proportion of Overall Agreement, p_o (right ordinate axes). Results are shown for questions Q1, Q3, Q5, Q7 and Q9, and for each pairwise test between readers: 'R1 vs R2', 'R1 vs R3' and 'R2 vs R3'. Error bars indicate 95% confidence interval in Kappa coefficient calculations

6.3.8 Results - Part II: Detectability and Characterization in CE-bCT vs CE-DBT

Majority Opinion for Q1 (lesion existence)
Table 6.7 shows the overall distribution of majority opinion for Q1 (lesion detection), for both CE-DBT and CE-bCT. In each cell, the number of each majority opinion answers against the Gold is displayed and, in brackets, its percentage with respect to the total number of answers in each column is also provided. The percentages in the diagonal cells represent the majority opinion sensitivity or specificity. The distribution of majority opinions for questions Q3, Q5, Q7 and Q9 was represented in the same manner.

The overall majority opinion sensitivity for lesion existence ($Gold(Q1) = 1$), *i.e.* considering both CE-DBT and CE-bCT, was $198/210 = 94\%$. As shown in Table 6.7, the majority opinion sensitivity for CE-DBT was $108/108 = 100\%$ against $90/102 = 88\%$ for CE-bCT. However, the difference in sensitivity between the acquisition geometries was not statistically significant (homogeneity test, $p < 0.0002$, exact test). Moreover, sensitivity was not influenced by any other factor.

The overall majority opinion specificity ($Gold(Q1) = 0$), considering both CE-DBT and CE-bCT cases was $74/75 = 99\%$. Due to the high specificity, no further study of variation was performed.

Table 6.7: Q1 (lesion existence): distribution of majority opinion answers vs Gold, for CE-DBT and CE-bCT

		Gold(Q1)	
		0	1
maj	0	36 (**100%**)	0 (0%)
	1	0 (0%)	108 (**100%**)

CE-DBT

		Gold(Q1)	
		0	1
maj	0	38 (**97%**)	12 (12%)
	1	1 (3%)	90 (**88%**)

CE-bCT

Majority Opinion for Q3 (mass-like and non-mass-like lesions)
Table 6.8 shows the overall distribution of majority opinion for Q3 (mass-like or non-mass like lesions), for both CE-DBT and CE-bCT. Sensitivity and specificity were 100%, and therefore no further study of variation was performed. This result indicates that the distinction between mass-like and linear lesion was evident in both CE-DBT and CE-bCT.

Table 6.8: Q3 (mass/non-mass): distribution of majority opinion answers vs Gold, for CE-DBT and CE-bCT

		Gold(Q3)	
		mass	non-mass
maj	mass	93 (**100%**)	0 (0%)
	non-mass	0 (0%)	12 (**100%**)

CE-DBT

		Gold(Q3)	
		mass	non-mass
maj	mass	76 (**100%**)	0 (0%)
	non-mass	0(0%)	3 (**100%**)

CE-bCT

Majority Opinion for Q5 (lesion shape)
Table 6.9 shows the overall distribution of majority opinion for Q5 (lesion shape), for CE-DBT and CE-bCT. The overall majority opinion sensitivity for lesion shape ($Gold(Q5) = round$) was

145/167 = 87%. As shown in Table 6.9, the majority opinion sensitivity for CE-DBT was 77/92 = 84% against 68/75 = 91% for CE-bCT.

Table 6.9: Q5 (shape): distribution of majority opinion answers vs Gold, for CE-DBT and CE-bCT

		Gold(Q5) round
majority	round	77 (**84%**)
	oval	9 (10%)
	irregular	5 (5%)
	no majority	1 (1%)

CE-DBT

		Gold(Q5) round
majority	round	68 (**91%**)
	oval	1 (1%)
	irregular	3 (4%)
	no majority	3 (4%)

CE-bCT

Table 6.10 summarizes the multivariable logistic model results for Q5 (lesion shape) sensitivity, for different influencing factors: acquisition geometry, iodine concentration, true lesion extent, background texture type, lesion eccentricity (or ovality) and lesion margin (Gold(Q7)). For each factor, the statistical significance is evaluated by the associated p-value. The level of significance for the p-values was set at 0.05. The odds ratio (OR) quantify how strongly sensitivity is affected by variable 'A' relative to a variable 'B' (illustrated as 'A vs. B' in the table) describing each factor. If $OR < 1$, sensitivity is higher for variable 'A' and if $OR > 1$ sensitivity is higher for variable 'B'. In the case numerical variables (as for 'iodine concentration' and 'true lesion extent' factors), $OR > 1$ indicates an increase in sensitivity with the increasing variable value, and vice versa. Precision of the calculated OR values is indicated by the 95% confidence interval (CI).

Table 6.10: Q5 **Sensitivity** analysis results using multivariable logistic model

Factor	**p-value**	**odd ratio**	**95% CI**	
Acq. Geometry	0.14			
CE-bCT vs CE-DBT		2.3	0.77	7.2
Iodine concentration	0.18	1.3	0.88	2.0
True lesion extent	0.16	0.88	0.74	1.1
Bg texture type	0.84			
ACR 3 vs ACR2		1.1	0.32	3.6
Ovality*	0.94			
$\{\epsilon_{x,z} < 0.9 \cup \epsilon_{x,z} > 1.11\}$ vs $0.9 < \epsilon_{x,z} < 1.1$		0.95	0.29	3.1
Gold(Q7): margin	0.02			
smooth vs. irregular		0.046	0.005	0.40
smooth vs. spiculated		0.060	0.006	0.59

*33 observations were deleted due to missing values for the response or explanatory variables

By analyzing Table 6.10, we conclude that smooth margins, *i.e., Gold*(*Q*7) factor, were associated with increased sensitivity ($p = 0.02$, $OR < 1$), as illustrated in Table 6.11. No statistically significant difference was observed between CE-DBT and CE-bCT.

Since the ovality factor was not found to be an important variable in the model ($p = 0.94$), in order to increase the statistical power in the presence of the variable 'lesion margin' and obtain

Table 6.11: Majority opinion **Sensitivity** for Q5 when gold is "round", per geometry and per Gold(Q7) variable (lesion margin)

Gold(Q7) 'lesion margin'	CE-DBT	CE-bCT
round	98%	97%
irregular	65%	85%
spiculated	74%	84%

the 33 observations which were previously not considered, the sensitivity analysis was repeated without the ovality factor. In this case, lesion margin strengthened its association with sensitivity ($p = 0.005$), but the acquisition geometry was still not a significant factor ($p = 0.19$).

Majority Opinion Analysis for Q7 (lesion margin)
Table 6.12 shows the overall distribution of majority opinion for Q7 (lesion margin), for both CE-DBT and CE-bCT. The overall majority opinion sensitivity for smooth lesion margin ($Gold(Q7) = smooth$) was $63/82 = 77\%$. As shown in Table 6.12, the majority opinion sensitivity for CE-DBT was $46/46 = 100\%$ against $17/36 = 47\%$ for CE-bCT.

The sensitivity varied with acquisition geometry ($p < 0.0001$), but did not varied with any other factor. Table 6.13 illustrates the difference in sensitivity for CE-DBT and CE-bCT, by displaying sensitivity values as function of the lesion iodine concentration. Because of the very low p-value and 100% sensitivity for CE-DBT, the multivariable logistic model fails to distinguish variations sensitivity from the other factors. Hence, we could not build a full table with p-values and OR values for all considered influencing factors.

Table 6.12: Q7 (margin): distribution of majority opinion answers vs Gold, for CE-DBT and CE-bCT

		Gold(Q7)		
		smooth	irregular	spiculated
majority	smooth	46 (**100%**)	7 (30%)	5 (22%)
	irregular	0 (0%)	5 (**22%**)	1 (4%)
	spiculated	0 (0%)	10 (43%)	17 (**74%**)
	no majority	0 (0%)	1 (4%)	0 (0%)

CE-DBT

		Gold(Q7)		
		smooth	irregular	spiculated
majority	smooth	17 (**47%**)	4 (20%)	4 (21%)
	irregular	13 (36%)	7 (**35%**)	7 (37%)
	spiculated	2 (6%)	6 (30%)	7 (**37%**)
	no majority	4 (11%)	3 (15%)	1 (5%)

CE-bCT

iodine conc. (mg/cm^3)	CE-DBT	CE-bCT
0.5	100%	0%
1.0	100%	55%
2.0	100%	60%
4.0	100%	42%

Table 6.13: Majority opinion **Sensitivity** for Q5 when gold is "round", per geometry and per iodine concentration

iodine conc. (mg/cm^3)	CE-DBT	CE-bCT
0.5	18%	75%
1.0	82%	50%
2.0	100%	91%
4.0	92%	100%

Table 6.14: Majority agreement **Specificity** for Q5 when gold is "irregular $\vee$ spiculated", per geometry and per iodine concentration

Also from Table 6.12, we see that the overall majority opinion specificity for smooth lesion

margin (*i.e.*, $Gold(Q7) = irregular \vee spiculated$[6]) was 65/84 = 76%. The majority opinion sensitivity for CE-DBT was 34/46 = 74% against 31/39 = 79% for CE-bCT.

Table 6.15 summarizes the multivariable logistic model results for Q7 (lesion margin) specificity, for the different influencing factors. The specificity increased with iodine concentration ($p = 0.001$, $OR > 1$), as can be seen in Table 6.14, and did not vary with acquisition geometry ($p = 0.94$).

Table 6.15: Q7 **Specificity** analysis results using multivariable logistic model. The level of significance for the p-values was set at 0.05

Factor	**p-value**	**odd ratio**	**95% CI**	
Protocol	0.94			
CEbCT vs CEDBT		1.05	0.32	3.4
Iodine conc (mg/cm^3)	0.001	4.5	1.8	11
True lesion extent	0.85	0.98	0.80	1.2
Bg texture type	0.96			
ACR 3 vs ACR 2		1.2	0.28	4.8

Majority Opinion Analysis for Q9 (lesion internal enhancement)
Table 6.16 shows the overall distribution of majority opinion for Q9 (lesion internal enhancement), considering both CE-DBT and CE-bCT cases. Given the excellent sensitivity/specificity, no further study was performed. This result indicates that the distinction between homogeneous and rim enhancements was evident in both CE-DBT and CE-bCT.

Table 6.16: Q9 (internal enhancement): distribution of majority opinion answers vs Gold, for CE-DBT and CE-bCT

		Gold(Q9)	
		homog.	rim
maj	homog.	69 (**100%**)	0 (0%)
	rim	0 (0%)	23 (**100%**)

CE-DBT

		Gold(Q9)	
		homog.	rim
maj	homog.	58 (**100%**)	0 (0%)
	rim	0 (0%)	17 (**100%**)

CE-bCT

Majority Opinion Analysis for Q11 (lesion extent)
For lesion extent measurement analysis, unanimity opinion on lesion existence (Q1) was 184/210 = 87%, with 102/108 = 97% agreement for CE-DBT and 79/102 = 77% agreement for CE-bCT.

Using the 184 unanimity opinion samples, Figures 6-16a and 6-16b illustrate the Bland-Altman plots for the median extent error (*i.e.* difference of the median measure for Q11 and the true lesion largest extent) for CE-DBT and CE-bCT, respectively. We note two main groups of measurement points, which are associated to the two main populations of mass-like lesions: one with ∼5 mm diameter and the other with ∼10 mm diameter. The sparse measurement points are associated to Linear Enhancement lesions. A preliminary visual inspection of Figures 6-16a and 6-16b reveal a small difference in lesion estimation precision between CE-DBT and CE-bCT. This can be observed from the dotted lines, which indicate ±2 standard deviations in median extent error.

Table 6.17 summarizes the results of median extent error analysis using the multivariable logistic model, for the different influencing factors. For a better analysis, we did not considered Linear

[6]We define ∧ and ∨ as, respectively, the conjunction ("AND") and disjunction ("OR") operators

Enhancement lesions, since they introduce high variations to the model and weaken the statistical power (cf. measured points above 10 mm in Figure 6-16). In this case, for mass-like lesions, the median extent accuracy increases with the true lesion extent ($p < 0.0001$) and is better (*i.e.* lower average error) for CE-DBT when compared to CE-bCT ($p < 0.0001$). The variance of the median extent error is only affected by the acquisition geometry ($p = 0.02$), with better precision (*i.e.* lower standard deviation) with CE-DBT.

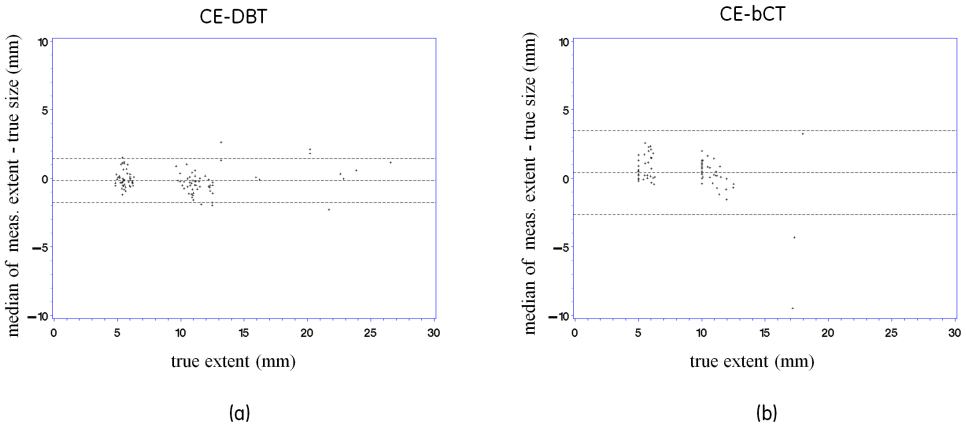

Figure 6-16: Bland-Altman plot of median measured extents among the three readers for (a) CE-bCT and (b) CE-DBT. Markers indicate median values, while the dotted lines indicate ±2 standard deviations

Table 6.17: Q11 (lesion extent) analysis results using multivariable linear model. Linear lesions were excluded from the analysis. The level of significance for the p-values was set at 0.05

Factor	**df**	**p-value (accuracy)**	**p-value (precision)**
Protocol	1	< 0.0001	0.02
Iodine conc (mg/cm3)	1	0.18	0.24
True lesion extent	1	< 0.0001	0.46
Bg texture type	2	0.81	0.19

6.3.9 Discussion

This section presented a human observer study comparing iodine-enhanced lesion depiction and characterization in simulated CE-DBT and CE-bCT iodine-enhanced images. Compressed and uncompressed computational breast phantoms, with average size and glandularity, were embedded with iodine-enhanced lesions of different morphologies, sizes and iodine concentrations levels expected in clinical practice. Idealistic hypothesis were made for the X-ray source (isotropic point source emitting optimal monochromatic X-ray beams, with no tube motion blur), the imaged breast (no patient motion) and the X-ray detector (blur-free perfect energy-integrating detector). For CE-DBT, projection images were simulated with cone-beam topology similar to a GE Senographe DS system, and reconstructed by FBP to generate iodine-equivalent images at 100×100 μm^2 pixel pitch and 1 mm slice spacing. For CE-bCT, projection images were simulated with a cone-beam topology similar to that published by Boone *et al.* [103] and reconstructed by FBP to generate iodine-equivalent images at 410×410 μm^2 pixel size, and 1 mm slice thickness. For both CE-DBT and CE-bCT, ACR 2 and ACR 3 anatomical background types taking 0.2 $mg\ I/cm^3$ contrast were considered, emulating residual background texture. Average glandular dose for CE-DBT

and CE-bCT were set respectively to 1.86 and 3.72 mGy, *i.e.* one and twofold the dose used in clinical contrast-enhanced mammography acquisitions. Simulated reconstructed iodine-equivalent images were shown to three different readers, who scored the visibility and characterization of iodine-enhanced lesions.

Analysis of Cohen's Kappa coefficient, κ_C, and the proportion of overall agreement, p_o, showed an overall good to excellent agreement among the readers, depending on the question under analysis. Although the interpretation of Kappa magnitude as a quantitative measurement of agreement can be controversial [289,290], better results can be achieved by fine tuning the classification of κ_C value ranges with respect to our specific study. This can be performed, for example, by training the readers until κ_C values attains a predefined substantial level.

Also to assess reader agreement, we analyzed the readers' frequency distribution of Likert items, per acquisition geometry and per question. Results showed similar confidence behaviors among the three readers when reviewing images originated from the different acquisition geometries. Although not statistically confirmed, a tendency of decreasing confidence of each individual reader can be observed when passing from CE-DBT to CE-bCT. Additional samples are required to strengthen the statistical power and confirm if it really exists a difference in overall preference. A linearly weighted Kappa coefficient calculation [293, 294], using Likert items as weights, could in this case provide quantitative assessment.

Statistical analysis for sensitivity and specificity was performed for the different acquisition geometries, with a detailed comparison study on the performance of CE-DBT versus CE-bCT. Results showed no statistically significant difference in sensitivity and specificity between CE-DBT and CE-bCT in lesion depiction (Q1) and characterization of its mass or non-mass nature (Q3), overall shape (Q5) and internal enhancement (Q9). On the other hand, CE-DBT demonstrated significant better sensitivity for characterizing lesions with smoothed margins (Q7). Additionally, there was no difference in specificity for the complementary lesion set, *i.e.* lesions with irregular or spiculated margins being characterized as having smooth margins. These results indicate that in CE-bCT lesions with smooth margins could be seen as having irregular or spiculated margins. Therefore, considering the other results of the study, this can only be explained by the lower signal-to-noise ratio in CE-bCT images, as can be noticed in Figure 6-11, despite the fact that CE-bCT protocol makes use of twice the dose used for CE-DBT.

The assessment of lesion extent accuracy and precision was also compared between CE-DBT and CE-bCT, using a median extent measure (Q11) from samples which had unanimity opinion on lesion depiction. For CE-DBT, readers measured lesion extent only in the x-z plane, *i.e.* the plane parallel to the detector surface. In CE-bCT readers took the largest extent in all three axes as lesion extent measurement. A multivariable linear model analysis indicated better lesion extent estimation accuracy (*i.e.* lower average error) and precision (*i.e.* lower standard deviation) with CE-DBT. Results also indicated that lesion extent accuracy in both CE-DBT and CE-bCT are affected by the true lesion size. Background type and iodine concentration did not affect lesion extent estimation accuracy and precision.

Lesion extent assessment results come in complement to the investigations carried in Section 6.1. In the previous investigation, lesion extent was assessed by a mathematical estimator and in noiseless CE-DBT and CE-bCT images, with homogeneous background and the same spatial resolution in the x-z plane considered in this section. The previous results indicated no statistically significant difference in lesion extent estimation in the x-z plane. In comparison to the previous investigation, in this section we introduced quantum noise and residual texture, whilst lesion extent was assessed by human observers. Since results indicated that background texture does not affect lesion extent accuracy and precision, it can be concluded that the differences between CE-DBT and CE-bCT evidenced in this section originated either from the introduction of quantum noise or from the observer variability, rather than being affected the acquisition geometries themselves. Additionally, it must be emphasized that the simulated mass-like lesions had an approximate spherical shape. If however ellipsoidal lesions with low eccentricity in CE-DBT depth-direction are considered, CE-DBT performance in the presence of quantum noise should decrease due to the

loss in lesion contrast and CNR, as demonstrated in Section 6.2.

The comparison study presented in this section was performed assuming blur-free perfect energy-integrating detectors. If current design constraints such as a CsI-based scintillator with finite thickness are applied (for example, 100 or 250 μm thick layer in current GE Senographe DS and Essential systems, and 600 μm in current bCT prototypes) difference in lesion detectability might be evidenced, as suggested in Section 5.6, due to CNR degradation. In this case, CE-DBT is expected to have a substantial loss in CNR but to keep a high spatial resolution, while for CE-bCT thicker CsI layer is expected to maintain the CNR close to ideal levels but to have a substantial loss spatial resolution. Additionally, in a realistic setting, it can be expected that X-ray detectors for CE-bCT and CE-DBT would present different efficiencies, in particular since geometric parameters such as pixel size, angular sampling, acquisition time and so on, would impose certain constraints to the detector performance (*e.g.*, quanta spreading, lag, electronic noise, ...).

With respect to the X-ray source and acquisition modeling, it is expected that passing from monochromatic to polychromatic input X-ray fluence spectra entails in a small CNR degradation, as discussed in Section 5.4, due to increased quantum noise (sub-optimal photon energy weighting) and residual textured noise (incomplete beam-hardening correction). As consequence, a possible degradation in lesion detectability can also be expected. However, we believe this degradation to be comparable[7] for both CE-bCT and CE-DBT, and would ultimately be insufficient to affect the comparison results between both techniques. In this case, a monochromatic simulation is justified since it allows for much faster calculation, especially in the light of the great number of images simulated for this study. On the other hand, a finite-sized focal spot, emitting different X-ray fluences from inside its surface, would definitely impact the system's spatial resolution through *focal spot blurring* [149]. The latter would consequently lead to degradation of iodine-enhanced lesion characterization. Furthermore, it is expected that this impact would be different for CE-bCT and CE-DBT, due to their individual acquisition geometry.

Another important hypothesis made during our investigation was that AGD for CE-bCT simulations was twice the AGD used for CE-DBT. As previously discussed, this choice was made assuming a two-view clinical protocols for CE-DBT, while a single CE-bCT acquisition would provide complete 3D information. However, if both views were available to the observers during image review we could expect better results for CE-DBT, specially in terms of lesion characterization and extent estimation. Further studies are therefore required to prove that a 2-view CE-DBT protocol is statistically better than a half dose 1-view protocol with respect to characterization tasks.

Morphological information of the breast available in low-energy images were not explored during image review. As it is performed today in clinical practice with CESM, the images acquired with LE spectra are similar (in terms of X-ray acquisition spectra and dose) to a standard mammogram and could can be used for anatomic landmark and *a posteriori* confirmation of lesion morphologic characteristics and localization. They provide complementary morphologic information on the mammary gland, eventual enhanced and unenhanced masses, as well as microcalcifications clusters and other typical and relevant mammographic findings. Moreover, since anatomical background is different in reconstructed morphological CE-bCT and CE-DBT volumes [124, 125], we can also expect that the differences in detectability and characterization between CE-bCT and CE-DBT will increase. CE-bCT would benefit from the lower anatomical noise in morphologic bCT images when compared to DBT [124, 296] for better unenhanced masses depiction and characterization, while CE-DBT would benefit from higher spatial resolution for microcalcification depiction and characterization.

[7]For CE-DBT, Puong *et al.* [226, 257, 295] showed a ∼35% decrease in CNR in a 5 cm-thick 50% fibroglandular equivament phantom, when passing from optimal theoretical monochromatic X-ray beams to optimal acquisition parameters constrained by a CE-DBT prototype based on GE Senographe DS. For CE-bCT, we showed in Section 5.5 a ∼40% decrease in CNR in a 14 cm diameter 12.5% fibroglandular equivalent phantom, when passing from optimal theoretical monochromatic X-ray beams to optimal acquisition parameters for a 1-Source 2-kV 2-filter implementation constrained by typical tube power and acquisition time used in current clinical breast CT prototypes.

6.4 Conclusions

In this chapter, using previously obtained optimal dual-energy acquisition parameters for CE-bCT (from Chapter 5) and CE-DBT (from previously published work), the quantitative potential of both modalities was evaluated through a series of experiments assuming primary mono-energetic X-ray point source and perfect energy-integrating noise-free blur-free detectors.

The first section focused on the quantitative potential of cone-beam CE-bCT and cone-beam CE-DBT in the assessment of lesion 3D extent. Using a mathematical estimator, lesion extent in all three axes was assessed in noiseless CE-DBT images at 100×100 μm^2 pixel pitch and 1 mm slice spacing, and CE-bCT images at $410 \times 410 \times 410$ μm^3 pixel size, both with homogeneous background. In the absence of noise, we showed that CE-DBT and CE-bCT precision to estimate lesion extent was similar in the in-plane direction, while CE-bCT was superior to estimate lesion extent in the depth direction. A full factorial analysis showed that lesion extent estimation precision in CE-DBT was affected by lesion size and iodine concentration, and only by lesion size in CE-bCT.

In a second study, using the same topological parameters of the previous investigation, iodine uptake quantification in lesions with different sizes, shapes and iodine concentrations was compared. In this study, we demonstrated that CE-bCT was superior in quantifying their true iodine concentration, while the artifacts caused by CE-DBT limited depth resolution prevented any precise quantification of iodine uptake. Indeed, results show that iodine uptake quantification in CE-DBT is only possible with *a priori* knowledge of the iodine-enhanced lesion dimensions in all axes, particularly because lesion contrast depends not only on the lesion shape as seen in its in-focus plane image, but depends also on its depth extent.

Finally, a human observer study comparing iodine-enhanced lesion depiction and characterization in simulated CE-bCT and CE-DBT iodine-enhanced images was performed. For CE-DBT, iodine-equivalent images were generated at 100×100 μm^2 pixel pitch and 1 mm slice spacing, while for CE-bCT, iodine-equivalent images at 410×410 μm^2 pixel size, and 1 mm slice thickness. For both CE-DBT and CE-bCT, ACR 2 and ACR 3 anatomical background types taking 0.2 $mg\ I/cm^3$ contrast were considered, emulating residual background. Average glandular dose for CE-DBT and CE-bCT were set respectively to 1.86 and 3.72 mGy, *i.e.* one and twofold the dose used in clinical contrast-enhanced mammography acquisitions. Through the statistical analysis of a preference questionnaire, results revealed that sensitivity and specificity in iodine-enhanced lesion detectability and characterization were not statistically different between the two techniques, except for lesion margin characterization (*e.g.* spicules) for which CE-DBT demonstrated superior sensitivity. Results also showed that CE-DBT is more accurate and more precise in estimating lesion dimensions in the x-z plane (DBT in-focus plane) than CE-bCT. However, this result was based in mass-like lesions with approximate spherical shape. If non-symmetric-shaped lesions are considered, CE-DBT performance in the presence of quantum noise would drastically decrease due to lesion contrast dependency on its depth extent and consequent effects on CNR.

The inferior performance of CE-bCT in lesion margin characterization and lesion extent precision was in contrast to what expected from the previous results, where no quantum noise, residual texture nor observer variability were included. Naturally, since both tasks are directly related to spatial resolution, this result can be in part associated to CE-DBT's higher in-plane spatial resolution (100 μm pixel pitch) when compared to CE-bCT (410 μm pixel pitch). However, since noiseless simulations revealed no difference in lesion extent estimation and since residual texture did not have a statistically significant effect on extent estimation, we can conclude that quantum noise was the true limiting factor in CE-bCT performance. Nonetheless, it must stay clear that CE-bCT presents the clear advantage of being able to characterize and estimate iodine-enhanced lesion extent in all directions, while CE-DBT is limited to the lesion's in-focus plane only. Moreover, if again non-symmetric-shaped lesions are considered, CE-DBT performance should also decrease due to variations in lesion contrast, CNR, and likely, detectability.

While assuming idealistic hypothesis for X-ray source and detector, the experiments presented in this chapter allowed to evaluate and compare the performance of CE-bCT and CE-DBT topolo-

gies on different quantification tasks. The only parameters influencing their performance were linked to the cone-beam geometry (pixel size, distances, cone-angles), the X-ray beam energy, acquisition trajectory and angular sampling (full 360° or limited angle), and the phantom thickness. Any further assumption on the X-ray source (focal spot size, X-ray tube tilt, Heel effect degradation, acquisition time, tube power) and the detector (*e.g.* quanta spreading, lag, electronic noise, ...) would impose the choice of engineering design constraints which would drive us away from the main approach held so far. This method allowed us to understand and quantify the impact of individual parameters on image quality. Nonetheless, in order to reveal more significant differences between two practical CE-bCT and CE-DBT implementations on their ability to detect and characterize contrast-enhanced lesion through localization, morphology, and the associated contrast uptake, further studies considering more realistic X-ray imaging systems are still needed.

In summary, both CE-DBT and CE-bCT topologies present their advantages and limitations. Both topologies presented equivalent performance in iodine-enhanced lesion detectability and characterization. While CE-DBT with 100 μm pixel size demonstrated equal or superior performance in tasks requiring better spatial resolution (lesion margin characterization and extent measurement in the presence of noise), CE-bCT proved to be more adapted for iodine uptake quantification tasks.

It remained clear for us, however, that CE-bCT lower performance was especially influenced by the presence of high quantum noise levels when assuming typical dose levels of two-view standard mammography. In this scope, in the next chapter we present two post-processing techniques, specifically designed for dual-energy imaging, and aiming to enhance the quality of CE-bCT iodine-equivalent images.

Chapter 7

Towards Low-Dose Fully 3D Quantitative Breast X-ray Imaging

In the optimization study of Chapter 5 and in the human observer study described in Section 6.3, a cone-beam breast CT geometry defined by a 776 μm detector element pitch, a Hamming-windowed ramp kernel and tomographic reconstructed slice images with 0.41×0.41 mm^2 pixel size and 1 mm slice thickness was considered ($0.41 \times 0.41 \times 1.0$ mm^3 voxel size; cf. Section 5.2 for further details). As discussed in Sections 5.3 and 5.5, based on contrast-to-noise ratio measurements and Rose's detectability criterion [246, 247], we showed that in an average-sized breast and with dose levels comparable to a two-view mammogram, this cone-beam geometry allowed to barely depict a 2 mm diameter lesion containing 0.5 mg/cm^3 of iodine, *i.e.* the smallest lesion and iodine uptake clinically expected. Moreover, when considering human observers, we showed that iodine uptake detectability in CE-bCT images was not significantly different from CE-DBT, and that noise was the limiting factor for CE-bCT.

In this chapter, two different post-processing denoising strategies are evaluated to reduce noise and potentially improve iodine-enhanced lesion detectability in recombined CE-bCT images. The radiation dose required by an optimized CE-bCT acquisition such as to enable the depiction of lesions with minimal size and minimal iodine uptake expected in clinical practice is object of discussion. CE-bCT dose requirements are compared to those used in current two-view standard mammography.

In Section 7.1, an Anti-Correlated Noise Reduction (ACNR) technique is described for the dual-energy three-material decomposition problem of CE-bCT. In section 7.2, a previously developed Total Variation regularization algorithm is described under the assumptions that contrast uptakes in CE-bCT images have piecewise-constant properties. In Section 7.3, the two described techniques are leveraged to improve lesion detectability using the effective Contrast-to-Noise Ratio and Rose's threshold as Figure-of-Merit.

7.1 Anti-Correlated Noise Reduction

In a dual-energy material decomposition context, Anti-Correlated Noise Reduction (ACNR) techniques leverage the fact that quantum noise in the two different material basis images are anti-correlated (the mathematical framework for image anti-correlation is briefly described below). From this hypothesis, various denoising algorithms were developed to carefully combine a given basis material image with filtered versions of the complementary basis images, reducing the total covariance of the multispectral transformation [297–302].

Since this technique requires perfect spatial correlation between low-energy (LE) and high-energy (HE) images, its application to dual-energy breast imaging is however limited to conditions without breast motion artifacts. At this time, resilience to motion artifact makes fast acquisition techniques more favorable for anti-correlated noise reduction. Appropriate motion correction algorithms may make it pertinent for acquisition techniques with lower frame rates [303].

Noise Propagation in Dual-Energy Imaging

As described in Chapter 4, dual-energy material decomposition is summarized in transforming low and high energy log-projections p^{LE} and p^{HE} into basis material projections δ_1 and δ_2:

$$(p^{LE}, p^{HE}) \xrightarrow{\mathcal{T}_{DE}} (\delta_1, \delta_2) \tag{7.1}$$

where $\mathcal{T}_{DE}$ denotes the dual-energy material separation. This transformation was described in Chapter 4 and expressed by Equation 4.3, which can be re-written as:

$$p = -ln\left(\frac{SI}{SI_0}\right) = -ln\int_0^\infty w(E)dE \cdot exp\left[\delta_1\left(\frac{\mu}{\rho}\right)_1(E) + \delta_2\left(\frac{\mu}{\rho}\right)_2(E)\right] \tag{7.2}$$

where SI is the signal intensity in the projections, SI_0 is the signal intensity in projections without the imaged object, $w(E)$ is the normalized spectrum weight (cf. Equation 4.4) and $({}^{\mu}/_{\rho})_m(E)$ is the linear mass attenuation coefficient of basis material $m \in 1, 2$ at energy E.

Since the p^{LE} and p^{HE} are obtained from independent acquisitions, signal intensity fluctuations depend solely on their individual photon statistics and, as consequence, the expectation $\mathbb{E}(p^{LE} \cdot p^{HE}) = 0$. Hence, if $(\sigma^{LE})^2$ and $(\sigma^{HE})^2$ are the variance of signal intensities in the log-projections p^{LE} and p^{HE}, respectively, the variance and covariance of the material basis projections can be expressed as:

$$Var(\delta_m) = \left(\frac{\partial\delta_i}{\partial p^{LE}}\right)^2 \cdot \left(\sigma^{LE}\right)^2 + \left(\frac{\partial\delta_i}{\partial p^{HE}}\right)^2 \cdot \left(\sigma^{HE}\right)^2, \qquad m = 1, 2 \tag{7.3}$$

and

$$Cov(\delta_1, \delta_2) = \left(\frac{\partial\delta_1}{\partial p^{LE}}\right) \cdot \left(\frac{\partial\delta_2}{\partial p^{LE}}\right) \cdot \left(\sigma^{LE}\right)^2 + \left(\frac{\partial\delta_1}{\partial p^{HE}}\right) \cdot \left(\frac{\partial\delta_2}{\partial p^{HE}}\right) \cdot \left(\sigma^{HE}\right)^2 \tag{7.4}$$

If quantum noise (modeled as a Poisson distribution) is the main source of fluctuation, and assuming a stationary and shift-invariant system, the partial derivatives $({}^{\partial\delta_1}/_{\partial p^{LE}}) \cdot ({}^{\partial\delta_2}/_{\partial p^{LE}})$ in the first term of Equation 7.4 have opposite signs [297]. The same happens to the partial derivatives $({}^{\partial\delta_1}/_{\partial p^{HE}}) \cdot ({}^{\partial\delta_2}/_{\partial p^{HE}})$ in the second term of Equation 7.4. As consequence,

$$Cov(\delta_1, \delta_2) < 0 \tag{7.5}$$

The full mathematical expression for $Cov(\delta_1, \delta_2)$ and the proof of its negativity was derived previously by Alvarez *et al.* [304, 305]. Moreover, the derivative terms $({}^{\partial\delta_i}/_{\partial p^{LE,HE}})$ can be calculated analytically using the transformation equation for δ_i, which in this thesis was modeled as a weighted sum of the integrals in Equation 7.2, as suggested by Alvarez and Macovski [204, 216] (cf. Chapter 4).

Although the noise propagation properties described above were derived for a set of material projection images, they can be extended to the material equivalent volumes f_{iodine}, f_{gland} and $f_{adipose}$, which are the main outputs of the proposed Dual-Energy bCT framework in this thesis. In order to do so, we will make use of the following theorem:

Theorem 7.1. *If a tomographic reconstruction method $\mathcal{R}$ can be expressed as a linear transformation, then a negative covariance among a set of projection images p_1 and p_2 results in a negative covariance among the respective set of tomographic reconstructed volumes $\mathcal{R}\{p_1\}$ and $\mathcal{R}\{p_2\}$:*

$$Cov(p_1, p_2) < 0 \implies Cov(\mathcal{R}\{p_1\}, \mathcal{R}\{p_2\}) < 0 \tag{7.6}$$

as long as $Cov(p_1(i), p_2(j)) = 0$, where i and j are the index for two different detector elements ($i \neq j$).

Proof. A theoretical demonstration of Theorem 7.1 is provided in Annex D.

Corollary 7.1. *(Projection-based Recombination) The covariance negativity between the material projections δ_1 and δ_2 are transferred to the reconstructed material volumes $\rho_1(\boldsymbol{r})$ and $\rho_2(\boldsymbol{r})$, and further on to the material equivalent volumes $f_{iodine}(\boldsymbol{r})$, $f_{gland}(\boldsymbol{r})$ and $f_{adipose}(\boldsymbol{r})$.*

Corollary 7.2. *(Image-based Recombination) Covariance negativity found after the transformation $\mathcal{T}_{DE}$ of the log-projections $p^{LE,HE}$ is found in the reconstructed low and high-energy volumes $\mu^{LE,HE}(\boldsymbol{r})$ transformed by $\mathcal{T}_{DE}$, as long as the 3D volume data are spatially correlated, i.e. without truncation artifacts nor non-rigid transformation such as patient movement. This implies that covariance negativity will also be found in the material equivalent volumes $f_{iodine}(\boldsymbol{r})$, $f_{gland}(\boldsymbol{r})$ and $f_{adipose}(\boldsymbol{r})$.*

Algorithm for Noise Reduction

To illustrate the property of negative covariance, we make use of the simulation results carried in Section 5.4, using projection-based recombination. Figure 7-1a illustrates a short profile of signal intensities in δ_{iodine} and δ_{gland}, taken at the same detector positions (the profiles were centered at their mean value and normalized to their respective variances, only to allow an illustration in the same range of the ordinate axis range). Although the profiles have different low-frequency behavior, the changes in intensity between consecutive pixels have opposite directions. The same happens to the reconstructed material volumes $\rho_{iodine}(\mathbf{r})$ and $\rho_{gland}(\mathbf{r})$, as foreseen by the Theorem 7.1 and illustrated in Figure 7-1b.

The ACNR technique reduces noise in a given material image, say δ_{iodine}, by applying a high-pass filter to the complementary image δ_{gland}. The filtered image will no longer contain anatomical structures (*i.e.*, low-frequency contents), leaving only the quantum noise, which is anti-correlated to the quantum noise in δ_{iodine}. Finally, the target material image is added to the filtered complementary image, weighted by a parameter w_c:

$$\delta_{ACNR}(u, v) = \delta_{iodine}(u, v) + w_c \delta_{gland}(u, v) * h_{HPF}(u, v) \tag{7.7}$$

where (u, v) are the 2D detector coordinates. The choice of w_c can be determined analytically through the minimization of quantum noise [305] or empirically through the quantitative or qualitative assessment of a given Figure-of-Merit. The same reasoning could be applied to reduce noise in δ_{gland}, while using δ_{iodine} as complementary image.

Application to Three-Material Decomposition

In our case, we are mainly interested in reducing noise in the iodine-equivalent volume $f_{iodine}(\mathbf{r})$, resulting of the three-material recombination. It must be noticed however that, independent of the recombination method (image-based or projection-based) the linear system of three-material recombination has two inputs (p^{LE} and p^{HE}) and three outputs ($f_{iodine}(\mathbf{r})$, $f_{gland}(\mathbf{r})$ and $f_{adipose}(\mathbf{r})$).

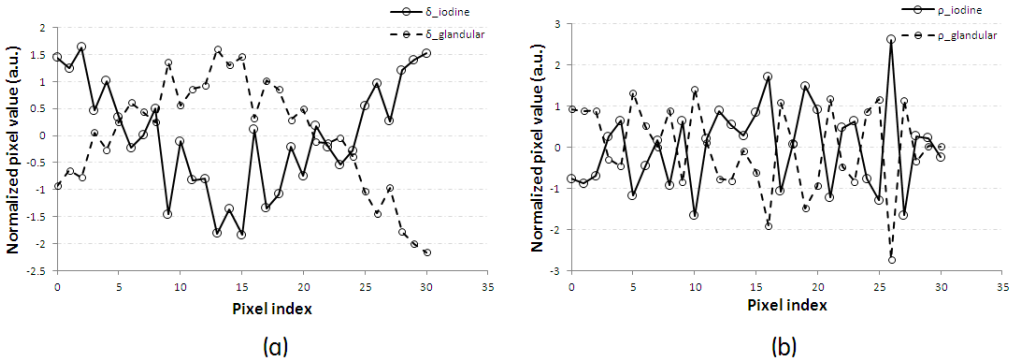

Figure 7-1: Centered and normalized pixel values in (a) material projections δ_{iodine} and δ_{gland}, and in (b) their respective tomographic reconstructed images $\rho_{iodine}(\mathbf{r}) = \mathcal{R}\{\delta_{iodine}\}$ and $\rho_{gland}(\mathbf{r}) = \mathcal{R}\{\delta_{gland}\}$, where $\mathcal{R}$ is the FBP reconstruction transformation

Hence, if no other source of fluctuation beside quantum noise is involved, we have:

$$Cov(f_{iodine}, f_{gland}) = -Cov(f_{iodine}, f_{adipose}) \tag{7.8}$$

which means that the complementary image can be either f_{gland} or $f_{adipose}$, since both covariances will be reduced simultaneously.

As mentioned previously, the noise reduction algorithm can be implemented in both projection and image domains. In the image domain, the implementation is straightforward and, similarly to Equation 7.7, the final denoised image, $f_{ACNR}(x, y, z)$, is found as

$$f_{ACNR}(x, y, z) = f_{iodine}(x, y, z) + w_c f_{gland}(x, y, z) * h_{HPF}(x, y, z) \tag{7.9}$$

where (x, y, z) are the 3D volume coordinates and h_{HPF} is a high-pass filter kernel.

In the projection domain, we recall the fact that the projections of f_{iodine} and f_{gland}, represented here by t_{iodine} and t_{gland}, respectively, can be written as linear combinations of δ_{iodine} and δ_{gland} (cf. Section 4.4), such as:

$$\begin{cases} t_{iodine} = \displaystyle\int_{L_{i,s}} f_{iodine}(\mathbf{r})dl = a_1\delta_{iodine} + a_2\delta_{gland} + a_3 \\ t_{gland} = \displaystyle\int_{L_{i,s}} f_{gland}(\mathbf{r})dl = b_1\delta_{iodine} + b_2\delta_{gland} + b_3 \end{cases} \tag{7.10}$$

where dl is the incremental chord length of the beam path $L_{i,s}$ between the X-ray source s and the detection element i, and a_i's and b_i's are the recombination coefficients for texture cancellation in f_{iodine} and f_{gland}, respectively. Finally, the ACNR technique can be applied to denoise t_{iodine}, obtaining after reconstruction, the final iodine-equivalent volume $f_{ACNR}(x, y, z)$:

$$\begin{cases} t_{ACNR}(u, v) = t_{iodine}(u, v) + w_c t_{gland}(u, v) * h_{HPF}(u, v) \\ f_{ACNR}(x, y, z) = \mathcal{R}\left\{t_{ACNR}(u, v)\right\} \end{cases} \tag{7.11}$$

where $\mathcal{R}\{\cdot\}$ is the linear reconstruction method, in this case, FBP.

7.2 Total-Variation Regularization

Total variation (TV) regularization for image denoising/restoration was first introduced by Rudin *et al.* [306]. It is based on the assumption that a signal with excessive high-frequency detail has high total variation. As described in Ref. [306], TV minimization algorithms, constrained to be faithful to the original data, remove noise whilst preserving the sharpness of edges.

TV-based regularization algorithms are particularly effective for piecewise-constant images. If applied to images that are not piecewise constant, TV-minimization may lead to so-called staircase or stepping artifacts. However, recent developments on new regularization strategies suggest that discrete image arrays which are close enough to be piecewise-constant do not necessarily lead to stepping artifacts [307].

In breast imaging, constrained TV minimization has been used in iterative image reconstruction problems such as microcalcifications restoration under poorly sampled acquisitions [133,308], total patient dose reduction while optimizing the trade-off between number of views and the dose level per view [238,309], as well as a regularization term for noise reduction and edge preservation [108,310].

Previous work on breast CT data segmentation suggest that, excluding the skin and eventual presence of microcalcifications, we may assume the breast to be composed of fibroglandular and adipose tissues, or some combination of the two [311, 312]. In the construction of digital breast phantoms, although density differentiation was found to provide better emulation of the marbling effect [312, 313], binary classification between fibroglandular and adipose tissue also lead to realistic anatomic texture [296, 314]. As a consequence, we may conclude that a piecewise-constant assumption for breast CT images is justified, making them suitable for TV-based regularization.

Piecewise-constant assumption becomes even truer for contrast-enhanced iodine-equivalent images, were any density variation between fibroglandular and adipose tissue is supposedly cancelled. The exception would be in the case where the contrast agent is not homogeneously distributed, due to gradients of vascularity or due to diffusion in the breast tissue. However, these effects will not be discussed in this thesis and we assume, as in the previous sections, a homogeneous uptake of iodine in the cancerous tissue volume.

In this section, we make use of a TV-minimization algorithm previously developed within GE Healthcare by Reshef *et al.* [315] in the context of Compressed Sensing approaches for iterative reconstruction in Rotational Angiography [316–318] and Subtraction Rotational Angiography [319]. We assumed that the contrast uptake in Contrast-Enhanced Dual-Energy breast CT images have similar piecewise-constant properties as the injected vessels in angiography images. The algorithm implementation follows the framework of Alternating Direction Method of Multipliers (ADDM) introduced by Goldstein and Osher [320].

Algorithm Description

For Contrast-Enhanced Dual-Energy breast CT, we leverage the TV-minimization algorithm exclusively as a filtering process for noise reduction and edge preservation. The algorithm is therefore applied as a post-processing of previously obtained reconstructed iodine-equivalent volume data, f_{iodine} (output of either image-based or projection-based decomposition algorithms – cf. Section 4.4). For simplicity, the input iodine-equivalent volume will only be referred as f_0 (as for the initial observed data).

One typical way of representing the TV denoising problem for obtaining the uncorrupted image f is the following [306]:

$$f = \arg\min_f \{ \underbrace{\frac{1}{2}\|f - f_0\|_2^2}_{\text{data constraint term}} + \underbrace{\lambda \cdot \chi(Af)}_{\text{regularization term}} \} \tag{7.12}$$

where $\chi(\cdot)$ is a convex regularization function, A is a linear operator and λ is the regularization

parameter controlling how much smoothing is performed.

The Split Bregman technique defined in Ref. [320] is used to solve this problem in a very efficient way, even for isotropic TV minimization problems. It consists in splitting Equation 7.12 into a joint minimization problem over image f and a supporting variable $g = Af$. The optimization problem is then written as:

$$f, g = \arg\min_{f,g} \left\{ \frac{1}{2}\|f - f_0\|_2^2 + \frac{\mu}{2}\|g - Af\|_2^2 + \lambda \cdot \chi(Af) \right\} \tag{7.13}$$

with any $\mu > 0$ (typically we chose μ equal to 1). The algorithm alternatively minimizes Equation 7.13 along direction f with g fixed, then along direction g with f fixed. To enforce the piecewise constant assumption, a common approach is to penalize the image gradient $g = Af = \nabla f$, using either anisotropic ℓ_1-norm, $\chi = \|\cdot\|_1$,

$$\|g\|_1 = \sum_k \|g_k\|_1 = \sum_k |g_k^x| + |g_k^y| + |g_k^z| \tag{7.14}$$

or isotropic ℓ_1-norm, $\chi = \|\cdot\|_{1,2}$,

$$\|g\|_{1,2} = \sum_k \|g_k\|_2 = \sum_k \sqrt{|g_k^x|^2 + |g_k^y|^2 + |g_k^z|^2} \tag{7.15}$$

where g_x, g_y and g_z are, respectively, the x, y and z components of the image gradient g. A variable b is used in the term $\|g - Af - b\|_2^2$ in order to track the error of the gradient inversion $g - Af$ and is reinjected in the iterations.

7.3 Assessment of Iodine-Enhanced Lesion Detectability Improvement in CE-bCT

In this section we perform a preliminary feasibility assessment of the proposed Cone-Beam DE-bCT system in terms of the depiction of iodine in iodine-equivalent images, when the total Average Glandular Dose is kept at the same level of a two-view standard mammogram. We leverage the two denoising techniques described in Sections 7.1 and 7.2 to improve iodine-enhanced lesion detectability, using the effective Contrast-to-Noise Ratio and Rose's criterion as minimum threshold for detectability.

Simulation Setup
An average-sized anthropomorphic breast phantom, containing minimum iodine concentration was simulated. The 14 cm diameter phantom was constituted by a complex structure of $0.5mg/cm^3$ of iodine mixed with 50% fibroglandular equivalent background (reference image in Figure 7-2).

As in Section 5.3, six-hundred projections were simulated using a 0.776 mm detection element pitch, at optimal monochromatic LE and HE spectra and AGD repartition (*i.e.* $LE = 30keV$, $HE = 34keV$ and 50/50% dose repartition - cf. Table 5.1). The choice of using monochromatic spectra as input was to optimize computational efforts. Since we demonstrated good texture cancellation at optimal polychromatic spectra (cf. Section 5.4), we can expect noise reduction with monochromatic spectra to be in the same order of magnitude if polychromatic acquisitions entailing same noise levels are used. The total AGD was kept at 3 mGy, corresponding to dose levels of a two-view standard mammogram.

LE and HE 512×512 reconstructed images were reconstructed using FBP algorithm, with $0.41 \times 0.41mm^2$ pixel size, and 1 mm slice thickness. Contrast-to-Noise Ratio (CNR) per pixel between contrast uptake and the background in recombined iodine-equivalent images was calculated and translated into an effective CNR (CNR_{eff}), as defined by Rose [246,247], for a 2 mm diameter circular lesion:

$$CNR_{eff} = \frac{SI_{iodine} - SI_{bg}}{\sigma_{bg}} \times \sqrt{\text{lesion area in pixels}} \tag{7.16}$$

where SI_{iodine} and SI_{bg} are respectively the means per-pixel SI in an iodine-enhanced region of interest (ROI) and a non-iodine enhanced neighboring background ROI, and σ_{bg} is the standard deviation of the SI in the non-iodine enhanced neighboring breast background ROI. Rose's threshold for minimum lesion depiction is achieved for CNR_{eff} values above 5.

CNR_{eff} was evaluated for different reconstruction filter kernels (ideal ramp alone and ideal ramp with Shepp-Logan and Hamming apodizing windows), with additional anti-correlated noise reduction (ACNR) and Total Variation minimization. For the ACNR implementation, the high-pass filter kernel in Equation 7.9 was defined as $h_{HPF}(x,y,z) = 1 - h_{LPF}(x,y,z)$, where $h_{LPF}(x,y,z)$ is a low-pass filter. Through qualitative assessment, we found that a 5×5 average kernel as low-pass filter showed good results in terms of noise reduction while including minimal edge artifacts. For the TV minimization, different values of regularization parameter λ were tested. We will illustrate only two λ values entailing a soft and a strong smoothing, preserving in both cases the overall appearance of the original images.

Results
Figure 7-2 summarizes the results of iodine-enhanced lesion detectability study using the anthropomorphic phantom. It illustrates the worst-case scenario in terms iodine uptake at low patient dose, which explains the rather noisy images. The first row shows coronal slices of iodine-equivalent images acquired with a 30 keV/34 keV LE/HE pair and using a 50% LE dose repartitioning ratio, for the different denoising schemes. The second row represents zoomed 60×60 pixels ($24.6 \times 24.6\ mm^2$)

ROIs. All images are displayed using the same window and level values. The last row of Figure 7-2 shows CNR_{eff} calculated for a 2 mm diameter lesion and for the difference denoising schemes.

In comparison to the Shepp-Logan windowed implementation, similar increase in CNR_{eff} values was observed when applying a Hamming window and when combining the Shepp-Logan window with the ACNR technique. However, CNR_{eff} doubled when the Shepp-Logan window and the ACNR implementation are combined with a soft TV regularization, and quadruplicate when combined with a strong TV regularization. Although we found improvements in CNR_{eff} for the different denoising schemes, they were also correlated with an overall loss in spatial resolution, as can be seen in the coronal slices illustrated in Figure 7-2. The images tended to be more blurred as CNR_{eff} increased. This is particularly true from TV implementation, where in addition, "salt and pepper" artifacts were introduced when high λ values were used.

Figure 7-3 shows the AGD required to achieve $CNR_{eff} = 5$ for a 2 mm diameter lesion and 0.5 mg/cm^3 of iodine concentration, as function of the different denoising schemes combinations. For reference, the 3 mGy AGD corresponding to approximate dose levels of two-view standard mammography is also draw. Notice that the results in Figure 7-3 reflects those presented in Figure 7-2, by a squared root factor: $CNR_{eff} \propto \sqrt{AGD}$.

Discussion

Under the idealistic hypothesis of this study, both ACNR and TV regularization improved iodine detectability in a CE-bCT setup.

Figure 7-2 showed that the CNR_{eff} threshold of 5 was not achieved when only the ideal ramp or ideal ramp with Shepp-Logan apodization were used. For the Hamming windowed ramp kernel and Shepp-Logan+ACNR implementations, CNR_{eff} values were slightly above 5. However, the ACNR implementation demonstrated the possibility of keeping higher spatial resolutions, while reducing noise. A greater improvement was observed with TV regularization. CNR_{eff} approximately double when including a soft λ smoothing. Further improvement was achieved when including a strong λ smoothing. Although CNR_{eff} also approximately double when compared to a soft λ, "salt and pepper" artifacts were present. A soft regularization may therefore be preferred and possibly sufficient.

The ACNR technique provided much lower relative improvement, when compared to TV. This is may be partially attributed to the fact that LE and HE reconstructed images were highly correlated, due to the proximity in LE and HE monochromatic beams energies. Hence, not much anti-correlation was left to be filtrated. If polychromatic spectra are used, lower correlation will be present and the algorithm is expected to provide better improvement in CNR.

Although the inclusion of TV regularization showed high improvements in CNR, it must stay clear that the algorithm should have a worse performance for images with higher noise and entailing in contrast uptakes below detectable levels. In other words, it is highly uncertain that a TV filtration could recover a signal that is already not detectable, but will rather provide great improvement in terms of signal-to-noise ratios in situations where the signal can already be slightly detected. Additionally, it must also be emphasized that the detectability improvement results based solely on CNR measurements are likely to be different from the potential improvement in detectability seen by a human observer. The loss in spatial resolution and the appearance of "salt and pepper" artifacts from TV regularization should affect the improvement factors found in this study.

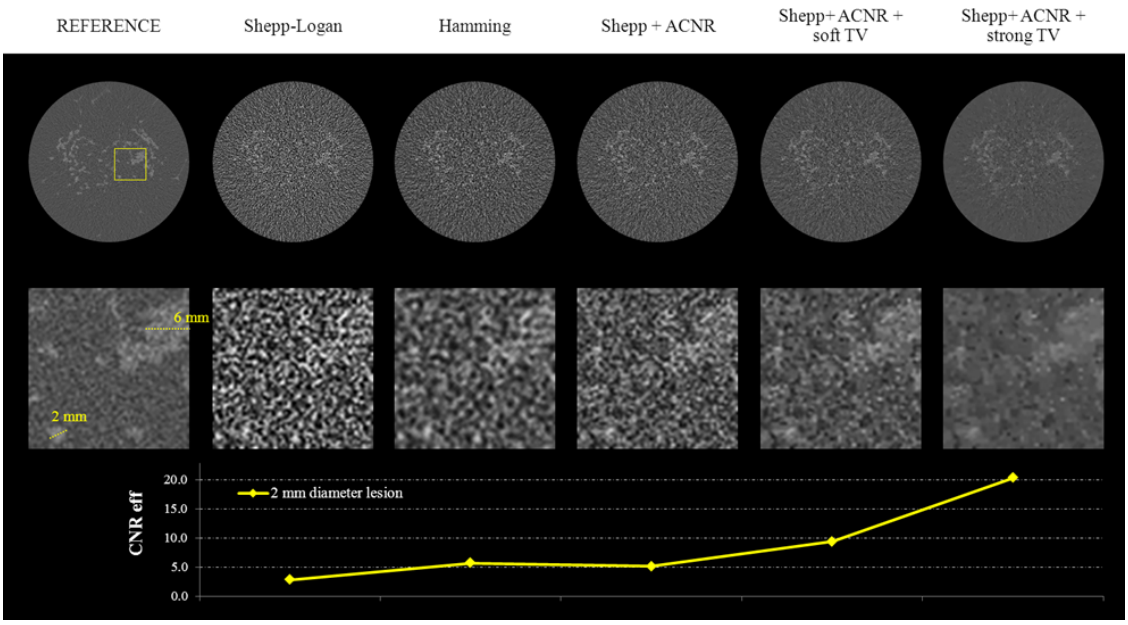

Figure 7-2: Detectability improvement in Iodine-equivalent slices of a textured phantom. The reconstructed images were processed using different combination of denoising schemes. The second row shows a zoomed 60×60 pixels (24.6×24.6 mm) ROI. The third row shows CNR_{eff} calculated for a 2 mm diameter lesion. The results are based on a 50% fibroglandular 14 cm diameter phantom with 0.5 mg/cm^3 iodine uptake

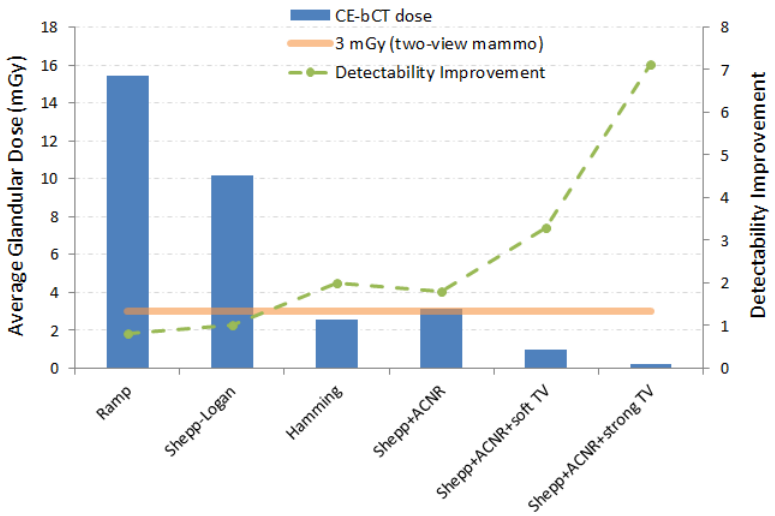

Figure 7-3: Bar plot of Average Glandular Dose required to achieve $CNR_{eff} = 5$ for a 2 mm diameter lesion and minimal 0.5 mg/cm^3 of iodine concentration, as function of the different denoising schemes combinations (left ordinate axis). The dashed line shows the CNR improvement factor with respect to Shepp-Logan filtration only (right ordinate axis). The solid line indicate the 3 mGy level of a two-view mammogram

7.4 Conclusions

In this chapter two post processing techniques, an Anti-Correlated Noise Reduction (ACNR) technique and a Total-Variation (TV) regularization, specifically designed for dual-energy imaging, where evaluated to improve the detectability of iodine uptake in a dual-energy CE-bCT setup.

With the same breast CT geometry and under the idealistic assumptions of the previous chapters (primary monochromatic X-rays photons and a perfect energy-integrating noise-free blur-free detector), we showed that both post-processing schemes allowed to improve detectability and depict iodine-enhanced lesions with minimal size and uptake expected clinically at dose levels of standard mammography. We showed that the combination of ACNR and a soft TV regularization gave optimal results in terms of CNR improvement while keeping minimum artifacts.

In the implemented ACNR technique, a high-pass filter kernel was defined as $h_{HPF}(x, y, z) = 1 - h_{LPF}(x, y, z)$, where $h_{LPF}(x, y, z)$ was a 5×5 average kernel as low-pass filter. This choice was based on preliminary observations in terms of noise reduction and introduction minimal edge artifacts. Theoretically, any high-pass filter (or complementary low-pass filters) could have been implemented. More importantly, the better filter choice would be the one adapted to the type of texture in the image such as to avoid the appearance of artifact generated from filtration. In literature, average [298] and Gaussian [301] low-pass filters with different kernel sizes have been used for anti-correlated noise reduction in dual-energy imaging.

In our investigation, FBP reconstruction was chosen as the main algorithm for both CE-bCT and CE-DBT. This type of algorithm is easy to implement, and present high stability and linearity properties. The latter allows us for instance to extrapolate simulation results to scenarios under different noise levels. In literature, different iterative reconstruction algorithms have been implemented for single-energy breast CT acquisitions, supported by regularized or penalized gradient-descent [106, 238, 309], statistical models of quantum variation [134], as well as more complex algorithms integrating various physical models of an X-ray system acquisition chain [108]. As far we know, the potential of iterative algorithms on reconstructing functional iodine-equivalent data in a dual-energy CE-bCT setup, especially in their ability to exploit iodine-equivalent image noise and sparsity properties, is still unknown. In this chapter, a TV regularization algorithm provided preliminary assessment on the exploitation of sparsity properties of iodine-equivalent images. Although the algorithm was not coupled to an iterative reconstruction framework, noise reduction was evident, leaving good perspectives for future research work.

In summary, during the spectral optimization studies described in Chapter 5. CE-bCT performance in the depiction of the smallest lesion size and iodine concentration expected in clinical practice, at dose levels comparable to a 2-view mammogram, was either insufficient or just above Rose's detectability criterion, depending on the input parameters and the dual-energy acquisition strategy. Moreover, as discussed in the human observers study presented in Section 6.3, maintaining CNR close to detectable levels came in expense of CE-bCT spatial resolution, as observed by the inferior performance in high-frequency tasks such as lesion characterization and lesion extent estimation, when compared to CE-DBT.

Accordingly, aiming to improve CE-bCT performance, in this chapter we showed that both ACNR and TV-regularization techniques can be leveraged as post-processing techniques to decrease noise in iodine-equivalent images and potentially ameliorate detectability in CE-bCT.

Conclusions and Perspectives

The purpose of this PhD thesis research has been to study the technical feasibility of iodine-enhanced dual-energy Contrast-Enhanced Breast CT (CE-bCT) and its potential to accurately depict and localize tumors, as well as to provide accurate quantitative information on contrast uptake morphology and concentration, at radiation dose levels comparable to a two-view mammogram. To understand the incremental value of CE-bCT over Contrast-Enhanced Digital Breast Tomosynthesis (CE-DBT), the quantitative potential of both technologies have been compared.

Implemented Methods
A cone-beam CT geometry was considered for CE-bCT technique since there is an interest in investigating techniques based on typical mammography geometries and equipment. This geometry also allows for an easier comparison with CE-DBT. A cone-beam breast CT topology similar to that published by Boone *et al.* [103] was adopted.

In order to meet the objectives of this research, a software platform allowing to simulate, optimize and compare 2D/3D cone-beam X-ray imaging systems was implemented. The platform was based on CatSim, a virtual X-ray imaging tool in continuous development within GE Global Research Center and GE Healthcare. We developed modules for CatSim simulation chain aiming to model X-ray projections of breast phantoms at the energy range of breast imaging. X-ray fluence spectrum models for anode materials and energy ranges used in breast imaging were discussed and implemented. Analytical and mesh-based digital breast phantoms were implemented to emulate the compressed and uncompressed breast anatomy. Monte Carlo models of X-ray scattering and absorbed radiation dose occurring in breast phantoms were described. Signal and noise propagation were described for an ideal blur-free detector, which was the main model used throughout this thesis. For experimental validation purpose, signal and noise propagation inside a realistic indirect conversion scintillator-based detector was also described.

In order to make sure that the implemented simulation chain is capable of emulating realistic physical phenomena underlying an X-ray breast imaging system, we performed an extensive validation of the developed models with regard to previously published and experimentally obtained data. The experiments were focused on X-ray photon energies, breast thicknesses and compositions expected in breast imaging. Beam penetrating quality of X-ray spectrum models showed to be in agreement with the behavior of a realistic X-ray tube, with error below 2% on average. Monte Carlo based simulation of scattered photon intensity showed good qualitative agreement with previously reported results. Peak scatter-to-primary ratio values were within ∼5% error. Monte Carlo based estimation of absorbed average glandular dose (AGD) were compared to previously published results and agreed within ∼4% error for both typical mammography and breast CT geometries. Detector spatial resolution (pre-sampling MTF) and Noise Power Spectrum (NPS) simulations qualitatively agreed to those of real X-ray image systems. Signal intensity and Signal-to-Noise ratio for low-energy spectra (below 33.2 keV) agreed within ∼5% error when compared to a real X-ray mammography system, while signal intensity and Signal-to-Noise ratio for high-energy spectra (above 33.2 keV) agreed within ∼8% error when compared to a real X-ray fluoroscopy system. In sum, our results provided qualitative and quantitative evidence that developed acquisition simulation chain is in agreement with realistic X-ray imaging systems.

A dual-energy three-material decomposition framework allowing for iodine K-edge imaging in a breast CT geometry setup was formulated. We described algorithms allowing to recombined low-energy (HE) and high-energy (HE) acquisitions in both image and projection domains. The image-based recombination algorithm was based on the linear recombination of measured LE and HE attenuation volumes, while projection-based recombination algorithm was based on Alvarez and Macovski [204, 216] high-order polynomial recombination of LE and HE projection data. We demonstrated that it is possible to find for CE-DBT and CE-bCT, high and low energy acquisition spectra pairs, meeting the spectral conditions for three-material separation, benefiting from improved contrast enhancement of K-edge imaging. Additionally, we proposed a material decomposition calibration method to ensure optimal recombined iodine-equivalent images during CE-bCT acquisition parameters optimization. The implemented method showed to be robust, providing maximum background texture cancellation and minimum cupping artifact to a large set of input LE and HE spectra, independently of the decomposition domain.

Since in this PhD thesis research we have been manipulating simulated data, Alvarez and Macovski [204,216] polynomial approach was chosen for projection-based material decomposition. This allowed for faster calculation and little stability problems during spectral optimization. In a real case scenario however, photon starvation and other nonlinear imaging artifacts could lead polynomial fit approaches to erroneous decomposition. Elsewhere, look-up table methods [206,218] were proposed for dual-energy imaging in order to address the fluctuations of polynomial coefficient calibration in the presence of high quantum noise levels and image artifacts. Furthermore, these methods could, in theory, be conceived such as to better handle the K-edge discontinuity. Another approach proposed in literature to decompose dual-energy data consists in using iterative methods [211, 219]. They present the possibility of being incorporated in an iterative reconstruction algorithm workflow and benefit from noise regularization and artifact management. Both look-up table and iterative approaches deserve further investigation to evaluate their potential in better handling real CE-bCT data.

Optimal Dual-Energy Acquisition Technique for CE-bCT

In order to reveal the dual-energy acquisition strategy and acquisition parameters maximizing the performance of CE-bCT technique in the depiction of contrast-agent uptakes, a spectral optimization study was performed. The optimization assumed ideal detectors, *i.e.*, with no blur and perfect efficiency, and X-ray point sources emitting monochromatic and polychromatic beams. Rose's detectability criterion based on Contrast-to-Noise Ratio (CNR) measurements [246, 247] was used to assess the detectability of iodine-enhanced lesion at optimal input parameters. We assumed a 2 mm diameter lesion enhanced by 0.5 mg/cm^3 of iodine as the minimum lesion size and iodine concentration expected in clinical practice. Detectability was assessed at 3 mGy AGD, which corresponds approximately to the screening AGD for a two-view examination of an average-sized breast using the AOP[1] Contrast mode of GE Senographe® Essential system [248].

The spectral optimization started by identifying LE and HE monochromatic spectra and average glandular dose repartitioning between the LE and HE acquisitions, for which dose-dependent detectability criteria were maximized. We showed that in order to obtain optimal iodine detectability in recombined dual-energy images, LE and HE spectra need to bracket the iodine K-edge (33.2 keV) and an approximate 50%-50% average glandular dose repartitioning between LE and HE exposures is required. For microcalcification and mass depiction in LE morphologic images, we found that optimal LE values were close to those optimizing iodine depiction, demonstrating the feasibility, in term of spectra, of a CE-bCT system capable to provide both functional and morphological information. For instance, 27keV/34keV, 30keV/34keV and 33keV/34keV LE/HE pairs were found to provide a good compromise in performance for iodine, microcalcification and mass detectability in respectively small, average and large diameter phantoms. For an average-sized breast, CNR of target iodine-enhanced lesion was slightly above Rose's criterion.

In a second step of CE-bCT acquisition parameter optimization, the results of the monochro-

[1] AOP – Automatic Optimization of Parameters for exposure control system

matic optimization were used as first approximation for the optimal polychromatic acquisition parameters. X-ray fluence spectra generated from a Tungsten anode and filtered with Tin (Sn, K-edge: 29 keV) and Copper (Cu) were chosen to provide LE and HE spectra with mean energies close to optimal monochromatic beam energies found previously, while enabling flexibility to minimize superposition. While LE and HE X-ray spectra approaching monochromaticity provide optimal lesion contrast and noise weighting, minimal spectral superposition between them avoids undesired uncorrelated noise from the complementary spectral image. Four dual-energy acquisition strategies were considered: i) 2 sources, 2 kVs and 2 filters (Sn/Cu); ii) 1 source, 2 kVs and 2 filters (Sn/Cu); iii) 1 source, 2 kVs and 1 filter (Cu); and iv) 1 source, 1 kV, 1 filter (Cu) and an energy-discriminating detector. By comparing the different DE acquisition strategies we revealed that iodine K-edge imaging with both ideal energy-discriminating and non-discriminating detectors are feasible in terms of background texture cancellation and cupping artifact magnitude, which showed to be below the minimum target iodine-enhanced lesion concentration ($0.5\ mg\ I/cm^3$).

The performance of the four acquisition strategies was compared under a *constant tube power* constraint for the LE and HE acquisitions. A dual-energy implementation leveraging an ideal photon-counting energy-discriminating detector showed highest iodine uptake detectability, due to perfect spectral separation and proximity of LE and HE bins mean energies to the optimal mono-chromatic beam energies. On the other hand, DE acquisitions with a single source/filter pair showed lowest detectability, due to the high tube power required by LE acquisitions. Non-discriminating techniques applying dedicated filtration for LE and HE acquisitions showed intermediate performance. Assuming 300 LE and HE projections acquired in 16.6 seconds with a 1kW tube power constraint, the photon-counting energy-discriminating technique alone presented CNR of target iodine-enhanced lesion at 3 mGy AGD above Rose's criterion.

As stated above, the optimization studies just described assumed ideal detectors. At the same time, columnar structured Cesium Iodide (CsI) scintillators have been widely used for digital breast X-ray imaging since the last decade. Several research papers optimizing dual-energy spectra for iodine-enhanced breast imaging with CsI-based detectors found counter-intuitive results, where optimal spectra do not bracket the iodine K-edge as close as expected [226, 257]. We performed, a monochromatic optimization study considering different CsI layer thicknesses, and hence different absorption efficiencies, aiming to provide an explanation to these observations. This study revealed preliminary evidence that optimal dual-energy X-ray spectra strongly depend on detector scintillator thickness. Optimal LE increases with CsI layer thickness and phantom diameter, while optimal HE beam energy occurs just above the K-edges of I and Cs. The same reasoning could be used to explain the behavior of optimal dual-energy spectra in imaging systems based on other scintillator materials and thicknesses.

In this PhD thesis, a throughout evaluation of topological parameters, detector technology and other energy-independent system design parameters impact on CE-bCT image quality was not in the main objectives. In reality, energy-independent system design components defining spatial resolution and noise propagation have been intensively studied for single-energy cone-beam breast CT acquisitions. In particular system topology [119–123], acquisition orbit [118, 136, 137] and reconstruction algorithms [133, 134, 238] impact on the detectability of fibroglandular tissue and microcalcifications have been investigated. Assuming linearity and stationarity of first- and second-order statistics, it was assumed that these results could be extrapolated to describe spatial resolution and noise propagation in dual-energy imaging. With respect to the detector technology, since the spectral optimization studies just described assumed mainly ideal detectors, the derived optimal parameters and feasibility conclusions could be used as *a priori* information for future studies on real X-ray systems. Nonetheless, further investigations taking into account energy-dependent inefficiencies of realistic energy-integrating detectors (*e.g.*, scintillator materials and thicknesses) and realistic energy-discriminating detectors (*e.g.* photon pile-up for photon-counting technology, spectral distortion and realistic frame rates) are necessary to evaluate their actual degradation in image quality and the impact on dose-dependent detectability. For instance, although in this study the ideal energy-discriminating photon-counting detector presented highest iodine uptake detectability, previously published studies has shown that current energy-discriminating capabil-

ities of photon-counting detectors are far from ideal and that state-of-the-art dual kVp methods are still competitive with current photon-counting-based dual-energy systems [140, 264, 267].

Quantitative Comparison of CE-bCT vs. CE-DBT
Using previously obtained optimal dual-energy acquisition parameters for CE-bCT and CE-DBT, their quantitative potential was evaluated through a series of experiments. In a study comparing iodine uptake quantification accuracy in lesions with different sizes, shapes and iodine concentrations, we demonstrated that CE-bCT was superior in quantifying their true iodine concentration, while the artifacts caused by CE-DBT limited depth resolution prevented any precise quantification of iodine uptake. Indeed, results showed that iodine uptake quantification in CE-DBT would only be possible with *a priori* knowledge of the iodine-enhanced lesion dimensions in all axes, particularly because lesion contrast-to-background depends not only on the lesion shape as seen in its in-focus plane image, but depends also on its depth extent. Results were independent of noise.

In another experiment, a human observer study comparing iodine-enhanced lesion depiction and characterization in simulated CE-bCT and CE-DBT iodine-enhanced images was performed, while fixing radiation dose at levels comparable to a two-view mammogram. Under idealistic assumptions for the X-ray source and detector, we revealed that sensitivity and specificity in iodine-enhanced lesion detectability and characterization were not statistically different between the two techniques, except for lesion margin characterization (*e.g.* spicules) for which CE-DBT demonstrated superior sensitivity. We also showed that, for essentially round lesions, CE-DBT is more accurate and more precise in estimating lesion dimensions in the x-z plane (DBT in-focus plane) than CE-bCT. If however, non-symmetric-shaped lesions are considered, CE-DBT performance in the presence of quantum noise would drastically decrease due to lesion contrast dependency on its depth extent and consequent effects on detectability.

In these comparison studies, we assumed the use of ideal CE-bCT and CE-DBT detectors. In a more realistic setting, it is expected that X-ray detectors for CE-bCT and CE-DBT present different efficiencies, in particular since geometric parameters such as pixel size, angular sampling, acquisition time and so on, may impose certain constraints to the detector performance (*e.g.* quanta spreading, lag, electronic noise,...). Additional investigations considering a more realistic implementation for CE-bCT and CE-DBT techniques could be of interest to provide further understanding on iodine-enhanced lesion detectability and characterization. We may expect to find statistically significant differences in sensitivity and specificity, which was not observed during our investigations.

Idealistic hypothesis for the X-ray source were also performed during the comparisons. For instance, in the human observer study, an isotropic point source emitting optimal monochromatic X-ray beams was considered. Indeed, it is expected that assuming polychromatic X-ray fluence spectrum would entail a small degradation in lesion detectability, due to CNR degradation. However, this degradation was assumed to be comparable for both CE-bCT and CE-DBT, and that it would ultimately be insufficient to affect the comparison results between both techniques. In this case, a monochromatic implementation is preferable, since it allows for much faster calculation, especially in the light of the great number of images to be simulated for this study. On the other hand, a finite-sized focal spot, emitting different X-ray fluences from inside its surface, would definitely impact the system's spatial resolution through *focal spot blurring* [149]. The latter would consequently lead to degradation of iodine-enhanced lesion characterization. Furthermore, it is expected that this impact would be different for CE-bCT and CE-DBT, due to their respective acquisition geometry. In this research, these aspects were however disregarded since it would impose the choice of engineering design constraints such as power requirements for a given focal spot size, X-ray tube tilt angles followed by Heel effect degradation, acquisition time and detector frame rates, and other factors that would drive us away from the main theoretical approach held so far. Further studies considering a more realistic X-ray source model, with focal spot sizes adapted for each technique, are still needed to better evaluate their individual iodine-enhanced lesion characterization performance.

In addition to the iodine-equivalent images explored in the observer study, it is also of great interest to provide morphologic images which are spatially correlated to the functional images. They provide complementary morphologic information on the mammary gland, eventual enhanced and unenhanced masses, as well as microcalcification clusters and other typical and relevant mammographic findings. As a consequence, it is expected that detectability and characterization of cancerous lesions would increase when both types of information are available. Since anatomical background is different in reconstructed morphological CE-bCT and CE-DBT volumes [124, 125], we can also expect that the differences in detectability and characterization between CE-bCT and CE-DBT will increase. Hopefully, such scenario could possibly reveal a statistically significant difference between both techniques. CE-bCT would this case benefit from the lower anatomical noise in morphologic bCT images when compared to DBT [124, 296], while CE-DBT would benefit from higher spatial resolution for microcalcification depiction and characterization. Additional human observer studies with available morphological information are required to assess the potential increase in iodine-enhanced lesion detectability and characterization, as well as to verify its added value for each technique.

CE-bCT Feasibility at Dose Levels of Standard Mammography
Under the idealistic hypothesis of this study, a careful choice of topologic parameters for CE-bCT (*e.g.*, pixel and voxel sizes) in combination with noise-attenuating FBP reconstruction kernels and post-processing denoising schemes, an Anti-Correlated Noise Reduction (ACNR) technique and a Total-Variation (TV) regularization, specifically designed for dual-energy imaging, allowed to depict iodine-enhanced lesions with minimal size and uptake expected in clinical practice at dose levels of standard mammography.

In our investigations, FBP reconstruction was chosen as the main algorithm for both CE-bCT and CE-DBT. This type of algorithm is easy to implement, and presents high stability and linearity properties. The latter allows us for instance to extrapolate simulation results to scenarios under different noise levels. On the other hand, the availability of large computational capacities in normal workstations has driven the development of iterative reconstruction algorithms in the past decades. Their ability to include a higher degree of acquisition modeling has allowed to reduce image noise and artifacts, recover spatial resolution and account for uncommon trajectories or incomplete data. Different algorithms have been implemented for single-energy breast CT acquisitions, supported by regularized/penalized gradient-descent [106, 238, 309], statistical models of quantum variation [134], as well as more complex algorithms integrating various physical models of an X-ray system acquisition chain [108]. However, as far as we know, the potential of iterative algorithms on reconstructing functional iodine-equivalent data in a dual-energy CE-bCT setup, especially in their ability to exploit iodine-equivalent image noise and sparsity properties, is still unknown. In this PhD thesis, a TV regularization algorithm provided preliminary assessment of the exploitation of sparsity properties in iodine-equivalent images. Although the algorithm was not implemented in an iterative way, noise reduction was evident, leaving good perspectives for future research work. While computing power may still be a challenge in a more complex modeling of dual-energy acquisitions, X-ray scattering and patient motion compensation, further investigations leveraging model-based iterative algorithms for dual-energy CE-bCT would certainly be beneficial.

Appendix A

Fundamentals of 3D X-ray Imaging

This chapter provides a short overview on the physics of medical imaging and imaging science on which dual-energy X-ray imaging is based. Here, a snapshot of X-ray production, their main interactions with matter as well as the X-ray photons detection with digital detectors are described. Next, the X-ray image signal provided through any given acquisition angle is formalized, while defining the Radon transform and the principles of tomosynthesis and CT reconstruction techniques.

A.1 X-ray Production

X-ray imaging systems use an *X-ray tube* to produce photons, leveraging the fact that highly energetic electrons interacting with matter convert their kinetic energy into electromagnetic radiation.

Figure A-1a illustrates a simplified diagram of a *Coolidge tube*, the most widely adopted design for X-ray generation. It is also called hot cathode tube, since it produces electrons by thermionic effect from a tungsten filament heated by an electric current. A large electrical potential, or *tube voltage*, is applied between the cathode (source of electrons) and the anode (target). Electrons are accelerated and focused to collide with the target anode. The region in which the collisions occur is called the *thermal focal spot*, since only a small fraction (typically less than 1%) of the energy deposited in the X-ray tube is converted into X-rays; the rest appearing in the form of heat. When an electron comes within the proximity of a positively charged nucleus, it undergoes a change in the initial trajectory and a deceleration, which causes a significant loss of kinetic energy. The energy lost during this process is used to produce X-ray photon radiation, named *Bremsstrahlung radiation*, usually emitted perpendicular to the path of the electron beam. The amount of kinetic energy of the electrons transferred to X-ray photons is inversely proportional to their distance to the nucleus. The probability of interactions of electrons with the nucleus is increasing with their distance to the nucleus, and therefore a Brehmstralung spectrum decreases with energy. The maximum energy of the generated X-ray spectrum corresponds therefore to the electron's acceleration energy in the electric field generated between the anode and the cathode, *i.e.* a complete energy transfer; for a X-ray tube with 90 kV potential, the maximum electron energy is 90 keV (cf. the "triangular" shape of the unfiltered Bremsstrahlung spectrum in Figure A-1b). Low-energy photons in the Brehmstralung spectrum have short lifetime and are predominantly absorbed by the anode material itself, due to photoelectric interaction (cf. Section A.2 for more details on photoelectric interaction). In other words, the Brehmstralung spectrum is intrinsically shaped by the anode material itself before leaving X-ray tube (cf. filtered Bremsstrahlung spectrum

in Figure A-1b). For a tilted anode, different beam path lengths inside anode also generate non-isotropic X-ray fluence emission, as in typical mammography X-ray tubes. This effect is known as *Heel Effect*.

It is also possible for an accelerated electron to collide with an electron from the atom's electronic shell, resulting in its ejection and the atom's ionization. The vacancy is filled by an electron of an outer shell. This transition causes the emission of a photon with energy equal to the difference between the binding energies of both shells. This discrete radiation is called *characteristic radiation*. For K shell characteristic rays, the radiation emitted by an electron from the L shell replacing a vacant K shell electron is called K-alpha (K_α), while the radiation emitted by an electron from the M shell replacing a vacant K-shell electron is called K-beta (K_β). The same reasoning can be applied to other electronic shells. Since binding energies are unique to a given element, the characteristic radiation energy depends on the target material. In the case of a Tungsten target for example, K shell characteristic rays are located at 59.3 keV (K-alpha) and 69.5 keV (K-beta), as illustrated in Figure A-1b.

The remaining low-energy photons from Bremsstrahlung radiation are usually absorbed in the upper layers of body. They do not contribute to the final image signal but increase the total radiation dose absorbed by the patient. To reduce this amount of low-energy X-rays in the X-ray spectrum, an additional filtration is applied using *flat filters* to better shape the emitted spectrum. Flat filters are typically thin flat sheets of metallic alloy of high atomic number, high purity and homogeneous thickness. Through mainly Photoelectric interactions, low-energy photons are absorbed, shifting the average energy of the spectrum to higher energies. Filter materials with K-shell binding energy in the anode's spectrum range, highly attenuate photons with energies higher than its shell's binding energy, due to Photoelectric interactions. Hence, the so-called *K-edge filters* create discontinuities in the filtered energy spectrum. K-edge filtration is an essential concept for spectral separation in spectral imaging, and discussed on in Chapter 4.

A.2 X-ray Interactions with Matter in Diagnostic Imaging

Whenever electromagnetic waves travel through matter, the initial number of photons in a given beam path is reduced due to their interactions with atoms. In the energy range of X-ray imaging, between 10 and 140 keV, three main types of interactions may occur: Photoelectric absorption, Compton scattering and Rayleigh scattering. An overview of the mechanisms of these interactions is described below. We refer to the work of Johns & Cunningham [146] for a more in depth description.

Main X-ray Interactions with Matter

In the Photoelectric absorption process, a photon undergoes an interaction with an electron of the K, L,M, ... shell of an absorber atom. The energy of the photon is completely absorbed; its energy is transferred to the electron, and the latter is ejected from the electronic cloud. The electron shell vacancy can be filled with an electron from a higher shell generating a fluorescent X-ray with energy equal to the difference between the binding energies of both shells. Alternatively, the excess energy may also result in the ejection of another outer shell electron, also called *Auger electron*. The probability of occurrence of a Photoelectric event is dependent upon the incident photon energy E and is proportional to $1/E^3$ rate [204, 321]. The probability of Photoelectric effect occurrence as a function of incident photon energy exhibits sharp discontinuities at the binding energies of the different electrons in the atom, called *absorption edges*. They are commonly designated by the name of the newly available electron shell (*e.g.*, K-edge). The photoelectric interaction is most likely to occur if the energy of the incident photon is just greater than the binding energy of the electron with which it interacts. Below that energy, Photoelectric interaction is energetically unfeasible. The probability of Photoelectric interaction per atom is proportional to Z^3 for high Z materials and proportional to $Z^{3.8}$ for low Z materials. X-ray contrast agents commonly used

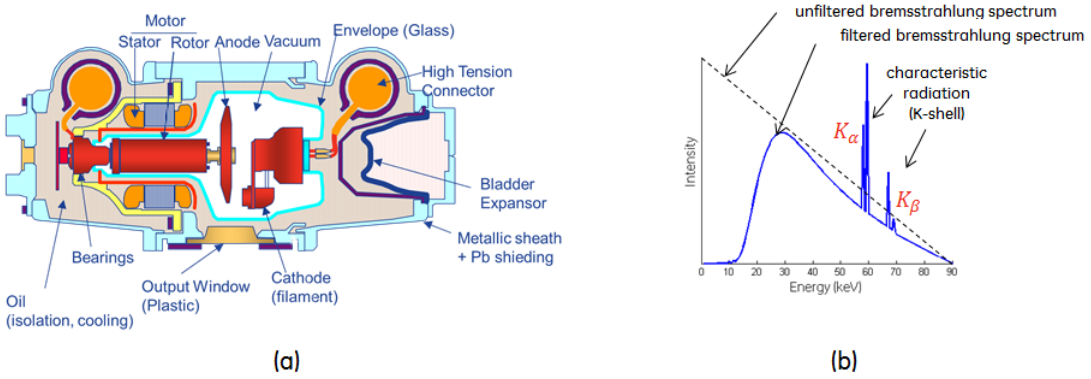

Figure A-1: (a) X-ray Tube illustration; (b) Tungsten anode X-ray intensity spectrum: the Bremsstrahlung energy distribution for 90 keV tube potential, without and with intrinsic anode material filtration, and with added characteristic radiation

in the energy range of radiography leverage the absorption edges discontinuities to enhance X-ray attenuation of an enhancing tissue with respect to unenhanced soft tissue background. Iodine ($Z = 53$) and Barium ($Z = 56$) are two examples, with K-absorption edges at 33.2 and 37.4 keV, respectively.

Compton (or Inelastic, or Incoherent) scattering is the main type of interaction which X-ray photons in the energy range of radiographic imaging are subject, occurring predominantly with soft tissue. One exception is standard mammography, which makes use of X-ray spectra within the energy range of 15 to 30 keV, and for which Photoelectric interactions are predominant. Compton scattering originates from the interaction of an incident X-ray photon with free electrons. In Compton scattering, the incoming X-ray photon is deflected through an certain angle with respect to its original direction. The photon transfers a portion of its energy to the electron (assumed to be initially at rest), which is then known as a recoil electron, or a Compton electron, and scattered with another angle. Because of the energy loss of the incident photon, Compton scattering is also called inelastic scattering. The energy lost during the Compton effect depends on the scattering angle, whose probability distribution as a function of its incident photon energy is described by the Klein-Nishina equation [322]. In the energy range of X-ray imaging, the probability of occurrence of a Compton event is almost independent of the atomic number Z and of the photon initial energy E.

Rayleigh (or Elastic, or Coherent) scattering can be better understood by considering the incident X-ray beam as an electromagnetic wave. During a Rayleigh scattering event the incident photon interacts with the entire atom. More precisely, the electric field of the incident electromagnetic wave expends energy, causing all of the electrons in the atom to oscillate in phase. The atom's electron cloud, now an oscillating dipole, immediately radiates this energy emitting a photon with same energy but in a slightly different direction. This interaction occurs mainly with very low energy X-rays, such as those in the energy range of standard mammography (15 to 30 keV).

Linear Attenuation Coefficient

Figure A-2 shows the probability of occurrence of Photoelectric, Compton and Rayleigh effects as a function of the photon's incident energy considering water as interaction material. This figure illustrates the dependency of each effect as function of the incident photon energy, for a water-based object.

The measurement of probability that a photon, with initial energy E, will undergo an interaction while crossing a given material is also called *cross section*, usually noted σ. The total interaction

cross section $\sigma(E)$ is therefore defined as the sum of the individual cross sections of each interaction type:

$$\sigma(E) = \sigma_{photo}(E) + \sigma_{compton}(E) + \sigma_{rayleigh}(E) \tag{A.1}$$

Let us consider a monochromatic X-ray pencil beam, with initial energy E and containing a total number of photons I_0. The photons hit the surface of a homogeneous block of a given material, which is composed of a single kind of atom and with density ρ_A in atoms per unit of volume (cm^{-3}). The number of photons I after crossing a thickness l of the material can be expressed in the derivative form as:

$$\frac{dI(E)}{dI_0(E)} = -\sigma(E)\rho_A dl \tag{A.2}$$

The product $\sigma(E)\rho_A$ is defined as the *linear attenuation coefficient* of the concerning atom, usually noted as $\mu(E)$ and in units of cm^{-1}. It translates the probability of a photon being removed from the primary X-ray beam path (either by absorption or scattering) per unit of crossed material thickness. For mixtures and compounds the total attenuation coefficient is obtained through the sum of the *mass attenuation coefficients* of the k-th atomic constituents, $(^{\mu}/_{\rho})_k$, weighted by their weight fraction, w_k:

$$(^{\mu}/_{\rho}) = \sum_k w_k \, (^{\mu}/_{\rho})_k \tag{A.3}$$

By integrating Equation, A.2 we express the number of transmitted photons as a function of the crossed thickness dl inside a given material, which is known as the Beer-Lambert Law:

$$I(E) = I_0(E) e^{-\int_{L_{i,s}} \mu(E) dl} \tag{A.4}$$

where $L_{i,s}$ is the X-ray beam path between the source s and the detector element i.

Figure A-3 shows the linear attenuation coefficients, $\mu(E)$, of fibroglandular and adipose tissues, hydroxyapatite (emulating microcalcifications) and iodine, a typical basis material for radiographic contrast agents. We can notice the discontinuity on iodine attenuation coefficients at 33.2 keV, due to the K-shell absorption.

A.3 X-ray Detection

The role of an X-ray image detector is to absorb the incoming X-ray photons, transform them into intermediate carriers that can be sampled and converted to a digital signal to form a digital image. Most modern digital X-ray detector can be classified according to these two properties: detection and signal conversion. Photon detection can be performed either directly or indirectly, whereas image signal formation can be performed by integrating or counting electric charges.

During direct detection, X-rays photons are absorbed within a semiconductor generating electron-hole pairs. If this absorption occurs within the semiconductor's depletion zone, the electrons and holes are separated by the internal electric field. While holes rapidly undergo recombination, the generated electrons are accumulated in the semiconductor until being read-out. The number of electron-hole pairs is directly related to the energy of the incident photons. Common semiconductors used in X-ray imaging are Silicon or Germanium doped with Lithium, Si(Li) and Ge(Si), amorphous Selenium (a-Se), Cadmium Telluride (CdTe) and Cadmium-Zinc-Telluride (CdZnTe) [129, 323–325].

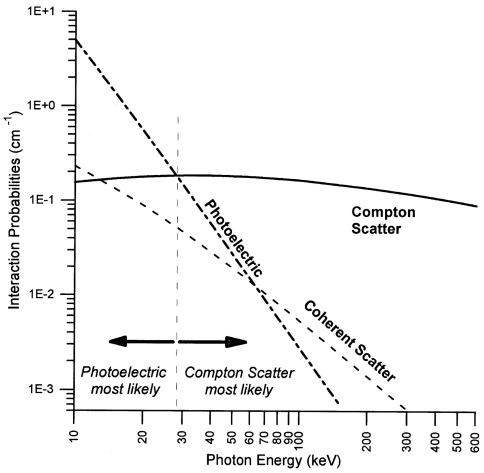

Figure A-2: Probabilities of Photoelectric, Rayleigh and Compton interactions in water

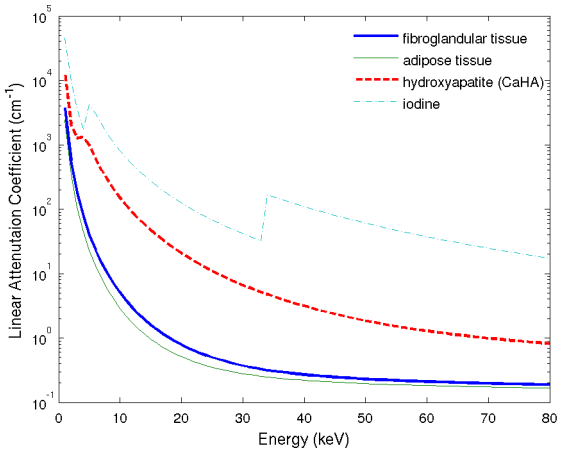

Figure A-3: Linear attenuation coefficients, $\mu(E)$, of fibroglandular and adipose tissues, hydroxyapatite (emulating microcalcifications) and iodine

Indirect detectors use scintillation crystals as an intermediate step in X-ray photon detection. The scintillator first absorbs the incident X-rays and emits visible light photons. The generated light quanta will be afterwards detected by a photodiode and converted into an electric signal. Common scintillation crystal materials are Cadmium Tungstate ($CdWO_4$), Gadolinium Oxysulfide doped with Praseodymium (Gd_2O_2S:Pr or GOS) and Cesium Iodide doped with Thallium (CsI:Tl) [271, 323, 326]. Figure A-4 illustrates the main steps in indirect and direct detection processes.

Once the signal is generated either by direct or indirect detection of X-ray photons, an Analog-to-Digital (A/D) conversion process is used to output a digital signal, normally sampled in a pixelated matrix array, and form an intensity image. This is usually performed either by reading the generated signal accumulated over a limited period of time, leading to *energy-integrating* (or *charge-integrating*) detectors, or by counting the number of electric signals generated by the incoming quanta, as in a *photon-counting* detectors.

Energy-integrating scintillation detectors are the most commonly used technology for medical CT systems [323]. A number of X-ray detectors developed specifically for mammography are also based on this technology, including the GE Senographe® DS and GE Senographe® Essential systems (GE Healthcare; Chalfont St Giles, UK). They are based on amorphous Silicon (a-Si) technology with integrated CsI:Tl scintillators, and their specific characteristics can be found in Annex B, respectively. Integrating scintillation detectors are the main detector technology investigated in this thesis and a more detailed description of image signal formation and noise propagation is available in Section 2.7.2. Energy-integrating direct conversion detectors based on amorphous Selenium (a-Se) are also used in mammography systems [323].

Recent advances have been made to enable photon counting capabilities in direct conversion detectors based on Cd:Tl and CdZnTd semiconductors [130]. The requirements of high detector readout time rates to match the frequency of incoming X-ray photons can be achieved, making it possible to identify individual photons and their respective energies. This allows for a certain degree of energy discrimination, for instance by setting different energy thresholds for electric charge registration and providing images associated to a chosen energy range in the beam spectrum.

For more details on X-ray detectors for digital mammography, including description on other technologies such as photo stimulated luminescence (PSL) in barium fluorobromide doped with europium (BaFBr:Eu) plates and gaseous ionization detectors, we refer the reader to the work of Yaffe and Mainprize [251].

X-ray Image Formation

The generation, attenuation and detection of X-ray photons can be formalized into one mathematical expression. Disregarding nonlinearities associated to the detector technology (*e.g.* lag, photon crosstalk, blur,...), the detected noise-free per-pixel signal intensity $SI(i)$, associated to a detection element i in the pixelated matrix array, can be approximated as:

$$SI(i) = \kappa \int_0^\infty \xi(E)\eta(E) \left[I_{scatter}(E,i) + I_{net}(E,i) \cdot e^{-\int_{L_{i,s}} \mu(\mathbf{r},E)dl} \right] dE \tag{A.5}$$

where κ is a scaling factor, $\xi(E)$ is the detector conversion response, $\eta(E)$ is a function translating an eventual energy-dependent efficiency in detecting photons, $I_{net}(E,i)$ is the net/filtered X-ray intensity spectrum generated by the X-ray source s and towards the detection element i, $\mu(\mathbf{r},E)$ is the linear attenuation coefficient of the imaged breast at energy E and position $\mathbf{r}$ in its volume, dl is the incremental thickness of the traversed breast in the beam path $L_{i,s}$ and $I_{scatter}(E)$ is the X-ray intensity spectrum incident over the detector element surface resulting from photon scattering.

For integrating and counting detectors $\xi(E) = E$ and $\xi(E) = 1$, respectively, which translates the integration or counting processes. The function $\eta(E)$ can be an extremely complex function accounting for different energy-dependent inefficiencies during the detection process, such as the absorption of X-ray photons within the scintillators or the spectral response of energy-discriminating photon-counting detectors during energy threshold.

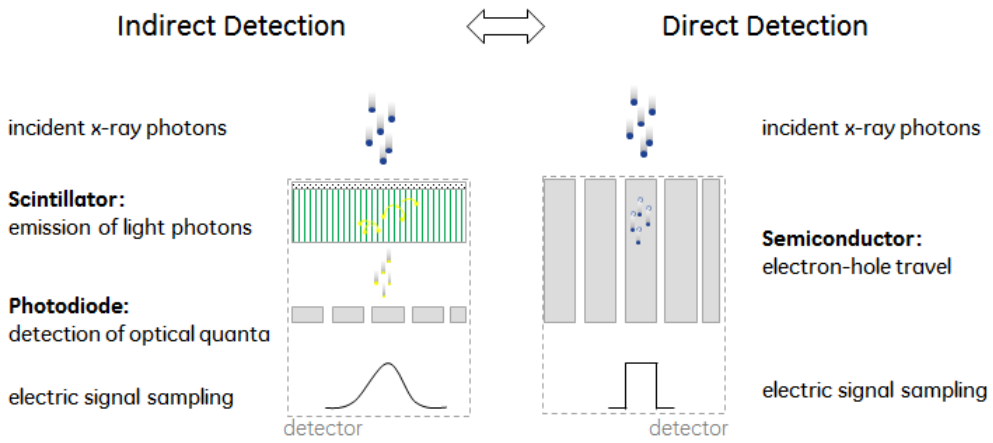

Figure A-4: Illustration of indirect and direct detection processes

A.4 Acquisition Gantry

The third main component of an X-ray system, besides de X-ray source and detector, is the gantry. It links both the X-ray source and the detector in order to offer them a certain freedom of rotation around one or multiple axes. Hence, the gantry allows the X-ray system to image an object from different acquisition *views*.

For example, in the case of standard mammography, the source and the detector are conserved in the same relative position, allowing to image the complete compressed breast in a single view (cf. Figure A-5a). It is also common to define different incidences of the gantry relative to the compressed breast. The two most common views are the cranio-caudal (CC) view and the mediolateral-oblique (MLO) view. In breast tomosynthesis, the detector can either be static or rotate, and gantry allows the source (or source-detector couple) to rotate around an axis, usually located inside the compressed breast. Multiple oblique views of the object are acquired, totaling a limited angular span (cf. Figure A-5b). In current dedicated breast CT prototypes, the source and the detector are usually fixed with respect to the other. The gantry rotates the detector-source pair around an axis located at the center of the longitudinal section of the uncompressed breast, performing a given orbit around the breast. Full 360° scans (cf. Figure A-5c), half 180° scans, saddle and other complex trajectories have been studied for dedicated breast CT [118, 327–330].

Whenever the gantry rotates on its axis, from its initial state to a view angle β, we can associate the detected intensity profile with the view angle β. Disregarding scattered radiation and assuming a monochromatic beam with energy E, Equation A.5 can be rewritten into

$$p(\beta, i) = -ln\left(\frac{SI(i,\beta)}{SI_0(i,\beta)}\right) = \int_{L_{i,s}} \mu(\mathbf{r}, E)dl \tag{A.6}$$

where p is the *log-projection* and SI_0 is the per-pixel signal intensity acquired without any object, *i.e.* an *airscan*.

A.5 Tomographic Reconstruction

The objective of tomographic reconstruction is to recover the volumetric distribution of linear attenuation coefficients $\mu(\mathbf{r})$ from the measured log-projections $p(\beta, i)$. Various methods were proposed to analytically [331, 332] or iteratively [333] invert the Radon Transform.

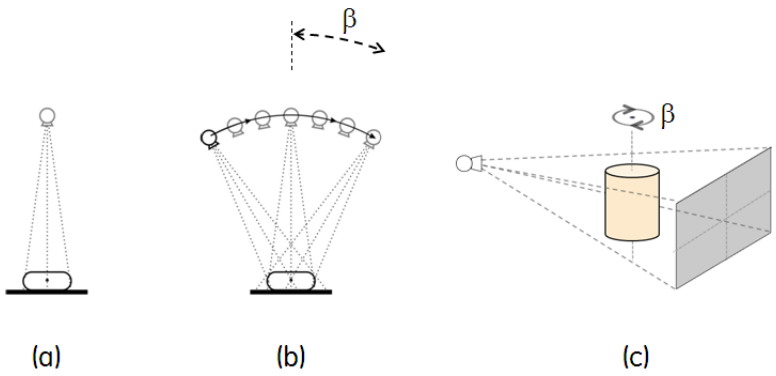

Figure A-5: Typical (a) Mammography, (b) Tomosynthesis and (c) circular dedicated breast CT acquisition geometries

Analytic methods are based on the mathematical inversion of the Radon Transform for a complete or approximate recover of the 3D object, depending on the acquisition trajectory. Filtered backprojection is the most commonly known analytical algorithm for DBT and CT reconstructions, and will be the standard reconstruction method used throughout this PhD thesis.

Iterative reconstruction methods rely on the minimization of the error between the projection of the reconstructed object at a given iteration $k-1$ and the measured projection data. At each iteration, the error information is reconstructed and used to update the reconstructed object to the iteration k. After a predefined number of successive iterations or when the fulfilment of an image quality criterion is achieved, we obtain an estimation of the 3D object. Iterative reconstruction algorithms may allow for patient dose reduction due to a more precise modeling of the acquisition process, *e.g.* statistics of detected photons. Iterative reconstruction methods have not been investigated this PhD thesis research.

For more in-depth description on the different analytical and iterative reconstruction techniques in X-ray imaging, as well as an overview on the different image artifacts found in clinical practice, we refer the reader to the work of J. Hsieh [334].

Radon Transform

Equation A.6 is an equivalent form of the *Radon Transform* if a geometric transformation $\mathbf{r} = l_{\beta,t}(\alpha) : \mathbb{R} \rightarrow \mathbb{R}^2$, associating a volume element in $\mathbf{r}$ with a parametrized expression of the X-ray beam path $l_{\beta,t}(\alpha)$ is applied:

$$p(\beta, t) = \int_{L(\beta,t)} \mu(l_{\beta,t}(\alpha))d\alpha \tag{A.7}$$

where β is an angular parameter, t a distance to the origin of coordinates and α is the parametrization variable. In CT, the set of log-projections $p(\beta, t)$ is called the *sinogram* of the imaged object, since each object point appears along a sinusoidal curve in the projection space $\beta - t$.

The *Central Slice Theorem* (or *Fourier Slice Theorem*) states that the Fourier Transform of a log-projection $p(\beta, t)$ at given view angle is found along a radial line in the 2D Fourier Transform of the imaged object. As a consequence, a complete representation of the imaged object in the frequency domain is obtained from a set of parallel projections covering an angular span of length π. This angular sampling concept is key for 3D reconstruction of the object, especially when the angular covering hypothesis is not met, such as in Tomosynthesis acquisitions. Figure A-6a illustrates the projection geometry and the Radon Transform at a given angle β, while Figure A-6b illustrates the corresponding Fourier Transform.

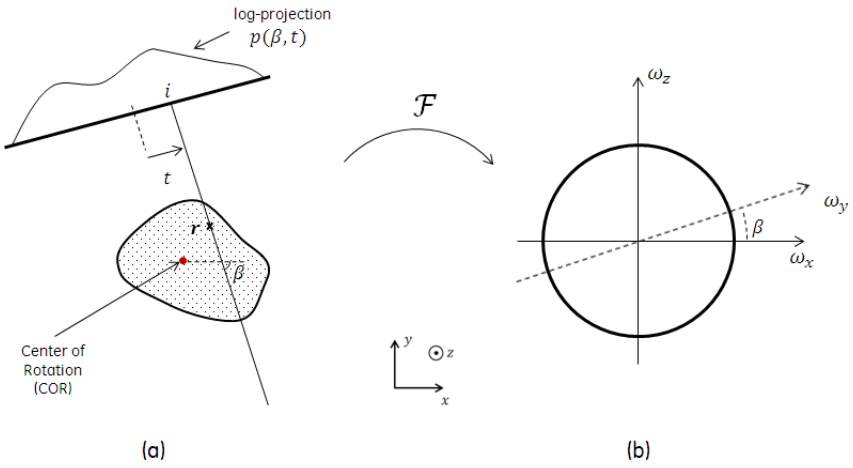

Figure A-6: (a) Parallel projection geometry for Radon Transform; (b) representation of the Central Slice Theorem

Beam Hardening

Notice that the inversion of Equation A.6/A.7 through tomographic reconstruction provides a linear relationship to the object's attenuation coefficient distribution $\mu(\mathbf{r}, E)$ when the incident beam is monochromatic. In the case of an incident polychromatic spectrum, this relation is no longer linear and $\mu(\mathbf{r}, E)$ becomes an effective linear attenuation $\bar{\mu}(\mathbf{r})$. Indeed, low-energy photons are more likely to be absorbed than high-energy photons, which cause the X-ray spectra to shift to higher energies, or to *harden*, as the beam propagates through the object. *Beam hardening* entails in a two different artifacts in reconstructed volumes: cupping and appearance of shading or streaks.

Cupping artifacts refers to the differences in beam hardening occurring in a central region of the object with respect to its edges, due to differences in crossed thickness. Because the beam becomes harder at the center of the object, reconstructed effective attenuation coefficient values are smaller than at the periphery, resulting in an image profile which appears as a "cup". The same cupping effect occurs in the presence of X-ray scattering, where additional detector signal is generated from scattered X-rays occurring more likely at a X-ray beam path crossing the center of a cylindrical object. Hence, according to Equation A.6/A.7, the increased projected signal is translated into decreased log-projection values $p(\beta, i)$ and, as consequence, the decrease in reconstructed attenuation coefficients $\bar{\mu}(\mathbf{r})$.

Alternatively, shadings or streaks occur when beam hardening inside the imaged object is different according to the acquisition view. The presence of high attenuating materials will favors the appearance of stronger cupping in a particular direction, especially when other high attenuating areas are present, creating therefore streaks.

Filtered Backprojection Algorithm

For cone-beam CT geometries, the approximate analytic inversion formula proposed by Feldkamp [335] is the most used technique for 3D cone-beam reconstruction. Its implementation is very simple and provides good results for circular trajectories with small cone angles [335]. The method is a reinterpretation of the 2D fan-beam *Filtered BackProjection* (FBP) extended to 3D reconstruction of cone-beam data. The algorithm can be summarized into three main steps: pre-filter rescaling, high-pass filtration and backprojection.

1. **Rescaling:** it can be interpreted as a geometric correction of each detector element to compensate for the cone-beam acquisition. The scaling factor is equal to the cosine of the

angle between the ray and the central ray of the projection. If α_i and γ_i are the fan and cone angles associated to the detector element i, the corrected log-projections can be written as:

$$p'(\beta, i) = p(\beta, i) \cos\alpha_i \cos\gamma_i \tag{A.8}$$

2. **Filtering:** it is needed to equalize the contributions of all frequencies in the Fourier Transform's polar grid. This can be done by individually convolving the signal of each detector row with a high-pass filter kernel $h(\cdot)$. In this way, the magnitudes of the existing higher-frequency samples in each projection are scaled up to compensate for their lower amount. If we associate the detector element i position with a u-v coordinate plane over the detector, we have:

$$p''(\beta, i) = p'(\beta, u, v) * h(v) = \sum_{v^*} p'(\beta, u, v) h(v - v^*) \tag{A.9}$$

where u and v indicate the detector columns and rows, respectively.

3. **Backprojection:** the filtered log-projections values are backprojected to a 3D voxelized volume. For every voxel in a position $\mathbf{r}$ in space, there is a given set $\Omega_{\mathbf{r}}$ of projected data pairs (β, i) which contribute to the voxel signal if the beam path linking a point source s and the pixel element i intersects the voxel. The contribution is normally weighted and interpolated to account for partial volume effects, magnification, etc. The backprojected data $b(\mathbf{r})$ can therefore be expressed as:

$$b(\mathbf{r}) = \sum_{(\beta,i)\in\Omega_{\mathbf{r}}} \frac{w_B(\beta, i)}{L_{is}^2} p''(\beta, i) \tag{A.10}$$

where L_{is} is the distance between the source s and the detector element i, and $w_B(\beta, i)$ is a weight.

In summary, from Equations A.8, A.9 and A.10, we can express the FBP algorithm in a single equation:

$$\bar{\mu}(\mathbf{r}) = \underbrace{\sum_{(\beta,i)\in\Omega_{\mathbf{r}}} w'_B(\beta, i) \underbrace{\sum_{v^*} h(v - v^*) \underbrace{p(\beta, u, v) \cos\alpha_i \cos\gamma_i}_{rescaling}}_{filtering}}_{backprojection} \tag{A.11}$$

where $w'_B(\beta, i)$ is an overall weighting function comprising the necessary scaling factors to obtain the linear attenuation coefficients $\bar{\mu}(\mathbf{r})$ from $b(\mathbf{r})$.

Reconstruction of Dedicated Breast CT Data

Tomographic reconstruction of cone-beam CT data acquired with a circular trajectory, suffers from data incompleteness (cf. Data Sufficient Condition - DSC - in Ref. [331,336,337]). Through simple FBP reconstruction, the mid-slice of the object (plane perpendicular to the detector and passing through the source and the gantry's center of rotation) can be perfectly reconstructed, while object points further away from this plane will exhibit artifacts called *cone-beam artifacts*.

The cone-beam artifacts of a reconstructed image tend to become stronger with larger cone angles and away from the mid-plane [338]. They result in geometric distortion of the imaged objects and inaccuracy of reconstructed linear attenuation coefficient (decreased intensity in reconstructed pixels corresponding to larger cone angles).

In standard CT, and more recently in dedicated breast CT, more complex trajectories (*e.g.* "circle-plus-arcs", "circle-plus-line", "circle-plus-circle", saddle, ...) have been introduced in order

to meet the DSC and reduce cone-beam artifacts [338–340]. In breast CT, they were also an attempt to avoid eventual limitations on the gantry and improve patient table designs, therefore enabling to perform acquisition closer to the chest wall and image the axillary tail [118, 327, 328, 330, 341].

Reconstruction of Breast Tomosynthesis Data

As explained in the introductory chapter, breast tomosynthesis (DBT) reduces tissue overlapping compared to digital mammography, offering enhanced depiction of structures. Since DBT projections have limited angular span around the object, 3D reconstruction of the object becomes a substantially ill-conditioned inversion problem with respect to the Central Slice Theorem. Figure A-7 illustrates the partial angular sampling data and its translation into a cone in the Fourier domain. Nonetheless, the limited data in the Fourier domain can be used to generate a pseudo-3D representation of the object in the Fourier domain.

In order to understand the basic principle behind tomosynthesis reconstruction, we recall a simple algorithm called *Shift-and-Add* [342], illustrated in Figure A-8a. It states that it is possible to recover, to a certain extent, the attenuation information in a plane crossing the object by analyzing the structural displacement in the projections. In other words, let us consider an object which contains a structure at a given plane, parallel to the detector (x-z plane) and at a given height along the y-axis. While projecting this structure over the different angles, its displacement in the projections will be different from structures localized on other planes of the object. By adding the projections with a well-defined geometrical weight, it is possible to construct an image plane in which only the structures crossed by the plane will be sharp (or *in-focus*), while the other structures become blurred. The method can be applied so as to reconstruct parallel planes of the entire object.

It must be noticed, however, that since the object sampling is incomplete, the reconstructed structures across the many planes will appear deformed and elongated along the direction of the X-ray beam, *i.e.* perpendicular to the parallel planes (y-axis), as illustrated in Figure A-8b. Moreover, high contrast signals present outside the in-focus plane, such as microcalcifications, will create artifacts [87]. The resolution along the y-axis is therefore inferior to the resolution in the x-z plane in order avoid the influence of outer planes. Nevertheless, the resolution in the x-z plane can be as high as the native resolution of the projection images, favoring the depiction of small structures such as microcalcifications.

As in cone-beam CT data, FBP reconstruction can also be applied to reconstruct parallel planes of the object. In addition to the standard high-pass filter, a low-pass filter (or *slice thickness filter*) can be applied in the y-axis direction to reduce the influence of incomplete sampling and provide an approximately constant slice profile [343]. There have been numerous attempts to leverage

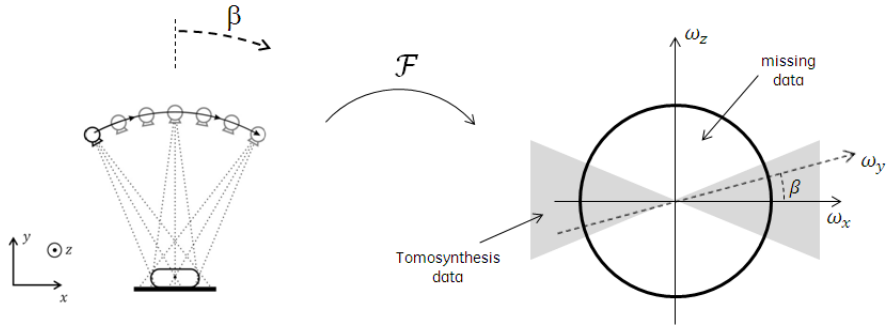

Figure A-7: Tomosynthesis projection at angle β and its corresponding representation in the Fourier domain, as described by the Central Slice Theorem. The limited angular span is translated into a cone in the Fourier space

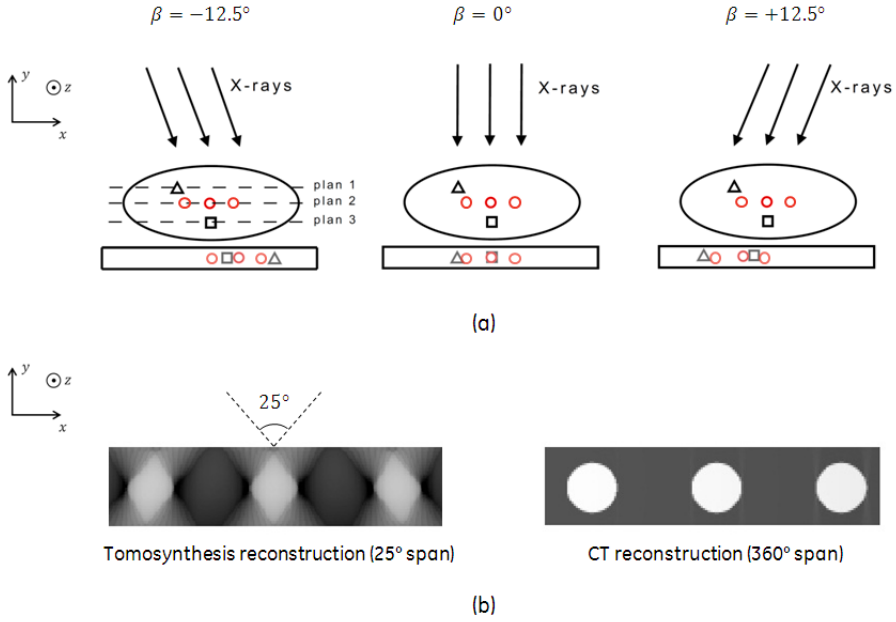

Figure A-8: (a) Illustration of tomosynthesis reconstruction with Shift-and-Add algorithm; (b) example of geometric deformation in the y-axis when the spheres in plane 2 are reconstructed using 25˚angular span, when compared to a full 360˚circular orbit

the benefits of noise reduction in iterative reconstruction methods with the speed of FBP. This can be performed for example by selecting a high-pass filter which emulates the image quality of iterative algorithms [275, 343]. However, besides the drawback of their longer calculation time, iterative algorithms allow for better management of out-of-plane artifacts, such as those caused by high-contrast structures [344, 345].

For deeper insight on reconstruction techniques for digital breast tomosynthesis data, we refer the reader to the work of I. Sechopoulos [346].

Appendix B

Reference Apparatus

In this PhD thesis research, three different X-ray imaging systems were exploited both for validation purposes and as reference geometry for the simulated acquisition chains: a GE Senographe® DS and a GE Senographe® Essential mammography systems (GE Healthcare; Chalfont St Giles, UK) using low-energy spectra, as well as a GE Innova™ Interventional Image Guided System (IGS) 620 (GE Healthcare; Chalfont St Giles, UK), using high-energy spectra.

The three different X-ray imaging system are illustrate in Figure B-1. Table B.1 below summarizes their main technical information.

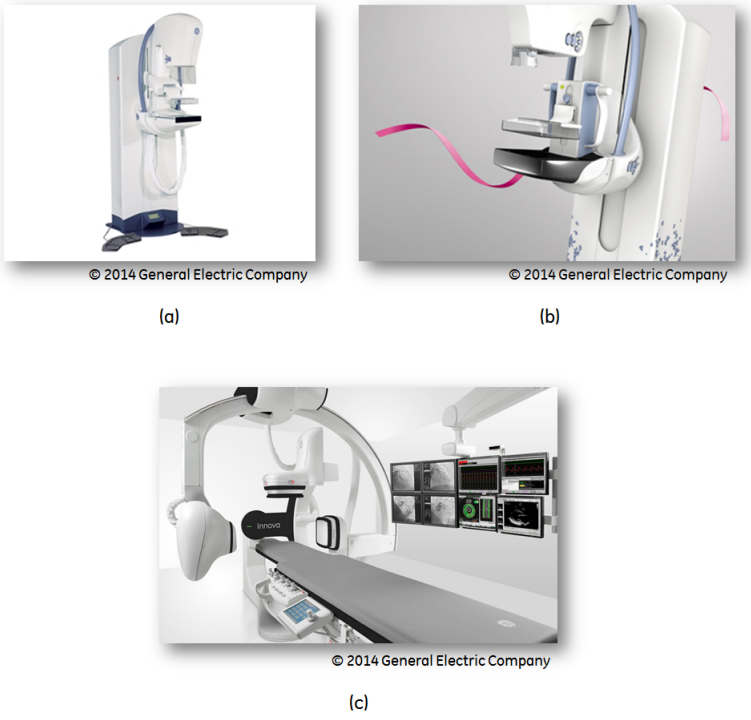

Figure B-1: (a) GE Senographe DS, (b) GE Senographe Essential and (c) GE Innova IGS620

Table B.1: Technical information on the three X-ray imaging system exploited in our investigations

System Parameters		Senographe DS	Senographe Essential	Innova IGS620
Topology	beam shape	cone-beam	cone-beam	cone-beam
	SDD	660 mm	660 mm	1280 mm
	SID	620 mm	620 mm	720 mm
	0° incidence	center col, first row	center col, first row	detector center
	gantry orbit	source circular arc	source circular arc	free C-arm orbit
Generator	technology	HF single-phase power supply	HF single-phase power supply	
	acquisition mode	continuous	continuous	pulsed
	power	5 kW	5 kW	
	pulse width	N/A	N/A	> 10 ms
X-ray Source	technology	Coolidge, rotating anode	Coolidge, rotating anode	Coolidge, rotating anode
	tube tilt angle	22.5°	22.5°	11°
	anode material	Mo, Rh	Mo, Rh	W
	focal spot size	0.1 - 0.3 mm	0.1 - 0.3 mm	0.6 mm
	kV range	22 - 49 kV	22 - 49 kV	60 - 140 kV
	available filtration	Mo 30 μm	Mo 30 μm	Cu 0.3 mm
		Rh 25 μm	Rh 25 μm	
		Cu 0.3 mm + Al 0.3 mm	Cu 0.3 mm + Al 0.3 mm	
Detector	technology	CsI on a-Si TFT	CsI on a-Si TFT	CsI on a-Si TFT
	matrix size	1914 x 2294	2394 x 3062	1024 x 1024
	nominal pixel pitch	100 μm	100 μm	200 μm
	frame rate			7.5, 15, 30 FPS
	fill factor	$\sim 0.71 \times 0.71$	$\sim 0.79 \times 0.79$	$\sim 0.8 \times 0.8$
	scintillator thickness	100 μm	250 μm	780 μm
	MTF at 1.0×Nyquist	0.31	0.18	0.15
	MTF at 0.4×Nyquist	0.7	0.64	0.65
	anti-scatter grid	yes	yes	yes

Appendix C

Scattered Radiation Impact on Image Quality

As described in Annex A.2, in the energy range of X-ray imaging, typically between 10 and 140 keV, X-ray photons interaction with matter can be summarized into three main processes: photo-electric effect, Compton (or incoherent) and Rayleigh (or coherent) scattering. Compton scattering originates from the interaction of an incident X-ray photon with an atom's electron, which results in a change on the photon's direction and loss of its initial energy. Rayleigh scattering is associated with the electric polarization of the atom and the radiation of an electromagnetic wave with the same energy as the incoming beam, but with a slight difference in the trajectory.

In practice, due to both Compton and Rayleigh scattering, incident X-ray photons will deviate from its original primary path and change the detected signals from the expected primary X-ray intensities. They will therefore affect object contrast (since it contains little information about its original path) and increase noise in the projection images. In the case of tomographic imaging, the additional scattered contribution will influence the quality of reconstructed images in three different ways:

1. **Non-homogeneity in CT numbers:** it is usually presented as negative shifts in the expected values, causing cupping artifacts. Additional shadings or streaks might occur whether high attenuating objects are present or not
2. **Degradation of object contrast:** it affects the quantification HU units in single-energy imaging or contrast agent uptake values in contrast-enhanced dual-energy imaging
3. **Degradation of object detectability:** due to the increased number of scattered photons adding stochastic noise but not contributing to the object signal, the overall detectability of objects is reduced

The impact of Compton and Rayleigh scattering on the final trajectory and energy of an incident photon depends on its initial energy, as described by Klein-Nishina and Lorenz-Mie equations, respectively. Hence, the image artifacts generated by scattered radiation will differ according to the input spectrum.

As preliminary step in the optimization of Dual-Energy Contrast-Enhanced Breast CT technique described in Chapter 5, we assessed the scattered radiation impact on image quality due to cupping artifacts and object detectability degradation as a function of the incident photon energy. The main objective was to provide evidence that image quality degradation (in terms of detectability) due to X-ray scattering has little energy-dependency and would not have significant influence on the optimization studies of Chapter 5. This result was observed elsewhere by Glick *et al.* [163]

but for a different experimental setup. Here, it remained to be confirmed that this statement still held for the setups investigated in this PhD thesis research.

Scatter-to-Primary Ratio (SPR) was used as metric to quantify the magnitude of scatter. In order to assess the detrimental effect of scatter on image quality, the magnitude of the cupping artifact and Contrast-to-Noise Ratio were used as figures of merit.

C.1 Materials and Methods

Simulation Setup
The cone-beam CT geometry described in Section 5.2 and illustrate in Figure 5-2 was simulated. A 14 cm diameter (D), 10.5 cm height (3D/4) cylindrical phantoms and composed of homogeneous 50% fibroglandular equivalent was chosen to mimic an average uncompressed breast (cf. Figure C-1). The cylinder contained eight 10 mm diameter cylindrical inserts distributed parallel to the main cylinder axis. The inserts 1 to 4 correspond to 0, 25, 75 and 100% fibroglandular equivalent tissues. Inserts 5 to 8 correspond to homogeneous mixtures of 50% fibroglandular tissue and 0.5, 1.0, 2.5 and 5.0 mg/cm^3 of iodine.

The scattered photon fluence contribution $S_{scatter}(E, i)$ was simulated using CatSim's hybrid approach (cf. Section 2.5 for details), where approximately one million photons undergoing Rayleigh, Compton and photoelectric interactions were tracked in $2 \times 2 \times 2\ mm^3$ voxels. It is fair to assume that the amount of scattered radiation $S_{scatter}(E, i)$ would remain approximately unchanged if an individual low-contrast object is placed or not in the beam path between the source and the detector element i. Therefore, $S_{scatter}(E, i)$ was estimated using only the homogeneous 50% fibroglandular equivalent cylinder, and the result extrapolated to projections acquired with the inserts. This approach allows for much faster calculation since, for a symmetric homogeneous object, the same noiseless 2D scatter intensity estimation is found for each acquired projection. This allows us to compute scatter intensity for one projection and use the results in the other projections.

Both primary only (P) and primary+scattered (P+S) radiations were detected in a perfect blur-free energy-integrating detector with 776 μm pixel pitch. Three hundred projections were simulated equally spaced over a 360° trajectory. In-plane slices, separated by 1 mm in the z-axis direction and with a $0.41 \times 0.41\ mm^2$ pixel size, were reconstructed using a FBP algorithm and an ideal ramp filter. The procedure was repeated for monochromatic input beams with energy ranging from 10 to 80 keV, while the total AGD was kept constant at 50 mGy, avoiding this way streak artifacts attributed to a lack of quanta.

SPR and Cupping Artifact Quantification
Similarly to Chapter 3, SPR values were estimated using mean signal intensities per pixel at the

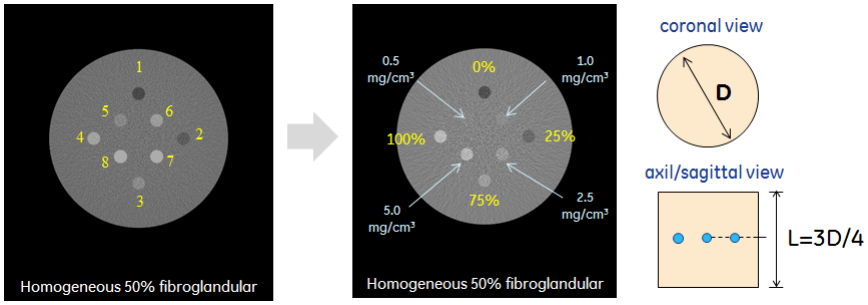

Figure C-1: Cross section slice of the cylindrical phantom containing the different embedded inserts

center of primary-only projections SI_P^{proj} and scatter-only projections SI_S^{proj}:

$$SPR = \frac{SI_S^{proj}}{SI_P^{proj}} \tag{C.1}$$

where the index *proj* denotes SI values measured in *projections* images.

Cupping artifact in the reconstructed images was quantified as the normalized difference between CT numbers in a circular ROI at cylinder's center position and in a circular ROI at the cylinder's edge, measured it the slice corresponding to the cylinder's mid-depth:

$$cupping(\%) = 100 \times \frac{SI_{edge}^{img} - SI_{center}^{img}}{SI_{edge}^{img}} \tag{C.2}$$

where the index *img* denotes SI values measured in *reconstructed* images.

Contrast, Noise, and CNR Quantification
Embedded insert contrast in reconstructed slice images was measured as difference between the mean SI per pixel of an ROI inside a reference insert, SI_{insert}^{img}, and the mean SI per pixel of an ROI on the insert's surrounding background, SI_{bg}^{img}. The standard deviation of signal intensities in the background ROI, σ_{bg}^{img}, was used as estimate of background noise. Contrast-to-noise ratio per pixel between the insert and the background normalized to the square root of the total AGD (CNRD) was calculated as figure of merit for detectability:

$$CNRD_{insert-bg} = \frac{SI_{insert}^{img} - SI_{bg}^{img}}{\sigma_{bg}^{img}\sqrt{AGD}} \tag{C.3}$$

C.2 Results

Figure C-2a shows the SPR values as function of the incident monochromatic beam energy. For energies below $\sim 25\ keV$, the scatter contribution to signal intensity is more important than the contribution of primary radiation ($SPR > 1$). SPR values decreases rapidly from 20 to $\sim 30\ keV$, and more slowly afterwards.

Figure C-2b shows *cupping*(%) as function of the incident monochromatic beam energy. Cupping artifact decreases with the increasing energy. Cupping can be as high as 20% for 20 keV, and stays between 5 and 10% above 30 keV.

For a visual assessment of the cupping artifact, Figure C-3 illustrates the reconstructed slices for 20, 40, 60 and 80 keV, with window width and level set to display the whole image histogram. The 20% cupping at 20 keV is clearly distinguishable, while above 40 keV the difference in cupping is subtle.

Figures C-4a, C-4b and C-4c illustrate, respectively, insert contrast, background noise and resulting CNRD values as function of the incident monochromatic beam energy, for simulations carried without X-ray scattering (solid lines) and with X-ray scattering (dashed lines). They also show the ratio between results with X-ray scattering and without X-ray scattering (round markers). Contrast and background noise decreases with input X-ray beam energy, for both simulations without and with scattered radiation. CNRD increases at low energies since the background noise decreases more rapidly than contrast, function of the photon energy, achieving a broad maximum, and decreases steadily at higher energies mainly influenced by the decreasing insert contrast.

According to the ratio curves in Figures C-4a to c, both contrast and background noise decrease in the presence of scattered photons. In the considered energy range, the drop in contrast was

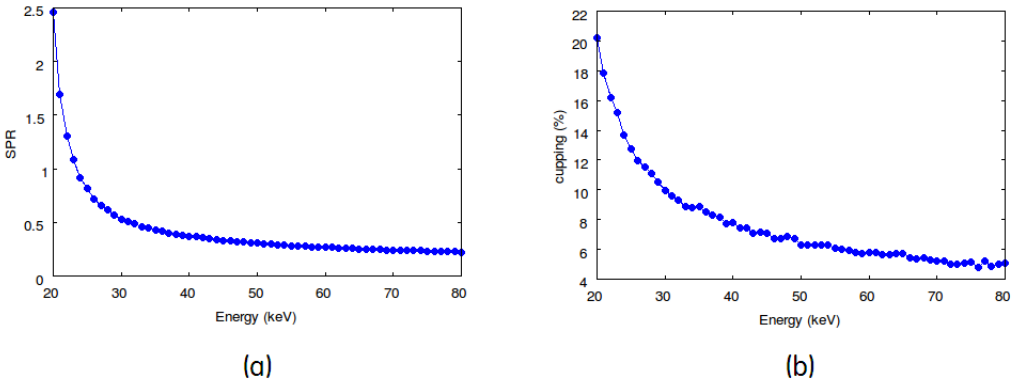

Figure C-2: (a) SPR and (b) *cupping*(%) as function of the monochromatic beam energy incident on a 14 cm diameter 50% fibroglandular equivalent cylinder

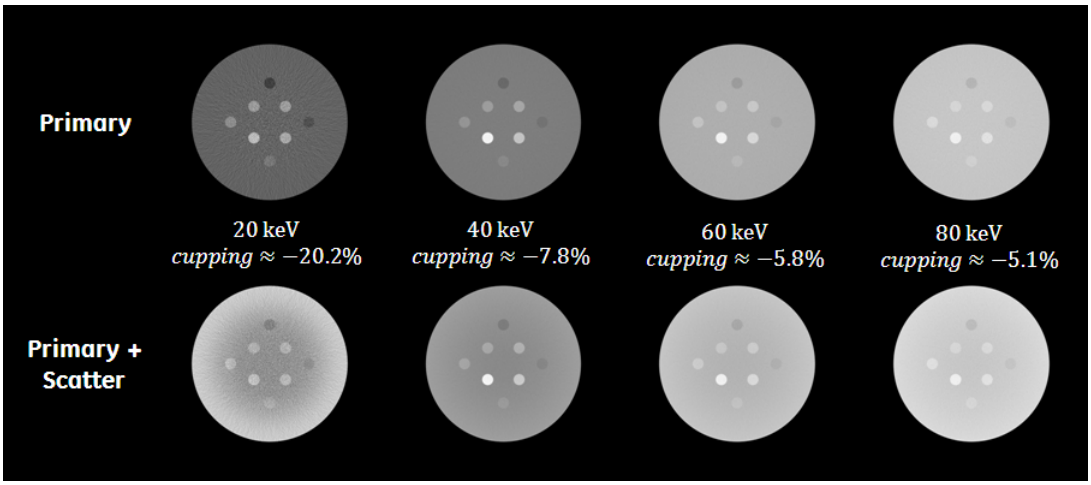

Figure C-3: Cupping artifact in reconstructed volume due to scatter for 20, 40, 60 and 80 keV monochromatic beam incident on a 14 cm diameter 50% fibroglandular equivalent cylinder. The top and bottom columns illustrate a slice reconstructed with primary photons and primary+scatter photons, respectively

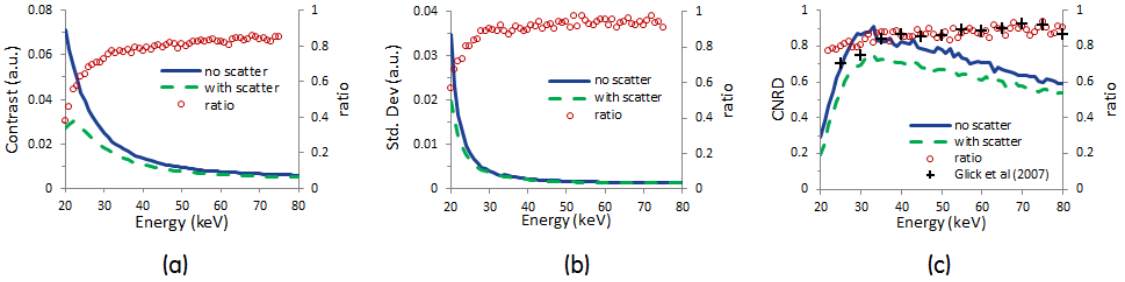

Figure C-4: (a) Contrast, (b) background noise std. deviation and (c) CNRD as function of the incident monochromatic energy. Solid and dashed lines represent data obtained without and with X-ray scattering, respectively. Round markers represent the ratio between simulations with scatter and without scatter. Crosses represent reference data from Ref. [163]. All values were obtained at constant AGD of 50 mGy

in the range of approximately 20 to 60% (ratio values between 0.4 and 0.8), while the drop in noise was in the range of 5 to 40% (ratio values between 0.6 and 0.95), resulting in a CNRD drop between 10 and 20% (ratio values between 0.8 and 0.9). All degradations were more expressive for energies below 30 keV, due to the increased cupping.

Figure C-4c also shows the degradation of CNRD as function of the monochromatic energy obtained from Ref. [163], measured by the ratio of CNRD obtained with and without X-ray scattering (crossed markers). We notice that the drop in CNRD is similar between our geometry and that of the reference.

Figure C-5 summarizes the CNRD results in Figure C-4c and makes the link with the optimization studies presented in Chapter 5. We can notice that CNRD reduction varies slowly as function of the incident monochromatic beam energy, staying between approximately 10 to 20%, when changing from 20 to 80 keV. More importantly, when considering the expected optimal energy ranges for LE and HE spectra discussed in Chapter 5 and highlighted in Figure C-5 (25-33 keV for LE and 34-50 keV for HE), CNRD reduction is limited to the range of 14 to 19% (ratio values between 0.81 and 0.86).

C.3 Discussion and Conclusions

In breast CT with the patient in prone position, the uncompressed breast shape can be considered a cylinder (or semi-ellipsoid) with its major axis perpendicular to the incident X-ray beam [104, 165–168]. The shape of the detected x-ray scatter profile perpendicular to the major cylinder axis (cf. Figures 3-6b, 3-8a and 3-9a) can be explained by two major contributions. At one hand, the detected scatter profile decreases with increasing thickness of the cylinder, *i.e.* proportionally with increased primary X-ray attenuation as a function of increased phantom thickness. However, because the spatial extent of the cylinder is finite and supposing that the air surrounding the phantom does not contribute to X-ray scatter, the scatter signal below the center of the cylinder is received from a phantom scattering medium over 360 degrees, while the scatter signal below the edge of the cylinder is received from about half of a 360 degrees (since ≈180 degrees adjacent to the cylinder edge consists of air). The latter explains why the scatter signal intensity is increasing at the phantom edges.

The additional detector signal generated by scattered photons when compared to primary photons (scatter-to-primary ratio) is higher below the center of the cylinder and decreases toward the detector periphery (cf. Figures 3-7b, 3-8c and 3-9c). After reconstruction, this additional signal is translated into an artificial decrease in effective attenuation coefficients, with CT numbers

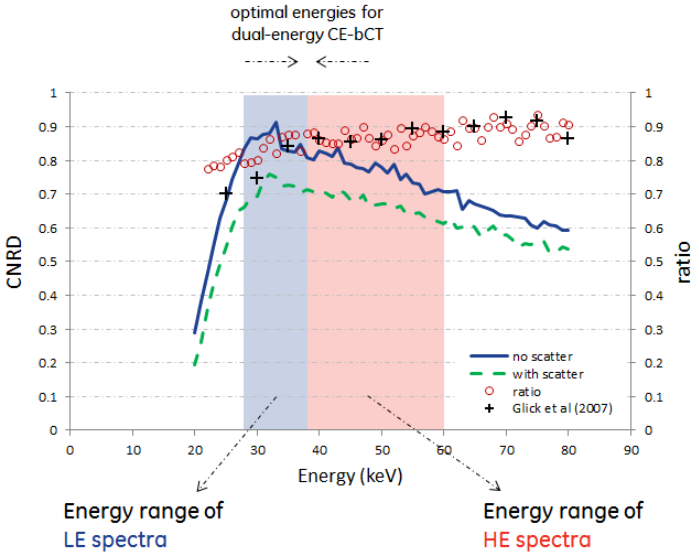

Figure C-5: CNRD as function of the incident monochromatic energy. Solid and dashed lines represent data obtained without and with X-ray scattering, respectively. Round markers represent the ratio between simulations with scatter and without scatter. Crosses represent reference data from Ref. [163]. Shade areas show the energy range of LE (blue) and HE (red) spectra considered during dual-energy spectra optimization

being lower at inner parts of the breast when compared to those at its periphery, forming this way a cupping artifact. This effect is illustrated in Figure C-3.

With respect to object detectability, since the decrease in object contrast was larger than the decrease in background noise, for all considered energies, CNRD was ultimately reduced, as can be seen in Figure C-4c. however, when considering the expected optimal energy ranges for LE and HE spectra discussed in Chapter 5, CNRD reduction is limited to the range of 14 to 19% (ratio values between 0.81 and 0.86).

We may conclude that, although scatter has a moderate effect on CNRD, the degradation showed little energy-dependency. This result was also noticed by Glick *et al.* [163], as can be seen from the published data in Figure C-4c. Moreover, an interesting fact is that the results presented in Ref. [163] were based on a full cascade system analysis of a 600 μm thick CsI:Tl-based detector, including optical spreading, K-fluorescence, energy-dependent QDE, and other inefficiencies.

We recall that in Chapter 5 we demonstrated that in the absence of scatter, optimal CNRD surfaces as function of the input monochromatic LE and HE beam energies are rather broad around their peak values. Hence, if scatter is included, we assumed that small variation of CNRD with the input monochromatic energy would have little effect on spectra optimization for Dual-Energy bCT, and was therefore be disregarded in the investigations.

Appendix D

Proof of Theorems

D.1 Basic Properties of Covariance

Let, $\mathbf{x} = (x_1, x_2 \ldots, x_n)$ and $\mathbf{y} = (y_1, y_2 \ldots, y_n)$ be two random $1 \times n$ variables and $Cov(\mathbf{x}, \mathbf{y})$ their $n \times n$ cross-covariance matrix. Accordingly, the following basic properties apply:

Property D.1. *If $\boldsymbol{A}$ is a $m \times n$ matrix, then*

$$Cov(\boldsymbol{A}\boldsymbol{x}) = \boldsymbol{A}Cov(\boldsymbol{x})\boldsymbol{A}^T \tag{D.1}$$

Property D.2. *From Property D.1, if $\boldsymbol{A}$ and $\boldsymbol{B}$ are $m \times n$ matrices, and $\boldsymbol{a}$ and $\boldsymbol{b}$ are $m \times 1$ vectors, then it is easy to derive that*

$$Cov(\boldsymbol{A}\boldsymbol{x} + \boldsymbol{a}, \boldsymbol{B}\boldsymbol{y} + \boldsymbol{b}) = \boldsymbol{A}Cov(\boldsymbol{x}, \boldsymbol{y})\boldsymbol{B}^T \tag{D.2}$$

Property D.3. *For real-valued random variables x, y, w and v and constants ("non-random") a, b, c, d, we can write*

$$Cov(ax + by, cw + dv) = ac\,Cov(x, w) + ad\,Cov(x, v) + bc\,Cov(y, w) + bd\,Cov(y, v) \tag{D.3}$$

D.2 Proof of Theorem 7.1

Proposition D.1. *(Theorem 7.1) If a tomographic reconstruction method $\mathcal{R}$ can be expressed as a linear transformation, then a negative covariance among a set of projection images $\boldsymbol{x}$ and $\boldsymbol{y}$ results in a negative covariance among the respective set of tomographic reconstructed volumes $\mathcal{R}\{\boldsymbol{x}\}$ and $\mathcal{R}\{\boldsymbol{y}\}$:*

$$Cov(\boldsymbol{x}, \boldsymbol{y}) < 0 \implies Cov(\mathcal{R}\{\boldsymbol{x}\}, \mathcal{R}\{\boldsymbol{y}\}) < 0 \tag{D.4}$$

as long as $Cov(x_i, y_j) = 0$, where i and j are the index for two different detector elements ($i \neq j$).

Hypothesis D.1. *(Uncorrelation) If i and j are the indexes of detector elements or pixels in the projections images $\boldsymbol{x} = (x_1, x_2 \ldots, x_n)$ and $\boldsymbol{y} = (y_1, y_2 \ldots, y_n)$, we assume that:*

$$Cov(x_i, y_i) = 0, \quad \forall i \neq j, \quad i, j \in \{1, 2, \cdots, n\} \tag{D.5}$$

In other words, we assume that different pixels in projection images $\boldsymbol{x}$ and $\boldsymbol{y}$ are uncorrelated.

As discussed in Annex A.5, we can write the reconstruction method $\mathcal{R}$ as the concatenation of three basic operations: scaling, filtration and backprojection. We will separate the demonstration of Theorem 7.1 into these three parts, such as:

$$(\mathbf{x},\mathbf{y}) \underbrace{\xrightarrow{scaling} (\mathbf{x}',\mathbf{y}') \xrightarrow{filtration} (\mathbf{x}'',\mathbf{y}'') \xrightarrow{backprojection}}_{\mathcal{R}\{\cdot\}} (\mathbf{x}''',\mathbf{y}''')$$

or

$$(\mathbf{x},\mathbf{y}) \xrightarrow{\mathcal{R}\{\cdot\}} (\mathbf{x}''',\mathbf{y}''') \stackrel{def}{=} (\mathcal{R}\{\mathbf{x}\},\mathcal{R}\{\mathbf{y}\})$$

Hence, to demonstrate the proposition of Equation D.4, we need to show that the concatenation of three basic operations entails in:

I. **Scaling**: $Cov(\mathbf{x},\mathbf{y}) < 0 \implies Cov(\mathbf{x}',\mathbf{y}') < 0$

II. **Filtration**: $Cov(\mathbf{x}',\mathbf{y}') < 0 \implies Cov(\mathbf{x}'',\mathbf{y}'') < 0$

III. **Backprojection**: $Cov(\mathbf{x}'',\mathbf{y}'') < 0 \implies Cov(\mathbf{x}''',\mathbf{y}''') < 0$

I. Scaling

Proposition D.2. *Let the scaling operation be expressed by a transformation $s : \mathbb{R}^n \to \mathbb{R}^n$ and a $n \times n$ positive diagonal matrix $\boldsymbol{s}$ containing the weights associated to each detector element. If $\boldsymbol{x}$, $\boldsymbol{x}'$, $\boldsymbol{y}$ and $\boldsymbol{y}'$ are projection data represented as $n \times 1$ vectors, then*

$$Cov(\boldsymbol{x},\boldsymbol{y}) < 0 \implies Cov(\boldsymbol{sx},\boldsymbol{sy}) = Cov(\boldsymbol{x}',\boldsymbol{y}') < 0 \tag{D.6}$$

Proof. If $\mathbf{x}$ and $\mathbf{y}$ are projection data represented as $n \times 1$ vectors, their scaled versions are simply the multiplications $\mathbf{x}' = \mathbf{sx}$ and $\mathbf{y}' = \mathbf{sy}$, respectively. By applying Property D.2, the covariance of the backprojected data is:

$$Cov(\mathbf{sx},\mathbf{sy}) = \mathbf{s}Cov(\mathbf{x},\mathbf{y})\mathbf{s}^T$$

and since $\mathbf{s}$ is diagonal,

$$Cov(\mathbf{sx},\mathbf{sy}) = \mathbf{s}^2\, Cov(\mathbf{x},\mathbf{y})$$

In other words, the scaling operator conserves the sign of $Cov(\mathbf{x},\mathbf{y})$. Finally, since $\mathbf{s}^2$ is strictly positive, we can write:

$$Cov(\mathbf{x},\mathbf{y}) < 0 \implies Cov(\mathbf{sx},\mathbf{sy}) = Cov(\mathbf{x}',\mathbf{y}') < 0$$

□

II. Filtration

Proposition D.3. *Let h be a filter kernel with limited support Ω_K, represented by a $K \times 1$ vector $\boldsymbol{h}$. If $\boldsymbol{x}'$, $\boldsymbol{x}''$, $\boldsymbol{y}'$ and $\boldsymbol{y}''$ are projection data represented as $n \times 1$ vectors, then*

$$Cov(\boldsymbol{x}', \boldsymbol{y}') < 0 \quad \implies Cov(\boldsymbol{h} * \boldsymbol{x}', \boldsymbol{h} * \boldsymbol{y}') = Cov(\boldsymbol{x}'', \boldsymbol{y}'') < 0 \tag{D.7}$$

Proof. The filtration step is defined as the convolution of the projection data $\mathbf{x}'$ and $\mathbf{y}'$ with the kernel $\mathbf{h}$:

$$(h * x')(i) \overset{def}{=} \sum_{k \in \Omega_K} h(k)x'(i-k)$$
$$(h * y')(i) \overset{def}{=} \sum_{k \in \Omega_K} h(k)y'(i-k)$$

where i and k are indexes for spatial variations in $\mathbf{h}$, $\mathbf{x}'$ and $\mathbf{y}'$.

We start by picking the K-th element in the kernel support Ω_K and expanding the convolution $(h * x)(i)$ and $(h * y)(i)$ into two terms:

$$(h * x')(i) = \underbrace{\sum_{k \in \Omega_{K-1}} h(k)x'(i-k)}_{\Phi_x^{K-1}(i)} + h(K)x'(i-K) = \Phi_y^{K-1}(i) + h(K)x'(i-K)$$
$$(h * y')(i) = \underbrace{\sum_{k \in \Omega_{K-1}} h(k)y'(i-k)}_{\Phi_y^{K-1}(i)} + h(K)y'(i-K) = \Phi_y^{K-1}(i) + h(K)y'(i-K)$$

where $\Phi_x^{K-1}(i)$ and $\Phi_y^{K-1}(i)$ are auxiliary random variables denoting the products inside the convolution, for the support $\Omega_{K-1} = \{\Omega_K - K\}$. Note that the convolutions $x''(i) = (h * x')(i)$ and $y''(i) = (h * y')(i)$ are equivalent to $\Phi_x^K(i)$ and $\Phi_y^K(i)$, respectively.

The covariance $Cov(\mathbf{h} * \mathbf{x}', \mathbf{h} * \mathbf{y}') = Cov(h * x', h * y')(i) = Cov(\Phi_x^K, \Phi_y^K)(i)$ can therefore be written as

$$Cov(\Phi_x^K, \Phi_y^K)(i) = Cov(\Phi_x^{K-1}(i) + h(K)x'(i-K), \Phi_y^{K-1}(i) + h(K)y'(i-K))$$

and using Property D.3, we have

$$\begin{aligned} Cov(\Phi_x^K, \Phi_y^K)(i) = {} & Cov(\Phi_x^{K-1}, \Phi_y^{K-1})(i) + h(K) \cdot Cov(\Phi_x^{K-1}(i), y'(i-K)) + \\ & + h(K) \cdot Cov(x'(i-K), \Phi_y^{K-1}(i)) + h(K)^2 \cdot Cov(x'(i-K), y'(i-K)) \end{aligned} \tag{D.8}$$

The second and third terms of Equation D.8 can be further expanded in a similar manner using Property D.3, such as

$$Cov(\Phi_x^{K-1}(i), y'(i-K)) = \sum_{k \in \Omega_{K-1}} h(k)Cov(x'(i-k), y'(i-K))$$
$$Cov(x'(i-K), \Phi_y^{K-1}(i)) = \sum_{k \in \Omega_{K-1}} h(k)Cov(x'(i-K), y'(i-k))$$

Assuming that $x'(i-k)$ and $y'(i-K)$ are uncorrelated for $k \neq K$ (Hypothesis D.1),

$$\begin{aligned} & Cov(x(i-k), y(i-K)) = 0 \quad \text{and} \quad Cov(x(i-K), y(i-k)) = 0 \\ \therefore \quad & Cov(\Phi_x^{K-1}(i), y(i-K)) = 0 \quad \text{and} \quad Cov(x(i-K), \Phi_y^{K-1}(i)) = 0 \end{aligned}$$

This result allows us to simplify Equation D.8 and write the covariance $Cov(\Phi_x^K, \Phi_y^K)$ in a recursive way:

$$Cov(\Phi_x^K, \Phi_y^K)(i) = Cov(\Phi_x^{K-1}, \Phi_y^{K-1})(i) + h(K)^2 \cdot Cov(x'(i-K), y'(i-K)) \tag{D.9}$$

The term $Cov(\Phi_x^{K-1}, \Phi_y^{K-1})$ in Equation D.9 can be expanded using Equation D.8 and simplified using Hypothesis D.1 for all elements k in the support of the filter kernel h. In the end, the expression for the covariance $Cov(\Phi_x^K, \Phi_y^K)$ can be reduced to:

$$Cov(\Phi_x^K, \Phi_y^K)(i) = \sum_{k \in \Omega_{K-1}} h(k)^2 \cdot Cov(x'(i-k), y'(i-k))$$

Finally, since $h(k)^2 > 0 \quad \forall k \in \Omega_K$, we have

$$Cov(x(i-k), y(i-k)) < 0, \quad \forall k \in \Omega_K \implies Cov(\Phi_x^K, \Phi_y^K)(i) < 0$$

or alternatively

$$Cov(\mathbf{x}', \mathbf{y}') < 0 \quad \implies Cov(\mathbf{h} * \mathbf{x}', \mathbf{h} * \mathbf{y}') = Cov(\mathbf{x}'', \mathbf{y}'') < 0$$

□

III. Backprojection

Proposition D.4. *Let the backprojection operation be expressed by a transformation $B : \mathbb{R}^n \to \mathbb{R}^m$ and a $m \times n$ positive matrix $\boldsymbol{B}$ containing the weights of ray-tracing and interpolation processes. If $\boldsymbol{x}''$, $\boldsymbol{y}''$ are projection data represented as $n \times 1$ vectors, and $\boldsymbol{x}'''$, $\boldsymbol{y}''$ are volume data represented as $m \times 1$ vectors, then*

$$Cov(\boldsymbol{x}'', \boldsymbol{y}'') < 0 \implies Cov(\boldsymbol{Bx}, \boldsymbol{By}) = Cov(\boldsymbol{x}''', \boldsymbol{y}''') < 0 \tag{D.10}$$

Proof. If $\mathbf{x}''$, $\mathbf{y}''$ are projection data represented as $n \times 1$ vectors their backprojected volumes in $\mathbb{R}^m$ are simply the multiplications $\mathbf{Bx}''$ and $\mathbf{By}''$, respectively. By applying Property D.2, the covariance of the backprojected data is:

$$Cov(\mathbf{Bx}'', \mathbf{By}'') = \mathbf{B} Cov(\mathbf{x}'', \mathbf{y}'') \mathbf{B}^T$$

and since the elements in $\mathbf{B}$ are all positive,

$$Cov(\mathbf{x}'', \mathbf{y}'') < 0 \quad \implies \quad Cov(\mathbf{Bx}, \mathbf{By}) = \underbrace{\mathbf{B} \underbrace{Cov(\mathbf{x}, \mathbf{y}) \mathbf{B}^T}_{<0}}_{<0}$$

Finally, we can write:

$$Cov(\mathbf{x}'', \mathbf{y}'') < 0 \implies Cov(\mathbf{Bx}, \mathbf{By}) = Cov(\mathbf{x}''', \mathbf{y}''') < 0$$

□

In summary, by using the projections images $\mathbf{x}$ and $\mathbf{y}$ as input for the concatenations of the processes (scaling, filtration and backprojection),

$$(\mathbf{x}, \mathbf{y}) \xrightarrow{\mathcal{R}\{\cdot\}} (\mathcal{R}\{\mathbf{x}\}, \mathcal{R}\{\mathbf{y}\})$$

and from Equations D.6, D.7 and D.10, we have:

$$Cov(\mathbf{x}, \mathbf{y}) < 0 \quad \Longrightarrow Cov\left(\mathcal{R}\{\mathbf{x}\}, \mathcal{R}\{\mathbf{y}\}\right) < 0$$

□

List of Publications

- P. M. Carvalho, A.-K. Carton, R. Iordache, S. Saab-Puong, and S. Muller, "Comparison of Lesion Extent and Contrast-Agent Uptake in Breast Tomosynthesis versus Cone-Beam Breast CT," *Breast Imaging (IWDM)*, vol. 7361, pp. 434–441, 2012
- P. M. Carvalho, A.-K. Carton, S. Saab-Puong, R. Iordache, and S. Muller, "Spectra optimization for dual-energy contrast-enhanced breast CT," *SPIE Medical Imaging*, 2013
- C. Zeng, P. M. Carvalho, L. Pierce, K. Kanal, L. MacDonald, B. DeMan, P. FitzGerald, S. Muller, and P. Kinahan, "Quantitative Assessment of Attenuation Correction for a Combined PET/MX Scanner for Breast Cancer," in *Biomedical Engineering Society (BMES)*, (Seattle, USA), 2013
- P. M. Carvalho, A.-K. Carton, R. Iordache, S. Saab-Puong, and S. Muller, "Optimization of X-ray Spectra for Dual-Energy Contrast-Enhanced Breast Imaging: Dependency on CsI Detector Scintillator Thickness," *Breast Imaging (IWDM)*, vol. 8539, pp. 95–102, 2014
- A.-K. Carton, A. Grisey, P. M. Carvalho, C. Dromain, and S. Muller, "A Virtual Human Breast Phantom Using Surface Meshes And Geometric Internal Structures," *Breast Imaging (IWDM)*, vol. 8539, pp. 356–363, 2014
- A.-K. Carton, P. M. Carvalho, Z. Li, C. Dromain, S. L. Muller, "Assessment of Mass Detection Performance in Contrast Enhanced Digital Mammography," *SPIE Medical Imaging*, 2015
- L. Vancamberg, A.-K. Carton, I. Hadjabderrahmane, G. J. Palma, P. M. Carvalho, R. Iordache, S. L. Muller, "Influence of DBT Reconstruction Algorithm on Power Law Spectrum Coefficient," *SPIE Medical Imaging*, 2015

Bibliography

[1] J. Ferlay, I. Soerjomataram, M. Ervik, R. Dikshit, S. Eser, C. Mathers, M. Rebelo, D. Parkin, D. Forman, and F. Bray, "GLOBOCAN 2012 v1.0, Cancer Incidence and Mortality Worldwide: IARC CancerBase No. 11.," 2013.

[2] InVS and INCa, "Projection de l'incidence et de la mortalité par cancer en France en 2011," tech. rep., Saint-Maurice: Institut de veille sanitaire, 2011.

[3] M. Kalager and M. Zelen, "Effect of screening mammography on breast-cancer mortality in Norway," *New England Journal of Medicine*, 2010.

[4] M. Kriege, C. Brekelmans, C. Boetes, P. Besnard, H. Zonderland, I. Obdeijn, R. Manoliu, T. Kok, H. Peterse, M. Tilanus-Linthorst, S. Muller, S. Meijer, J. Oosterwijk, L. Beex, R. Tollenaar, H. De Koning, E. Rutgers, and J. Klijn, "Efficacy of MRI and mammography for breast-cancer screening in women with a familial or genetic predisposition," *New England Journal of Medicine*, vol. 351, pp. 427–437, 2004.

[5] C. Kuhl, S. Schrading, C. Leutner, N. Morakkabati-Spitz, E. Wardelmann, R. Fimmers, W. Kuhn, and H. Schild, "Mammography, breast ultrasound, and magnetic resonance imaging for surveillance of women at high familial risk for breast cancer," *Journal of Clinical Oncology*, vol. 23, pp. 8469–8476, 2005.

[6] J. Folkman, "Angiogenesis in cancer, vascular, rheumatoid and other disease.," *Nature medicine*, vol. 1, pp. 27–31, Jan. 1995.

[7] R. M. Mann, C. K. Kuhl, K. Kinkel, and C. Boetes, "Breast MRI: guidelines from the European Society of Breast Imaging.," *European radiology*, vol. 18, pp. 1307–18, July 2008.

[8] C. Hagay, P. J. Cherel, C. E. de Maulmont, M. M. Plantet, R. Gilles, J. L. Floiras, J. R. Garbay, and C. M. Pallud, "Contrast-enhanced CT: value for diagnosing local breast cancer recurrence after conservative treatment.," *Radiology*, vol. 200, pp. 631–8, Sept. 1996.

[9] T. A. Heusner, S. Kuemmel, L. Umutlu, A. Koeninger, L. S. Freudenberg, E. A. M. Hauth, K. R. Kimmig, M. Forsting, A. Bockisch, and G. Antoch, "Breast cancer staging in a single session: whole-body PET/CT mammography.," *Journal of nuclear medicine : official publication, Society of Nuclear Medicine*, vol. 49, pp. 1215–22, Aug. 2008.

[10] N. Lassau, S. Koscielny, P. Opolon, T. De Baere, P. Peronneau, J. Leclère, and A. Roche, "Evaluation of contrast-enhanced colour Doppler ultrasound for the quantification of angiogenesis in vivo," *Investigative Radiology*, vol. 36, pp. 50–55, 2001.

[11] M. Skarpathiotakis, M. J. Yaffe, A. K. Bloomquist, D. Rico, S. Muller, A. Rick, and F. Jeunehomme, "Development of contrast digital mammography.," *Medical Physics*, vol. 29, no. 10, pp. 2419–2426, 2002.

[12] C. Marx, M. Facius, S. L. Muller, K. Benali, A. Malich, and W. Kaiser, "Contrast-enhanced digital mammography (CEDM): phantom experiment and first clinical results," *Proceedings of SPIE*, vol. 4682, pp. 174–181, 2002.

[13] R. Jong, M. Yaffe, M. Skarpathiotakis, R. Shumak, N. Danjoux, A. Gunesekara, and D. Plewes, "Contrast-enhanced digital mammography: initial clinical experience," *Radiology*, vol. 228(3), pp. 842–850, 2003.

[14] C. Dromain, C. Balleyguier, S. Muller, M.-C. Mathieu, F. Rochard, P. Opolon, and R. Sigal, "Evaluation of tumor angiogenesis of breast carcinoma using contrast-enhanced digital mammography.," *Ajr American Journal Of Roentgenology*, vol. 187, no. 5, pp. W528–W537, 2006.

[15] F. Diekmann, C. Marx, R. Jong, C. Dromain, A. Toledano, and U. Bick, "Diagnostic accuracy of contrast-enhanced digital mammography as an adjunct to mammography," European Congress of Radiology, pp. B–171, 2007.

[16] J. M. Lewin, P. K. Isaacs, V. Vance, and F. J. Larke, "Dual-energy contrast enhanced digital subtraction mammography: feasilibility," *Radiology*, vol. 229, pp. 261–268, 2003.

[17] S. Puong, F. Patoureaux, R. Iordache, X. Bouchevreau, and S. Muller, "Dual-energy contrast enhanced digital breast tomosynthesis: concept, method, and evaluation on phantoms," *Proceedings of SPIE*, vol. 6510, no. 0, pp. 65100U–65100U–12, 2007.

[18] A.-K. Carton, K. Lindman, C. Ullberg, T. Francke, and A. D. a. Maidment, "Dual-energy subtraction for contrast-enhanced digital breast tomosynthesis," *Proceedings of SPIE*, pp. 651007–651007–12, 2007.

[19] S. J. Glick and C. Didier, "A computer simulation for evaluating dual-energy, contrast-enhanced breast tomosynthesis," in *Medical Image 2007: Physics of Medical Imaging* (M. Flynn and J. Hsieh, eds.), vol. 6510 of *Proc. SPIE*, p. 65102V, 2007.

[20] R. Saunders, E. Samei, C. Badea, H. Yuan, K. Ghaghada, Y. Qi, L. Hedlund, and S. Mukundan, "Optimization of dual-energy contrast enhanced breast tomosynthesis for improved mammographic lesion detection and diagnosis," in *Medical Image 2008: Physics of Medical Imaging* (J. Hsieh and E. Samei, eds.), vol. 6913 of *Proc. SPIE*, p. 69130Y, 2008.

[21] A.-K. Carton, C. Ullberg, K. Lindman, T. Francke, and A. Maidment, "Optimization of a dual-energy contrast-enhanced technique for a photon counting digital breast tomosynthesis system," in *Digital Mammography: 9th International Workshop, IWDM 2008* (E. Krupinski, ed.), Proc. IWDM, pp. 116–123, 2008.

[22] A.-K. Carton, J. A. Currivan, E. Conant, and A. Maidment, "Temporal Subtraction Versus Dual-Energy Contrast-Enhanced Digital Breast Tomosynthesis: A Pilot Study," *Digital Mammography*, pp. 166–173, 2008.

[23] A.-K. Carton, C. Ullberg, K. Lindman, R. Acciavatti, T. Francke, and A. D. A. Maidment, "Optimization of a dual-energy contrast-enhanced technique for a photon-counting digital breast tomosynthesis system: I. A theoretical model," *Medical Physics*, vol. 37, no. 11, p. 5896, 2010.

[24] R. Iordache, M. Lohezic, G. Palma, S. Puong, and S. Muller, "Noise Reduction in Dual-Energy Contrast Enhanced Digital Breast Tomosynthesis Using Regularization," *Digital Mammography*, vol. 6136, pp. 92–99, 2010.

[25] F. Schmitzberger and E. Fallenberg, "Development of low-dose photon-counting contrast-enhanced tomosynthesis with spectral imaging," *Radiology*, no. May, 2011.

[26] M. D. Hörnig, L. Bätz, and T. Mertelmeier, "Design of a contrast-enhanced dual-energy tomosynthesis system for breast cancer imaging," in *SPIE Medical Imaging* (N. J. Pelc, R. M. Nishikawa, and B. R. Whiting, eds.), p. 83134O, International Society for Optics and Photonics, Feb. 2012.

[27] B. D. Man, S. Basu, N. Chandra, B. Dunham, P. Edic, and M. Iatrou, "CatSim: a new computer assisted tomography simulation environment," *Proceedings of SPIE*, vol. 6510, pp. 1–8, 2007.

[28] D. Dronkers, J. H. C. L. Hendriks, R. Holland, and G. Rosenbusch, *The practice of mammography: pathology, technique, interpretation, adjunct modalities.* Thieme, 1st editio ed., 2002.

[29] S. W. Hutson, P. N. Cowen, and C. C. Bird, "Morphometric studies of age related changes in normal human breast and their significance for evolution of mammary cancer.," *Journal of clinical pathology*, vol. 38, pp. 281–7, Mar. 1985.

[30] D. Geddes, "Inside the lactating breast: the latest anatomy research," *Journal of Midwifery & Women's Health*, vol. 52, no. 6, pp. 556–63, 2007.

[31] J. C. Boughey, J. Wagner, B. J. Garrett, L. Harker, L. P. Middleton, G. V. Babiera, F. Meric-Bernstam, A. Lucci, K. K. Hunt, and I. Bedrosian, "Neoadjuvant chemotherapy in invasive lobular carcinoma may not improve rates of breast conservation.," *Annals of surgical oncology*, vol. 16, pp. 1606–11, June 2009.

[32] A. P. Cooper, *On the anatomy of the breast.* 1840.

[33] G. Gasparini, "Clinical significance of determination of surrogate markers of angiogenesis in breast cancer," *Critical Reviews in Oncology and Hematology*, vol. 37, pp. 97–114, 2001.

[34] N. Weidner, J. P. Semple, W. R. Welch, and J. Folkmann, "Tumor angiogenesis and metastasis: correlation in invasive breast carcinoma," *New England Journal of Medicine*, vol. 324, pp. 1–8, 1991.

[35] K. Axelsson, B. M. Ljung, D. H. Moore, A. D. Thor, K. L. Chew, S. M. Edgerton, H. S. Smith, and B. H. Mayall, "Tumor angiogenesis as a prognostic assay for invasive ductal breast carcinoma," *Journal of the National Cancer Institute*, vol. 87, pp. 997–1008, 1995.

[36] N. Weidner and J. Folkmann, "Tumoral vascularity as a prognosis factor in cancer," in *Important Advances in Oncology* (V. T. DeVita, S. Hellman, and S. A. Rosenburg, eds.), pp. 167–190, Lippincott-Raven, 1996.

[37] N. Weidner, J. Folkman, F. Pozza, P. Bevilacqua, E. Allred, D. Moore, S. Meli, and G. Gasparini, "Tumor angiogenesis: a new significant and independent prognostic indicator in early-stage breast carcinoma," *Journal of the National Cancer Institute*, vol. 84, pp. 1875–1887, 1992.

[38] A. Guidi, L. Fischer, J. Harris, and S. Schnitt, "Microvessel density and distribution in ductal carcinoma in situ of the breast," *Journal of the National Cancer Institute*, vol. 86, pp. 614–619, 1994.

[39] B. Uzzan, P. Nicolas, M. Cucherat, and G. Perret, "Microvessel density as a prognostic factor in women with breast cancer: a systematic review of the literature and meta-analysis," *Cancer Research*, vol. 64, pp. 2941–2955, 2004.

[40] A. Rogel, A. Belot, F. Suzan, N. Bossard, M. Boussac, P. Arveux, A. Buémi, M. Colonna, A. Danzon, O. Ganry, A.-V. Guizard, P. Grosclaude, M. Velten, E. Jougla, J. Iwaz, J. Estève, L. Chérié-Challine, and L. Remontet, "Reliability of recording uterine cancer in death certification in France and age-specific proportions of deaths from cervix and corpus uteri," *Cancer Epidemiology*, vol. 35, no. 3, pp. 243–249, 2011.

[41] A. Belot, P. Grosclaude, N. Bossard, E. Jougla, E. Benhamou, P. Delafosse, A.-V. Guizard, F. Molinié, A. Danzon, S. Bara, A.-M. Bouvier, B. Trétarre, F. Binder-Foucard, M. Colonna, L. Daubisse, G. Hédelin, G. Launoy, N. Le Stang, M. Maynadié, A. Monnereau, X. Troussard,

J. Faivre, A. Collignon, I. Janoray, P. Arveux, A. Buemi, N. Raverdy, C. Schvartz, M. Bovet, L. Chérié-Challine, J. Estève, L. Remontet, and M. Velten, "Cancer incidence and mortality in France over the period 1980-2005.," *Revue d'épidémiologie et de santé publique*, vol. 56, pp. 159–75, June 2008.

[42] S. Duffy, I. Tabar, and B. Vitak, "The relative contribution of screen-detected in situ and invasive breast carcinomas in reducing mortality from the disease," *European Journal of Cancer*, vol. 39, pp. 1755–1760, 2003.

[43] "Loi de santé publique du 9 août 2004, NOR: SANX0300055L Version consolidée au 12 août 2011, TITRE Ier : POLITIQUE DE SANTÉ PUBLIQUE.."

[44] I. Tabar, B. Vitak, H. Chen, M. Yen, S. Duffy, and R. Smith, "Beyond randomized controlled trials: organized mammographic screening substantially reduces breast cancer mortality," *Cancer*, vol. 91, pp. 1724–1731, 2001.

[45] K. Kerlikowske, "Efficacy of screening mammography among women aged 40 to 49 years and 50 to 69 years: comparison of relative and absolute benefit," *Journal of the National Cancer Institute*, vol. 22, pp. 79–86, 1997.

[46] P. Grosclaude, *Survie des patients atteints de cancer en France.* Springer, 2007.

[47] D. B. Kopans, *Breast Imaging.* Lippincott-Raven, 1998.

[48] M. Leach, C. Boggis, A. Dixon, D. Easton, R. Eeles, D. Evans, F. Gilbert, I. Griebsch, R. Hoff, P. Kessar, S. Lakhani, S. Moss, A. Nerurkar, A. Padhani, L. Pointon, D. Thompson, and R. Warren, "Screening with magnetic resonance imaging and mammography of a UK population at high familial risk of breast cancer: a prospective multicentre cohort study (MARIBS)," *Lancet*, vol. 365, pp. 1769–1778, 2005.

[49] C. Lehman, J. Blume, P. Weatherall, D. Thickman, N. Hylton, E. Warner, E. Pisano, S. Schnitt, C. Gatsonis, and M. Schnall, "Screening women at high risk for breast cancer with mammography and magnetic resonance imaging," *Cancer*, vol. 103, pp. 1898–1905, 2005.

[50] D. Saslow, C. Boetes, W. Burke, S. Harms, M. Leach, C. Lehman, E. Morris, E. Pisano, M. Schnall, S. Sener, R. Smith, E. Warner, M. Yaffe, K. Andrews, and C. Russell, "American Cancer Society guidelines for breast screening with MRI as an adjunct to mammography," *AC Cancer Journal for Clinicians*, vol. 57, pp. 75–89, 2007.

[51] F. Sardanelli, C. Boetes, B. Borisch, T. Decker, M. Federico, F. J. Gilbert, T. Helbich, S. H. Heywang-Köbrunner, W. a. Kaiser, M. J. Kerin, R. E. Mansel, L. Marotti, L. Martincich, L. Mauriac, H. Meijers-Heijboer, R. Orecchia, P. Panizza, A. Ponti, A. D. Purushotham, P. Regitnig, M. R. Del Turco, F. Thibault, and R. Wilson, "Magnetic resonance imaging of the breast: recommendations from the EUSOMA working group.," *European journal of cancer (Oxford, England : 1990)*, vol. 46, pp. 1296–316, May 2010.

[52] Q. Zhong, C.-F. Chen, P.-L. Chen, and W.-H. Lee, "BRCA1 facilitates microhomology-mediated end joining of DNA double strand breaks.," *The Journal of biological chemistry*, vol. 277, pp. 28641–7, Aug. 2002.

[53] A. Baeyens, H. Thierens, K. Claes, B. Poppe, L. Messiaen, L. De Ridder, and A. Vral, "Chromosomal radiosensitivity in breast cancer patients with a known or putative genetic predisposition.," *British journal of cancer*, vol. 87, pp. 1379–85, Dec. 2002.

[54] S. N. Powell and L. A. Kachnic, "Roles of BRCA1 and BRCA2 in homologous recombination, DNA replication fidelity and the cellular response to ionizing radiation.," *Oncogene*, vol. 22, pp. 5784–91, Sept. 2003.

[55] B. Ernestos, P. Nikolaos, G. Koulis, R. Eleni, B. Konstantinos, G. Alexandra, and K. Michael, "Increased chromosomal radiosensitivity in women carrying BRCA1/BRCA2 mutations assessed with the G2 assay.," *International journal of radiation oncology, biology, physics*, vol. 76, pp. 1199–205, Mar. 2010.

[56] F. Sardanelli and F. Podo, "Breast MR imaging in women at high-risk of breast cancer. Is something changing in early breast cancer detection?," *European radiology*, vol. 17, pp. 873–87, Apr. 2007.

[57] C. Lehman, C. Isaacs, and M. Schnall, "Cancer Yield of Mammography, MR, and US in High-Risk Women: Prospective Multi-Institution Breast Cancer Screening Study 1," *Radiology*, vol. 244, no. 2, pp. 381–388, 2007.

[58] C. Frouge, J. Guinebretière, R. Di Paola, G. Contesso, and M. Blery, "Correlation between contrast enhancement in dynamic magnetic resonance imaging of the breast and tumor angiogenesis," *Investigative Radiology*, vol. 29, pp. 1043–1049, 1994.

[59] N. Tuncbilek, E. Unlu, H. M. Karakas, B. Cakir, and F. Ozyilmaz, "Evaluation of tumor angiogenesis with contrast-enhanced dynamic magnetic resonance mammography," *The Breast Journal*, vol. 9, pp. 403–408, 1993.

[60] W. Kaiser and E. Zeitler, "MR imaging of the breast: fast imaging sequences with and without Gd-DTPA. Preliminary observations," *Radiology*, vol. 170, pp. 681–686, 1989.

[61] S. Heywang-Kobrunner, "Contrast-enhanced magnetic resonance imaging of the breast," *Investigative Radiology*, vol. 29, pp. 94–104, 1994.

[62] W. A. Berg, L. Gutierrez, M. S. NessAiver, W. B. Carter, M. Bhargavan, R. S. Lewis, and O. B. Ioffe, "Diagnostic accuracy of mammography, clinical examination, US, and MR imaging in preoperative assessment of breast cancer.," *Radiology*, vol. 233, no. 3, pp. 830–849, 2004.

[63] C. C. Riedl, L. Ponhold, D. Flöry, M. Weber, R. Kroiss, T. Wagner, M. Fuchsjäger, and T. H. Helbich, "Magnetic resonance imaging of the breast improves detection of invasive cancer, preinvasive cancer, and premalignant lesions during surveillance of women at high risk for breast cancer.," *Clinical cancer research : an official journal of the American Association for Cancer Research*, vol. 13, pp. 6144–52, Oct. 2007.

[64] C. D. Lehman, C. Gatsonis, C. K. Kuhl, R. E. Hendrick, E. D. Pisano, L. Hanna, S. Peacock, S. F. Smazal, D. D. Maki, T. B. Julian, E. R. DePeri, D. A. Bluemke, and M. D. Schnall, "MRI evaluation of the contralateral breast in women with recently diagnosed breast cancer.," Tech. Rep. 13, University of Washington Medical Center, Seattle, WA 98109, USA. lehman@u.washington.edu, 2007.

[65] D. C. Abraham, R. C. Jones, S. E. Jones, J. H. Cheek, G. N. Peters, S. M. Knox, M. D. Grant, D. W. Hampe, D. A. Savino, and S. E. Harms, "Evaluation of neoadjuvant chemotherapeutic response of locally advanced breast cancer by magnetic resonance imaging.," *Cancer*, vol. 78, no. 1, pp. 91–100, 1996.

[66] E. L. Rosen, K. L. Blackwell, J. A. Baker, M. S. Soo, R. C. Bentley, D. Yu, T. V. Samulski, and M. W. Dewhirst, "Accuracy of MRI in the detection of residual breast cancer after neoadjuvant chemotherapy," *American Journal of roentgenology*, no. November, pp. 1275–1282, 2003.

[67] J.-P. Delille, P. Slanetz, E. Yeh, D. Kopans, and L. Garrido, "Physiologic changes in breast magnetic resonance imaging during the menstrual cycle: perfusion imaging, signal enhancement, and influence of the t1 relaxation time of breast tissue," *The Breast Journal*, vol. 11(4), pp. 236–41, 2005.

[68] S. Heywang-Kobrunner, A. Schlegel, R. Beck, T. Wendt, W. Kellner, B. Lommatzsch, M. Untch, and W. Nathrath, "Contrast-enhanced MRI of the breast after limited surgery and radiation therapy," *Journal of Computer Assisted Tomography*, vol. 17(6), pp. 891–900, 1993.

[69] I. Griebsch, J. Brown, C. Boggis, A. Dixon, M. Dixon, D. Easton, R. Eeles, D. G. Evans, F. J. Gilbert, J. Hawnaur, P. Kessar, S. R. Lakhani, S. M. Moss, A. Nerurkar, A. R. Padhani, L. J. Pointon, J. Potterton, D. Thompson, L. W. Turnbull, L. G. Walker, R. Warren, and M. O. Leach, "Cost-effectiveness of screening with contrast enhanced magnetic resonance imaging vs X-ray mammography of women at a high familial risk of breast cancer.," *British journal of cancer*, vol. 95, pp. 801–10, Oct. 2006.

[70] C. Taneja, J. Edelsberg, D. Weycker, A. Guo, G. Oster, and J. Weinreb, "Cost effectiveness of breast cancer screening with contrast-enhanced MRI in high-risk women.," *Journal of the American College of Radiology : JACR*, vol. 6, pp. 171–9, Mar. 2009.

[71] Sécurité sociale - l'Assurance Maladie, "Mammographie bilatérale," *http://www.ameli.fr/accueil-de-la-ccam/trouver-un-acte/fiche-abregee.php?code=QEQK001*.

[72] C. D. Lehman, J. D. Blume, D. Thickman, D. A. Bluemke, E. Pisano, C. Kuhl, T. B. Julian, N. Hylton, P. Weatherall, M. O'loughlin, S. J. Schnitt, C. Gatsonis, and M. D. Schnall, "Added cancer yield of MRI in screening the contralateral breast of women recently diagnosed with breast cancer: results from the International Breast Magnetic Resonance Consortium (IBMC) trial.," *Journal of surgical oncology*, vol. 92, pp. 9–15; discussion 15–6, Oct. 2005.

[73] C. Dromain, C. Jeunehomme, F. Oppolon, P. Herlin, and M.-C. Mathieu, "Evaluation of tumor angiogenesis of breast carcinoma using contrast full-field digital mammography: preliminary results," *Scientific Assembly and Annual Meeting Program 2004, RSNA, Chicago:567, 717.*, 2004.

[74] J. Muller, P. F. G. M. van Waes, and P. R. Koehler, "Computed tomography of breast lesions: comparison with X-ray mammography," *Journal of Computer Assisted Tomography*, 1983.

[75] C. H. Chang, D. E. Nesbit, D. R. Fisher, S. L. Fritz, S. J. Dwyer, A. W. Templeton, F. Lin, and W. R. Jewell, "Computed tomographic mammography using a conventional body scanner.," *AJR. American journal of roentgenology*, vol. 138, pp. 553–8, Mar. 1982.

[76] F. Sardanelli, M. Calabrese, F. Zandrino, E. Melani, R. C. Parodi, A. Imperiale, T. Massa, G. Parodi, and G. Canavese, "Dynamic helical CT of breast tumors," *Journal of Computer Assisted Tomography*, vol. 22, no. 3, pp. pp 398–407, 1998.

[77] M. Inoue, T. Sano, R. Watai, R. Ashikaga, K. Ueda, M. Watatani, and Y. Nishimura, "Dynamic multidetector CT of breast tumors: diagnostic features and comparison with conventional techniques.," *AJR. American journal of roentgenology*, vol. 181, pp. 679–86, Sept. 2003.

[78] K. Miyake, K. Hayakawa, M. Nishino, Y. Nakamura, T. Morimoto, Y. Urata, H. Ueda, M. Tanikake, S. Kanao, T. Shiozaki, and A. M. Yamamoto, "Benign or malignant?: differentiating breast lesions with computed tomography attenuation values on dynamic computed tomography mammography," *Journal of Computer Assisted Tomography*, vol. 29, no. 6, pp. 772–779, 2005.

[79] A. Shimauchi, T. Yamada, A. Sato, K. Takase, S. Usami, T. Ishida, T. Moriya, and S. Takahashi, "Comparison of MDCT and MRI for evaluating the intraductal component of breast cancer.," *AJR. American journal of roentgenology*, vol. 187, pp. 322–9, Aug. 2006.

[80] S. J. Glick, "Breast CT," in *Cone Beam Computed Tomography*, p. 235, Taylor & Francis, 2014.

[81] T. Heusner, S. Kuemmel, L. Umutlu, A. Koeninger, L. Freudenberg, E. Hauth, K. Kimmig, M. Forsting, A. Bockisch, and G. Antoch, "Breast cancer staging in a single session: whole-body PET/CT mammography," *Journal of Nuclear Medicine*, vol. 49(8), pp. 1215–1222, 2008.

[82] O. Schillaci, R. Danieli, L. Filippi, P. Romano, E. Cossu, C. Manni, and G. Simonetti, "Scintimammography with a hybrid SPECT/CT imaging system," *Anticancer Research*, vol. 27, pp. 557–562, 2007.

[83] R. Kedar, D. Cosgrove, V. McCready, J. Bamber, and E. Carter, "Microbubble contrast agent for color Doppler US: effect on breast masses," *Radiology*, vol. 198, pp. 679–686, 1996.

[84] N. Lassau and A. Roche, "Imagerie et angiogénèse: la DCE-US (dynamic contrast enhanced-ultrasonography," *Bulletin du Cancer*, vol. 94, pp. S247–S253, 2007.

[85] T. Niklason, B. T. Christian, L. E. Niklason, D. B. Kopans, B. H. Opsahl-Ong, E. Landberg, A. Giardino, P. F. Fitzgerald, F. Fobare, B. W. Giambattista, R. F. Kwasnick, S. J. Lubowski, E. Possin, F. Richotte, R. F. Wirth, and E. Castleberry, "Digital tomosynthesis in breast imaging," *Radiology*, vol. 205, no. 2, pp. 399–406, 1997.

[86] B. Ziedses des Plantes, "Eine neue methode zur differenzierung in der roentgenographie (planigraphie)," *Acta Radiologica*, vol. 13, pp. 182–192, 1932.

[87] Y. Hu, W. Zhao, T. Mertelmeier, and J. Ludwig, "Image artifact in digital breast tomosynthesis and its dependence on system and reconstruction parameters," *Digital Mammography*, pp. 628–634, 2008.

[88] J. T. Dobbins and D. J. Godfrey, "Digital x-ray tomosynthesis: current state of the art and clinical potential.," *Physics in medicine and biology*, vol. 48, pp. R65–106, Oct. 2003.

[89] D. Gur, G. S. Abrams, D. M. Chough, M. a. Ganott, C. M. Hakim, R. L. Perrin, G. Y. Rathfon, J. H. Sumkin, M. L. Zuley, and A. I. Bandos, "Digital breast tomosynthesis: observer performance study.," *AJR. American journal of roentgenology*, vol. 193, pp. 586–91, Aug. 2009.

[90] G. Gennaro, A. Toledano, C. di Maggio, E. Baldan, E. Bezzon, M. La Grassa, L. Pescarini, I. Polico, A. Proietti, A. Toffoli, and P. C. Muzzio, "Digital breast tomosynthesis versus digital mammography: a clinical performance study.," *European radiology*, vol. 20, pp. 1545–53, July 2010.

[91] S. C. Chen, A.-K. Carton, M. Albert, E. F. Conant, M. D. Schnall, and A. D. A. Maidment, "Initial clinical experience with contrast-enhanced digital breast tomosynthesis.," *Academic Radiology*, vol. 14, no. 2, pp. 229–238, 2007.

[92] A.-K. Carton, J. Li, M. Albert, S. Chen, and A. D. A. Maidment, "Quantification for contrast-enhanced digital breast tomosynthesis," *Proceedings of SPIE*, vol. 6142, pp. 61420D–61420D–11, 2006.

[93] A.-K. Carton, J. Li, S. Chen, E. Conant, and A. Maidment, "Optimization of contrast-enhanced digital breast tomosynthesis," in *Digital Mammography: 8th International Workshop, IWDM 2006* (S. Astley, M. Brady, C. Rose, and R. Zwiggelaar, eds.), Proc. IWDM, pp. 183–189, 2006.

[94] M. Nock, M. Kempston, J. Mainprize, and M. Yaffe, "Quantitative flow phantom for contrast-enhanced breast tomosynthesis," in *Medical Image 2007: Physics of Medical Imaging* (M. Flynn and J. Hsieh, eds.), vol. 6510 of *Proc. SPIE*, p. 65102W, 2007.

[95] M. Hill, J. Mainprize, and M. Yaffe, "Sensitivity of Contrast-Enhanced Digital Breast Tomosynthesis to Changes in Iodine Concentration during Acquisition," *Digital Mammography*, vol. 5116, pp. 643–650, 2008.

[96] A. K. Carton, S. C. Gavenonis, J. A. Currivan, E. F. Conant, M. D. Schnall, and A. D. A. Maidment, "Dual-energy contrast-enhanced digital breast tomosynthesis–a feasibility study.," 2010.

[97] V. Froeling, F. Diekmann, D. M. Renz, E. M. Fallenberg, I. G. Steffen, S. Diekmann, R. Lawaczeck, and F. F. Schmitzberger, "Correlation of contrast agent kinetics between iodinated contrast-enhanced spectral tomosynthesis and gadolinium-enhanced MRI of breast lesions.," *European radiology*, vol. 23, pp. 1528–36, June 2013.

[98] J. J. Gisvold, P. R. Karsell, and E. C. Reese, "Clinical evaluation of computerized tomographic mammography.," *Mayo Clinic proceedings. Mayo Clinic*, vol. 52, pp. 181–5, Mar. 1977.

[99] C. H. Chang, J. L. Sibala, J. H. Gallagher, R. C. Riley, A. W. Templeton, P. V. Beasley, and R. A. Porte, "Computed tomography of the breast. A preliminary report.," *Radiology*, vol. 124, pp. 827–9, Sept. 1977.

[100] C. H. Chang, J. L. Sibala, S. L. Fritz, J. H. Gallagher, S. J. Dwyer, and A. W. Templeton, "Computed tomographic evaluation of the breast.," *AJR. American journal of roentgenology*, vol. 131, pp. 459–64, Sept. 1978.

[101] C. H. Chang, J. L. Sibala, S. L. Fritz, S. J. Dwyer, and A. W. Templeton, "Specific value of computed tomographic breast scanner (CT/M) in diagnosis of breast diseases.," *Radiology*, vol. 132, pp. 647–52, Sept. 1979.

[102] J. J. Gisvold, D. F. Reese, and P. R. Karsell, "Computed tomographic mammography (CTM).," *AJR. American journal of roentgenology*, vol. 133, pp. 1143–9, Dec. 1979.

[103] J. Boone, T. Nelson, K. Lindfors, and J. Seibert, "Dedicated Breast CT: Radiation Dose and Image Quality Evaluation1," *Radiology*, vol. 221, no. 3, p. 657, 2001.

[104] B. Chen and R. Ning, "Cone-beam volume CT breast imaging: Feasibility study," *Medical Physics*, vol. 29, no. 5, p. 755, 2002.

[105] S. Glick, S. Vedantham, and A. Karellas, "Investigation of optimal kVp settings for CT mammography using a flat-panel imager," *Proceedings of SPIE Medical Imaging*, pp. 392–402, May 2002.

[106] M. P. Tornai, "Design and development of a fully 3D dedicated x-ray computed mammotomography system," *Proceedings of SPIE*, vol. 5745, pp. 189–197, 2005.

[107] J. M. Boone, A. L. C. Kwan, K. Yang, G. W. Burkett, K. K. Lindfors, and T. R. Nelson, "Computed tomography for imaging the breast.," *Journal of mammary gland biology and neoplasia*, vol. 11, pp. 103–11, Apr. 2006.

[108] W. A. Kalender, M. Beister, J. M. Boone, D. Kolditz, S. V. Vollmar, and M. C. C. Weigel, "High-resolution spiral CT of the breast at very low dose: concept and feasibility considerations.," *European radiology*, June 2011.

[109] P. M. Shikhaliev, T. Xu, and S. Molloi, "Photon counting computed tomography: Concept and initial results," *Medical Physics*, vol. 32, no. 2, p. 427, 2005.

[110] R. Bhagtani and T. G. Schmidt, "Simulated scatter performance of an inverse-geometry dedicated breast CT system," *Medical Physics*, vol. 36, no. 3, p. 788, 2009.

[111] J. M. Boone, N. Shah, and T. R. Nelson, "A comprehensive analysis of DgN[sub CT] coefficients for pendant-geometry cone-beam breast computed tomography," *Medical Physics*, vol. 31, no. 2, p. 226, 2004.

[112] S. C. Thacker and S. J. Glick, "Normalized glandular dose (DgN) coefficients for flat-panel CT breast imaging," *Physics in Medicine and Biology*, vol. 49, pp. 5433–5444, Dec. 2004.

[113] B. Liu, S. Glick, and C. Groiselle, "Characterization of scatter radiation in cone beam CT mammography," *Proceedings of SPIE Medical Imaging*, vol. 5745, pp. 818–827, 2005.

[114] A. L. C. Kwan, J. M. Boone, and N. Shah, "Evaluation of x-ray scatter properties in a dedicated cone-beam breast CT scanner," *Medical Physics*, vol. 32, no. 9, p. 2967, 2005.

[115] C.-J. Lai, C. C. Shaw, L. Chen, M. C. Altunbas, X. Liu, T. Han, T. Wang, W. T. Yang, G. J. Whitman, and S.-J. Tu, "Visibility of microcalcification in cone beam breast CT: Effects of x-ray tube voltage and radiation dose," *Medical Physics*, vol. 34, no. 7, p. 2995, 2007.

[116] M. Weigel, S. V. Vollmar, and W. A. Kalender, "Spectral optimization for dedicated breast CT," *Medical Physics*, vol. 38, no. 1, p. 114, 2011.

[117] N. D. Prionas, S.-Y. Huang, and J. M. Boone, "Experimentally determined spectral optimization for dedicated breast computed tomography," *Medical Physics*, vol. 38, no. 2, p. 646, 2011.

[118] R. L. McKinley, "Investigation of cone-beam acquisitions implemented using a novel dedicated mammotomography system with unique arbitrary orbit capability (Honorable Mention Poster Award)," *Proceedings of SPIE*, vol. 5745, pp. 609–617, 2005.

[119] A. L. C. Kwan, J. M. Boone, K. Yang, and S.-Y. Huang, "Evaluation of the spatial resolution characteristics of a cone-beam breast CT scanner," *Medical Physics*, vol. 34, no. 1, p. 275, 2007.

[120] K. Yang, A. L. C. Kwan, and J. M. Boone, "Computer modeling of the spatial resolution properties of a dedicated breast CT system," *Medical Physics*, vol. 34, no. 6, p. 2059, 2007.

[121] K. Yang, A. L. C. Kwan, S.-Y. Huang, N. J. Packard, and J. M. Boone, "Noise power properties of a cone-beam CT system for breast cancer detection," *Medical Physics*, vol. 35, no. 12, p. 5317, 2008.

[122] R. B. Benítez, R. Ning, D. Conover, and S. Liu, "NPS characterization and evaluation of a cone beam CT breast imaging system.," *Journal of X-ray science and technology*, vol. 17, pp. 17–40, Jan. 2009.

[123] Y. Shen, Y. Zhong, C.-J. Lai, T. Wang, and C. C. Shaw, "Cone beam breast CT with a high pitch (75 μm), thick (500 μm) scintillator CMOS flat panel detector: visibility of simulated microcalcifications.," *Medical physics*, vol. 40, p. 101915, Oct. 2013.

[124] G. J. Gang, D. J. Tward, J. Lee, and J. H. Siewerdsen, "Anatomical background and generalized detectability in tomosynthesis and cone-beam CT," *Medical Physics*, vol. 37, no. 5, p. 1948, 2010.

[125] L. Chen, J. M. Boone, A. Nosratieh, and C. K. Abbey, *NPS comparison of anatomical noise characteristics in mammography, tomosynthesis, and breast CT images using power law metrics*, vol. 7961. COPYRIGHT Society of Photo-Optical Instrumentation Engineers (SPIE). Downloading of the abstract is permitted for personal use only., Mar. 2011.

[126] M. C. Altunbas, C. C. Shaw, L. Chen, C. Lai, X. Liu, T. Han, and T. Wang, "A post-reconstruction method to correct cupping artifacts in cone beam breast computed tomography," *Medical Physics*, vol. 34, no. 7, p. 3109, 2007.

[127] K. Lindfors, J. Boone, T. Nelson, K. Yang, A. Kwan, and D. Miller, "Dedicated Breast CT: Initial Clinical Experience," *Radiology*, vol. 246, no. 3, p. 725, 2008.

[128] A. O'Connell, D. L. Conover, Y. Zhang, P. Seifert, W. Logan-Young, C.-F. L. Lin, L. Sahler, and R. Ning, "Cone-beam CT for breast imaging: Radiation dose, breast coverage, and image quality.," *AJR. American journal of roentgenology*, vol. 195, pp. 496–509, Aug. 2010.

[129] P. M. Shikhaliev, "Tilted angle CZT detector for photon counting/energy weighting x-ray and CT imaging.," *Physics in medicine and biology*, vol. 51, pp. 4267–87, Sept. 2006.

[130] P. M. Shikhaliev, "Computed tomography with energy-resolved detection: a feasibility study.," *Physics in medicine and biology*, vol. 53, pp. 1475–95, Mar. 2008.

[131] K. Kalluri, M. Mahd, and S. J. Glick, "Comparing human observer performance in detecting microcalcifications with energy weighting and photon counting breast CT," *SPIE Medical Imaging*, vol. 8313, pp. 83130B–83130B–9, 2012.

[132] S. Rudin, A. T. Kuhls, G. K. Yadava, G. C. Josan, Y. Wu, R. N. Chityala, H. S. Rangwala, N. Ciprian Ionita, K. R. Hoffmann, and D. R. Bednarek, "New light-amplifier-based detector designs for high spatial resolution and high sensitivity CBCT mammography and fluoroscopy.," *Proceedings - Society of Photo-Optical Instrumentation Engineers*, vol. 6142, pp. 61421R–61421R–11, Dec. 2006.

[133] J. Jorgensen, E. Sidky, and X. Pan, "Ensuring convergence in total-variation-based reconstruction for accurate microcalcification imaging in breast X-ray CT," *Nuclear Science Symposium and Medical Imaging Conference (NSS/MIC), 2011 IEEE*, vol. 2, no. 3, pp. 2640 – 2643, 2011.

[134] A. Makeev, M. Das, and S. J. Glick, "Investigation of statistical iterative reconstruction for dedicated breast CT," *Proceedings of SPIE Medical Imaging*, vol. 8313, pp. 83131W–83131W–7, 2012.

[135] Y. Shen, Y. Yi, Y. Zhong, C.-J. Lai, X. Liu, Z. You, S. Ge, T. Wang, and C. C. Shaw, "High resolution dual detector volume-of-interest cone beam breast CT–Demonstration with a bench top system.," *Medical physics*, vol. 38, p. 6429, Dec. 2011.

[136] D. Crotty and P. Madhav, "Patient bed design for an integrated SPECT-CT dedicated mammotomography system," *IEEE Nuclear Science Symposium Conference Record*, pp. 3915–3919, 2006.

[137] D. J. Crotty, R. L. McKinley, P. Madhav, S. J. Cutler, and M. P. Tornai, "Initial investigation of novel trajectories to improve chest wall imaging in a dedicated breast computed tomography system," *Proceedings of SPIE*, vol. 7258, no. 1, pp. 72585L–72585L–10, 2009.

[138] N. Prionas, K. Lindfors, S. Ray, and S. Huang, "Contrast-enhanced Dedicated Breast CT: Initial Clinical Experience," *Radiology*, vol. 256, no. 3, 2010.

[139] C. H. J. Chang, J. L. Sibala, S. L. Fritz, S. J. Dwyer, A. W. Templeton, F. Lin, and W. R. Jewell, "Computed tomography in detection and diagnosis of breast cancer," *Cancer*, vol. 46, pp. 939–946, Aug. 1980.

[140] P. M. Shikhaliev and S. G. Fritz, "Photon counting spectral CT versus conventional CT: comparative evaluation for breast imaging application.," *Physics in medicine and biology*, vol. 56, pp. 1905–30, Apr. 2011.

[141] J. D. Silkwood, K. L. Matthews, and P. M. Shikhaliev, "Photon counting spectral breast CT: effect of adaptive filtration on CT numbers, noise, and contrast to noise ratio.," *Medical physics*, vol. 40, p. 051905, May 2013.

[142] U. Nyman, B. Elmstå hl, P. Leander, M. Nilsson, K. Golman, and T. Almén, "Are gadolinium-based contrast media really safer than iodinated media for digital subtraction angiography in patients with azotemia?," *Radiology*, vol. 223, pp. 311–8; discussion 328–9, May 2002.

[143] M. Tepel, P. Aspelin, and N. Lameire, "Contrast-induced nephropathy: a clinical and evidence-based approach.," *Circulation*, vol. 113, pp. 1799–806, Apr. 2006.

[144] W. P. Segars, G. Sturgeon, S. Mendonca, J. Grimes, and B. M. W. Tsui, "4D XCAT phantom for multimodality imaging research," *Medical Physics*, vol. 37, no. 9, p. 4902, 2010.

[145] K. Doi, L. Loo, and H. Chan, "X-ray tube focal spot sizes: comprehensive studies of their measurement and effect of measured size in angiography.," *Radiology*, pp. 383–393, 1982.

[146] H. E. Johns and J. R. Cunningham, *The physics of radiology*. American lecture series, Charles C. Thomas, 1983.

[147] X. Gong, S. J. Glick, B. Liu, A. A. Vedula, and S. Thacker, "A computer simulation study comparing lesion detection accuracy with digital mammography, breast tomosynthesis, and cone-beam CT breast imaging," *Medical Physics*, vol. 33, no. 4, p. 1041, 2006.

[148] X. Qian, A. Tucker, E. Gidcumb, J. Shan, G. Yang, X. Calderon-Colon, S. Sultana, J. Lu, O. Zhou, D. Spronk, F. Sprenger, Y. Zhang, D. Kennedy, T. Farbizio, and Z. Jing, "High resolution stationary digital breast tomosynthesis using distributed carbon nanotube x-ray source array.," *Medical physics*, vol. 39, pp. 2090–9, Apr. 2012.

[149] E. Nickoloff, E. Donnelly, L. Eve, J. Atherton, and T. Asch, "Mammographic resolution: influence of focal spot intensity distribution and geometry," *Medical physics*, 1990.

[150] J. Zhou, B. Zhao, and W. Zhao, "A computer simulation platform for the optimization of a breast tomosynthesis system," *Medical Physics*, vol. 34, no. 3, p. 1098, 2007.

[151] B. Zhao and W. Zhao, "Three-dimensional linear system analysis for breast tomosynthesis," *Medical Physics*, vol. 35, no. 12, p. 5219, 2008.

[152] E. Wilkinson, P. N. Johnston, and J. C. Heggie, "A comparison of mammography spectral measurements with spectra produced using several different mathematical models.," *Physics in medicine and biology*, vol. 46, pp. 1575–89, May 2001.

[153] M. R. Ay, S. Sarkar, M. Shahriari, D. Sardari, and H. Zaidi, "Assessment of different computational models for generation of x-ray spectra in diagnostic radiology and mammography," *Medical Physics*, vol. 32, no. 6, p. 1660, 2005.

[154] R. Birch and M. Marshall, "Computation of bremsstrahlung X-ray spectra and comparison with spectra measured with a Ge(Li) detector," *Physics in Medicine and Biology*, vol. 24, pp. 505–517, May 1979.

[155] J. M. Boone and J. A. Seibert, "An accurate method for computer-generating tungsten anode x-ray spectra from 30 to 140 kV.," *Medical physics*, vol. 24, pp. 1661–70, Nov. 1997.

[156] K. Cranley, B. Gilmore, G. Fogarty, and L. Desponds, "Catalogue of Diagnostic X-Ray Spectra and Other Data," tech. rep., IPEM report 78, Institute of Physics and Engineering in Medicine, York, 1997.

[157] T. Fewell, R. Shuping, and K. J. Hawkins, "Handbook of computed tomography x-ray spectra. Final report," Apr. 1981.

[158] T. Fewell and R. Shuping, "Handbook of mammographic x-ray spectra. Final report," Oct. 1978.

[159] G. R. Hammerstein, D. W. Miller, D. R. White, M. E. Masterson, H. Q. Woodard, and J. S. Laughlin, "Absorbed radiation dose in mammography.," *Radiology*, vol. 130, pp. 485–91, Feb. 1979.

[160] J. M. Boone, "Normalized glandular dose (DgN) coefficients for arbitrary x-ray spectra in mammography: Computer-fit values of Monte Carlo derived data," *Medical Physics*, vol. 29, no. 5, p. 869, 2002.

[161] J. M. Boone, K. K. Lindfors, V. N. Cooper, and J. A. Seibert, "Scatter/primary in mammography: comprehensive results.," *Medical physics*, vol. 27, pp. 2408–16, Oct. 2000.

[162] J. M. Boone, A. L. C. Kwan, J. A. Seibert, N. Shah, K. K. Lindfors, and T. R. Nelson, "Technique factors and their relationship to radiation dose in pendant geometry breast CT," *Radiology*, pp. 3767–3776, 2005.

[163] S. J. Glick, S. Thacker, X. Gong, and B. Liu, "Evaluating the impact of x-ray spectral shape on image quality in flat-panel CT breast imaging," *Medical Physics*, vol. 34, no. 1, p. 5, 2007.

[164] Y. Chen, B. Liu, J. M. O'Connor, C. S. Didier, and S. J. Glick, "Characterization of scatter in cone-beam CT breast imaging: Comparison of experimental measurements and Monte Carlo simulation," *Medical Physics*, vol. 36, no. 3, p. 857, 2009.

[165] K. Bliznakova, Z. Bliznakov, V. Bravou, Z. Kolitsi, and N. Pallikarakis, "A three-dimensional breast software phantom for mammography simulation.," *Physics in medicine and biology*, vol. 48, pp. 3699–719, Nov. 2003.

[166] C. Brzymialkiewicz, M. Tornai, R. McKinley, S. Cutler, and J. Bowsher, "3D data acquisition sampling strategies for dedicated emission mammotomography for various breast sizes," *IEEE Symposium Conference Record Nuclear Science 2004.*, vol. 00, no. C, pp. 2596–2600, 2004.

[167] Y. Yi, C.-J. Lai, T. Han, Y. Zhong, Y. Shen, X. Liu, S. Ge, Z. You, T. Wang, and C. C. Shaw, "Radiation doses in cone-beam breast computed tomography: A Monte Carlo simulation study," *Medical Physics*, vol. 38, no. 2, p. 589, 2011.

[168] X. Tang, W. Zhao, Y.-F. Wang, H. Shu, C.-L. Sun, C.-F. Wei, D.-Q. Cao, J.-M. Que, R.-J. Shi, and L. Wei, "Monte Carlo simulation of glandular dose in a dedicated breast CT system," *Chinese Physics C*, vol. 36, pp. 675–680, July 2012.

[169] S.-Y. Huang, J. M. Boone, K. Yang, N. J. Packard, S. E. McKenney, N. D. Prionas, K. K. Lindfors, and M. J. Yaffe, "The characterization of breast anatomical metrics using dedicated breast CT," *Medical Physics*, vol. 38, no. 4, p. 2180, 2011.

[170] A.-K. Carton, A. Grisey, P. M. Carvalho, C. Dromain, and S. Muller, "A Virtual Human Breast Phantom Using Surface Meshes And Geometric Internal Structures," *Breast Imaging (IWDM)*, vol. 8539, pp. 356–363, 2014.

[171] P. R. Bakic, M. Albert, D. Brzakovic, and A. D. A. Maidment, "Mammogram synthesis using a three-dimensional simulation. III. Modeling and evaluation of the breast ductal network," *Medical Physics*, vol. 30, p. 1914, June 2003.

[172] D. T. Ramsay, J. C. Kent, R. A. Hartmann, and P. E. Hartmann, "Anatomy of the lactating human breast redefined with ultrasound imaging.," *Journal of anatomy*, vol. 206, pp. 525–34, June 2005.

[173] S. Huang, J. Boone, and K. Yang, "The effect of skin thickness determined using breast CT on mammographic dosimetry," *Medical physics*, vol. 35, p. 1199, Mar. 2008.

[174] X. R. Yang, J. D. Figueroa, R. T. Falk, H. Zhang, R. M. Pfeiffer, S. M. Hewitt, J. Lissowska, B. Peplonska, L. Brinton, M. Garcia-Closas, and M. E. Sherman, "Analysis of terminal duct lobular unit involution in luminal A and basal breast cancers.," *Breast cancer research : BCR*, vol. 14, p. R64, Jan. 2012.

[175] R. D. Cardiff, U. Wagner, J. A. Evans, C. M. Santos, J. Wolski, and L. Hennighausen, "Structure of the Terminal Ductal Lobular Unit (TDLU)," *[Online]. Available: http://ccm.ucdavis.edu/bcancercd/21/TDLU1.html. [Accessed: 17-Aug-2012].*

[176] W. A. Kalender, "Monte Carlo calculations of x-ray scatter data for diagnostic radiology.," *Physics in medicine and biology*, vol. 26, pp. 835–49, Sept. 1981.

[177] H. P. Chan and K. Doi, "The validity of Monte Carlo simulation in studies of scattered radiation in diagnostic radiology.," *Physics in medicine and biology*, vol. 28, pp. 109–29, Feb. 1983.

[178] J. M. Boone and V. N. Cooper, "Scatter/primary in mammography: Monte Carlo validation.," *Medical physics*, vol. 27, pp. 1818–31, Aug. 2000.

[179] M. Endo, T. Tsunoo, N. Nakamori, and K. Yoshida, "Effect of scattered radiation on image noise in cone beam CT," *Medical Physics*, vol. 28, no. 4, p. 469, 2001.

[180] A. Badal and A. Badano, "Accelerating Monte Carlo simulations of photon transport in a voxelized geometry using a massively parallel graphics processing unit," *Medical Physics*, vol. 36, no. 11, p. 4878, 2009.

[181] I. Kawrakow and M. Fippel, "Investigation of variance reduction techniques for Monte Carlo photon dose calculation using XVMC," *Physics in Medicine and Biology*, vol. 45, pp. 2163–2183, Aug. 2000.

[182] A. Colijn and F. Beekman, "Accelerated simulation of cone beam X-ray scatter projections," *Medical Imaging, IEEE Transactions on*, vol. 23, pp. 584–590, May 2004.

[183] C. Leliveld, "A fast Monte Carlo simulator for scattering in X-ray computerized tomography," *Doctoral, Zurich, Switzerland*, 1996.

[184] P. Johns and M. Yaffe, "Scattered radiation in fan beam imaging systems," *Medical physics*, vol. 9, p. 231, Mar. 1982.

[185] P. Joseph and R. Spital, "The effects of scatter in x-ray computed tomography," *Medical physics*, vol. 9, p. 464, July 1982.

[186] Geant4 Collaboration, "Geant4 physics reference manual," *http://www.cern.ch/geant4*, 1999.

[187] MC Team, "MCNP–A General Monte Carlo N-Particle Transport Code, Version 5," Tech. Rep. March, 2003.

[188] W. Nelson, H. Hirayama, and D. Rogers, "EGS4 code system," Dec. 1985.

[189] J. Boone, "Glandular Breast Dose for Monoenergetic and High-Energy X-ray Beams: Monte Carlo Assessment," *Radiology*, pp. 23–37, 1999.

[190] L. Wilkinson and J. C. Heggie, "Glandular Brest Dose: Potential Errors," 2000.

[191] X. Wu, G. Barnes, and D. Tucker, "Spectral dependence of glandular tissue dose in screen-film mammography.," *Radiology*, Aug. 1991.

[192] J. H. Siewerdsen, L. E. Antonuk, Y. El-Mohri, J. Yorkston, W. Huang, and I. A. Cunningham, "Signal, noise power spectrum, and detective quantum efficiency of indirect-detection flat-panel imagers for diagnostic radiology," *Medical Physics*, vol. 25, p. 614, May 1998.

[193] A.-K. Carton, D. Vandenbroucke, L. Struye, A. D. A. Maidment, Y.-H. Kao, M. Albert, H. Bosmans, and G. Marchal, "Validation of MTF measurement for digital mammography quality control," *Medical Physics*, vol. 32, no. 6, p. 1684, 2005.

[194] M. Freed, S. Park, and A. Badano, "A fast, angle-dependent, analytical model of CsI detector response for optimization of 3D x-ray breast imaging systems," *Medical Physics*, vol. 37, pp. 2593–2605, June 2010.

[195] J. G. Mainprize, A. K. Bloomquist, M. P. Kempston, and M. J. Yaffe, "Resolution at oblique incidence angles of a flat panel imager for breast tomosynthesis," *Medical Physics*, vol. 33, no. 9, p. 3159, 2006.

[196] G. Hajdok and I. Cunningham, "Penalty on the detective quantum efficiency from off-axis incident x rays," *SPIE Medical Imaging*, vol. 5368, pp. 109–118, May 2004.

[197] W. Zhao, G. Ristic, and J. A. Rowlands, "X-ray imaging performance of structured cesium iodide scintillators," *Medical Physics*, vol. 31, no. 9, p. 2594, 2004.

[198] S. Puong, X. Bouchevreau, F. Patoureaux, R. Iordache, and S. Muller, "Dual-energy contrast enhanced digital mammography using a new approach for breast tissue canceling," *Proceedings of SPIE*, vol. 33, no. 0, pp. 65102H–65102H–12, 2007.

[199] J. M. Boone, M. H. Buonocore, and V. N. Cooper, "Monte Carlo validation in diagnostic radiological imaging," *Medical Physics*, vol. 27, p. 1294, June 2000.

[200] Y. Kyriakou, T. Riedel, and W. A. Kalender, "Combining deterministic and Monte Carlo calculations for fast estimation of scatter intensities in CT.," *Physics in medicine and biology*, vol. 51, pp. 4567–86, Sept. 2006.

[201] I. Sechopoulos, S. Suryanarayanan, S. Vedantham, C. D'Orsi, and A. Karellas, "Computation of the glandular radiation dose in digital tomosynthesis of the breast," *Medical Physics*, vol. 34, no. 1, p. 221, 2007.

[202] Y.-H. Kao, M. Albert, A.-K. Carton, H. Bosmans, and A. D. A. Maidment, "A software tool for measurement of the modulation transfer function," *Proceedings of SPIE*, vol. 5745, pp. 1199–1208, 2005.

[203] L. M. Zatz and R. E. Alvarez, "An Inaccuracy in Computed Tomography: The Energy Dependence of CT Values," *Radiology*, vol. 124, pp. 91–97, July 1977.

[204] R. E. Alvarez and A. Macovski, "Energy-selective reconstructions in X-ray computerized tomography.," *Physics in medicine and biology*, vol. 21, pp. 733–44, Sept. 1976.

[205] F. Kelcz, C. Mistretta, and S. Riederer, "Spectral considerations for absorption-edge fluoroscopy," *Medical Physics*, vol. 4, p. 26, 1977.

[206] W. A. Kalender, "Evaluation of a prototype dual-energy computed tomographic apparatus. I. Phantom studies," *Medical Physics*, vol. 13, p. 334, May 1986.

[207] F. Kelcz and C. Mistretta, "Absorption-edge fluoroscopy using a three-spectrum technique," *Medical Physics*, vol. 3, no. 3, p. 159, 1976.

[208] E. Roessl and R. Proksa, "K-edge imaging in x-ray computed tomography using multi-bin photon counting detectors.," *Physics in medicine and biology*, vol. 52, pp. 4679–96, Aug. 2007.

[209] J. P. Schlomka, E. Roessl, R. Dorscheid, S. Dill, G. Martens, T. Istel, C. Bäumer, C. Herrmann, R. Steadman, G. Zeitler, A. Livne, and R. Proksa, "Experimental feasibility of multi-energy photon-counting K-edge imaging in pre-clinical computed tomography.," *Physics in medicine and biology*, vol. 53, pp. 4031–47, Aug. 2008.

[210] T. P. Szczykutowicz and G.-H. Chen, "Dual energy CT using slow kVp switching acquisition and prior image constrained compressed sensing.," *Physics in medicine and biology*, vol. 55, pp. 6411–29, Nov. 2010.

[211] B. Heismann and M. Balda, "Quantitative image-based spectral reconstruction for computed tomography," *Medical Physics*, vol. 36, no. 10, p. 4471, 2009.

[212] R. E. Alvarez, J. A. Seibert, and S. K. Thompson, "Comparison of dual energy detector system performance," *Medical Physics*, vol. 31, no. 3, p. 556, 2004.

[213] G. T. Herman, "Correction for beam hardening in computed tomography.," *Physics in medicine and biology*, vol. 24, pp. 81–106, Jan. 1979.

[214] M. Kachelrieß, K. Sourbelle, and W. A. Kalender, "Empirical cupping correction: A first-order raw data precorrection for cone-beam computed tomography," *Medical Physics*, vol. 33, no. 5, p. 1269, 2006.

[215] C. Maaß, M. Baer, and M. Kachelrieß, "Image-based dual energy CT using optimized precorrection functions: A practical new approach of material decomposition in image domain," *Medical Physics*, vol. 36, no. 8, p. 3818, 2009.

[216] L. Lehmann, R. Alvarez, and A. Macovski, "Generalized image combinations in dual KVP digital radiography," *Medical physics*, 1981.

[217] S. Riederer and C. Mistretta, "Selective iodine imaging using K-edge energies in computerized x-ray tomography," *Medical physics*, 1977.

[218] K. Chuang and H. Huang, "A fast dual-energy computational method using isotransmission lines and table lookup," *Medical physics*, 1987.

[219] Y. Zou and M. D. Silver, "Analysis of fast kV-switching in dual energy CT using a pre-reconstruction decomposition technique," *Proceedings of SPIE*, vol. 6913, pp. 691313–691313–12, 2008.

[220] F. Kelcz, P. Joseph, and S. Hilal, "Noise considerations in dual energy CT scanning," *Medical physics*, vol. 6, no. 5, p. 418, 1979.

[221] S. Puong, P. M. Carvalho, and S. Muller, "Triple-energy contrast enhanced digital mammography," in *SPIE Medical Imaging* (E. Samei and N. J. Pelc, eds.), pp. 762208–762208–11, International Society for Optics and Photonics, Mar. 2010.

[222] T. G. Flohr, C. H. McCollough, H. Bruder, M. Petersilka, K. Gruber, C. Süss, M. Grasruck, K. Stierstorfer, B. Krauss, R. Raupach, A. N. Primak, A. Küttner, S. Achenbach, C. Becker, A. Kopp, and B. M. Ohnesorge, "First performance evaluation of a dual-source CT (DSCT) system.," *European radiology*, vol. 16, pp. 256–68, Feb. 2006.

[223] B. Krauss, B. Schmidt, and T. G. Flohr, *Dual Energy CT in Clinical Practice*. Medical Radiology, Berlin, Heidelberg: Springer Berlin Heidelberg, Jan. 2011.

[224] M. Petersilka, H. Bruder, B. Krauss, K. Stierstorfer, and T. G. Flohr, "Technical principles of dual source CT.," *European journal of radiology*, vol. 68, pp. 362–8, Dec. 2008.

[225] S. J. Glick and C. Didier, "A computer simulation for evaluating dual-energy, contrast-enhanced breast tomosynthesis," *Proceedings of SPIE*, vol. 6510, pp. 65102V–65102V–7, 2007.

[226] S. Puong, X. Bouchevreau, N. Duchateau, R. Iordache, and S. Muller, "Optimization of beam parameters and iodine quantification in dual-energy contrast enhanced digital breast tomosynthesis," *Proceedings of SPIE*, vol. 6913, no. 0, pp. 69130Z–69130Z–11, 2008.

[227] D. Xu, D. A. Langan, X. Wu, J. D. Pack, T. M. Benson, J. E. Tkaczky, and A. M. Schmitz, "Dual energy CT via fast kVp switching spectrum estimation," *SPIE Medical Imaging*, pp. 72583T–72583T–10, Feb. 2009.

[228] F. Kelcz and C. Mistretta, "Absorption-edge fluoroscopy using a three-spectrum technique," *Medical physics*, vol. 3, no. 3, p. 159, 1976.

[229] D. Chakraborty and G. Barnes, "An energy sensitive cassette for dual-energy mammography," *Medical physics*, vol. 16, p. 7, Jan. 1989.

[230] S. Feuerlein, E. Roessl, R. Proksa, G. Martens, O. Klass, M. Jeltsch, V. Rasche, H.-J. Brambs, M. H. K. Hoffmann, and J.-P. Schlomka, "Multienergy photon-counting K-edge imaging: potential for improved luminal depiction in vascular imaging.," *Radiology*, vol. 249, pp. 1010–6, Dec. 2008.

[231] H. Bornefalk, J. M. Lewin, M. Danielsson, and M. Lundqvist, "Single-shot dual-energy subtraction mammography with electronic spectrum splitting: feasibility.," *European Journal of Radiology*, vol. 60, no. 2, pp. 275–278, 2006.

[232] P. Mendonça and R. Bhotika, "Multi-material decomposition of spectral CT images," *Proceedings of SPIE Medical Imaging*, 2010.

[233] L. Yu, X. Liu, and C. McCollough, "Pre-reconstruction three-material decomposition in dual-energy CT," *Proceedings of SPIE Medical Imaging*, vol. 7258, pp. 1–8, 2009.

[234] X. Liu, L. Yu, A. N. Primak, and C. H. McCollough, "Quantitative imaging of element composition and mass fraction using dual-energy CT: Three-material decomposition," *Medical Physics*, vol. 36, no. 5, p. 1602, 2009.

[235] H. Orbey and S. I. Sandler, "On the combination of equation of state and excess free energy models," *Fluid Phase Equilibria*, vol. 111, pp. 53–70, Oct. 1995.

[236] P. Stenner, T. Berkus, and M. Kachelriess, "Empirical dual energy calibration (EDEC) for cone-beam computed tomography," *Medical Physics*, vol. 34, no. 9, p. 3630, 2007.

[237] T. G. Schmidt, "Optimal "image-based" weighting for energy-resolved CT," *Medical Physics*, vol. 36, no. 7, p. 3018, 2009.

[238] J. H. Jorgensen, P. C. Hansen, E. Y. Sidky, I. S. Reiser, and X. Pan, "Toward optimal X-ray flux utilization in breast CT," *11th International Meeting on Fully Three-Dimensional Image Reconstruction in Radiology and Nuclear Medicine*, pp. 1–4, 2011.

[239] J. E. Tkaczyk, V. Lobastov, D. D. Harrison, P. Edic, H. Gao, and D. Rubin, "Equal-dose spectral optimization of spectral CT mono-energy photon counting," *SPIE Medical Imaging*, vol. 8313, pp. 831331–831331–8, 2012.

[240] M. Maddah, P. Mendonça, and R. Bhotika, "Physically meaningful virtual unenhanced image reconstruction from dual-energy CT," *Biomedical Imaging: From Nano to Macro, 2010 IEEE International Symposium on*, pp. 808 – 811, 2010.

[241] R. K. Kaza, E. M. Caoili, R. H. Cohan, and J. F. Platt, "Distinguishing enhancing from nonenhancing renal lesions with fast kilovoltage-switching dual-energy CT.," *AJR. American journal of roentgenology*, vol. 197, pp. 1375–81, Dec. 2011.

[242] J. Huesemann and P. Reimer, "Contrast Parameters for the Assessment of CT," in *Computer Assisted Radiology/ Computergestützte Radiologie* (H. Lemke, K. Inamura, C. Jaffe, and R. Felix, eds.), pp. pp 483–488, Springer Berlin Heidelberg, 1993.

[243] R. F. Wagner and D. G. Brown, "Unified SNR analysis of medical imaging systems," *Physics in Medicine and Biology*, vol. 30, no. 6, p. 489, 1985.

[244] F. Diekmann, S. Diekmann, F. Jeunehomme, S. Muller, B. Hamm, and U. Bick, "Digital mammography using iodine-based contrast media: initial clinical experience with dynamic contrast medium enhancement.," *Investigative radiology*, vol. 40, pp. 397–404, July 2005.

[245] F. Diekmann, "Contrast-enhanced dedicated breast CT.," *Radiology*, vol. 258, pp. 650; author reply 650–1, Feb. 2011.

[246] A. Rose, *Vision: human and electronic*. Optical physics and engineering, New York, NY: Plenum, 1973.

[247] A. Rose, "The sensitivity of the human eye on an absolute scale," *Journal of the Optical Society of America*, vol. 38(2), pp. 196–208, 1948.

[248] K. Young and J. Oduko, "Technical Evaluation of Profile Automatic Exposure Control Software on GE Essential Full Field Digital Mammography Systems," in *NHSBSP Equipment Report 0903*, no. May, Sheffield, UK: NHS Cancer Screening Programmes, 2009.

[249] P. C. Johns and M. J. Yaffe, "X-ray characterisation of normal and neoplastic breast tissues.," *Physics in medicine and biology*, vol. 32, pp. 675–95, June 1987.

[250] M. J. Yaffe and J. A. Rowlands, "X-ray detectors for digital radiography.," *Physics in medicine and biology*, vol. 42, pp. 1–39, Jan. 1997.

[251] M. J. Yaffe and J. G. Mainprize, "Detectors for digital mammography.," *Technology in cancer research & treatment*, vol. 3, pp. 309–24, Aug. 2004.

[252] B. D. Man and S. Basu, "Distance-driven projection and backprojection in three dimensions," *Physics in Medicine and Biology*, vol. 49, pp. 2463–2475, June 2004.

[253] M. J. Yaffe, J. M. Boone, N. Packard, O. Alonzo-Proulx, S.-Y. Huang, C. L. Peressotti, a. Al-Mayah, and K. Brock, "The myth of the 50-50 breast," *Medical Physics*, vol. 36, no. 12, p. 5437, 2009.

[254] Y. Jin, *Implementation and optimization of dual energy computed tomography*. PhD thesis, Friedrich-Alexander- Universität Eralngen- Nürnberg, 2011.

[255] R. Karunamuni, A. A. Zaki, A. V. Popov, E. J. Delikatny, S. Gavenonis, A. Tsourkas, and A. D. A. Maidment, "An Examination of Silver as a Radiographic Contrast Agent in Dual-Energy Breast X-ray Imaging," *Breast Imaging*, vol. 7361, pp. 418–425, Jan. 2012.

[256] T. R. C. Johnson, B. Krauss, M. Sedlmair, M. Grasruck, H. Bruder, D. Morhard, C. Fink, S. Weckbach, M. Lenhard, B. Schmidt, T. Flohr, M. F. Reiser, and C. R. Becker, "Material differentiation by dual energy CT: initial experience.," *European radiology*, vol. 17, pp. 1510–7, June 2007.

[257] S. Puong, R. Iordache, X. Bouchevreau, and S. Muller, "Dual-energy contrast enhanced digital mammography: theoretical and experimental study of optimal monoenergetic beam parameters using synchrotron radiation," *Proceedings of SPIE*, vol. 7258, no. 0, pp. 72583U–72583U–10, 2009.

[258] X. Wu, D. Langan, D. Xu, and T. Benson, "Monochromatic CT image representation via fast switching dual kVp," *Proc SPIE*, vol. 7258, pp. 725845–725845–9, Feb. 2009.

[259] W. Ito, K. Shimura, and N. Nakajima, "Improvement of detection in computed radiography by new single-exposure dual-energy subtraction," *Journal of Digital Imaging*, vol. 1, pp. 42–47, 1993.

[260] E. Fredenberg, M. Hemmendorff, B. Cederstrom, M. Aslund, and M. Danielsson, "Contrast-enhanced spectral mammography with a photon-counting detector," *Medical Physics*, vol. 37, no. 5, p. 2017, 2010.

[261] J. M. Boone, T. R. Fewell, and R. J. Jennings, "Molybdenum, rhodium, and tungsten anode spectral models using interpolating polynomials with application to mammography.," *Medical physics*, vol. 24, pp. 1863–74, Dec. 1997.

[262] S. J. Glick and K. Kalluri, "Investigating possible improvements in image quality with energy-weighting photon-counting breast CT," in *SPIE Medical Imaging* (N. J. Pelc, E. Samei, and R. M. Nishikawa, eds.), pp. 79611T–79611T–10, International Society for Optics and Photonics, Mar. 2011.

[263] J. D. Pack, D. A. Langan, X. Wu, D. Xu, T. M. Benson, A. M. Schmitz, J. E. Tkaczyk, W. Pavlicek, T. F. Boltz II, R. Payden, J. Leverentz, and P. Licato, "Fast kVp switching CT imaging of a dynamic cardiac phantom," in *SPIE Medical Imaging* (E. Samei and J. Hsieh, eds.), pp. 725843–725843–6, International Society for Optics and Photonics, Feb. 2009.

[264] A. S. Wang and N. J. Pelc, "A comparison of dual kV energy integrating and energy discriminating photon counting detectors for dual energy x-ray imaging," *SPIE Medical Imaging*, vol. 8313, pp. 83130W–83130W–13, 2012.

[265] B. Li, G. Yadava, and J. Hsieh, "Quantification of head and body CTDIVOL of dual-energy x-ray CTwith fast-kVp switching," *Medical physics*, pp. 76221Y–76221Y–12, Mar. 2011.

[266] I. Matsuda, M. Akahane, J. Sato, M. Katsura, S. Kiryu, N. Yoshioka, A. Kunimatsu, K. Ino, and K. Ohtomo, "Precision of the measurement of CT numbers: comparison of dual-energy CT spectral imaging with fast kVp switching and conventional CT with phantoms.," *Japanese journal of radiology*, vol. 30, pp. 34–9, Jan. 2012.

[267] X. Wang, D. Meier, and K. Taguchi, "Material separation in x-ray CT with energy resolved photon-counting detectors," *Medical Physics*, no. March, pp. 1534–1546, 2011.

[268] A. S. Wang, D. Harrison, V. Lobastov, and J. E. Tkaczyk, "Pulse pileup statistics for energy discriminating photon counting x-ray detectors," *Medical Physics*, vol. 38, no. 7, p. 4265, 2011.

[269] J. Cammin, S. Srivastava, Q. Tang, W. C. Barber, J. S. Iwanczyk, N. E. Hartsough, and K. Taguchi, "Compensation of nonlinear distortions in photon-counting spectral CT: dead-time loss, spectral response, and beam hardening effects," vol. 8313, no. 410, pp. 83131T–83131T–7, 2012.

[270] C. Ghetti, A. Borrini, O. Ortenzia, R. Rossi, and P. L. Ordonez, "Physical characteristics of GE Senographe Essential and DS digital mammography detectors," *Medical Physics*, vol. 35, no. 2, p. 456, 2008.

[271] P. Liaparinos and K. Bliznakova, "Monte Carlo performance on the x-ray converter thickness in digital mammography using software breast models," *Medical physics*, vol. 6, no. i, pp. 6638–6651, 2012.

[272] A.-K. Carton, R. Acciavatti, J. Kuo, and A. D. A. Maidment, "The effect of scatter and glare on image quality in contrast-enhanced breast imaging using an a-Si/CsI(Tl) full-field flat panel detector," *Medical Physics*, vol. 36, no. 3, p. 920, 2009.

[273] F. H. Seguin, P. Burstein, P. J. Bjorkholm, F. Homburger, and R. A. Adams, "X-ray computed tomography with 50-um resolution," *Applied Optics*, vol. 24, p. 4117, Dec. 1985.

[274] A.-K. Carton, S. Puong, R. Iordache, and S. Muller, "Effects of image lag and scatter for dual-energy contrast-enhanced digital breast tomosynthesis using a CsI flat-panel based system," in *Proceedings of SPIE*, vol. 7961, pp. 79611D–79611D–5, Mar. 2011.

[275] H. Kunze, W. Haerer, J. Orman, T. Mertelmeier, and K. Stierstorfer, "Filter determination for tomosynthesis aided by iterative reconstruction techniques," *9th International Meeting on Fully Three-Dimensional Image Reconstruction in Radiology and Nuclear Medicine*, pp. pp. 309–312, 2007.

[276] L. Apffel, G. Palma, S. Muller, and I. Bloch, "Fuzzy segmentation of masses in digital breast tomosynthesis images based on dynamic programming," in *International Conference on Imaging Theory and Applications (IMAGAPP), Angers, France (June 2010)*, 2010.

[277] S. Vedantham, L. Shi, A. Karellas, K. E. Michaelsen, V. Krishnaswamy, B. W. Pogue, and K. D. Paulsen, "Semi-automated segmentation and classification of digital breast tomosynthesis reconstructed images," in *Engineering in Medicine and Biology Society,EMBC, 2011 Annual International Conference of the IEEE*, pp. 6188–6191, Aug. 2011.

[278] G. Palma, I. Bloch, and S. Muller, "Detection of masses and architectural distortions in digital breast tomosynthesis images using fuzzy and a contrario approaches," *Pattern Recognition*, vol. 47, pp. 2467–2480, July 2014.

[279] Z. Chen, "3D tumor measurement in cone-beam CT breast imaging," *Proceedings of SPIE*, vol. 5367, pp. 558–569, 2004.

[280] S. Ray, N. D. Prionas, K. K. Lindfors, and J. M. Boone, "Analysis of breast CT lesions using computer-aided diagnosis: an application of neural networks on extracted morphologic and texture features," vol. 8315, no. Figure 2, pp. 83152E–83152E–6, 2012.

[281] H. Kuo, M. L. Giger, I. Reiser, J. M. Boone, K. K. Lindfors, K. Yang, and a. Edwards, "Evaluation of stopping criteria for level set segmentation of breast masses in contrast-enhanced dedicated breast CT," vol. 8315, pp. 83152C–83152C–7, 2012.

[282] L. Partain, S. Prionas, E. Seppi, G. Virshup, G. Roos, R. Sutherland, and J. Boone, "Iodine contrast cone beam CT imaging of breast cancer," *Proceedings of SPIE*, vol. 6510, pp. 65102U–65102U–8, 2007.

[283] S. Ulzheimer and T. Flohr, "Multislice CT: current technology and future developments," *Multislice CT*, 2009.

[284] J. Adamson, Z. Chang, Z. Wang, F. Yin, and J. Cai, "Maximum Intensity Projection (MIP) Imaging Using Multi-Slice Cine MRI," *Medical Physics*, vol. 37, pp. 3133–3133, June 2010.

[285] D. D. Michalski and D. M. S. Huq, *Maximum Intensity Projection (MIP) CT Volume*. Berlin, Heidelberg: Springer Berlin Heidelberg, Jan. 2013.

[286] I. Khurram, R. Beinart, V. Zipunnikov, H. Calkins, S. Nazarian, and S. Zimmerman, "Optimal Techniques for Late Gadolinium-Enhanced MRI: Comparison of Delay Time, Slice Thickness, and Multiplanar Reconstruction vs Maximum Intensity Projection for Assessment of Fibrosis in Atrial Fibrillation," *Heart Rhythm*, vol. 10, p. 1751, Nov. 2013.

[287] J. Cohen, "A Coefficient of Agreement for Nominal Scales," *Educational and Psychological Measurement*, vol. 20, pp. 37–46, Apr. 1960.

[288] J. R. Landis and G. G. Koch, "The Measurement of Observer Agreement for Categorical Data," *Biometrics*, vol. 33, p. 159, Mar. 1977.

[289] K. L. Gwet, *Handbook of Inter-Rater Reliability (3rd Edition): The Definitive Guide to Measuring the Extent of Agreement Among Multiple Raters.* Advanced Analytics Press, 2012.

[290] J. L. Fleiss, B. Levin, and M. C. Paik, *Statistical Methods for Rates and Proportions*, vol. 2004. 2004.

[291] A. R. Feinstein and D. V. Cicchetti, "High agreement but low kappa: I. The problems of two paradoxes.," *Journal of clinical epidemiology*, vol. 43, pp. 543–9, Jan. 1990.

[292] D. V. Cicchetti and A. R. Feinstein, "High agreement but low kappa: II. Resolving the paradoxes.," *Journal of clinical epidemiology*, vol. 43, pp. 551–8, Jan. 1990.

[293] R. L. Spitzer, "Quantification of Agreement in Psychiatric Diagnosis," *Archives of General Psychiatry*, vol. 17, p. 83, July 1967.

[294] J. Cohen, "Weighted kappa: Nominal scale agreement provision for scaled disagreement or partial credit.," *Psychological bulletin*, 1968.

[295] S. Puong, *Imagerie du sein multispectrale avec injection de produit de contraste*. Phd thesis, Université Paris XI, 2008.

[296] K. G. Metheany, C. K. Abbey, N. Packard, and J. M. Boone, "Characterizing anatomical variability in breast CT images," *Medical Physics*, vol. 35, no. 10, p. 4685, 2008.

[297] W. A. Kalender, E. Klotz, and L. Kostaridou, "An algorithm for noise suppression in dual energy CT material density images.," *IEEE transactions on medical imaging*, vol. 7, pp. 218–24, Jan. 1988.

[298] C. McCollough and M. V. Lysel, "A correlated noise reduction algorithm for dual-energy digital subtraction angiography," *Medical physics*, 1989.

[299] D. Ergun, C. Mistretta, and D. Brown, "Single-exposure dual-energy computed radiography: improved detection and processing.," *Radiology*, vol. 174, pp. 243–249, 1990.

[300] D. Ergun, "Dual-energy computed radiography: Improvements in processing," in *Proc. SPIE* (M. H. Loew, ed.), vol. 2167, pp. 663–671, International Society for Optics and Photonics, May 1994.

[301] S. Richard and J. H. Siewerdsen, "Comparison of model and human observer performance for detection and discrimination tasks using dual-energy x-ray images," *Medical Physics*, vol. 35, no. 11, p. 5043, 2008.

[302] S. Richard and J. H. Siewerdsen, "Cascaded systems analysis of noise reduction algorithms in dual-energy imaging," *Medical Physics*, vol. 35, no. 2, p. 586, 2008.

[303] G. J. Gang, C. A. Varon, H. Kashani, S. Richard, N. S. Paul, R. Van Metter, J. Yorkston, and J. H. Siewerdsen, "Multiscale deformable registration for dual-energy x-ray imaging," *Medical Physics*, vol. 36, no. 2, p. 351, 2009.

[304] R. Alvarez and A. Macovski, "Noise and Dose in Energy Dependent Computerized Tomography," in *Society of Photo-Optical Instrumentation Engineers (SPIE) Conference Series*, vol. 96, p. 131, 1976.

[305] R. Alvarez and E. Seppi, "A comparison of noise and dose in conventional and energy selective computed tomography," *Nuclear Science, IEEE Transactions on*, no. 2, pp. 2853–2856, 1979.

[306] L. I. Rudin, S. Osher, and E. Fatemi, "Nonlinear total variation based noise removal algorithms," *Physica D: Nonlinear Phenomena*, vol. 60, pp. 259–268, Nov. 1992.

[307] E. Y. Sidky, J. H. Jø rgensen, and X. Pan, "Sampling conditions for gradient-magnitude sparsity based image reconstruction algorithms," *Proceedings of SPIE Medical Imaging*, vol. 8313, no. 1, pp. 831337–831337–8, 2012.

[308] E. Y. Sidky, I. S. Reiser, R. M. Nishikawa, and X. Pan, "Preliminary study on the impact of digital breast tomosynthesis scanning angle on micro-calcification imaging," in *2008 IEEE Nuclear Science Symposium Conference Record*, pp. 4201–4204, IEEE, Oct. 2008.

[309] J. Bian, X. Han, K. Yang, E. Y. Sidky, J. M. Boone, and X. Pan, "A preliminary investigation of reduced-view image reconstruction from low dose breast CT data," *Proceedings of SPIE Medical Imaging*, vol. 8313, pp. 831325–831325–6, 2012.

[310] I. Kastanis, S. Arridge, A. Stewart, and S. Gunn, "3D digital breast tomosynthesis using total variation regularization," in *Digital Mammography* (E. A. Krupinski, ed.), pp. 621–627, Springer Berlin Heidelberg, 2008.

[311] N. Packard and J. M. Boone, "Glandular segmentation of cone beam breast CT volume images," 2007.

[312] J. Michael O'Connor, M. Das, C. S. Dider, M. Mahd, and S. J. Glick, "Generation of voxelized breast phantoms from surgical mastectomy specimens," *Medical Physics*, vol. 40, no. 4, p. 041915, 2013.

[313] C. M. Li, W. P. Segars, G. D. Tourassi, J. M. Boone, and J. T. Dobbins, "Methodology for generating a 3D computerized breast phantom from empirical data," *Medical Physics*, vol. 36, no. 7, p. 3122, 2009.

[314] N. Prionas, G. W. Burkett, S. E. McKenney, L. Chen, R. L. Stern, and J. M. Boone, "Development of a patient-specific two-compartment anthropomorphic breast phantom," *Physics in Medicine and Biology*, vol. 4293, 2012.

[315] H. Langet, A. Reshef, C. Riddell, Y. Trousset, A. Tenenhaus, E. Lahalle, G. Fleury, and N. Paragios, "Nonlinear diffusion constraints for reconstructing subsampled rotational angiography data," in *Proceedings of the 13th International Meeting on Fully Three - Dimensional Image Reconstruction in Radiology and Nuclear Medicine (Fully 3D'13)*, pp. 38–41, 2013.

[316] H. Langet, C. Riddell, Y. Trousset, A. Tenenhaus, E. Lahalle, G. Fleury, and N. Paragios, "Compressed sensing based 3D tomographic reconstruction for rotational angiography.," *Medical image computing and computer-assisted intervention : MICCAI ... International Conference on Medical Image Computing and Computer-Assisted Intervention*, vol. 14, pp. 97–104, Jan. 2011.

[317] H. Langet, C. Riddell, Y. Trousset, A. Tenenhaus, E. Lahalle, G. Fleury, and N. Paragios, "Compressed sensing subtracted rotational angiography with multiple sparse penalty," in *Biomedical Imaging (ISBI), 2012 9th IEEE International Symposium on*, pp. 884–887, 2012.

[318] H. Langet, C. Riddell, and Y. Trousset, "Compressed sensing dynamic reconstruction in rotational angiography," in *Medical Image Computing and Computer-Assisted Intervention - MICCAI 2012*, vol. 7510, pp. 223–230, 2012.

[319] H. Langet and C. Riddell, "Sparsity constraints and dedicated acquisition protocols for improved Digital Subtraction Rotational Angiography," *Proceedings of the 11th International Meeting on Fully Three - Dimensional Image Reconstruction in Radiology and Nuclear Medicine (Fully 3D'11)*, 2011.

[320] T. Goldstein and S. Osher, "The Split Bregman Method for L1-Regularized Problems," *SIAM Journal on Imaging Sciences*, vol. 2, pp. 323–343, Jan. 2009.

[321] J. Hale, *Fundamentals of radiological science*. Charles C Thomas, Publisher, Springfield, IL, Jan. 1974.

[322] O. Klein and Y. Nishina, "Über die Streuung von Strahlung durch freie Elektronen nach der neuen relativistischen Quantendynamik von Dirac," *Zeitschrift für Physik*, vol. 52, pp. 853–868, July 1929.

[323] P. Monnin, D. Gutierrez, S. Bulling, D. Guntern, and F. R. Verdun, "A comparison of the performance of digital mammography systems," *Medical Physics*, vol. 34, no. 3, p. 906, 2007.

[324] H. Q. Le, J. L. Ducote, and S. Molloi, "Radiation dose reduction using a CdZnTe-based computed tomography system: Comparison to flat-panel detectors," *Medical Physics*, vol. 37, no. 3, p. 1225, 2010.

[325] H. Bornefalk and M. Danielsson, "Photon-counting spectral computed tomography using silicon strip detectors: a feasibility study.," *Physics in Medicine and Biology*, vol. 55, no. 7, pp. 1999–2022, 2010.

[326] K. Bliznakova, Z. Kolitsi, and N. Pallikarakis, "Dual-energy mammography: simulation studies.," *Physics in medicine and biology*, vol. 51, pp. 4497–515, Sept. 2006.

[327] C. Archer, M. Tornai, J. Bowsher, and M. Bradshaw, "Initial investigation of circle-plus-arc orbit variants with a dedicated emission mammotomograph," *2002 IEEE Nuclear Science Symposium Conference Record*, pp. 1118–1122, 2003.

[328] R. Ning, X. Tang, D. Conover, and R. Yu, "Flat panel detector-based cone beam computed tomography with a circle-plus-two-arcs data acquisition orbit: Preliminary phantom study," *Medical Physics*, vol. 30, no. 7, p. 1694, 2003.

[329] C. Archer, M. Tornai, J. Bowsher, S. Metzler, B. Pieper, and R. Jaszczak, "Implementation and initial characterization of acquisition orbits with a dedicated emission mammotomograph," *IEEE Transactions on Nuclear Science*, vol. 50, pp. 413–420, June 2003.

[330] S. Vedantham, L. Shi, A. Karellas, and F. Noo, "Dedicated breast CT: radiation dose for circle-plus-line trajectory.," *Medical physics*, vol. 39, pp. 1530–41, Mar. 2012.

[331] H. K. Tuy, "An Inversion Formula for Cone-Beam Reconstruction," *SIAM Journal on Applied Mathematics*, vol. 43, pp. 546–552, June 1983.

[332] Z. Yin, B. De Man, and J. Pack, "3D analytic cone-beam reconstruction for multiaxial CT acquisitions.," *International journal of biomedical imaging*, vol. 2009, p. 538389, Jan. 2009.

[333] M. Beister, D. Kolditz, and W. A. Kalender, "Iterative reconstruction methods in X-ray CT.," *Physica medica : PM : an international journal devoted to the applications of physics to medicine and biology : official journal of the Italian Association of Biomedical Physics (AIFB)*, vol. 28, pp. 94–108, Apr. 2012.

[334] J. Hsieh, *Computed Tomography: Principles, Design, Artifacts, and Recent Advances*. SPIE Press, 2003.

[335] L. Feldkamp, L. Davis, and J. Kress, "Practical cone-beam algorithm," *Journal of the Optical Society of America A*, vol. 1, no. 6, pp. 612–619, 1984.

[336] S. S. Orlov, "Theory of three dimensional reconstruction: I. Conditions for a complete set of projections," *Sov. Phys Cristallogr*, 1975.

[337] S. S. Orlov, "Theory of three dimensional reconstruction: II. The recovery operator," *Sov. Phys Cristallogr*, 1976.

[338] X. Tang, J. Hsieh, A. Hagiwara, R. A. Nilsen, J.-B. Thibault, and E. Drapkin, "A three-dimensional weighted cone beam filtered backprojection (CB-FBP) algorithm for image reconstruction in volumetric CT under a circular source trajectory.," *Physics in medicine and biology*, vol. 50, pp. 3889–905, Aug. 2005.

[339] X. Tang and R. Ning, "A cone beam filtered backprojection (CB-FBP) reconstruction algorithm for a circle-plus-two-arc orbit," *Medical Physics*, vol. 28, no. 6, p. 1042, 2001.

[340] Y. Ye and G. Wang, "Filtered backprojection formula for exact image reconstruction from cone-beam data along a general scanning curve," *Medical Physics*, vol. 32, no. 1, p. 42, 2005.

[341] P. Madhav, D. J. Crotty, R. L. McKinley, and M. P. Tornai, "Evaluation of tilted cone-beam CT orbits in the development of a dedicated hybrid mammotomograph.," *Physics in medicine and biology*, vol. 54, pp. 3659–76, June 2009.

[342] E. Miller, E. McCurry, and B. Hruska, "An infinite number of laminograms from a finite number of radiograms," *Radiology*, vol. 98, pp. 249–255, 1971.

[343] J. Ludwig, T. Mertelmeier, H. Kunze, and W. Härer, "A novel approach for filtered back-projection in tomosynthesis based on filter kernels determined by iterative reconstruction techniques," *Digital Mammography*, pp. 612–620, 2008.

[344] T. Wu, R. H. Moore, and D. B. Kopans, "Voting strategy for artifact reduction in digital breast tomosynthesis," *Medical Physics*, vol. 33, no. 7, p. 2461, 2006.

[345] M. Das, H. Gifford, J. O'Connor, and S. Glick, "Penalized maximum likelihood reconstruction for improved microcalcification detection in breast tomosynthesis," *Medical Imaging, IEEE Transactions on*, vol. 30, no. 4, pp. 904–914, 2011.

[346] I. Sechopoulos, "A review of breast tomosynthesis. Part II. Image reconstruction, processing and analysis, and advanced applications," *Medical Physics*, vol. 40, no. 1, p. 014302, 2013.

[347] P. M. Carvalho, A.-K. Carton, R. Iordache, S. Saab-Puong, and S. Muller, "Comparison of Lesion Extent and Contrast-Agent Uptake in Breast Tomosynthesis versus Cone-Beam Breast CT," *Breast Imaging (IWDM)*, vol. 7361, pp. 434–441, 2012.

[348] P. M. Carvalho, A.-K. Carton, S. Saab-Puong, R. Iordache, and S. Muller, "Spectra optimization for dual-energy contrast-enhanced breast CT," *SPIE Medical Imaging*, 2013.

[349] C. Zeng, P. M. Carvalho, L. Pierce, K. Kanal, L. MacDonald, B. DeMan, P. FitzGerald, S. Muller, and P. Kinahan, "Quantitative Assessment of Attenuation Correction for a Combined PET/MX Scanner for Breast Cancer," in *Biomedical Engineering Society (BMES)*, (Seattle, USA), 2013.

[350] P. M. Carvalho, A.-K. Carton, R. Iordache, S. Saab-Puong, and S. Muller, "Optimization of X-ray Spectra for Dual-Energy Contrast-Enhanced Breast Imaging: Dependency on CsI Detector Scintillator Thickness," *Breast Imaging (IWDM)*, vol. 8539, pp. 95–102, 2014.